

Dark Matter Search with ANTARES

Suche nach Dunkler Materie mit ANTARES

Der Naturwissenschaftlichen Fakultät
der Friedrich-Alexander-Universität Erlangen-Nürnberg
zur
Erlangung des Doktorgrades Dr. rer. nat

vorgelegt von
Holger Martin Motz
aus Passau

Als Dissertation genehmigt von der Naturwissenschaftlichen Fakultät
der Friedrich-Alexander-Universität Erlangen-Nürnberg

Tag der mündlichen Prüfung:	17.11.2011
Vorsitzender der Prüfungskommission:	Prof. Dr. Rainer Fink
Erstberichterstattein:	Prof. Dr. Gisela Anton
Zweitberichterstattein:	Prof. Dr. Ulrich Katz

Abstract

Built in the deep sea of the Mediterranean near Toulon, France, the ANTARES neutrino telescope detects neutrinos which interact inside or close to the detector and bring forth a muon which emits Cherenkov light. The detector consists of a photomultiplier array mounted on flexible strings which are anchored on the seabed. From the position and time of the incident Cherenkov photons, the direction of the muon track and thereby that of its precursor neutrino are reconstructed.

Part of the project's physics program is to search indirectly for Dark Matter, by looking for neutrinos emitted in annihilation processes predicted by theories describing the yet unidentified Dark Matter particles. This thesis covers several aspects of searching for neutrinos from the annihilation of Dark Matter accumulating in the centres of the Earth and the Sun. Introductory, the evidences for the existence of Dark Matter are reviewed and the theoretical foundation of Dark Matter candidate particles are explained, before presenting the different methods of direct and indirect Dark Matter search and examining their prospects. Furthermore, overview of the ANTARES detector is given, with focus on data acquisition and alignment.

The sensitivity of ANTARES to the neutrinos from Dark Matter annihilation in the Sun predicted by the theory of minimal Supergravity (mSugra) is studied, finding that with five years of data parts of the mSugra parameter space could be excluded.

The neutrino reconstruction procedures applied in analysing the neutrino flux from the direction of the Earth's centre are introduced, highlighting the development of an efficient hit selection procedure and a dedicated low energy reconstruction algorithm. An improved Monte Carlo simulation of the atmospheric neutrinos and muons, which includes in situ measured optical background and photomultiplier gain distributions, is used to calculate the expected background for the analysis.

With these reconstruction and simulation methods an upper limit on the rate of Dark Matter annihilation inside Earth from the data taken in December 2010 is obtained, and the corresponding sensitivity of ANTARES for five years is calculated.

Zusammenfassung

Errichtet in der Tiefsee des Mittelmeers nahe Toulon, Frankreich, detektiert das ANTARES Neutrino-Teleskop Neutrinos, die in oder in der Nähe des Detektors interagieren und ein Myon erzeugen, das Cherenkov-Licht aussendet. Der Detektor besteht aus einer Anordnung von Photomultipliern, die an flexiblen, am Meeresboden verankerten, Leinen montiert sind. Aus dem Ort und der Ankunftszeit der detektierten Cherenkov-Photonen werden die Richtung der Myonenspurspur und damit die des ursprünglichen Neutrinos rekonstruiert.

Teil des Wissenschaftlichen Programms des Projektes ist es, indirekt nach Dunkler Materie zu suchen, über Neutrinos, die in Annihilationsprozessen ausgesandt werden, welche die Theorien vorhersagen, die die noch nicht identifizierten Teilchen der Dunklen Materie beschreiben. Diese Arbeit deckt zahlreiche Aspekte der Suche nach Neutrinos aus der Annihilation Dunkler Materie, welche sich im Zentrum von Erde und der Sonne anhäuft ab. Einführend werden die Hinweise auf die Existenz Dunkler Materie besprochen, und die Theoretischen Grundlagen der Teilchen, die Kandidaten für die Dunkle Materie sind, erklärt, bevor verschiedene Methoden der direkten und indirekten Suche nach Dunkler Materie vorgestellt, und ihre Möglichkeiten untersucht werden. Des Weiteren wird ein Überblick über den ANTARES Detektor gegeben, mit dem Schwerpunkt auf der Datennahme und der Ortskalibration.

Die Sensitivität von ANTARES auf Neutrinos aus der Annihilation Dunkler Materie in der Sonne, wie sie von der Theorie der minimalen Supergravitation (mSugra) vorhergesagt werden, wird untersucht, mit dem Ergebnis, dass in fünf Jahren Messzeit Teile des mSugra Parameterraums ausgeschlossen werden könnten.

Die Prozeduren zur Rekonstruktion von Neutrinos, die für eine Analyse des Neutrino-Flusses aus Richtung des Erdkerns werden eingeführt, wobei die Neuentwicklung einer effizienten Trefferselektion und eines dedizierten Rekonstruktionsalgorithmus hervorgehoben werden. Eine verbesserte Monte Carlo Simulation der atmosphärischen Neutrinos und Myonen, die vor Ort gemessenen optischen Untergrund und Photomultiplier-Verstärkungs-Verteilungen einschließt, wird zur Berechnung des erwarteten Untergrunds der Analyse verwendet.

Mit diesen Rekonstruktions- und Simulationsmethoden wird aus den im Dezember 2010 genommenen Daten eine obere Grenze für die Annihilationsrate Dunkler Materie in der Erde gewonnen, und die zugehörige Sensitivität für fünf Jahre berechnet.

Contents

1	Introduction	7
2	Dark Matter	10
2.1	Evidence for Dark Matter from Cosmology	10
2.1.1	The Concordance Model of Cosmology	10
2.1.2	Supernovae Type Ia	12
2.1.3	The Cosmic Microwave Background	13
2.1.4	Large Scale Structures	15
2.1.5	Cold Dark Matter Particles	15
2.1.6	Dark Matter Freeze-out	16
2.2	Evidence for Dark Matter from Astrophysical Observations .	16
2.2.1	Mass of Galaxy Clusters	17
2.2.2	Galaxy Rotation Curves	17
2.2.3	Modified Newtonian Dynamics	17
2.2.4	Merging Galaxy Clusters	18
3	Theoretical Background of Dark Matter	20
3.1	Supersymmetry	20
3.1.1	The Higgs Mass Fine Tuning Problem	20
3.1.2	MSSM	21
3.1.3	Soft Supersymmetry Breaking	21
3.1.4	Unification	23
3.1.5	The Neutralino	23
3.1.6	R-Parity	25
3.1.7	mSugra	25
3.2	Extra Dimension Theories	26
3.2.1	Universal Extra Dimensions	26
3.2.2	Warped Extra Dimensions	27

4	Search for Dark Matter	29
4.1	Direct Detection	29
4.1.1	WIMP nucleus interaction	29
4.1.2	Experimental Setups	29
4.2	Indirect Detection	30
4.2.1	Annihilation Products	30
4.2.2	Signals of Dark Matter Annihilation from the Galactic Centre	31
4.2.3	Neutrinos from Dark Matter Annihilation in the Sun	32
4.2.4	Neutrinos from Dark Matter Annihilation in the Earth	33
5	ANTARES	36
5.1	Operating Principle	36
5.2	Detector Environment	36
5.3	Detector Infrastructure	37
5.3.1	The ANTARES Lines	37
5.3.2	The ANTARES Storeys	39
5.3.3	Offshore Data Acquisition Electronics	39
5.4	Data Processing	40
5.4.1	Time Measurement and Timing calibration	41
5.4.2	Amplitude Measurement and Charge Calibration	42
5.4.3	Walk Effect Correction	43
5.4.4	Calibration Datasets	43
5.4.5	Triggering	44
5.4.6	OM Condition	45
5.4.7	In Situ Calibration with ^{40}K	46
5.5	Detector Alignment	46
5.5.1	Acoustic Positioning System	47
5.5.2	Storey Orientation Measurement	47
5.5.3	In Situ Calibration of Compasses and Tiltmeters	48
5.5.4	The Lineshape Formula	49
5.5.5	Fitting Algorithm	51
5.5.6	Alignment Precision	53
6	Sensitivity of ANTARES to mSugra	55
6.1	Effective Area in the Low Energy Regime	55
6.2	Signal Neutrino Flux	56
6.2.1	Regions of the mSugra Parameter Space	56
6.2.2	mSugra Parameter Space Scan	57
6.2.3	Calculation of the Neutrino Flux	57
6.3	Calculation of the Sensitivity	60

6.3.1	Signal Detection Rate	60
6.3.2	ANTARES Sensitivity for Five Years	60
6.4	Comparison to other Experiments	62
6.4.1	Spin Independent Cross Section	63
6.4.2	Spin Dependent Cross Section	63
7	Event Reconstruction	67
7.1	Background	67
7.1.1	Optical Background	68
7.1.2	Electromagnetic and Hadronic Showers	69
7.1.3	Atmospheric Muons	69
7.2	SeaTray Software Framework	71
7.3	Hit Selection Strategies	72
7.3.1	Triggered Hits	72
7.3.2	Cluster Hit Selection	72
7.4	BBFit Reconstruction	77
7.4.1	Quality Cuts	78
7.5	Artificial Neural Networks	78
7.5.1	Event Classification	78
7.5.2	Energy Reconstruction	79
7.6	Simulated Annealing Track Reconstruction	80
7.6.1	The Gulliver Reconstruction Framework	82
7.6.2	Track Parallel Parametrisation	82
7.6.3	Probability Density Function	83
7.6.4	Prefits	85
7.6.5	Final Fit	86
7.6.6	Event Preselection	86
7.6.7	Quality Cuts	88
7.6.8	Reconstruction Performance	89
7.7	Aart Reconstruction	92
7.7.1	Reconstruction Steps	92
7.7.2	Cut Parameters $\hat{\alpha}_\mu$ and Λ	93
8	Monte Carlo Simulation	94
8.1	Simulation Chain	94
8.1.1	Atmospheric Muon Simulation	94
8.1.2	Neutrino Simulation	96
8.1.3	Event Weights	97
8.1.4	Simulation of the PMT and DAQ Electronics	97
8.1.5	Addition of Optical Background from Minimum Bias Events	100

8.1.6	Generation of Monte Carlo Sets for Groups of Runs	102
8.1.7	Events from Dark Matter Annihilation	103
8.1.8	Events from Pure Optical Background	105
8.2	Comparison of Measured Data and Simulation	106
8.2.1	Trigger Level Hit Distributions	107
8.2.2	Reconstruction Level Event Distributions	108
8.2.3	Angular Distribution of Events	114
8.2.4	Energy Distribution of Events	119
8.2.5	Discussion	119
9	Limit on Dark Matter Annihilation	122
9.1	Data Preparation	122
9.1.1	Selection on Optical Modules	123
9.1.2	Timeframe Quality Selection	123
9.1.3	Retriggering of Events	123
9.2	Event Selection Cuts	124
9.2.1	Performance of the Event Classification	124
9.2.2	Cuts to Reject Atmospheric Muons for BBFit	124
9.2.3	Data to Monte Carlo Comparison on Neutrino Events	128
9.2.4	Cut to Reject Atmospheric Muons for the Simulated Annealing Fit	131
9.2.5	Search Cone Optimisation	131
9.2.6	Systematic Errors	135
9.3	Results	135
9.3.1	Limit from December 2010 Data	135
9.3.2	Sensitivity for Five Years	140
9.4	Performance of the Reconstruction Algorithms	144
9.4.1	Atmospheric Neutrino Flux	144
9.4.2	Signal Neutrino Flux	144
10	Conclusions and Outlook	151
10.1	Detector Alignment	151
10.2	Sensitivity Studies	152
10.3	Event Reconstruction	152
10.4	Understanding the Detector Properties	153
10.5	Physics Analysis	154
A	Runlist	156
B	Simulated Annealing Fit PDF	169

C List Of Figures	169
D List Of Tables	173
E Bibliography	174

Chapter 1

Introduction

"No amount of experimentation can ever prove me right; a single experiment can prove me wrong."

Albert Einstein

For centuries, cosmology has been a discipline shared more between religion and philosophy than being a part of science. But with the advent of nuclear and particle physics, together with Astronomy providing information on all kinds of processes and objects in outer space with ever better observations, it has brought forward detailed theories about the nature and development of the Universe. While the continued expansion of the Universe and its origin in a Big Bang, established by George Lemaître and Edwin Hubble in the 1920s, are accepted as common knowledge today, modern cosmology gives a far more detailed picture of the Universe. The development of the Universe from only shortly after the Big Bang to its present state is described by a cosmological theory, based on a series of observations, and predicting many observables allowing to test its truth. The most intriguing predictions are that of the existence of Dark Energy and Dark Matter. The first is an unknown form of energy, exerting a dispersing force on the Universe and thereby accelerating its expansion. The second is an invisible substance, by far exceeding the amount of visible matter, that keeps the Universe, Galaxy Clusters and individual Galaxies together by the gravity originating from its mass. Through observing its gravitational influence, the existence of Dark Matter is well established, and its distribution on large scales known. The concept of the Dark Matter consisting of yet undiscovered neutral elementary particles is well integrated in the theories describing the formation of large scale structures

from the primordial plasma filling the early Universe. In chapter 2 the evidences for the existence of Dark Matter and the constraints on its nature from the cosmological framework are summarised. Many theories reaching beyond the Standard Model of particle physics predict new particles that could form one or the sole component of the Dark Matter, with the majority comprising an annihilation process giving birth to high energy particles, including neutrinos. Chapter 3 gives an overview of those theories, especially Supersymmetry, which in the form of the Neutralino features one of the best studied Dark Matter candidates. The predictions on the properties of the Dark Matter particles from beyond the Standard Model theories allows to gain information on them through the efforts to detect Dark Matter particles. The methods used in direct Dark Matter search, which looks for collisions of the Dark Matter particles with nuclei, and indirect Dark Matter search, which is based on the detection of annihilation products, are introduced in chapter 4. Especially the indirect Dark Matter search, which is sensitive to the Dark Matter's annihilation reaction, uses the Universe as a laboratory for high energy physics. One of the most promising messenger particles utilised in indirect Dark Matter search is the neutrino, since it can convey information about annihilation processes within massive stellar objects, like Sun and Earth, in which the Dark Matter might accumulate.

Experimental neutrino physics started from experiments chemically detecting neutrino induced nuclear transmutations, such as the from 1970 till 1994 running Homestake experiment, headed by Raymond Davis and John Bahcall, that detected a deficiency of neutrinos from solar fusion reactions, the solar 'neutrino problem' which would later be solved by the introduction and discovery of neutrino oscillations. Today, the field of neutrino astronomy with Cherenkov detectors is emerging, studying distant astronomical objects in the light of neutrinos. It is spearheaded by Super-Kamiokande [1] and the Baikal Deep Underwater Neutrino Telescope [2], with the currently largest telescopes IceCube [3] on the Southern Hemisphere, built in the Antarctic ice at the South Pole, and ANTARES [4] on the Northern Hemisphere. The ANTARES neutrino telescope was built in the deep sea of the Mediterranean near Toulon, France, and detects neutrinos by the Cherenkov light emission of muons created in the rare interactions with matter of the former. Apart from indirect Dark Matter search, the experiment's broad physics program includes, the search for neutrino point sources, e.g. in the form of cosmic ray accelerators, diffuse cosmogenic neutrino fluxes, transient sources like Gamma Ray Bursts and the analysis of the neutrino flux from cosmic ray interactions in the atmosphere with the associated neutrino oscillation effects. The Cherenkov

light is detected by a photomultiplier array mounted on flexible strings affixed to the seabed, a construction described in detail in chapter 5, together with the principles and techniques employed to identify and reconstruct the signatures of neutrinos.

The above mentioned connection between Dark Matter and particle physics allows to use ANTARES results to probe theories, such as Supersymmetry. Minimal Supergravity (mSugra), a widely popular and established scenario, predicts significant neutrino fluxes from Neutralino annihilation for some combinations of its underlying parameters. Chapter 6 explores the sensitivity of ANTARES to constrain the mSugra parameter space by analysing the neutrino flux from the Sun for the predicted additional neutrinos.

The Earth, which like the Sun could be a gravitational trap hosting accumulated WIMPs, serves as the potential source studied in the physics analysis completing this thesis. Towards this end, the methods utilised for reconstruction of neutrinos are introduced in chapter 7, presenting innovations especially designed to help in the intended analysis. Processing the data from the Cherenkov light signatures in the detector to measured neutrinos with a known direction is mirrored by a Monte Carlo Simulation. The simulation is needed to make predictions on the expected number of events for the signal flux from Dark Matter annihilations and the irreducible background from atmospheric neutrinos. The elements of this simulation, improvements made to it in the context of this work and a general comparison of its results to the measured data are illustrated in chapter 8. Employing the newly developed techniques the data taken in December 2010 was analysed was an upper limit was set on Dark Matter annihilations inside Earth, which is presented in chapter 9.

Chapter 2

Dark Matter

Dark Matter does interact via gravity, yet does not interact directly with photons, the gauge bosons of electromagnetism. Dark Matter plays a crucial role in nearly all cosmological models discussed today as a major component of the energy content of the Universe, by far surpassing the amount of baryonic matter.

2.1 Evidence for Dark Matter from Cosmology

The development of the Universe as a whole is usually described as a dynamic system with the methods provided by the theory of General Relativity. The expansion of the Universe from the Big Bang onward is determined by the interplay between its matter and energy content and the curvature of spacetime.

2.1.1 The Concordance Model of Cosmology

The Friedman equation

$$H^2(t) = H_0^2 \left[\frac{\Omega_m}{a(t)^3} + \frac{1 - \Omega_m - \Omega_\Lambda}{a(t)^2} + \Omega_\Lambda \right] \quad (2.1)$$

describes the time evolution of the expansion rate of the Universe, represented by the Hubble Parameter H , as function of the scale factor a , with

$$H = \frac{\dot{a}}{a} \quad (2.2)$$

It is a solution of the Einstein Field Equation assuming a homogenous and isotropic universe. The parameter Ω_m represents the density of all

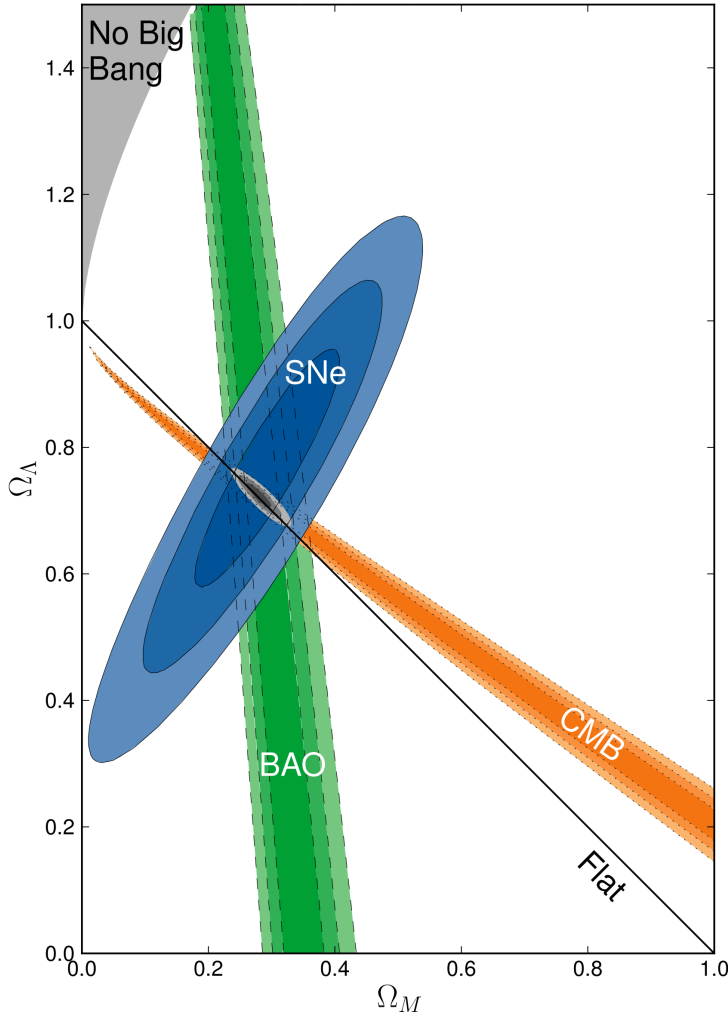


Figure 2.1: Three sources of information constrain the parameters of the Concordance Model of cosmology: SN Ia (SNe), the CMB and baryon acoustic oscillations (BAO) from which large scale structures originate. From [5]

matter in the Universe, both Dark Matter and visible matter, normalised to the critical density ρ_{crit} for which the curvature equals zero i.e. a flat Universe. $a(t)$ is dependent on the equation of state of the energy content of the Universe. Depending on the temperature, either a state equivalent to a photon gas with pressure $p = \frac{1}{3}\rho$ is realised, or the matter condensates and becomes pressure free.

Ω_Λ represents another form of energy, called Dark Energy. Its equation of state yields negative pressure, it thus accelerates the expansion of the Universe. While for a Universe without Dark Energy, the question whether it will expand forever or eventually collapse is tied to the curvature, the introduction of Dark Energy disentangles this relation.

Many experiments provide data to constrain these parameters to the scenario called the Concordance Model of Cosmology, in which $\Omega_m = 0.27$ and $\Omega_\Lambda = 0.73$ [6]. Surveys conducting a census of the luminous and visible matter in the Universe and the ratio of light elements from primordial nucleosynthesis measured in early stars allow to determine the contribution of baryonic matter Ω_b in Ω_m to 0.044, with luminous matter contributing even only $0.003 < \Omega_{lum} < 0.008$. With the remaining amount of matter unaccounted for, the Concordance Model makes a strong statement for the existence of an yet unknown Dark Matter component.

Three principal methods are used to pinpoint the exact cosmological configuration: Observation of supernovae of type Ia (SN Ia), measurements of the Cosmic Microwave Background (CMB) and analysis of the distribution of large scale structures. Together they pinpoint the cosmological parameters to the values above, as outlined in figure 2.1.

2.1.2 Supernovae Type Ia

SN Ia, which are distinguished from general type I supernovae by not only featuring no hydrogen spectral lines, but also by lacking those of silicon, have been found to be uniform in their luminosity and in their time evolution, the lightcurve.

They are thought to be caused by the collapse of a white dwarf, which has accreted mass from a companion star up to the Chandrasekhar limit of 1.38 solar masses. At this point the white dwarf, which up to then resisted the gravitational pressure due to the degeneracy of the electrons in its carbon and oxygen core, collapses to form a neutron star. This predetermined setup of all supernovae type Ia gives an explanation of their uniformity. The luminosities of these supernovae in visible light are spread at the peak of their lightcurves by up to about 0.4 mag [9], but a relation between the duration and luminosity exists, through which the observed luminosity can be normalised.

The redshift of each supernova is measurable through emission and absorption lines in their spectra, while the distance is determined by the observed luminosity. Analysing samples of supernovae with different redshifts, especially looking at early ones with high redshifts, makes it possible to study the expansion of the Universe with time. As conveyed by figure 2.2, the analysis of the available data corroborates the hypothesis of an universe with $\Omega_\Lambda = 0.73$ over one without Dark Energy.

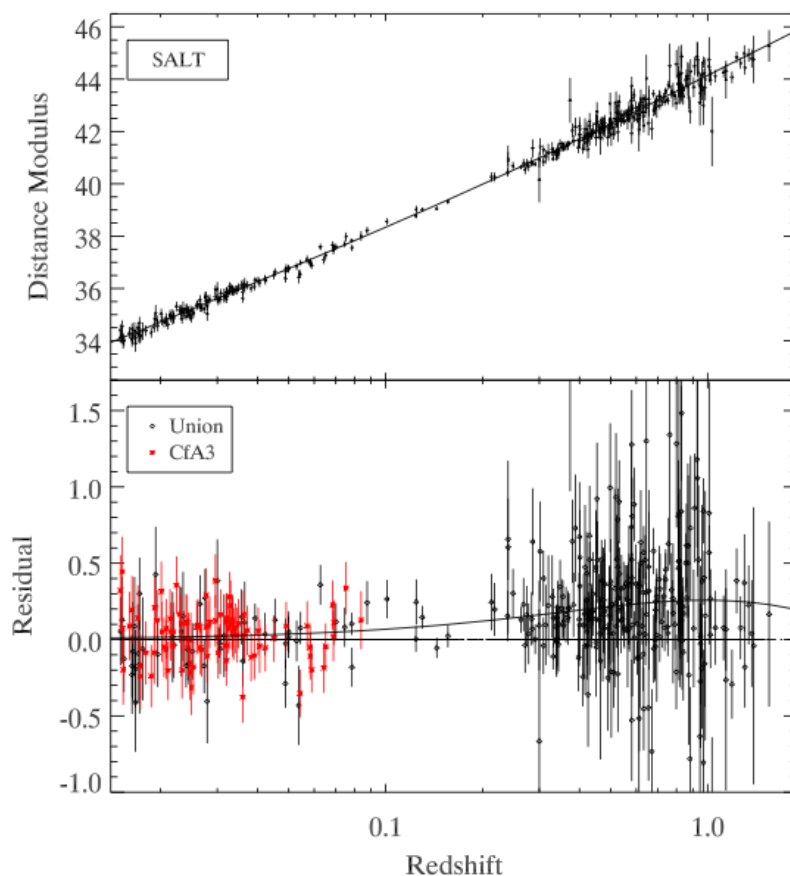


Figure 2.2: The Hubble diagram (top) and the residuals compared to a Universe without Dark Energy (bottom) for SN Ia from [7]. The lightcurves were normalised with SALT [8]

2.1.3 The Cosmic Microwave Background

The Cosmic Microwave Background is the radiation emitted when the temperature of the expanding universe dropped so far, that matter fell out of equilibrium with electromagnetic radiation. Due to the continued expansion of the universe this blackbody radiation spectrum has been redshifted to that emitted by a blackbody of about 3 K. Discovered in 1965 in a ground based antenna as background [10], observation of the CMB has moved to space based microwave spectrometers, able to measure tiny temperature fluctuations visible in the CMB. These fluctuations carry information about temperature differences and corresponding structures present

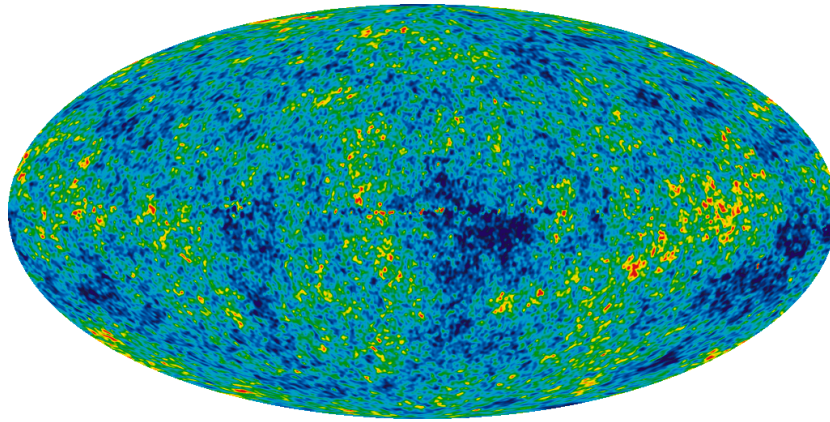


Figure 2.3: The skymap of the CMB as measured by WMAP, with the colour indicating temperature differences in a range of $\pm 200 \mu\text{K}$. From [6]

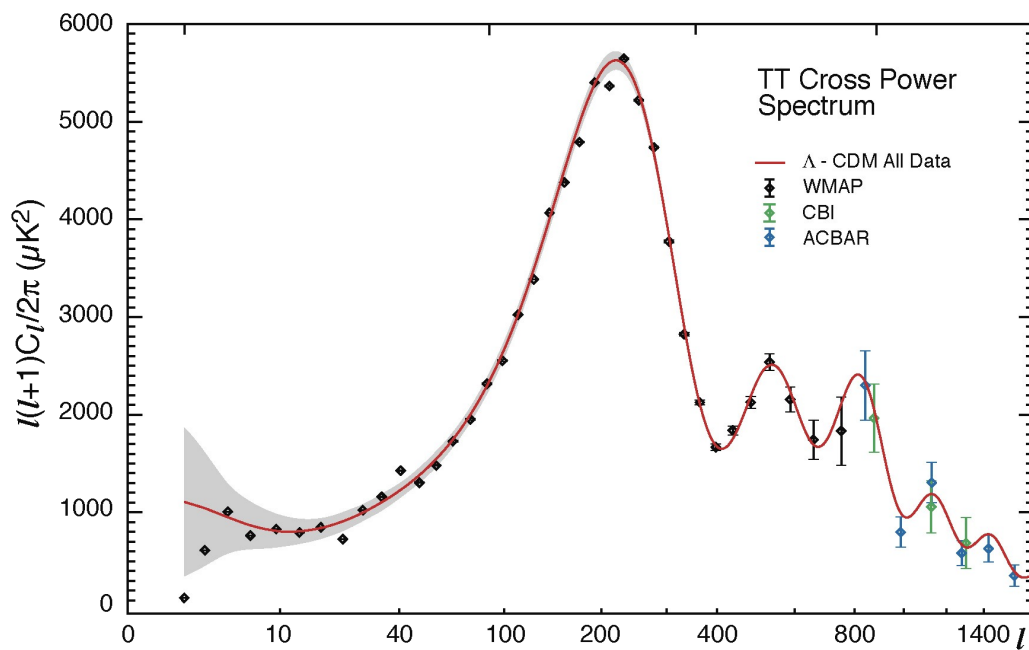


Figure 2.4: The multipole spectrum of the CMB as measured by WMAP. From [6]

in the primordial plasma shortly before the freeze-out. The resolution of the microwave image of the CMB, the one in figure 2.3 taken by the Wilkinson Microwave Probe (WMAP), improved continuously and is expected to improve further with WMAP's successor, the Planck spacecraft [11].

The expansion of the observed structures into multipole components, as depicted in figure 2.4, features a distinct peak at about $l = 200$, which is associated with structures of one degree. If assuming a flat Universe, the light moves unbent, and this peak is equivalent to the wavelength of the largest oscillations in the baryon-photon plasma. The wavelength in turn is linked to Ω_m and Ω_b , as it depends on the sound horizon in this plasma [12]. The initial cause for the oscillations is thought to be the formation of gravity wells from small perturbations magnified by a phase of inflation, in which Dark Matter is accumulated due to the cooling of the expanding Universe, further deepening the wells. This gravitational landscape is the basis for all later structure formation.

2.1.4 Large Scale Structures

The simulation of structure formation provides a theoretical foundation for the shapes of Dark Matter halos around galaxy clusters and galaxies. In those simulations, conducted as many-body calculations starting from the initial conditions of the early Universe with small perturbations, the Dark Matter condenses into a structure of filaments and clusters at their junctions. The baryonic matter, which is much less abundant and therefore only a second order component, accumulates in those gravity wells and forms galaxies and, on a larger scale, clusters of galaxies. The distribution of matter predicted is found again in the results published by sky surveys like 2DF [13] and SDSS [14].

2.1.5 Cold Dark Matter Particles

In order to allow the formation of structures, the Dark Matter has to consist of stable heavy particles in the GeV mass range to be a cold component within the early plasma. If it were of lighter particles, any emerging structures would be smeared out as the kinetic energy is much larger than the potential energy due to gravity [15]. This rules out the three generations of light neutrinos from the Standard Model as the primary Dark Matter component, but they form a component of Ω_m , as so-called Hot Dark Matter, since they are created from the plasma in a freeze-out analogous to the photons of the CMB. A generic Cold Dark Matter (CDM) particle candidate is

described by the acronym WIMP (Weakly Interacting Massive Particle), a particle with sufficient mass not to conflict with structure formation, which only interacts through gravity and the weak force.

2.1.6 Dark Matter Freeze-out

Any possible CDM particles have to originate from the particle soup in the early Universe, where they are created and annihilated in equilibrium with other particle types. With the expansion of the Universe this plasma cools down, the reaction rates decrease, and the Dark Matter freezes out. If the Dark Matter particle is a boson or a Majorana fermion, it can undergo a self-annihilation process and be the sole constituent of the CDM. In this case, the relic density is the endpoint of an evolution of the particle density n described by the Boltzmann-Equation dependent on the Hubble parameter H , the averaged product of self-annihilation cross section, relative particle velocity $\langle\sigma_{A\bar{v}}\rangle$ and the density at equilibrium n_{eq}^2 :

$$\frac{dn}{dt} = -3Hn - \langle\sigma_{A\bar{v}}\rangle \cdot (n^2 - n_{eq}^2) \quad (2.3)$$

Assuming homogeneity, its mass m then determines the fraction of CDM Ω_{CDM} of the total energy density of the Universe:

$$\Omega_{CDM} = \frac{m \cdot n}{\rho_{crit}}, \quad (2.4)$$

An alternative to the freeze-out scenario are non-thermal creation mechanisms, e.g. in the case of Axions [16], which as bosons could form a condensate with an uniform, extremely low kinetic energy. This would allow for the CDM to be made of particles in the mass range of a few eV or below.

2.2 Evidence for Dark Matter from Astrophysical Observations

While there is a need for a Dark Matter component in nearly all cosmological models, more direct evidence suggesting the existence of Dark Matter halos around galaxies and clusters of galaxies exists.

2.2.1 Mass of Galaxy Clusters

A first observation hinting at the existence of invisible matter was made by Zwicky in 1937 [17], when he studied the Coma Galaxy Cluster and found the component galaxies to move at higher velocities than predicted by the virial theorem for the mass of the observed luminous matter.

Another effect suggesting the presence of additional mass is gravitational lensing. The mass of galaxy clusters was probed by observing light from an object behind the cluster which is bent around it. This leads to an amplification of the light intensity, a doubling of the object, or its distortion into an Einstein Ring, depending on the exact relative positions [18]. Based on the Einstein Field Equations, the mass M of the foreground object with a known distance r , in this case the galaxy cluster in question, can be calculated from the angle of deflection Θ as

$$\Theta = \frac{4GM}{rc^2} \quad (2.5)$$

2.2.2 Galaxy Rotation Curves

On the scale of individual galaxies, the velocity of the outer regions in their rotation around the centre is found to be higher than expected from the mass of the visible matter. The rotation curves, which can be precisely measured through Doppler shift of spectral lines [19], are flat instead of falling with distance from the centre, examples of which are in figure 2.5, indicating not only an halo of invisible mass, but also that it extends further outward than the exponentially decreasing luminous matter. This feature was confirmed in extensive observation campaigns on several hundred galaxies [20].

The link between these discrepancies and the existence of an invisible Dark Matter component is based on the validity of Newtonian gravity and General Relativity (GR). Even though the application of GR lowers the required enclosed mass significantly, the observed rotation curves can not be explained without an additional mass component [22].

2.2.3 Modified Newtonian Dynamics

An alternative explanation of the faster rotation of the outer parts of galaxies is the assumption of Modified Newtonian Dynamics (MOND), for which several theories exist, reviewed e.g. in [23]. Independent of the underlying explanation for the effect, the gist of all MOND theories is the modification of the equality between the gravitational force $F = G \cdot m \cdot M \cdot r^{-2}$

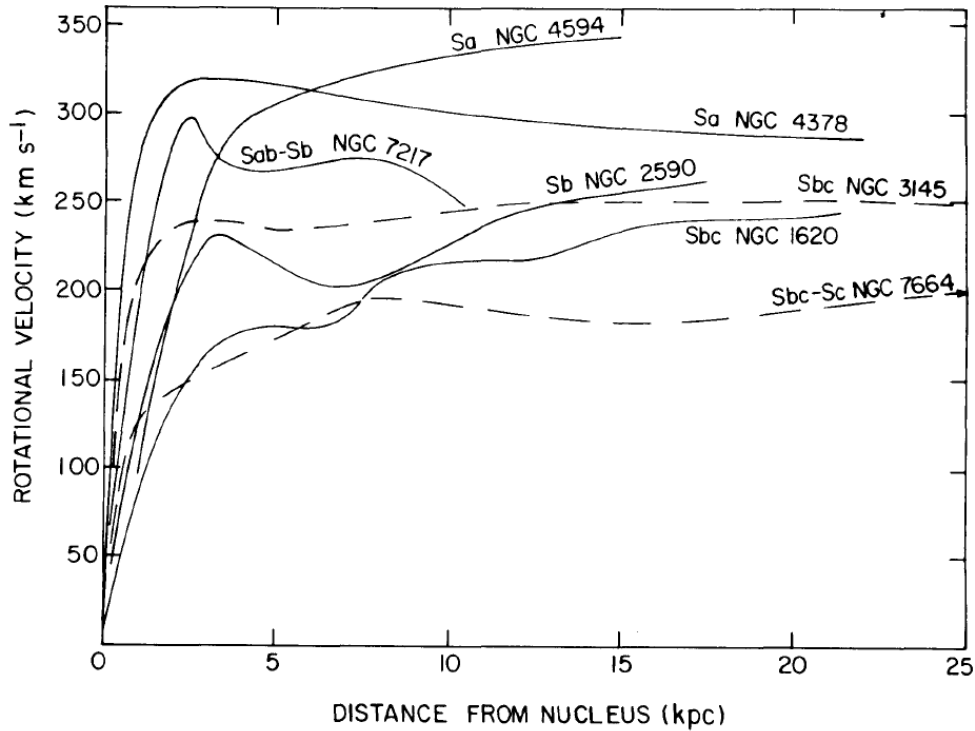


Figure 2.5: Examples of measured rotation curves of spiral galaxies from [21].

and Newton's second law $F = m \cdot a$ for small values of a . This is done by introducing a term a_0 for the case of $a \ll a_0$, so that the new equality reads

$$\frac{a^2}{a_0} = MG r^{-2} \quad (2.6)$$

while the original relation remains valid for $a \gg a_0$ [24]. Whether regarded as a modification of the law of inertia or of the theory of gravity, in either way the observed flat galactic rotation curves can be remodelled by assuming this modification and a suitable choice of a_0 [25]. Still, MOND fails to give predictions for other observables, which prevents it from being a viable substitute for the existence of Dark Matter.

2.2.4 Merging Galaxy Clusters

Since the presumed Dark Matter and the luminous matter in above mentioned cases occupy the same space or are in a configuration with a spherical or rotational symmetry, an explanation of the effects by a modified law

of gravity is possible. However, this ansatz gives no explanation for the behaviour of merging clusters, where a spatial separation of Dark Matter and the baryonic matter seems to occur. The visible matter of two merging clusters is traced by optical and X-Ray observation, while the general distribution of matter, dominated by Dark Matter, is probed through gravitational lensing. The baryonic matter of the two clusters, more precisely intergalactic plasma clouds which drag along the galaxies, interacts and gets slowed down, while the nearly collisionless Dark Matter halos propagate through each other without interference [26].

Chapter 3

Theoretical Background of Dark Matter

3.1 Supersymmetry

The concept of Supersymmetry introduces a way to connect the constituents of matter, fermions, and the exchange particles of the fundamental forces, gauge bosons, by extending the Poincaré group. A Lagrangian can be formulated in the representation of superfields, which contain both fermionic and bosonic fields as components. To the four bosonic (commuting) degrees of freedom of Minkowski space, four fermionic degrees of freedom are added on Grassmann coordinates whose algebra intrinsically provides the anticommutating relations required for fermionic fields [27]. The component fields of the superfields are linked by the Supersymmetry operator Q , which changes the spin by $1/2$, e.g. transforms a scalar boson with spin 0 into a fermion with spin $1/2$. The original field and the particle fields created in this way form supermultiplets, which through successive application of Q can contain an arbitrary number of them. A theory which allows for a single application of Q is called $N = 1$ Supersymmetry, if Q can be applied twice, $N = 2$ and so on.

3.1.1 The Higgs Mass Fine Tuning Problem

Though formulated earlier for aesthetic reasons, one motivation for the existence of Supersymmetry is the divergence arising from loop corrections to the mass of the Higgs boson. The Higgs boson which couples through Yukawa terms to all massive particles receives positive corrections to its mass from fermionic loops, while bosonic terms reduce it. Including only

H_1^0	neutral, cp-even
H_2^0	neutral, cp-even (lightest Higgs boson, also designated h)
A	neutral, cp-odd
H_1^-	charged
H_2^+	charged

Table 3.1: List of Higgs bosons in the MSSM

Standard Model particles, the loop terms diverge, which will only lead to a Higgs mass in the expected range, if the couplings are fine-tuned to cancel each other, though the individual terms are assumed to be cut off at the Planck Scale. Introduction of two bosonic fields for each pair of fermions, one each for left and right handed components, leads to natural cancellation of those terms, avoiding the divergence [28].

3.1.2 MSSM

The Minimal Supersymmetric Extension of the Standard Model (MSSM) adds a single superpartner to each Standard Model particle, including the Higgs sector. The single Higgs doublet from the Standard Model is expanded to two doublets. In this way one Higgs with positive vacuum expectation value gives mass to the top type quarks, and another to the bottom type quarks and the leptons. The Higgs Mechanism uses three degrees of freedom from the originally eight of the two Higgs doublets, to give mass to the massive gauge bosons. The remaining five form physical particles with the properties listed in table 3.1.

With this addition, the particle spectrum of the MSSM consists of chiral multiplets, which encompass fermionic Standard Model particles and their superpartners, and vector multiplets for the gauge bosons and their superpartners. The names of the superpartners are derived from their Standard Model base particles by adding a 's-' prefix in the case of chiral multiplets and by an '-ino' suffix in the case of vector multiplets. A list of the Standard Model particles and their associated superpartners is given in table 3.2.

3.1.3 Soft Supersymmetry Breaking

The operator Q changes the spin of a particle, while all other properties remain unchanged. Supersymmetry would postulate the existence of a set

standardmodel	name	spin	superpartner	name	spin
ν_e, ν_μ, ν_τ	neutrinos	1/2	$\tilde{\nu}_e, \tilde{\nu}_\mu, \tilde{\nu}_\tau$	sneutrinos	0
e	electron	1/2	\tilde{e}	selectron	0
μ	myon	1/2	$\tilde{\mu}$	smyon	0
τ	tau	1/2	$\tilde{\tau}$	stau	0
u, d, s, c, b, t	quarks	1/2	$\tilde{u}, \tilde{d}, \tilde{s}, \tilde{c}, \tilde{b}, \tilde{t}$	squarks	0
$H_1^0, H_2^0, H_1^-, H_2^+$	Higgs bosons	1	$\tilde{H}_1^0, \tilde{H}_2^0, \tilde{H}_1^-, \tilde{H}_2^+$	Higgsinos	1/2
g	gluons	1	\tilde{g}	gluinos	1/2
W^+, W^-, W^0	W-bosons	1	$\tilde{W}^+, \tilde{W}^-, \tilde{W}^0$	winos	1/2
B	B-boson	1	\tilde{B}	bino	1/2

Table 3.2: List of Standard Model particles and associated superpartners

of particles with the masses and charges of the Standard Model particles. The existence of those particles is of course easily excluded. Thus Supersymmetry is required to be a broken symmetry, in which the masses of the superpartners are large enough for them neither to exist naturally nor be detectable in experiments conducted so far. The breaking can be expressed as a potential V added to the Lagrangian, with a possible notation as follows [29]:

$$\begin{aligned}
 V = & \epsilon_{ij}(-\tilde{\mathbf{e}}_R^* \mathbf{A}_E \mathbf{Y}_E \tilde{\mathbf{l}}_L^i H_1^j - \tilde{\mathbf{d}}_R^* \mathbf{A}_D \mathbf{Y}_D \tilde{\mathbf{q}}_L^i H_1^j + \tilde{\mathbf{u}}_R^* \mathbf{A}_U \mathbf{Y}_E \tilde{\mathbf{q}}_L^i H_1^j - B_{WS} \mu H_1^i H_2^j + h.c.) \\
 & + H_1^{i*} m_1^2 H_1^i + H_2^{i*} m_2^2 H_2^i \\
 & + \tilde{\mathbf{q}}_L^{i*} \mathbf{M}_Q^2 \tilde{\mathbf{q}}_L^i + \tilde{\mathbf{l}}_L^{i*} \mathbf{M}_L^2 \tilde{\mathbf{l}}_L^i + \tilde{\mathbf{u}}_R^{i*} \mathbf{M}_U^2 \tilde{\mathbf{u}}_R^i + \tilde{\mathbf{q}}_R^{i*} \mathbf{M}_D^2 \tilde{\mathbf{q}}_R^i + \tilde{\mathbf{e}}_R^{i*} \mathbf{M}_E^2 \tilde{\mathbf{e}}_R^i \\
 & + \frac{1}{2} M_1 \tilde{B} \tilde{B} + \frac{1}{2} M_2 (\tilde{W}^0 \tilde{W}^0 + 2\tilde{W}^+ \tilde{W}^-) + \frac{1}{2} M_3 \tilde{g} \tilde{g}
 \end{aligned} \tag{3.1}$$

The Yukawa-couplings \mathbf{Y} , trilinear couplings \mathbf{A} and sfermion masses \mathbf{M} are 3×3 matrices over the particle generations. i and j are SU(2)-indices, with $\epsilon_{12} = +1$. Apart from the supersymmetric particle fields and the additional mass parameters for Higgsinos μ , Gauginos M_1, M_2, M_3 and the Higgs bosons m_1^2, m_2^2 , a common bilinear coupling constant B_{WS} remains a free parameter. In total 127 free parameters are needed to fully define the broken MSSM. Cancellation of loop terms to solve the Higgs mass fine tuning problem requires a similar mass for the particles compensating each other. The breaking of Supersymmetry is thus only 'soft', with a mass difference between superpartners and Standard Model particles not larger than approximately one TeV. Including phenomenological constraints, e.g. the cp-violation in the K-system, it is possible to link parameters with each other, defining the superpotential by 19 free parameters in the phe-

nomenological MSSM (pMSSM) scenario [30]. Other scenarios with further reduced number of free parameters exist, however these assume partly degenerate superpartner masses and couplings at the electroweak energy scale, which is in contrast to the widely split-up particle spectrum on the side of the Standard Model particles [31].

3.1.4 Unification

If going up in energy scale towards 10^{16} GeV though, the coupling constants of the different gauge fields are changed by loop corrections in a way suggesting their unification at that energy. It is shown in [32] that, in contrast to applying only standard model loop corrections, it is possible for all the coupling constants to meet in the MSSM scenario, as shown in figure 3.1. This is a prerequisite for a Grand Unified Theory (GUT) [33] in which interactions at and above the GUT energy scale of 10^{16} GeV are described by a single force and gauge symmetry represented by a Lie group like SU(5) or SO(10). For energies around the experimentally observed weak scale of 10^2 GeV, this symmetry is broken and split into the SU(3)×SU(2)×U(1) symmetries of the Standard Model.

Several scenarios for a ‘soft’ breaking of Supersymmetry in conjunction with a GUT exist [34]. They are discerned mostly by the mechanism transferring the breaking, which is assumed to happen unobservable in a hidden sector, unobservable by current experiments, to the particle spectra at low energy scales.

3.1.5 The Neutralino

The superpartners of neutral gauge bosons and Higgs bosons in a broken Supersymmetry are not necessarily mass Eigenstates. The mass Eigenstates are called Neutralinos $\tilde{\chi}_i^0$ and are linear combinations of \tilde{B} , \tilde{W}^0 , \tilde{H}_1^0 and \tilde{H}_2^0 . The composition of the Neutralinos is defined by the mass matrix

$$\mathcal{M}_{\tilde{\chi}_{1,2,3,4}^0} = \begin{pmatrix} M_1 & 0 & -\frac{g'v_1}{\sqrt{2}} & +\frac{g'v_2}{\sqrt{2}} \\ 0 & M_2 & +\frac{g'v_1}{\sqrt{2}} & -\frac{g'v_2}{\sqrt{2}} \\ -\frac{g'v_1}{\sqrt{2}} & +\frac{g'v_2}{\sqrt{2}} & \delta_{33} & -\mu \\ +\frac{g'v_1}{\sqrt{2}} & -\frac{g'v_2}{\sqrt{2}} & -\mu & \delta_{44} \end{pmatrix} \quad (3.2)$$

[29], in which M_1 and M_2 are the masses of the Gauginos \tilde{B} and \tilde{W}^0 , and g and g' the electroweak couplings. μ represents the Higgsino mass parameter, δ_{33} and δ_{44} are loop-corrections to the Neutralino masses and

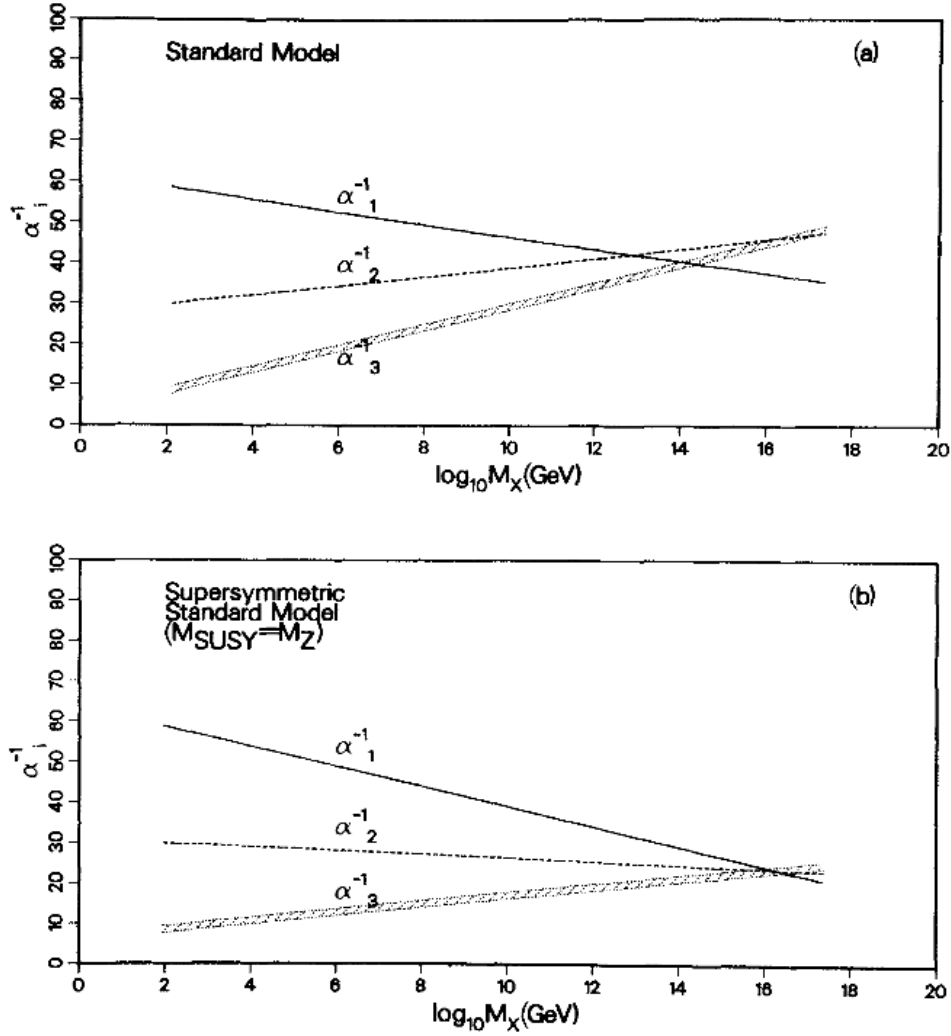


Figure 3.1: (a) Running couplings α_i in the Standard Model. (b) Running couplings in the MSSM. From [32]

v_1 and v_2 the vacuum expectation values of the two Higgs fields. The four Majorana states $\tilde{\chi}_i^0$ are ordered by mass: $m_{\tilde{\chi}_1^0} < m_{\tilde{\chi}_2^0} < m_{\tilde{\chi}_3^0} < m_{\tilde{\chi}_4^0}$. The lightest Neutralino $\tilde{\chi}_1^0$ is usually simply called 'the Neutralino' χ . Similarly, the Charginos $\tilde{\chi}_i^\pm$ are composed of \tilde{W}^+ , \tilde{W}^- , \tilde{H}_1^- and \tilde{H}_2^+ .

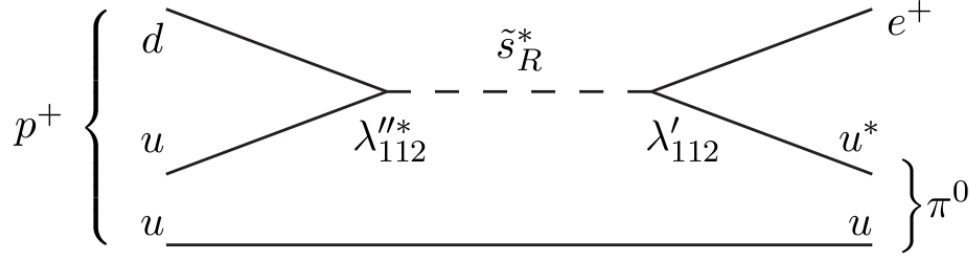


Figure 3.2: Feynman graph of a proton decay to positron and pion, mediated by strange-squark. From [28]

3.1.6 R-Parity

Supersymmetric particles with masses at the electroweak scale which can transition into Standard Model particles within interactions would violate lepton- and baryon number conservation. For instance, protons could decay into a pion and a positron by squark mediation, as illustrated in the Feynman graph 3.2 [28]. However, those processes are excluded by experiment up to a lifetime of $8.2 \cdot 10^{33}$ years, with pion plus anti-muon channels also excluded at a level of $6.6 \cdot 10^{33}$ years proton lifetime [35]. The masses of the Supersymmetric particles are at the weak scale due to the requirement of a soft SUSY breaking, therefore the propagator term does not sufficiently suppress these processes. This requires the introduction of a new conserved quantum number, the R-parity:

$$P_R = (-1)^{3(B-L)+2S} \quad (3.3)$$

It is composed of baryon number B , lepton number L and the particle's spin S , and yields $P_R = 1$ for Standard Model particles and $P_R = -1$ for their superpartners. As a multiplicative quantum number the R-Parity allows pairwise annihilation and creation of Supersymmetric particles, but does not allow their decay into all but Standard Model particles. As a result of this, the lightest Supersymmetric particle (LSP) has to be stable.

3.1.7 mSugra

One well studied theory which combines a unification with Supersymmetry is minimal Supergravity (mSugra). It predicts the superpartner and Higgs boson masses and couplings at the electroweak scale from masses

and couplings unified at the GUT scale. A quantum nature of gravity is assumed, which requires, compared to the MSSM, the addition of a graviton with spin 2 and its superpartner Gravitino with spin 3/2. When the Supersymmetry is broken, the Gravitino gains a mass while the graviton remains massless, which through loop corrections determines the mass spectrum of the Supersymmetric particles. The theory is defined by five parameters. At the GUT scale these are the common masses for scalar (m_0) and sfermion ($m_{1/2}$) particles, as well as the common trilinear coupling constant A_0 . From them, together with the ratio of the vacuum expectation values of the two Higgs fields

$$\tan(\beta) = \frac{v_{\text{top}}}{v_{\text{bottom}}} \quad (3.4)$$

and the sign of the Higgsino mass parameter μ , the masses and couplings at the electroweak scale are calculated via the Renormalisation Group Equation (RGE) [36].

3.2 Extra Dimension Theories

Another option to extend the Standard Model is the introduction of additional dimensions to the usually four-dimensional spacetime. This was first suggested by Theodor Kaluza in 1919 in order to formulate a unified theory of electromagnetism and gravitation within special relativity. Since no evidence of the existence of these extra dimensions has been observed, he proposed them to be curled up in itself, with a radius small enough to escape detection. Later theories solved this by allowing only some fields to propagate in the extra dimensions, while most Standard Model particles remain confined to the four-dimensional spacetime.

3.2.1 Universal Extra Dimensions

The theory of Universal Extra Dimensions (UED) is based on Kaluza's compactified dimension approach, with additional effects of quantum mechanics. All particle fields are allowed to propagate in the extra dimensions, which are compactified with a radius R and periodic boundary conditions. This makes the momentum in the extra dimension quantised in units of \hbar/R . Energy and momentum conservation in all dimensions then yield

$$\frac{E^2}{c^2} - \mathbf{p}^2 = \mathbf{m}^2 c^2 + \mathbf{p}_5^2 = \mathbf{m}^2 c^2 + \mathbf{m}_{\text{eff}}^2 c^2 \quad (3.5)$$

which shows that the additional momentum in the fifth dimension can be treated as an effective mass. With energy and momentum conservation observed in four dimensions, the momentum in the fifth dimension has to be conserved and quantised, which can be described by a multiplicative quantum number P_{KK} . For each Standard Model particle, a tower of in the extra dimension excited states exists, with the same quantum numbers except P_{KK} and mass. Conservation of P_{KK} inhibits decay into less excited states or the Standard Model ground state, only pairwise production and annihilation are allowed. Therefore the lightest particle of each excitation level is stable. The additional mass from the Kaluza Klein excitation is the same for all particles on tree level, but loop corrections modify the mass spectrum. The lightest particle of the lowest excitation level, if neutral, is a candidate for the Cold Dark Matter particle [37]. This could be either an excited B - or W -boson, or an excited neutrino. To be in conformity with the relic density requirement from the Concordance Model, its mass and thus the inverse of the compactification radius has to be about 600 GeV to 700 GeV.

3.2.2 Warped Extra Dimensions

The Randall-Sundrum Model also postulates the existence of an additional dimension [38], initially to address the hierarchy problem. The metric of the four-dimensional spacetime is scaled by a warp factor e^{-ky} along the extra dimension coordinate y , with k scaling the distance to the order of the Planck scale. The four-dimensional spacetime is located as a weak-scale 'brane' at $y = 0$, while depending on the variant of the theory a Planck-scale 'brane' exists either at a finite point of y or infinitely far away [39]. It was shown that unification of the gauge couplings in a $SU(5)$ or $SO(10)$ GUT is possible based on this approach if not only gravity but all fields propagate in five dimensions [40]. However the GUT X and Y bosons and/or Kaluza Klein excitations of Standard Model particles can contribute to proton decay, a problem which is fixed by assuming an underlying symmetry corresponding to conservation of a quantum number Z_3 , which is composed of baryon number and colour charge. It is zero for Standard Model particles. Any particle with non-zero Z_3 can only decay without changing this quantum number, therefore the lightest such particle, named LZP, has to be stable. The LZP is a KK-excited Dirac fermion, which is a valid Dark Matter candidate if it was the neutrino. The left-handed neutrino has a large coupling to the Z^0 , resulting in a too large cross section for scattering off nuclei as not to already have been detected in direct Dark

Matter searches. This leaves the right-handed neutrino as the favoured Dark Matter Candidate. The range of mass where its relic density would be matching the predictions from the Concordance Model is, because of dominant annihilation through these channels, either around half the Z^0 mass or, depending on the mass of the KK-excited gauge bosons, from 10^2 to 10^3 GeV [41].

Chapter 4

Search for Dark Matter

4.1 Direct Detection

One way to validate the theory of Cold Dark Matter being composed of some yet unknown WIMPs (see section 2.1.5), gravitationally and weakly interacting neutral particles, is to detect the deposited energy and transferred momentum from their scattering off nuclei.

4.1.1 WIMP nucleus interaction

The total scattering cross section is composed of a scalar term for coherent interaction with the nucleus as a whole and a term for the spin-spin interaction between the WIMP and unpaired nucleons. For heavy nuclei with more than 30 nucleons, the scalar term is dominant [42], especially if the WIMP is in the same mass range. For light nuclei with unpaired nucleons, especially hydrogen, the spin dependent component is the major interaction process [43].

4.1.2 Experimental Setups

WIMP scattering events transfer recoil energy in the order of a few 10 keV to the target nucleus [44], causing free charge through ionisation, which can be collected by a drift field onto electrodes. In a suitable target material also scintillation light is produced, which is observable with photomultipliers. Further, the deposited energy can be measured through heating up the target material, either with a calorimeter or by state transition of a superconductor in cryogenic detectors or by a phase transition of a superheated liquid in a bubble chamber.

Direct detection experiments are usually built underground to shield them from atmospheric muons, whose direct interference can be mitigated by employing a scintillator detector as veto. However, their interaction with matter creates neutrons, which also originate from natural radioactivity. To reduce background from neutron radiation, the whole detector is either surrounded with some hydrocarbon material, or outer layers of the detector material are used as a shield for the sensitive volume. Alternatively, neutrons can be discerned from WIMP events by the different scattering behaviour due to their lower mass and larger cross section, e.g. by observing multiple interactions. Background from γ and β radiation, which predominantly interacts with electrons instead of the nuclei, is discriminated in many experiments by using two of the above mentioned detection principles in parallel. Several collaborations operate direct detection experiments employing variations and combinations of the mentioned techniques, an overview of which is given in [45].

4.2 Indirect Detection

Indirect detection of Dark Matter relies on the detection of products from the (self)-annihilation of the Dark Matter particles. This makes it dependent on the existence of such a process, but also gives it the advantage of being able to obtain different information on the nature of Dark Matter than direct detection.

4.2.1 Annihilation Products

The annihilation of Dark Matter produces observable particles both directly and through decay of the primary annihilation products. Direct production results in a discrete line in energy while from the decay of primary products continuous spectra depending on the annihilation channel originate. Indirect detection experiments attempt to detect signatures of Dark Matter in γ radiation, high energy positron and electron flux, and anti-proton flux. Dark Matter annihilation is also assumed to yield high energy neutrinos, the search for which is the main subject of this work. For fermionic Majorana Dark Matter, like Neutralinos, the annihilation into pairs of light fermions of mass m_f from a state with total angular momentum $L = 0$ is suppressed by a factor m_f^2/m_{CDM}^2 due to helicity conservation, for an $L = 1$ state by a factor v_{rel}^2 where v_{rel} is the relative velocity of the annihilating particles. This is not the case for bosonic Dark Matter, like the LKP, whose annihilation therefore features a sharp line at the LKP

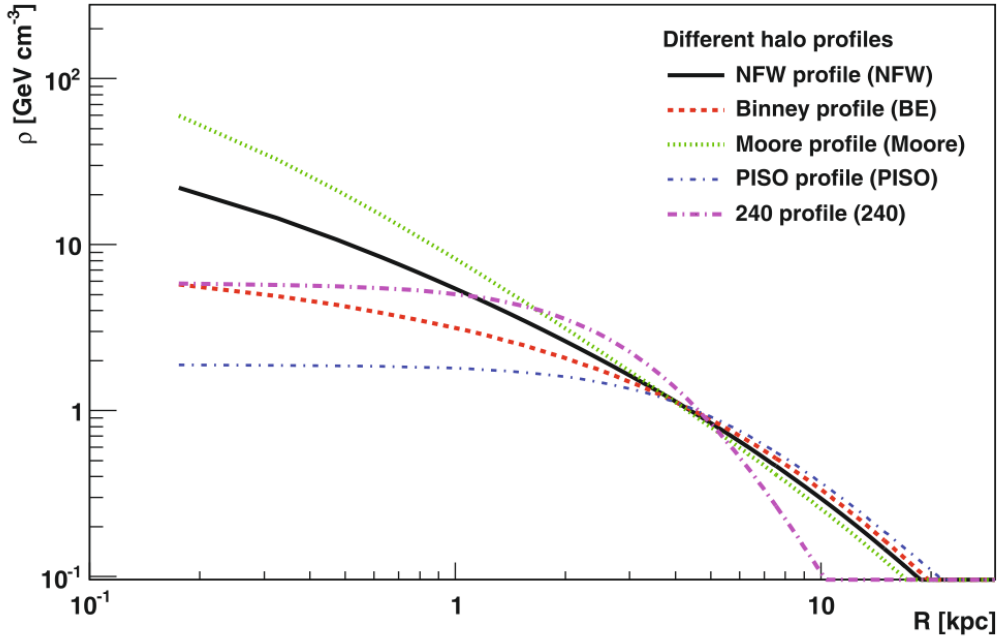


Figure 4.1: The dark matter density as a function of the distance R from the galactic centre for some halo profile models. From [47].

mass in electron/positron and neutrino spectra. Annihilation into gauge bosons depends on the weak hypercharge of the Dark Matter particle. It is dominant for a W^1 LKP and Wino LSP, while negligible for B^1 LKP and Bino LSP [46]. Higgsino LSP can annihilate through coupling to Higgs- and Z-bosons, which in turn partly decay into gauge bosons. Mixed mass Eigenstates annihilate according to their composition.

4.2.2 Signals of Dark Matter Annihilation from the Galactic Centre

The shape of the Dark Matter halo of our galaxy can be derived jointly by many-body simulations of its formation and from observation of the rotation curves of other galaxies with similar properties as the Milky Way. The density of the halo at the core of the galaxy is disputed and can - depending on the model - differ by several orders of magnitude, as shown in figure 4.1. With the annihilation rate proportional to the density squared, this region is a promising source for any high energy particle emission from Dark Matter annihilation, but with huge uncertainties on

the flux expectations. Non-uniform distribution of the Dark Matter on scales smaller than that of the general halo profile, which would enhance the annihilation rate, has been proposed, and is often used as a large 'Boost Factor' to fit Dark Matter annihilation spectra to observed particle spectra excesses, e.g. of photons [48], antiprotons and positrons [49]. Recent simulations of the formation of the halo suggest however, that the effective enhancement on diffuse fluxes is less than an order of magnitude [50]. Another difficulty is posed by the background from the abundant astrophysical objects also emitting γ and charged particle radiation at or within the line of sight to the Galactic Centre.

A similar approach is to look for emissions from the cores of other galaxies, either single or in a stacked analysis, averaging out some uncertainties, but with the disadvantage of much fainter expected signals due to the larger distances [51].

4.2.3 Neutrinos from Dark Matter Annihilation in the Sun

If the Dark Matter of the galactic halo is coupled to normal matter via the weak force, it can get gravitationally bound to massive stellar objects after losing energy by scattering. The Sun accounts for 99% of the matter in the Solar System, making it the primary target for WIMP scattering. If a WIMP is bound in an orbit after the first interaction it will subsequently cross the Sun's body again and lose more energy through scattering, until it is finally in thermal equilibrium with the matter at the Sun's core, a process happening at a timescale of about 10^3 years [52].

The density of WIMPs at the Sun's core increases by this capture process, which in turn enhances the annihilation rate, so that both processes are in equilibrium. In this way, the Sun becomes a source of neutrinos from annihilations, observable by neutrino telescopes on Earth, as outlined in figure 4.2. As the Sun consists primarily of hydrogen, the scattering of WIMPs is mostly on single protons, making the spin dependent component dominant. Due to the light nuclei present, also the capture of light WIMPs is favoured. The WIMP density at a distance of eight kiloparsec from the galactic centre, where the Solar System is located, is concordantly predicted to be about 0.3 ± 0.1 GeV per cm^3 [47] as pictured in figure 4.1, with a recent approach using Bayesian statistics pinpointing it at $0.39 \pm 7\%$ GeV per cm^3 [53]. Possible clumpiness of the Dark Matter does not show large effects, as the density fluctuations are averaged out by the accumulation process. Only those primary decay products with extremely short lifetimes contribute to the high energy neutrino flux, as others lose

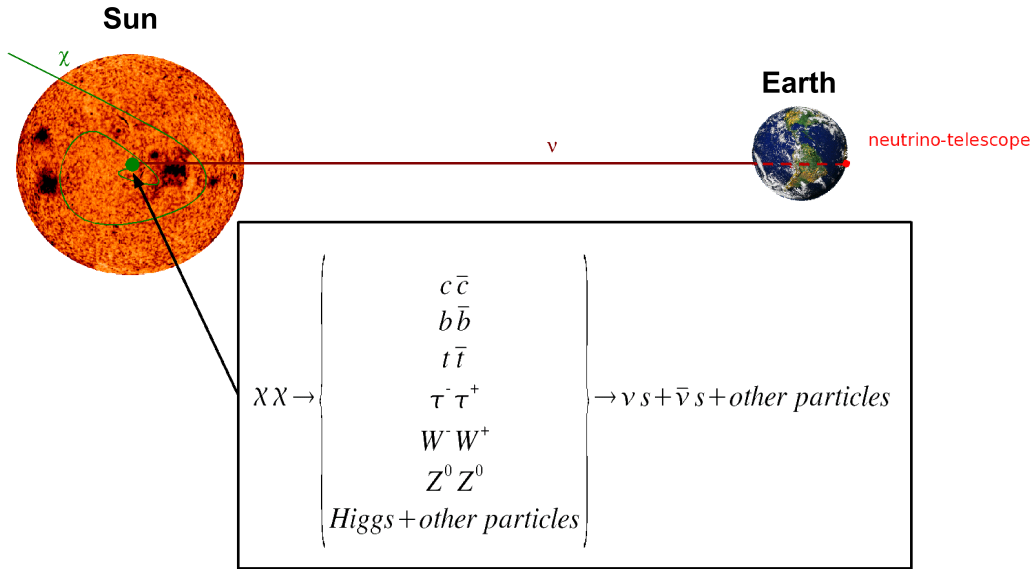


Figure 4.2: Schematic illustrating the chain from WIMP capture to neutrino detection for WIMPs accumulating inside the Sun.

their kinetic energy by interaction with the dense matter at the Sun's core before decaying to neutrinos. Even the neutrinos themselves are subject to significant absorption and matter induced oscillation effects while propagating to the surface. During the further propagation to Earth, vacuum oscillation also changes the flavour composition of the neutrino flux. The WIMP density falls quadratically with the distance from the Sun's centre, the scale depending on the WIMP mass, but the whole annihilation region can be considered a point source for any neutrino telescope.

4.2.4 Neutrinos from Dark Matter Annihilation in the Earth

Calculating the accumulation of WIMPs in the Earth is more complex than in the Sun. The Earth consists mostly of a mixture of heavy elements up to iron, which could act as targets for resonant scattering if the WIMP's mass was close to that of one type of these nuclei, enhancing the capture rate by a factor of 10 to 300 [55]. Scattering on heavy nuclei is dominated by the spin independent part of the cross section, which scales with the number of nucleons. The density of the matter at the Earth's core of 13 g/cm^3 [56] is much less than the density at the Sun's core, where it is 150 g/cm^3 . For this reason, the annihilation through light quarks and muons becomes

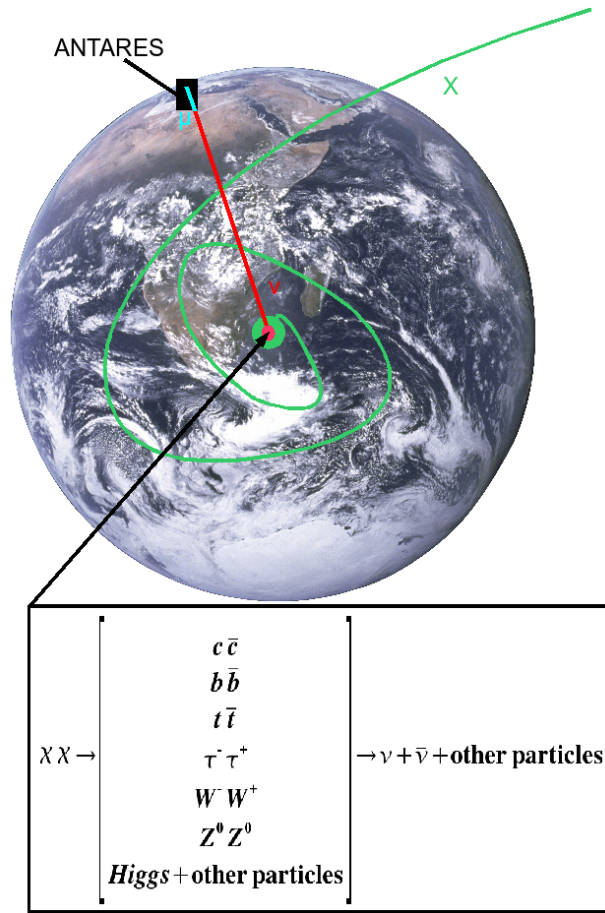


Figure 4.3: Schematic illustrating the chain from WIMP capture to neutrino detection for WIMPs accumulating inside the Earth.

important, as they are more likely to decay before reacting with matter. An uncertain aspect of the capture process is the role of WIMPs which have interacted with solar matter and became bound to the solar system. If stable orbits which cross Earth’s orbit exist for WIMPs, there could be an enhancement of the capture rate. Due to interference from other planets, calculation of possibly stable orbits for WIMPs is challenging, it was shown in [57], that such orbits exist. On the other hand, comparison to the also nearly collisionless population of asteroids in the Solar System suggests, that those with orbits possibly intersecting Earth are likely also to hit the Sun or be ejected from the Solar System on a rather short timescale [58].

Seen from a neutrino detector at the Earth’s surface, as sketched in figure 4.3, the annihilation region inside Earth is not a point source, but

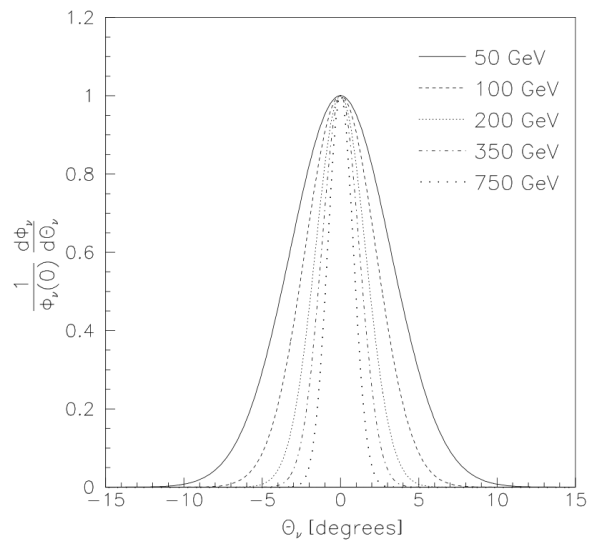


Figure 4.4: The angular distribution of neutrinos emitted by Dark Matter annihilation in the Earth for different WIMP masses. From [54].

a gaussian distributed source of several degree width, as shown in figure 4.4.

Chapter 5

ANTARES

5.1 Operating Principle

The ANTARES neutrino telescope is a Cherenkov detector using seawater as the target medium. High energy muon neutrinos which undergo a charged current (CC) interaction with a nucleus in or close to the detector give birth to muons with sufficiently high energy to traverse the water faster than the speed of light in the medium. Thereby the muons emit Cherenkov light at an angle Θ , given by $\cos(\Theta) = \frac{1}{n\beta}$, which is approximately 42° for very high energy particles with $\beta \rightarrow 1$ in seawater with refractive index $n = 1.34$. An array of photomultipliers (PMTs), which forms the main component of the ANTARES experiment, detects this light. From the position of the PMTs and the arrival time of the Cherenkov light, the muon track is reconstructed. The muon largely carries over the momentum and thus direction of the original neutrino. The mean angle $\langle \phi \rangle$ between neutrino and muon due to kinematics can be parametrised as

$$\langle \phi \rangle = \frac{0.7^\circ}{(E_\nu/\text{TeV})^{0.6}} \quad (5.1)$$

[59].

5.2 Detector Environment

The ANTARES detector was built in the deep sea of the Mediterranean near Toulon, Var, southern France at coordinates ($42^\circ 48'$ N $6^\circ 10'$ E) and a depth of 2475 m. The deep sea environment acts as a shield against muons generated in interactions of cosmic rays with the atmosphere, with only muons

above approximately 1 TeV energy being able to reach that depth. Also it provides an almost completely dark ambiance, necessary to detect the faint Cherenkov signatures. However, a certain photon background is present in the seawater coming from two sources. First, the Potassium isotope ^{40}K dissolved in the water decays to ^{40}Ca in a β^- process. The thereby emitted electron has an energy of up to 1.3 MeV, which is above the Cherenkov threshold of 0.78 MeV. Second, a wide spectrum of bioluminescent sea organisms emits light for various purposes, like communication, as a bait to attract prey or to deter predators. This background poses a certain challenge to the detection of neutrinos, because it is superimposed onto the Cherenkov light signature of the muon track to be reconstructed. The intensity of the biogenic background varies with time and, if high, also leads to deterioration and reduced performance of the PMTs.

The high pressure (250 atm) saltwater environment required the components of ANTARES to be constructed from strong and corrosion resistant materials, such as titanium, as well as high emphasis on their watertight assembly.

5.3 Detector Infrastructure

The PMT array to detect the Cherenkov light from the muon tracks is mounted on twelve strings fixed to the seafloor by anchors and straightened by buoys. They are placed with 70 m distance from each other and their total length is 500 m. The part starting at 100 m above seafloor is equipped with storeys spaced by 14.5 m, holding three 10 inch PMTs each, as depicted in figure 5.1. To determine the position of the PMTs in the required precision of a few centimetres, ANTARES features a positioning system described in section 5.5. As a research infrastructure, ANTARES serves as a platform for instruments of other projects, notably the AMADEUS project, which studies possible background for acoustic high energy neutrino detection, and a seismometer for earthquake detection. The ANTARES detector is connected to the shore station in La Seyne-sur-Mer by a 40 km long electro-optical cable. Close to the detector it is attached to a Junction Box (JB), from where power and data transmission to and from the individual lines is provided via interlink cables.

5.3.1 The ANTARES Lines

The twelve lines of the ANTARES detector are fixed to a Bottom String Socket (BSS), held on the sea bottom by an attached iron deadweight of

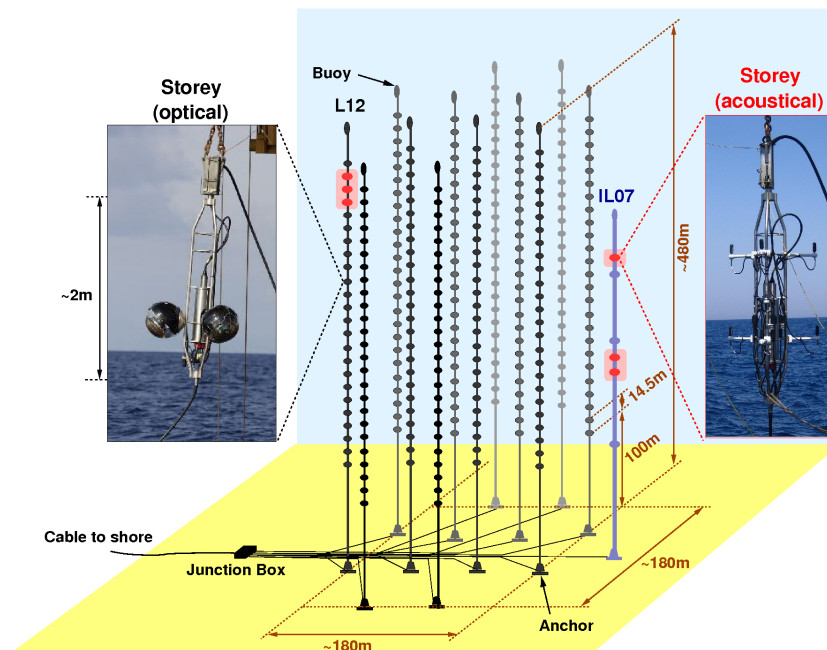


Figure 5.1: Schematic drawing of the ANTARES detector. The picture on the left shows a storey equipped with Optical Modules during deployment. The picture on the right shows an hydrophone equipped storey of the AMADEUS experiment, whose storeys are marked red in the schematic.

1.5 tons. The BSS contains the String Power Module (SPM), an emitting and receiving acoustic transponder of the positioning system and a mounting for the plug connector to the interlink cable to the JB. An autonomous release mechanism triggered by an acoustic transmission detaches the line from the deadweight for recovery. The line structure consists of segments of cables, which hold in their core glass fibres for optical data transmission, as well as copper strands for high voltage supply and for monitoring and controlling the apparatus (Slow Control). Around the core, three protective layers made out of - from inside to outside - polyethylene, Aramid and polyurethane provide watertightness, mechanical stability and protection. The 25 storeys are placed in between these cable segments of which the lowest one, connecting the BSS and the first storey, has a length of about 100 m, while the others are 12.5 m long. Line 12 differs from the other lines in that it features only 20 storeys equipped with PMTs, while another three storeys carry hydrophones of the AMADEUS project, and one the YODA device measuring the seawater's oxygen level. In addition to the twelve detector lines, an Instrumentation Line (IL) monitors

the ambient sea current by two Acoustic Doppler Current Profiler (ADCP) devices, as well as salinity, conductivity and the speed of sound [60]. It also carries two infrared cameras, to record nearby organisms when triggered by a bioluminescent emission, which is detected by a PMT coupled to each camera. Three more storeys devoted to AMADEUS, equipped with hydrophones, are also installed on the IL.

5.3.2 The ANTARES Storeys

A typical storey within the ANTARES detector, as shown in figure 5.2, is built around a titanium frame with a height of two meters. To this frame, a titanium cylinder containing readout electronics, called Local Control Module (LCM), and three 27 inch Benthos glass spheres are attached. The glass spheres contain a 10 inch PMT of type Hamamatsu R7081-20 each, the whole unit called an Optical Module (OM). The PMTs are directed downward and outward at an angle of 45° from the vertical axis. Selected storeys feature hydrophones for position calibration or LED Beacons for time calibration. The three OMs on a storey are referred to as OM0, OM1 and OM2.

5.3.3 Offshore Data Acquisition Electronics

The ANTARES Data Acquisition (DAQ) electronics housed in the LCMs is located on the Analogue Ring Sampler Mainboards (ARS-MB). Each OM is associated with one MB, and two ARS on it, with an additional one controlling the LED Beacon if one is mounted on that storey. An offshore clock system with 20 MHz frequency provides a time reference which is distributed via the fibres to the read out electronic. Using both rising and falling flanks of the pulse, a 25 ns timestamp is created. Within the timestamp interval provided by the clock, a time to voltage converter (TVC) measures the arrival time of the amplified signal at a precision of 0.2 ns, with the overall time resolution of the arrival of the incident photon dominated by the PMT transit time spread of 3 ns. The amplitude of the signal, normalised to be equivalent to the number of electrons emitted from the PMT's photocathode and thus expressed in units of photoelectrons (pe), is determined in a similar way by an amplitude to voltage converter (AVC). The analogue signals together with the timestamp are stored in a 16 cell buffer memory to free the TVC and AVC immediately for new input. Two eight bit analogue to digital converters (ADC) then digitise the data. The ADCs of the ANTARES readout electronic have 256 channels, the voltage

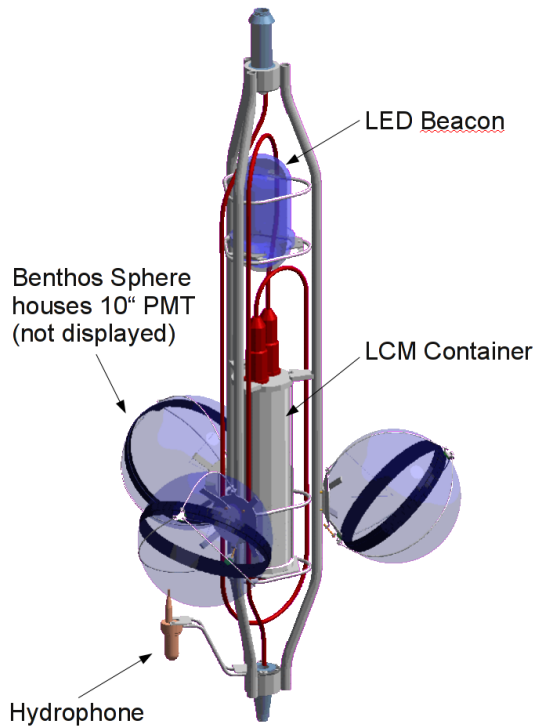


Figure 5.2: Computer generated image of an ANTARES detector storey. Hydrophones for position calibration and LED Beacons are only mounted on some storeys

ramp of the TVC and AVC however only covers part of them, resulting in a smaller dynamic range.

5.4 Data Processing

The ANTARES data processing follows an 'all data to shore' concept, according to which each signal received by a photomultiplier is digitised and transmitted to the shore station by optical fibre in the form of level 0 (L0) hits, defined by the OM they occurred on, their time and their amplitude. The datastream is divided into timeframes of 104 ms length, which are distributed to several computers running data filtering and trigger processes. These processes decide which parts of the stream are to be stored on disk. ANTARES can also take data in so called Waveform Mode, in which the full time evolution of the PMT output signal is digitised and stored. This results in a much higher data rate however, preventing the continuous transmission required by the 'all data to shore' concept. The recorded data

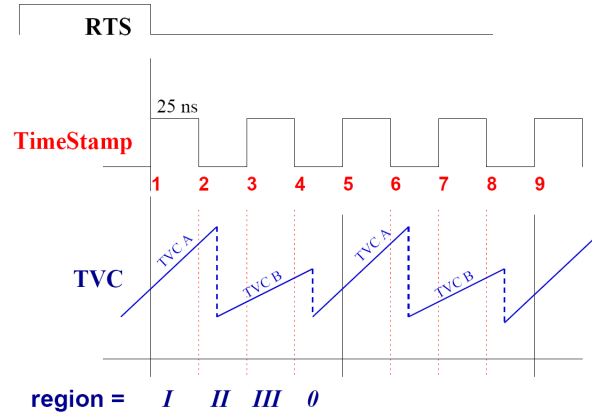


Figure 5.3: The selection of the correct TVC is determined by the timestamp modulo 4 since timestamp reset (RTS). For region I and III the indicated TVC is used, for regions II and 0 the TVC is also determined by whether the measured channel number is above or below the mean of 127. From [62]

is initially stored in the form of ROOT files [61] locally on disk at the shore station in La Seyne-sur-Mer, and transferred daily to the HPSS storage of the Centre de Calcul of IN2P3 in Lyon. Also at this computing centre, an ORACLE database is kept for storage of calibration values and other additional information.

5.4.1 Time Measurement and Timing calibration

In the case of the time measurement, the starting channel of the TVC ($channel_{TVC_min}$) and the slope of the voltage increase with time ($slope_{TVC}$) have to be calibrated. The two TVCs of each OM work in flip-flop mode, with one active at any time while the other is being reset. If the signal collected from the PMT reaches a preset threshold, called L0 trigger threshold, the voltage accumulated since the last reset, or rather since switching to this TVC, is measured. The channel number read out ($channel_{TVC}$) is converted into time by application of the calibration. The active TVC and the respective slope are determined from the timestamp (TS) as layed out in figure 5.3 from the timestamp count and the measured value itself. The time t of a hit is then calculated as

$$t_{hit} = T0 + TS \cdot 25 \text{ ns} + (channel_{TVC} - channel_{TVC_min}) \cdot slope_{TVC} \quad (5.2)$$

where $T0$ is determined from calibration runs using the LED Beacons and comprises the PMT transit time and the electronics delay.

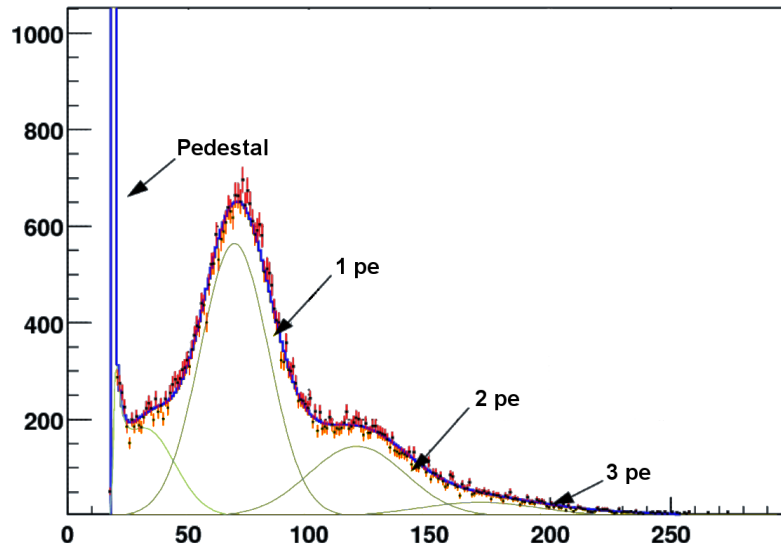


Figure 5.4: The predicted (blue line) and measured (black dots with red error bars) AVC spectrum from a laboratory test setup with the fitted contributions of the pedestal, 1 photoelectron (pe), 2 pe and 3 pe peaks (grey lines). The dynamic range of the ADC in this setup is reduced compared to the in situ setting. From [63]

5.4.2 Amplitude Measurement and Charge Calibration

For measurement of the amplitude, which is equivalent to the charge deposited at the PMT's final electrode, two AVCs work in serial mode. When the L0 threshold is reached, integration of the signal starts for a time of 25 ns. After recording a hit, it takes 13 ns to switch to the other AVC, which then is available to record another hit. After a hit each AVC enters a 250 ns dead time for reset. To calculate the amplitude from the channel number of the ADC ($channel_{AVC}$), the channel difference ($slope_{AVC}$) between the so called 'pedestal', the permanently present signal from pure electronics noise, and a single photoelectron (SPE) is required, as well as the value of the pedestal ($channel_{pedestal}$) itself. The pedestal is measured during a special calibration run in which the PMTs' high voltage is switched off. Since most hits originate from single photons, the channel number corresponding to 1 pe can be extracted from physics data, by fitting a Gaussian to the first peak of the distribution shown in figure 5.4. As a trade-off between sufficient separation of SPE hits from the pedestal, while packing a maximum of dynamic range into the 256 channels of the ADC, a slope

of 10 channels per photoelectron is foreseen. To achieve this, the possibility to tune the sensitivity of the ADC exists, limited by the occurrence of nonlinear behavior of the electronics [64], as well as the tuning of the high voltage.

$$amp_{hit} = (channel_{AVC} - channel_{pedestal}) \cdot slope_{AVC} \quad (5.3)$$

The best cut to separate the SPE hits from the electronics background is at the minimum between the pedestal and the first peak, which is at the channel corresponding to 0.3 pe if the PMT is tuned correctly. In the reverse manner the actual L0 threshold charge level for each PMT has to be determined. The L0 threshold setting is checked in situ from hits which just barely cross the threshold, which leads to a AVC and TVC reading, but without assigning the timestamp from the clock, which is instead set to zero. After application of the charge calibration hits are sometimes found to be below the aimed at threshold of 0.3 pe, or even at negative amplitude, due to a low L0 threshold.

5.4.3 Walk Effect Correction

The T_0 constant used for the time calibration is obtained from dedicated LED Beacon runs, by means of the known arrival time of light from flashes of the LED Beacons at the PMTs. The intensity of the flash is sufficiently large to reach the L0 threshold immediately. A smaller signal, as caused by single or few photons, reaches this threshold with a delay. This is called the walk effect. To compensate for this time offset, a correction according to figure 5.5 is applied to the time of the hit, based on its amplitude. The correction depends on the L0 threshold with a spread of about 1 ns for 1 pe hits.

5.4.4 Calibration Datasets

To calibrate the hits for triggering, the required constants are loaded from the database where they are stored in a dataset created from earlier periods, called Online Calibration. For the trigger algorithms, the geometry information of the detector is simplified to vertical lines with all PMTs centered on the line. For track reconstruction purposes, the better Offline Calibration calibration datasets valid for shorter timescales are applied, which may also be based on calibration runs from after the physics data was taken. Furthermore, they make use of the continuously aligned detector geometry obtained by the procedure described in section 5.5. As a time dependent effect of the charge calibration, the position of the SPE

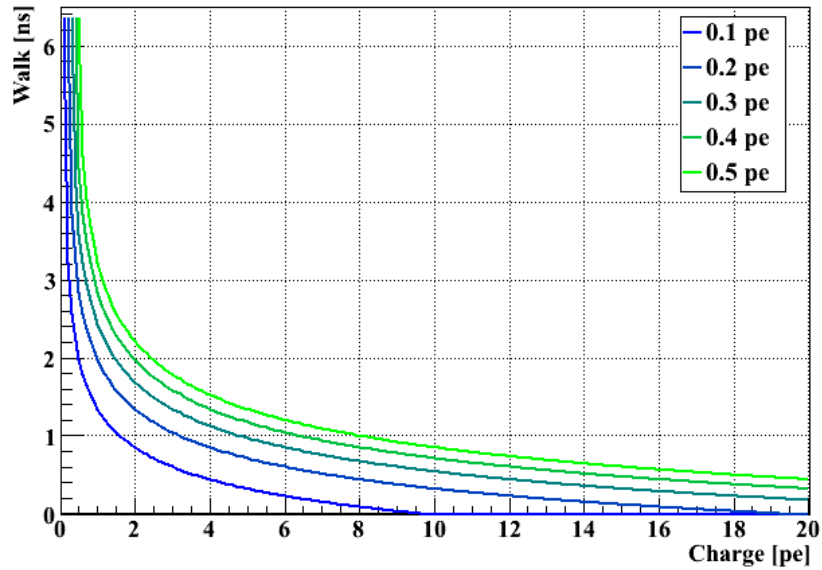


Figure 5.5: The correction for the time shift caused by the walk effect for different values of the L0 threshold. From [65]

peak changes slowly to lower channels, primarily by loss of gain through aging effects, on average 0.2 channels per month [66].

5.4.5 Triggering

From the L0 hits a secondary hit sample, called L1 hits is created, consisting of those hits, which have either an amplitude of more than 3 pe (2 pe or 10 pe on some trigger configurations), or are within a 20 ns time window around a hit on another PMT on the same storey. This L1 sample forms the basis of several trigger algorithms. The standard trigger for taking physics data is the 3N Trigger. It is based on the more basic 3D Trigger, which tests the causality condition based on the speed of light in the medium with refractive index n . This condition is given by

$$\Delta t \cdot c < d \cdot n \quad (5.4)$$

for all pairs of hits with a time difference Δt and a distance d . An event is triggered if a cluster of five hits, all connected to each other by this causality relation, exists. To reduce the rate of accidental triggering due to the optical background, the 3N Trigger extends the 3D Trigger by application of the 1D Trigger on a grid with 10° spacing. The 1D Trigger tests the hypothesis of a muon track from a given direction through a χ^2 fit assuming 10 ns time

resolution to determine its position and calculation of a normalised surface density ρ on the projection of the position of the L1 hits within a radius R_{max} on the plane perpendicular to the assumed direction. It is the ratio of their number $n_{R < R_{max}}$ to the set required number of hits for triggering n_{req} times the ratio of the considered area to the area of the convex hull A around all hits within it:

$$\rho = \frac{n_{R < R_{max}}}{n_{req}} \cdot \frac{\pi R_{max}^2}{A} \quad (5.5)$$

With a required number of hits is five and R_{max} set to 90 m, events preselected by the 3D Trigger which have a χ^2 better than 0.01 and ρ larger than 6.0 are triggered. The 2T3 Trigger requires the existence of two T3 clusters within a 2.2 μ s time window. A T3 cluster consists of a pair of L1 hits on adjacent storeys on a line, equal to a distance of 14.5 m, which have a time difference not larger than 100 ns, or a pair on next to adjacent storeys within 200 ns. When the conditions for one trigger occur within the datastream, a snapshot of all hits around the hits belonging to the trigger pattern, the triggered hits, is taken. This snapshot starts 88 timestamps (2200 ns) before the beginning of the timestamp interval of the first triggered hit and ends 88 timestamps after the interval containing the last triggered hit. Furthermore, on all runs which are to record physics data, a Minimum Bias Trigger is active, which takes snapshots of 4400 ns length every ten seconds (every second before 2008) and a trigger recording locally coincident hits to monitor the background rate from ^{40}K . Additional triggers active in some runsetups include a direction sensitive trigger directed towards the galactic centre as well as a trigger which is initiated by GRB alerts and stores all incoming data during the relevant period on disk for later analysis [67].

5.4.6 OM Condition

Since faulty Optical Modules which either are less sensitive to incident photons than assumed or show an excessive count rate can severely hamper event reconstruction, the status of each OM is constantly monitored. There are several conditions an OM can have. OMs which show the expected counting rate between 40 kHz and 400 kHz are designated as 'ok'. Those with lower rates as 'low' and those with higher rates as 'high'. If the rate is too high for the electronics to digitise the data continuously, the OM enters into the so called 'X-off' state. Those OMs which for some reason do not send digitised hits, but empty data frames, are called 'empty'. Finally the OMs which are known to be defunct, e.g. because their sphere is flooded, are in 'dead' state.

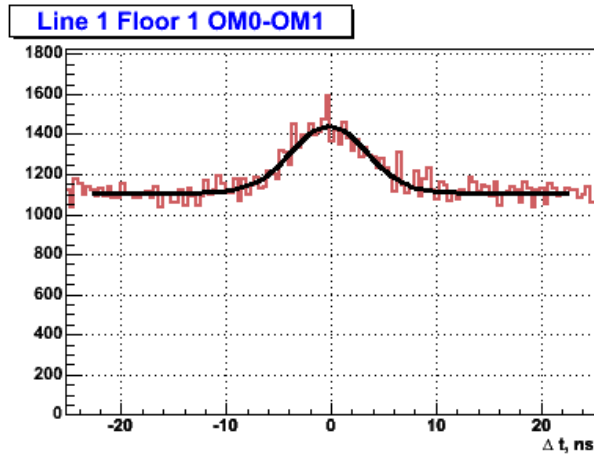


Figure 5.6: Gaussian excess on the distribution of time differences between hits on two OMs of Storey 1 on Line 1 from coincident hits caused by decay of ^{40}K [68]

5.4.7 In Situ Calibration with ^{40}K

Due to their energy of at maximum 1.3 MeV, electrons from the β -decay of ^{40}K emit Cherenkov light localized and virtually instantly, causing a certain rate of coincident hits on adjacent PMTs above the otherwise uncorrelated background. This known source is used to check the time calibration as well as to monitor the efficiency of the PMTs. The plot of the time differences between the hits on a pair of OMs on a storey, as shown in figure 5.6, features a distinct Gaussian excess around zero from the coincidentally arriving photons caused by ^{40}K close to the storey [68]. It was shown that the timing calibration is correct within the intended precision, as an offset would cause a deviation of the excess maximum from zero. The area below the curve, after subtraction of the background, is the measured coincidence rate, determined to be about 13 Hz.

5.5 Detector Alignment

The lines of the ANTARES neutrino telescope are flexible structures distorted by the sea current. Still, reconstruction of muon tracks requires precise information about the position of the optical modules. The procedure which in a large extend was implemented as part of this work and is commonly referred to as Detector Alignment - or just Alignment - provides this information in the form of a lookup table within the database.

5.5.1 Acoustic Positioning System

The ANTARES detector features a positioning system from the company GENISEA from Le Pradet, France, based on position measurement by acoustic triangulation. On each line, the 1st, 8th, 14th, 21st and 25th storey are equipped with a hydrophone, which measures the sound arrival time of signals emitted by transducers mounted at the BSS of all lines. The hydrophones are built from piezo sensors moulded in polyurethane connected with a cable to the LCM cylinder and attached to the storey frame at the tip of a 0.29 m lever arm. Their location relative to the other storey components is illustrated in the schematic 5.2. This system of emitters and receivers completes a cycle of measurements approximately every two minutes, the recorded raw data are the measured arrival times and logged emission times, which are transferred to the database. The first step to obtain the hydrophone positions is the calculation of distances between emitters and receivers from the recorded time differences between each pair. For the calculation the average speed of sound is needed, which is a function of the salinity of the seawater and the depth dependent pressure. As a second step based on the distances, the positions of the hydrophones are triangulated and put into the database for further processing. During this step noise is reduced by taking the sliding average over periods of 20 minutes and removal of values showing a strong deviation from the average.

5.5.2 Storey Orientation Measurement

The LCM of each storey contains internally a TCM2 tiltmeter or the replacement version TCM2.5 board from Precision Navigation Inc., Santa Rosa, CA, USA [69] to measure the inclination against the direction of gravity. The two-axis fluid filled mechano-electrical accelerometer measures the tilt in the vertical plane through OM0 ($Tilt_X$) and the orthogonal tilt component ($Tilt_Y$) with 0.1° resolution and 0.2° accuracy. The attached compass module measures the components of the Earth's magnetic field B_x, B_y and B_z as a basis to calculate the storey's horizontal orientation, designated heading h . The heading is defined as the clockwise positive angle between the plane through OM0 and north in the UTM coordinate system. To correct for the different directions towards the magnetic and the geographic north pole and the deviation between the UTM northing coordinate and geographic north, the two correction terms $\Delta h_{m/g} = 0.57^\circ$ and $\Delta h_{UTM} = 1.93^\circ$ are added [70]. The vertical component of the magnetic field B_z is also measured, but not necessary for calculation of the heading, since the inclination of the

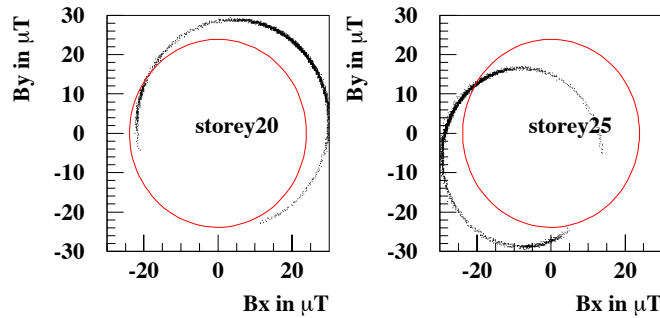


Figure 5.7: Measured magnetic field components on Storey 20 and Storey 25 of Line 12 in Nov./Dec. 2010 from the Earth's magnetic field before calibration. A correction offset and factor are determined for each component, so that the final values follow the red circle.

storeys is usually small and does not influence the horizontal components significantly. The heading is therefore calculated as follows:

$$h = \arctan\left(\frac{B_y}{B_x}\right) + \Delta h_{m/g} + \Delta h_{UTM} \quad (5.6)$$

The magnetic field values and inclinations are read out in a cycle with two minute repetition period and stored in the database.

5.5.3 In Situ Calibration of Compasses and Tiltmeters

Their placement inside the LCM close to large currents influences the B-field sensors. An in situ calibration is performed by recording the measured values through a complete turn of the storey during operation. The two components describe an ellipse which is shifted to a circle by adding offsets and multiplication by a correction factor as shown in figure 5.7. Those corrections are then applied to the magnetic field values before calculation of the heading. For the tiltmeters, the average value is determined over an extended period of operation and offsets are defined to reset the average to zero. That average value changes on the occasion of an OM's flooding, as the buoyancy of the storey is no longer evenly distributed. Since not the actual tilt of the storey, but the overall inclination of the line at the storey's height should enter into the formula, the offset is also chosen to negate the deviation from the average, as illustrated from figure 5.8.

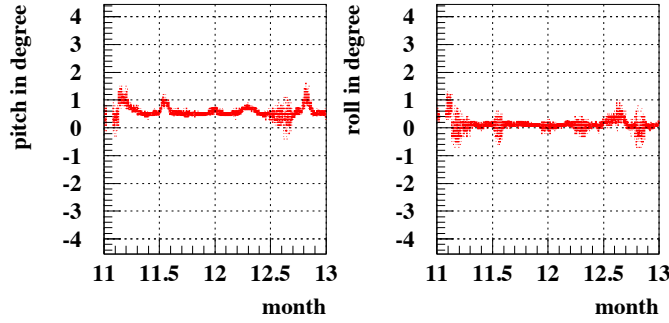


Figure 5.8: Measured tilt values on Storey 9 of Line 12 in Nov./Dec. 2010 before calibration. The average value is subtracted as a correction offset from each component, so that the final values are centred around zero.

5.5.4 The Lineshape Formula

From the measurements of the individual storeys the shape of the line is fitted to a formula derived from drag and buoyancy of the line components, with two orthogonal components of the sea current velocity as free parameters. The local zenith angle Θ_i (see figure 5.9 for illustration) of storey i is given by:

$$\tan(\Theta_i) = \frac{\sum_{j=i}^N F_j}{\sum_{j=i}^N P_j} \quad (5.7)$$

where

$$F_j = \frac{1}{2} \rho C_{w_j} A_j v^2$$

is the drag force from a current with velocity \mathbf{v} (of a medium with density ρ) on line element j out of N , with an area A_j towards the current and a drag coefficient C_{w_j} . P_j is the force resulting from the buoyancy of that line element. The forces are summed up for all elements above storey i . By transforming the forces on the elements to continuous functions $f(z)$ and $p(z)$ of height z above ground, the line inclination at any given height z_i can be written as an integral:

$$\frac{dr}{dz} = \frac{\int_{z_i}^h f(z) dz}{\int_{z_i}^h p(z) dz} \quad (5.8)$$

The displacement $r(z_i)$ in the direction of the sea current at height z_i is then $r(z_i) = \int_0^{z_i} \frac{dr}{dz} dz$, which, in the case of a line of total height h with N storeys

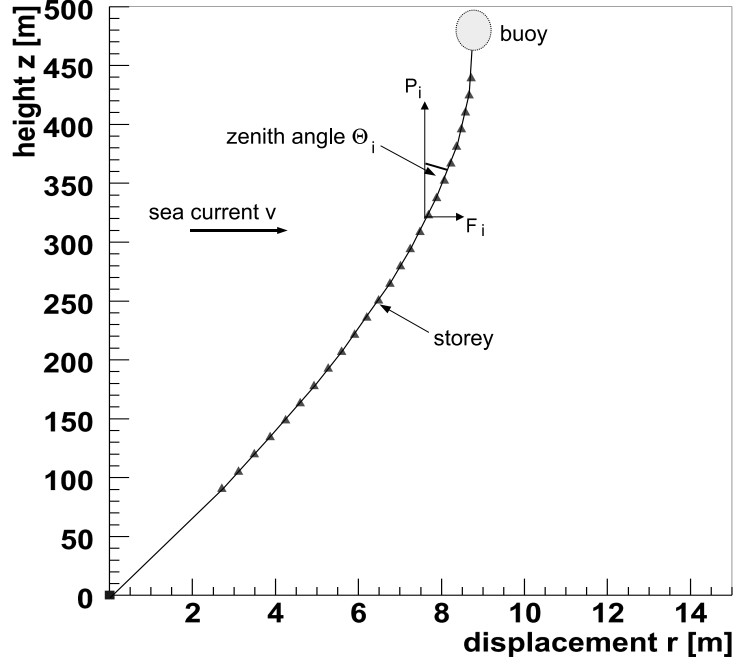


Figure 5.9: Drawing of an ANTARES line showing the displacement of the storeys from the vertical in the plane of the line's inclination which is identical to the current direction. Drag force F_i , buoyancy P_i and the local zenith angle Θ_i are plotted exemplary for Storey 17.

connected by identical cables and one buoy at the top, yields :

$$r(z_i) = v^2 \left(\frac{d}{b} z_i - \frac{c b - d a}{b^2} \ln \left(1 - \frac{b}{a} z_i \right) \right) \quad (5.9)$$

where

$$a = N(P_{\text{storey}} + P_{\text{cable}}) + P_{\text{buoy}}$$

$$b = \frac{N}{h} (P_{\text{storey}} + P_{\text{cable}})$$

$$c = \frac{\rho N}{2} (A_{\text{storey}} C_{w\text{storey}} + A_{\text{cable}} C_{w\text{cable}}) + \frac{\rho}{2} (A_{\text{buoy}} C_{w\text{buoy}})$$

$$d = \frac{\rho N}{2h} (A_{\text{storey}} C_{w\text{storey}} + A_{\text{cable}} C_{w\text{cable}})$$

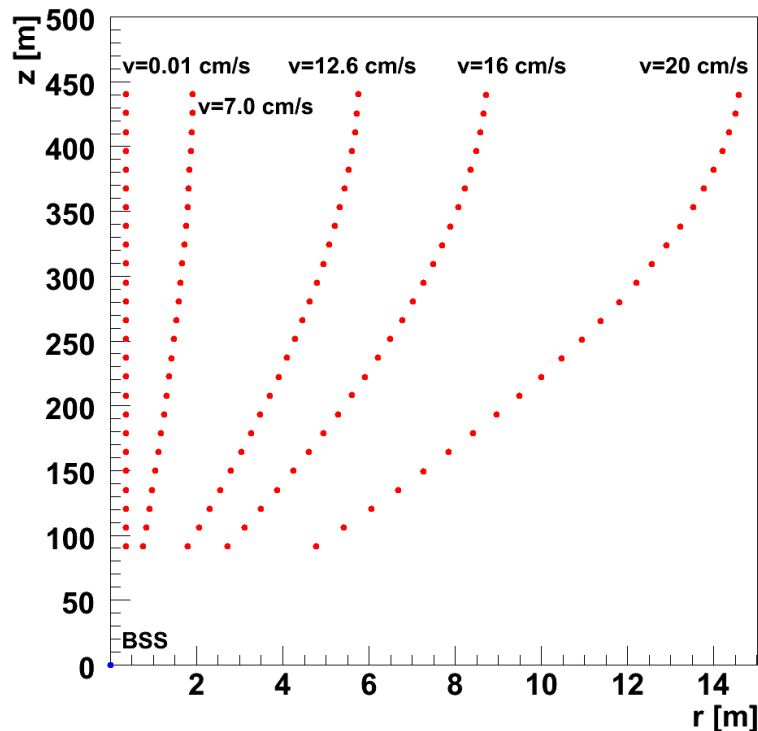


Figure 5.10: Radial displacement from the vertical of the storeys calculated for different sea current velocities v using the properties of Line 1.

Figure 5.10 shows this displacement for the storeys of Line 1.

5.5.5 Fitting Algorithm

To include the current direction, the lineshape formula is employed on two orthogonal planes x and y with current components v_x and v_y . These two parameters are used in a global χ^2 minimisation to fit the two independent lineshape formulae to the measured positions of the hydrophone-equipped storeys and the local zenith angles given by the tiltmeters. Since the hydrophones are mounted on a lever arm, the heading measured by the compass is used to calculate the position of the storey's centre. The tiltmeters together with the compass measure the inclination of the line, and the direction of that inclination. However, all storeys share a common plane of inclination due to the pull exerted by the cable, superseding the information from the compass. Therefore the projection of the measured

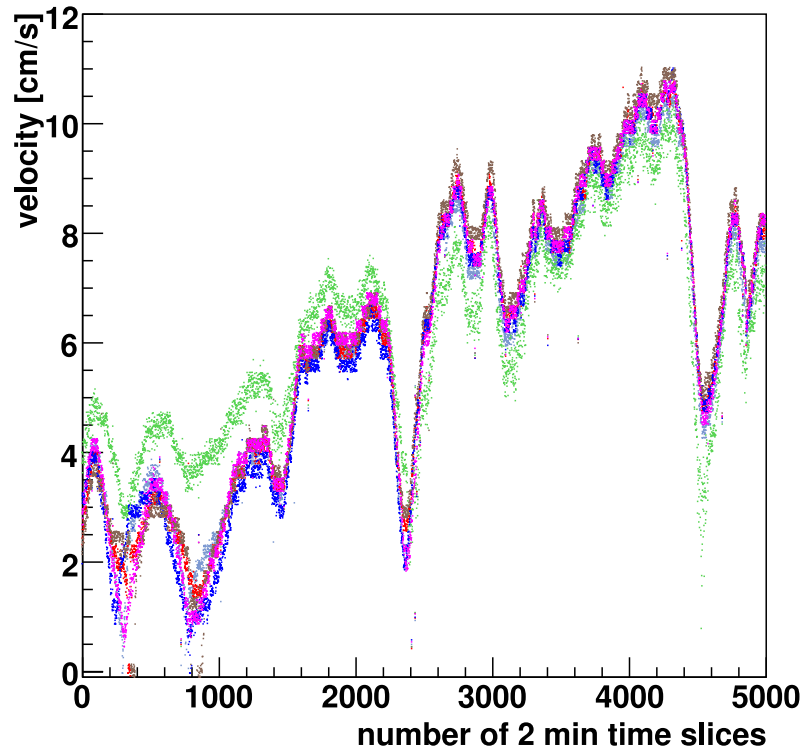


Figure 5.11: Comparison of the sea current velocity over the time of a week as a result from the fit of different lines distinguished by colour

inclination onto the plane of global line inclination given by the lineshape tested in the current iteration of the fit is used as local zenith Θ_i for storey i . Alternatively, the norm of the inclination vector can be used, but this overestimates the inclination of each storey at low sea current velocities, because errors on the tilt measurements add up. The ANTARES lines are not exactly equal in cable length and equipment on the storeys, this is taken into account by including the individual cable length and buoyancy values for each line. This virtual model of the detector geometry is also used to create the nominal geometry dataset with vertical lines used for triggering, as stated in section 5.4.5.

The sea current velocity is assumed to be constant within the detector area, therefore the velocities from fitting the individual lines should be the same. Still, unaccounted variations in the buoyancy, e.g. due to flooded OMs, result in slightly different velocities, which nevertheless agree within

a precision of 1 cm/s, as can be seen from figure 5.11. For lines on which no hydrophones are working at a time, the average velocity from the other lines is used to calculate the lineshape. As a further improvement a global fit over all lines is planned [71], to increase reliability and precision in the case of partial failure of hydrophones, tiltmeters and compasses.

5.5.6 Alignment Precision

The precision at which the position of the OMs is determined, is obtained from the error matrix of the lineshape fit. The uncertainties on the two velocity components are translated into error estimates of the positions of the individual storeys, and their inclination. The heading of the storey cannot be calculated from the velocity components, therefore the error estimate is that of the heading measurement itself and assumed to be 1° . For the position error, estimates of one centimetre are typical. In order to test for systematic errors, the results of the fit were compared to the position of a single hydrophone whose position was not used in the linefit. The results of this comparison for storey 20 of line 3, depicted in figure 5.12, show that the position of the not used hydrophone coincides well with the fit within its own precision of 5 cm. This also gives an upper boundary in reassuring the validity of the fit's statistical error estimate, which is otherwise not possible due to lack of an absolute reference point.

Another method to check the reliability of the alignment procedure is to compare the current direction and speed from the linefit with the values measured by the ADCP devices installed on the IL. As figure 5.13 shows, there is excellent agreement [72]. Thanks to the physics based lineshape formula, detector alignment can in principle be done even without acoustic triangulation, resorting only to tiltmeter and compass data, albeit at significantly lower precision.

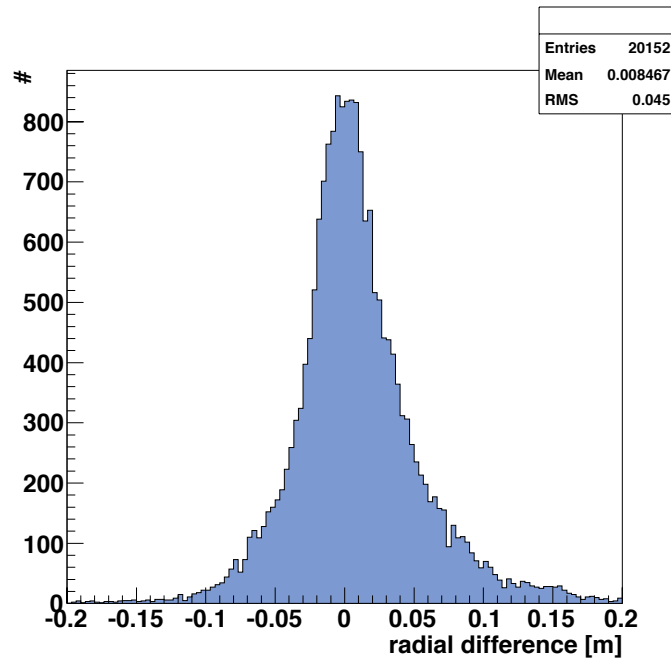


Figure 5.12: Difference of the triangulated position of Storey 20 on Line 3 and the position of the lineshape fitted without using the input from this storey's hydrophone

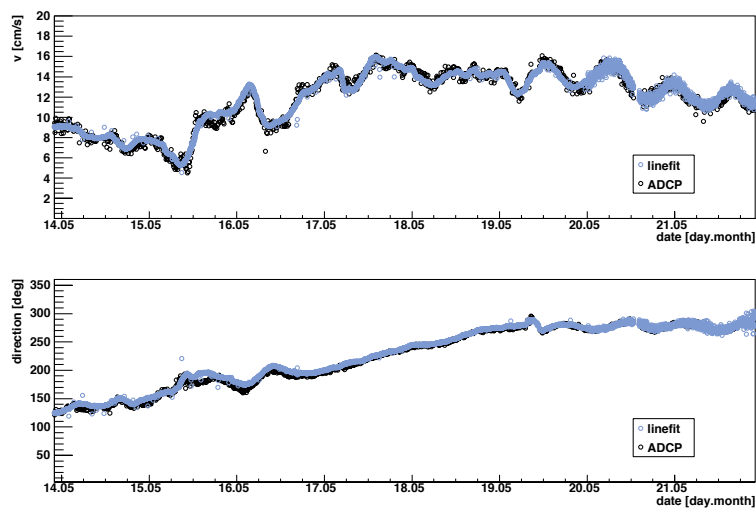


Figure 5.13: Comparison of sea current velocity from fitted lineshape and ADCP

Chapter 6

Sensitivity of ANTARES to mSugra

6.1 Effective Area in the Low Energy Regime

The effective area is a measure of the detector sensitivity, representing a virtual cross section for a neutrino to be detected. In general, it is a function of the neutrino energy and the direction.

Through a Monte Carlo (MC) simulation with the program packages GENHEN [73] for particle generation, KM3 [74] for light production and propagation, Calibrate [75] for the electronics simulation and TriggerEfficiency [76] for simulation of the ANTARES trigger and the Aart Strategy [77] as reconstruction, the effective area for detection of neutrinos with an energy between 10 GeV and 400 GeV was determined [78] [79]. An overview of the Aart Strategy reconstruction, on which this sensitivity study is based, is given in section 7.7, after the methods of event reconstruction in general are introduced at the beginning of chapter 7. The results obtained using the 3D Trigger and the optical background rate set to 60 kHz per OM are displayed in figure 6.1, averaged over direction. For the sensitivity calculations, a zenith angle dependent version effective area was also created. In addition to the reconstruction quality cuts $\hat{\alpha}_\mu < 1^\circ$ and $\Lambda > -5.3$, which are explained in section 7.7.2, a cut at 3° deviation of the reconstructed track from the the neutrino direction was applied. This cut serves the purpose to model the effect of a search cone with 3° opening angle oriented towards the Sun.

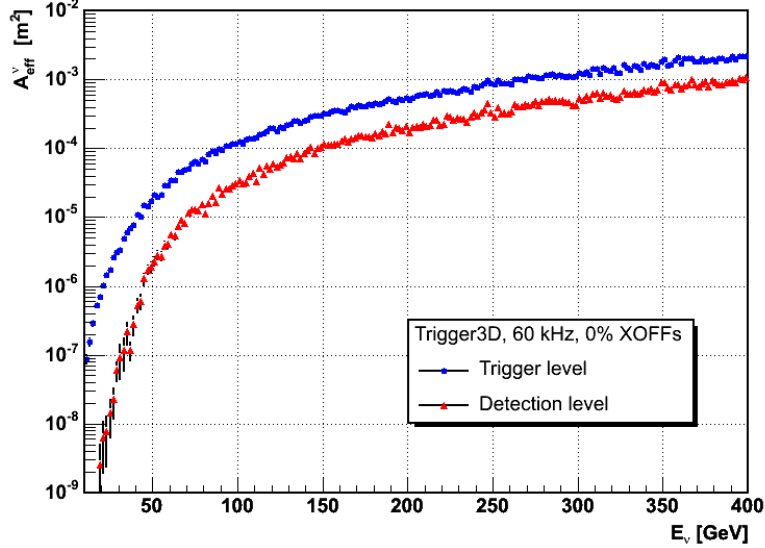


Figure 6.1: The effective area of ANTARES for 10 GeV to 400 GeV for triggered events and reconstructed events passing the quality cuts of $\hat{\alpha}_\mu < 1^\circ$ and $\Lambda > -5.3$.

6.2 Signal Neutrino Flux

6.2.1 Regions of the mSugra Parameter Space

The properties of the Supersymmetric particle spectrum predicted by mSugra depend on the five parameters introduced in section 3.1.7. For those parameter combinations, for which the Neutralino is the LSP, the relic density is a critical parameter to decide, whether it indeed is a valid Dark Matter candidate, as it needs to match the constraints from cosmology. The properties influencing the relic density are the Neutralino's mass, self-annihilation cross section and the mass difference to the Next to Lightest Supersymmetric Particle (NLSP), with which co-annihilations are possible. While for most of the parameter space, the relic density is higher than predicted, select regions exist where it is at the required value. One of them is the Bulk Region, where the common masses m_0 and $m_{\frac{1}{2}}$ are low, resulting in a light Neutralino. For the High $\tan(\beta)$ Region, also called A-Annihilation Region, the relic density is decreased because of a resonant self-annihilation through the CP-odd Higgs Boson A [80]. In the Co-Annihilation Region, the reduction of the relic density is due to a small

mass difference to the stau NLSP, which boosts coannihilations [81]. At the Focus Point Region [82], the Higgsino fraction of the Neutralino is high, which enhances the self-annihilation cross section by t-channel Chargino exchange. The Focus Point Region is of special interest, as it favours annihilation into gauge bosons. This leads to a hard neutrino spectrum compared to annihilation into quarks, and a generally high neutrino flux as is pointed out in figure 6.2 together with the locations of the above mentioned regions and their associated neutrino flux.

6.2.2 mSUGRA Parameter Space Scan

Since only a fraction of the mSUGRA parameter space fulfills the constraints placed on the CDM relic density by the Concordance Model, a method was required to scan especially the regions yielding the correct relic density. A Markov Chain Monte Carlo with variable step size based on the Metropolis Algorithm was performed using the relic density as the guidance parameter [83]. To avoid convergence of the Markov Chains at a perfect matching relic density, the step size of the scan was increased again when inside the WMAP compatible region. For each parameter set the relic density and other observables were calculated with the program package DarkSUSY [29]. For this study, DarkSUSY 4.1 was used, the calculation of the superpartner spectrum was performed using ISASUGRA [84]. Based on the WMAP result from 2003 [85], which give a 2σ precision value of $0.094 < \Omega_m h^2 < 0.129$, a scan of the mSUGRA parameter space was done within the following boundaries:

- $0 \text{ GeV} < m_0 < 8000 \text{ GeV}$
- $0 \text{ GeV} < m_{\frac{1}{2}} < 2000 \text{ GeV}$
- $0 < \tan \beta < 60$
- $-3m_0 < A_0 < 3m_0$

Furthermore, the mass of the top quark was set to 172.5 GeV, μ was chosen positive and the NFW-model for the Dark Matter halo of the galaxy [86] was used.

6.2.3 Calculation of the Neutrino Flux

The neutrino flux as it is shown in figure 6.2 was calculated by conducting a simulation of the decay of the annihilation products with the JETSET

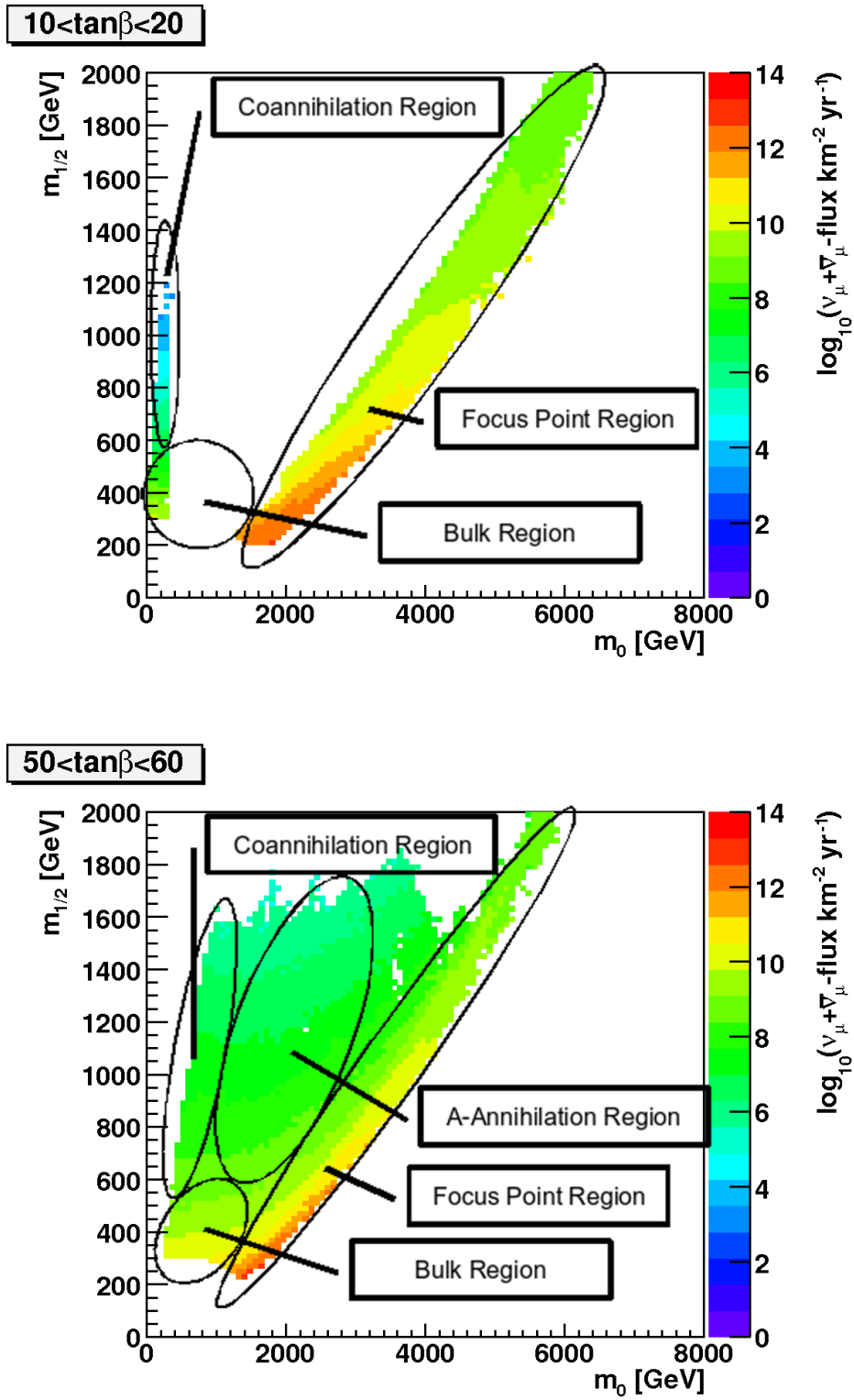


Figure 6.2: $\nu_\mu + \bar{\nu}_\mu$ flux integrated above threshold energy of 10 GeV for different values of $\tan(\beta)$ with the regions of cosmology compatible relic density indicated.

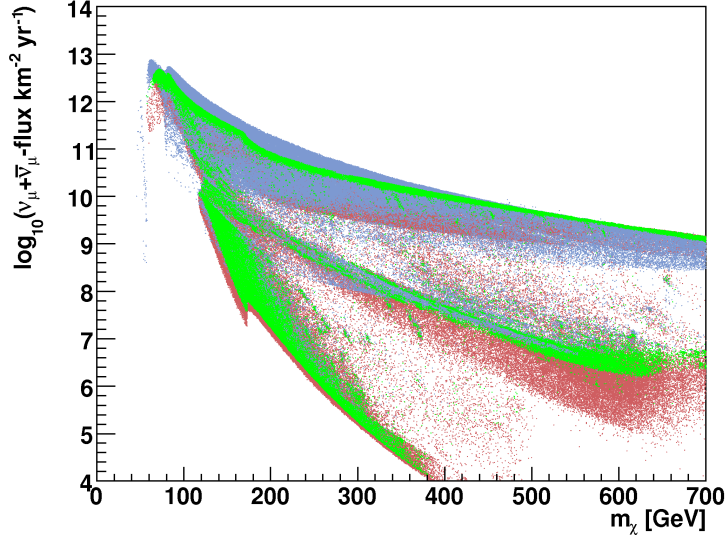


Figure 6.3: $\nu_\mu + \bar{\nu}_\mu$ flux from the Sun integrated above threshold energy of 10 GeV versus Neutralino mass m_χ . Blue: $\Omega h^2 < 0.094$, Green: $0.094 < \Omega h^2 < 0.129$, Red: $0.129 < \Omega h^2$. Green is plotted over blue, which is plotted over red.

and PYTHIA codes [87] and their propagation to earth. The neutrinos generated inside the Sun are subject to neutrino oscillations influenced by matter, including MSW-effect [88], when propagating to the Sun's surface, as well as in vacuum between Sun and Earth. To include these effects, the transition probabilities for the neutrinos were calculated using path ordered propagators [89], with LMA mass differences and mixing angles [90]. The resulting modified neutrino flux per annihilation for the different annihilation channels was tabulated and imported into DarkSUSY, which calculates a neutrino flux differential in energy from them, together with the model specific branching ratios and annihilation rates.

The integrated neutrino flux of each set of parameters from the parameter space scan is plotted versus the mass of the corresponding Neutralino in figure 6.3, with colour indicating the relic density. As different input parameters can give the same integral neutrino flux prediction and Neutralino mass, but different relic densities, there is an overlap of colours with green (2σ WMAP) plotted over blue (below WMAP), plotted over

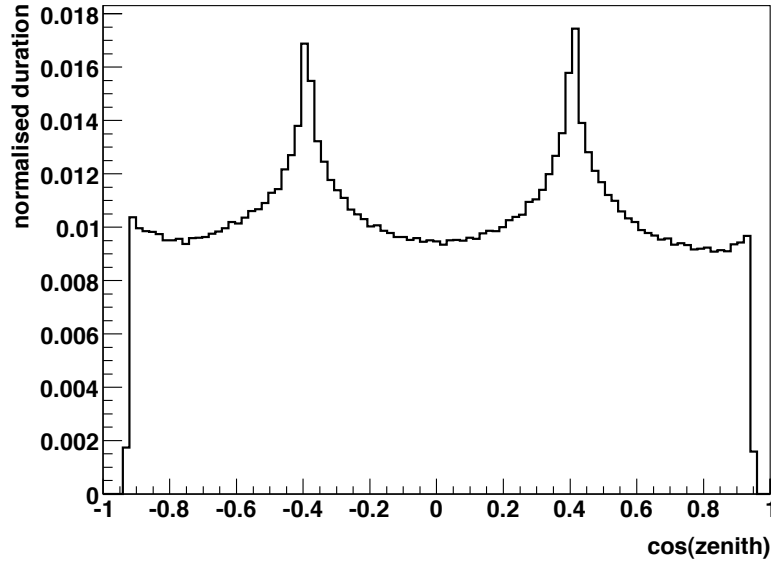


Figure 6.4: Zenith angle distribution of the Sun over the course of a year red (above WMAP).

6.3 Calculation of the Sensitivity

6.3.1 Signal Detection Rate

To obtain the signal detection rate in ANTARES, the differential flux was multiplied with the neutrino effective area from section 6.1 and summed up over energy. The zenith angle dependent effective area was multiplied with the Sun's zenith angle distribution as shown in figure 6.4, to create an effective area averaged with correct weights over the zenith range covered by the Sun.

The results for a period of five years of taking data, already corrected for the time when the Sun is over the horizon and unobservable, are the expected event numbers shown in figure 6.5.

6.3.2 ANTARES Sensitivity for Five Years

Since even the highest expected event rates are in the order of only a few ten events in five years (compare figure 6.5), the expected 90% CL

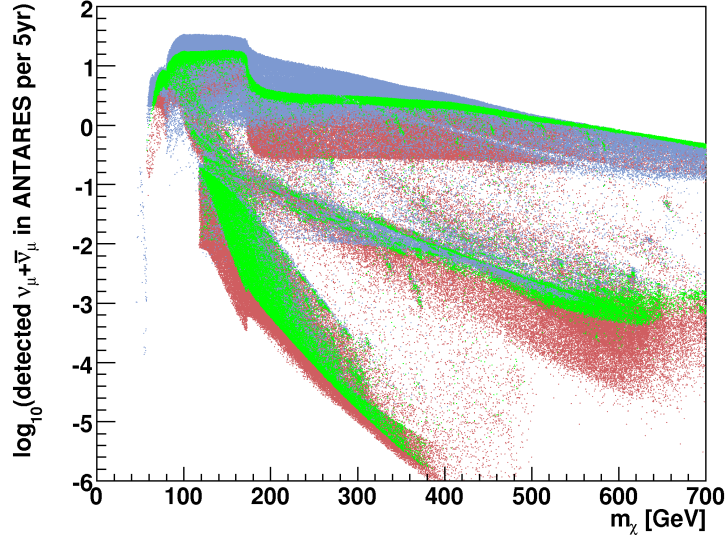


Figure 6.5: Expected events in ANTARES per five years versus $m_{\tilde{\chi}}$. Blue: $\Omega h^2 < 0.094$, Green: $0.094 < \Omega h^2 < 0.129$, Red: $0.129 < \Omega h^2$. Green is plotted over blue, which is plotted over red.

exclusion limits were calculated using the unified approach of Feldman and Cousins [91]. The atmospheric neutrino background was calculated according to the flux parametrisation of Bartol [92] [93], taking into account its zenith angle dependence, as well as that of the effective area and the Sun's zenith angle distribution, analogous to the calculation of the signal flux. The number of background events was multiplied by 1.1, in order to include the 10% additional background from atmospheric muons, which are reconstructed as upgoing, as implied by the quality cut of $\Lambda > -5.3$. In figure 6.6 the 90% CL limit achievable in five years is shown for the results of the scan in a event number versus Neutralino mass plot. Since the detection rate is compared directly to the limit which depends only on background, the separation from excludable to non-excludable models is a straight line in this representation. The ability to independently compare each set of parameters to this limit allows to present it with regard to other parameters, such as the integrated neutrino flux which is shown in figure 6.7.

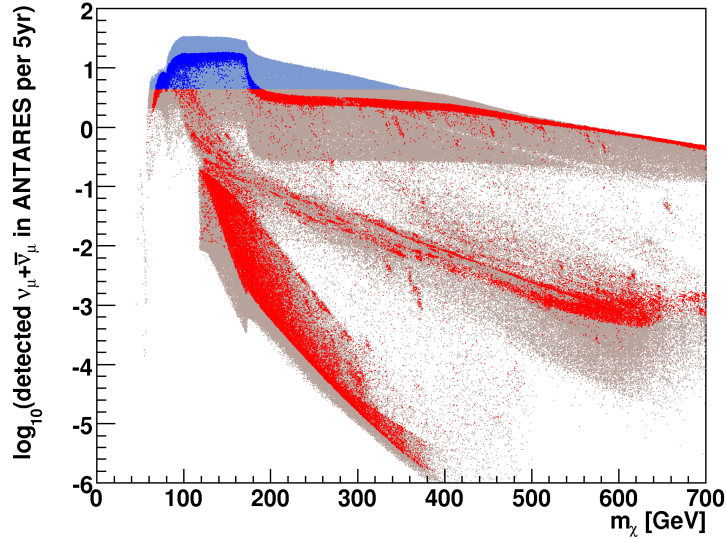


Figure 6.6: Expected events in ANTARES per five years versus m_χ . Blue: can be excluded 90% CL by ANTARES, Red: can't be excluded. Bright colours: within 2σ WMAP region, Faint colours: outside 2σ WMAP region

In order to show which part of the parameter space is accessible to ANTARES, figure 6.8 shows, if a region within a slice along the $\tan(\beta)$ axis of the parameter space can be excluded fully, partially, or not at all by ANTARES.

6.4 Comparison to other Experiments

To compare the sensitivity of ANTARES to constraints already provided by other experiments, their limits on scattering cross sections are shown together with the calculated cross section for the scanned parameter sets. The direct detection limits in this section were provided by the Dark Matter Limit Plot Generator [94].

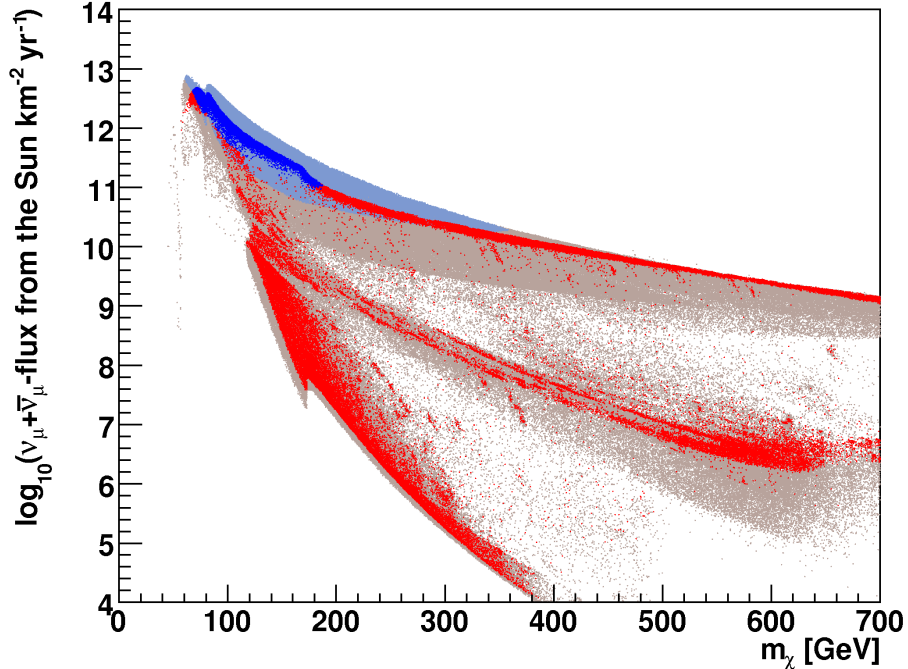


Figure 6.7: $\nu_\mu + \bar{\nu}_\mu$ flux from the Sun integrated above 10 GeV E_ν versus m_χ . Blue: can be excluded 90% CL by ANTARES, Red: can't be excluded. Bright colours: within 2σ WMAP region, Faint colours: outside 2σ WMAP region. Blue is plotted over red, inside 2σ WMAP over outside

6.4.1 Spin Independent Cross Section

Direct detection experiments search for Dark Matter by detecting the scattering of a WIMP at a nucleon within the detector (see section 4.1). Depending on the type of nucleus they put constraints on the spin dependent or the spin independent WIMP-nucleon cross section. The spin independent cross section is plotted versus the Neutralino's mass in figure 6.9.

6.4.2 Spin Dependent Cross Section

While direct detection experiments are much more sensitive to the spin independent scattering process, can the spin dependent cross section also

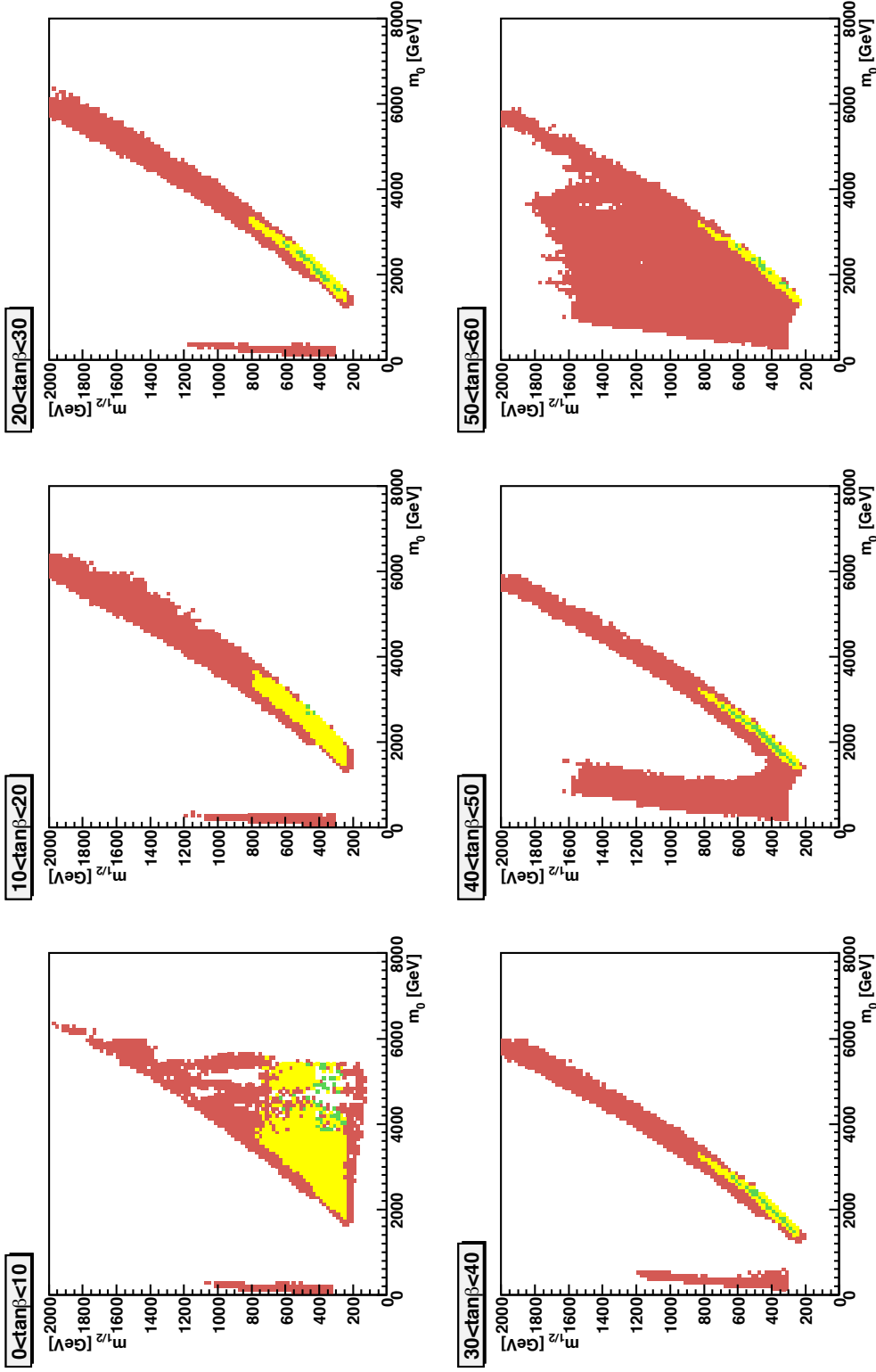


Figure 6.8: Exclusion capability in the m_0 - $m_{1/2}$ -plane for different values of $\tan(\beta)$. Green: all excludable, Yellow: partially excludable, Red: none excludable

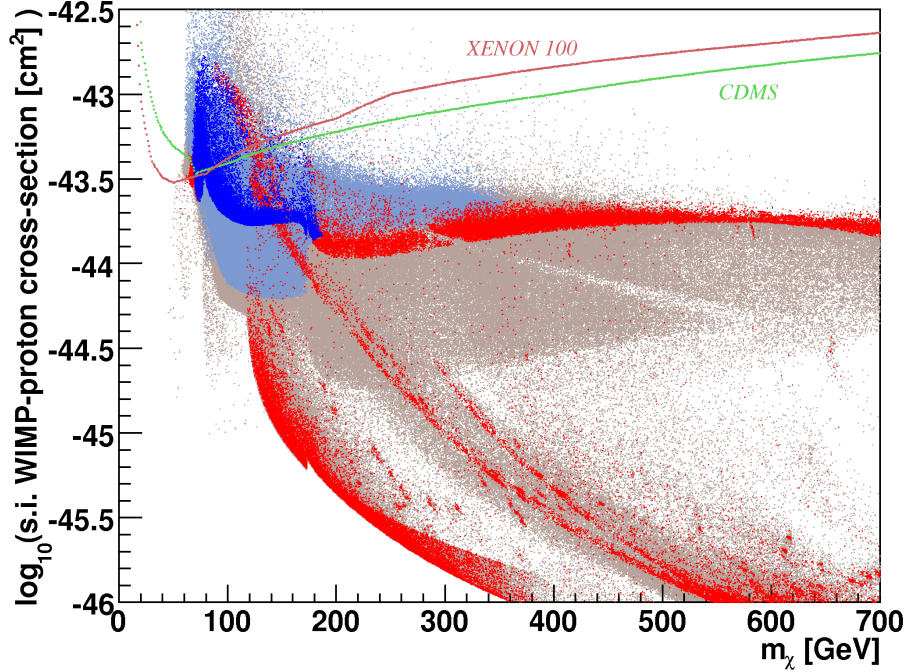


Figure 6.9: Direct detection limits shown on spin independent WIMP-nucleon cross section versus m_χ with ANTARES limit as colour. Blue: can be excluded 90% CL by ANTARES, Red: can't be excluded. Bright colours: within 2σ WMAP region, Faint colours: outside 2σ WMAP region

be probed in a largely model independent way by neutrino telescopes. This is due to direct link between the neutrino flux from the Sun and the spin dependent cross section. Since the WIMP annihilation rate is equal to the capture rate and, because the Sun consists mostly of hydrogen, the assumption of purely spin dependent scattering processes in the capture is valid to a high degree. Figure 6.10 shows the current limits from Super-Kamiokande [95] and IceCube [96] under this assumption, together with recent direct detection limits and the ANTARES sensitivity in the form of the scan results. The neutrino energy spectrum used for the Super-Kamiokande limit is that of the W^+W^- channel for WIMPs heavier than the W^+ and W^- , and that of the $\tau^+\tau^-$ channel below this threshold. For the IceCube limit, W^+W^- represents the hard annihilation channel and $b\bar{b}$

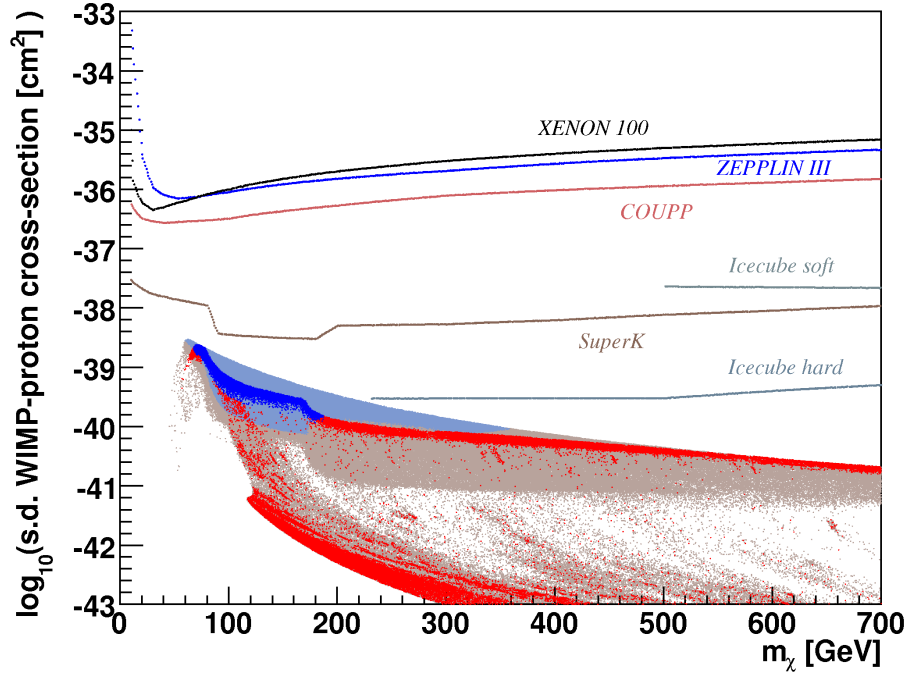


Figure 6.10: Direct detection limits shown on spin dependent WIMP-nucleon cross section versus m_χ with ANTARES limit as colour. Blue: can be excluded 90% CL by ANTARES, Red: can't be excluded. Bright colours: within 2σ WMAP region, Faint colours: outside 2σ WMAP region

the soft one. The depicted limits represent the current bounds set by those experiments, the IceCube experiment with the Deep Core extension for the detection of low energy neutrinos is expected to obtain a limit exceeding 10^{-40} cm^2 in five years [97].

Chapter 7

Event Reconstruction

Out of the three neutrino flavours, ANTARES is primarily built to detect (anti-)muon neutrinos, for which it possesses the highest sensitivity and the best angular resolution. To determine the direction of neutrinos, the track of a muon generated in a charged current interaction as pictured in figure 7.1 (b) has to be reconstructed. The basic principle for the reconstruction is to compare the arrival times of the emitted Cherenkov photons measured by the PMTs with the calculated arrival times from a track hypothesis, and to vary this hypothesis until an optimal match with the observed signature is found. The difference between expected and measured arrival time, the so-called time residual Δt , is not zero even for the true track, due to the time resolution of the OMs and scattering of light in the seawater. Assuming the muon propagates at the speed of light in vacuum, the muon track is characterised by six free parameters: The direction, which is defined through the zenith and azimuth angles, the three spatial coordinates of a point on the track and the time at which the muon passes this point. This parametrisation is sufficient if the interaction point is located outside the detector and the muon track also extends beyond it, as it is most often the case for muons at the TeV energy scale. For tracks starting or ending in the detector, the track length and the actual interaction vertex have to be considered as parameters, too.

7.1 Background

However, there are several effects complicating the identification and reconstruction of neutrino events. First, signatures identified by the trigger not only originate from upgoing neutrino events, but also from other particles, such as cosmic ray induced muons, as well as the light from bio-

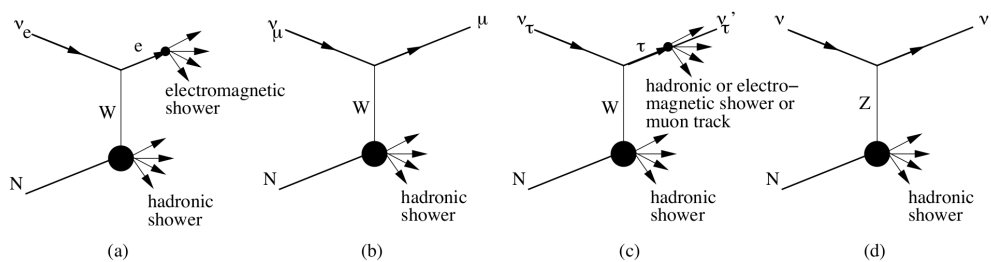


Figure 7.1: Diagrams of charged current interactions with a nucleus by ν_e (a), ν_μ (b), ν_τ (c) and neutral current reactions (d)

luminescent organisms and the radioactive decay of ^{40}K in the seawater. Second, even in upgoing neutrino events, not all light detected in the event is Cherenkov light emitted directly by the muon. The origin of those types of background and their impact on event reconstruction and data analysis are discussed in the following.

7.1.1 Optical Background

As mentioned in section 5.2, the deep sea environment in which the ANTARES detector is located, is not completely dark. ^{40}K decay causes a single hit rate of 40 kHz in each PMT, and also coincident hits in neighbouring PMTs at a rate of about 13 Hz, allowing for an in situ calibration of the timing and overall efficiency of the PMTs as described in section 5.4.7. The background from bioluminescent organisms consists of a component from bacteria and other microorganisms, only changing at timescales of hours, with a rate from 20 kHz up to several hundred kHz per OM. Together with the 40 kHz from ^{40}K decays this random background is referred to as the 'baseline'. On top of the baseline, bursts of bioluminescent light are emitted by larger organisms, increasing the background rate of local groups of OMs significantly, even up to the level of 1 MHz, where the OM shuts down, entering the 'x-off' state described in section 5.4.6. Pure optical background events are caused by random background hits incidentally matching the trigger pattern. The probability of such events to pass the reconstruction algorithm and the associated quality cuts is much smaller however, so they are generally neglected. A study investigating the actual importance of pure background events is later presented in the chapter on the Monte Carlo simulation, chapter 8.

7.1.2 Electromagnetic and Hadronic Showers

High energy muons can cause electromagnetic showers along their track by emission of δ electrons from the surrounding medium and hard bremsstrahlung photons. Electrons and positrons within these so-called subshowers, also emit Cherenkov light, but in a more fuzzy cone than the sharp 42° cone emitted by a muon. The hadronic shower created in addition to the muon in the charged current interaction of the neutrino with a nucleon, the vertex shower, contains particles emitting Cherenkov light, and creates secondary tracks by interaction with electrons in the water. If the interaction takes place within or close to the detector, this light is also detected and interferes with the signature of the muon track. In the case of electron neutrino charged current and neutral current reactions (figure 7.1 (a) and (d)), no muon track is produced, while in charged current tau neutrino interactions (figure 7.1 (c)), the created tau's decay can give birth to a muon, but also to another shower. In principle, hadronic showers could be mistaken for, and reconstructed, as a short muon track, since their light emission is also cone shaped [98]. The cone is more diffuse than for a muon though, thus quality cuts are likely to remove these events. Even if not, the shower's direction is aligned with neutrino's direction as a muon would be, yet with a larger scattering angle. Furthermore, since for those events the neutrino interaction has to occur in or extremely close to the detector, their rate is low and they pose no significant additional background.

7.1.3 Atmospheric Muons

Despite the shielding provided by the seawater above the detector, the rate of atmospheric muons exceeds that of upgoing atmospheric neutrinos by approximately six orders of magnitude. Since misreconstruction of even a small fraction as upgoing represents an additional background to any analysis, the identification of downgoing muon events is of great importance. The existence of an alternative reconstruction solution with a zenith angle tilted by two times the Cherenkov angle of 42° facilitates the reconstruction of downgoing muons as upgoing, as illustrated in figure 7.2. Even though the symmetry allowing this second solution is limited to cases with hits on a single line only, additional hits from optical background or several muon tracks can incidentally conspire a fake signature of an upgoing track on multiple lines. The frequent occurrence of several muon tracks passing the detector within the duration of a single event is due to their simultaneous production in the same cosmic ray interaction. Since only high energy muons reach the detector, the lateral spread of the so created

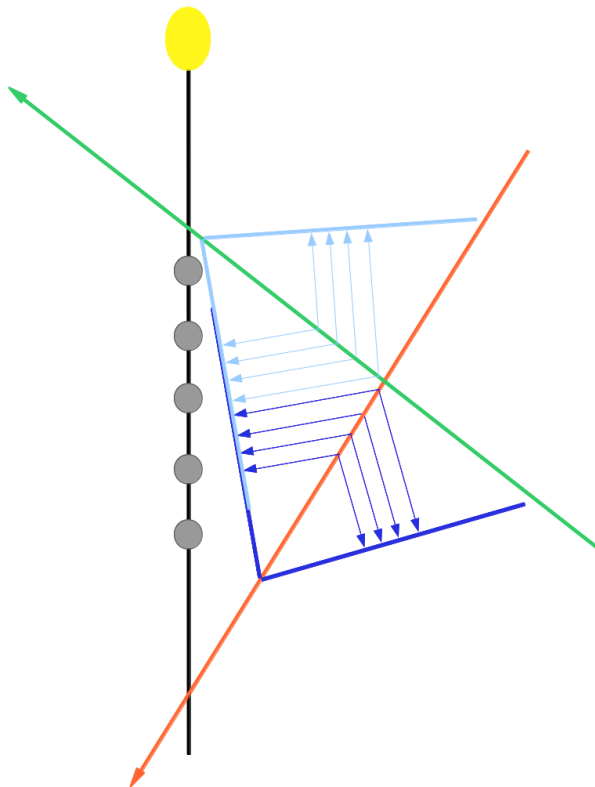


Figure 7.2: On single detector lines, the signature of an upgoing track (green) is almost identical to that of a downgoing track (red) which has a zenith angle different by twice the Cherenkov cone's angle of 42° . The Cherenkov light of the upgoing (light blue) and downgoing (dark blue) track arrives in the same time order at the OMs.

muon bundles at the detector's depth is only a few metres [99]. The OMs are oriented 45° downwards from the horizontal plane, therefore the cross section of their photocathode with the front of direct Cherenkov light from downgoing muon tracks is smaller than for upgoing tracks, depending on the track's zenith angle. For this reason, they are not only less sensitive to downgoing tracks, but the contribution of scattered light and light from electromagnetic subshowers to the detected hit pattern is increased, resulting in a worse time residual distribution compared to upgoing tracks. Downgoing neutrino events cannot be distinguished from the much more numerous atmospheric muon events, and are of significance only close to the horizon where the number of muons decreases, because they have to penetrate an increasing amount of matter to reach the detector.

7.2 SeaTray Software Framework

The data processing and event reconstruction of this work has been performed with programs embedded in the SeaTray Software framework [100]. This adaption of the IceCube collaboration's IceTray framework [101] provides a stream based environment to combine the physics data with the calibration, alignment and run information for processing in the correct time order. Each stream is divided into frames, which in the case of the physics stream correspond to events, in the case of the geometry stream to alignment timeslices of two minutes (see section 5.5). The frames of the calibration and run information streams are written for each calibration period and run respectively. The data processing is divided into modules through which the frames are passed. Each module reads out information packages called frame objects, performs its intended operation on them, adds new, deletes or modifies frame objects, and finally passes the frame to the next module. Code that operates independently from the physics stream is included as services, for example for reloading the alignment and calibration information from the database. Frame objects are adapted versions of common data types or more complex data storage classes. For reconstruction purposes, the hit and particle storage types are the most relevant ones. Hits are stored in maps with the OMs as keys, and a vector storing the individual hits. The individual hits can be of several types. Uncalibrated hits are stored in I3AntSPEHit format, which contains the timestamp, AVC and TVC values. Hits from a Monte Carlo simulation use the I3MCHit format holding the simulated arrival time of individual photons at the OMs and encoding the particle that caused the photons. Calibrated hits and MC hits after simulation of the DAQ electronics are processed as I3RecoPulses, in which the calibrated time and hit amplitude are stored. Muon tracks and particles in general are stored in the I3Particle format, which contains its type, energy, reconstruction status, position and direction. The framework is built around the Boost.Python [102] libraries, to make individual modules and services written in C++ callable from a Python script. The code necessary for a certain task, for example a reconstruction strategy, is put together as a project and is compiled into a single shared object library. It is also possible to write modules and services as Python classes. Thanks to the modular nature of the framework, data processing and MC simulations can be carried out partly using the same code, which reduces the risk of errors due to different treatment of measured data and simulation.

name	$n_{hit_{min}}$	RMS_{max}	$dist_{max}$	Δt_{max}	amp_{min}
X-Cluster	3	4 degree	45 m	150 ns	1.0 pe
Y-Cluster	2	-	5 m	50 ns	2.0 pe
Z-Cluster	4	4 degree	75 m	200 ns	1.5 pe

Table 7.1: The parameters for the sub-selections of the Cluster Hit Selection algorithm

7.3 Hit Selection Strategies

For the event reconstruction it is essential to remove hits from optical background as thoroughly as possible. Background hits from bioluminescence occur uncorrelated, except for bursts by larger organisms, which are identifiable by a significantly increased rate of an OM. In contrast, signal hits are correlated on the nanosecond timescale, leading either to high hit amplitudes if detected by a single OM within its integration time, or to locally coincident hits on neighbouring OMs. Hit selection algorithms separate the hits caused by background from those by muon tracks mainly based on this distinction. The quality of a hit selection strategy is characterised by two quantities: Purity, which is defined as the fraction of true signal hits out of all selected hits, and efficiency, defined as the fraction of signal hits selected out of all signal hits in the event.

7.3.1 Triggered Hits

The trigger algorithms as described in section 5.4.5 provide a first level of hit selection. The L1 hits are used as a seed to the trigger algorithms and the L2 hits are those hits, which are part of the triggered pattern. While the L1 hit selection is neither especially efficient nor pure, the L2 hit selection has a high purity but low efficiency, as demonstrated in figures 7.3 and 7.4. Still it is mostly confined to a single detector line, as evident from figure 7.5.

7.3.2 Cluster Hit Selection

The Cluster Hit Selection algorithm developed in the context of this work groups hits not only by their distance and time difference, but also by their arrangement to each other in time versus z-coordinate, which is the height of the hit OM on the line, as illustrated in figure 7.6. The generally

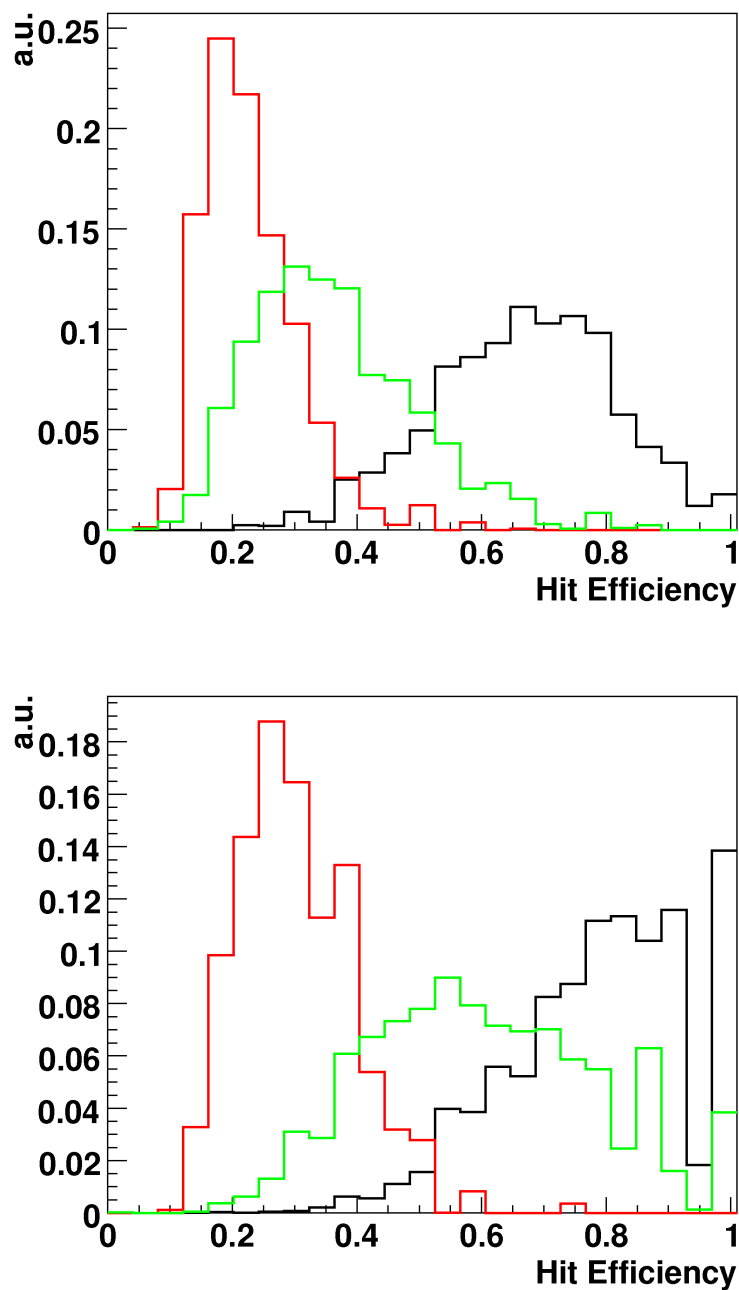


Figure 7.3: Hit selection efficiency distributions and average selection efficiencies for neutrino events with the atmospheric neutrino flux energy spectrum up to neutrino energies of 6 TeV (top) and 600 GeV (bottom), respectively. Black: Cluster hits, Red: L1 hits, Green: L2 hits. Average efficiency for top/bottom is for Cluster: 0.67/0.78, for L1: 0.23/0.30, for L2: 0.36/0.60

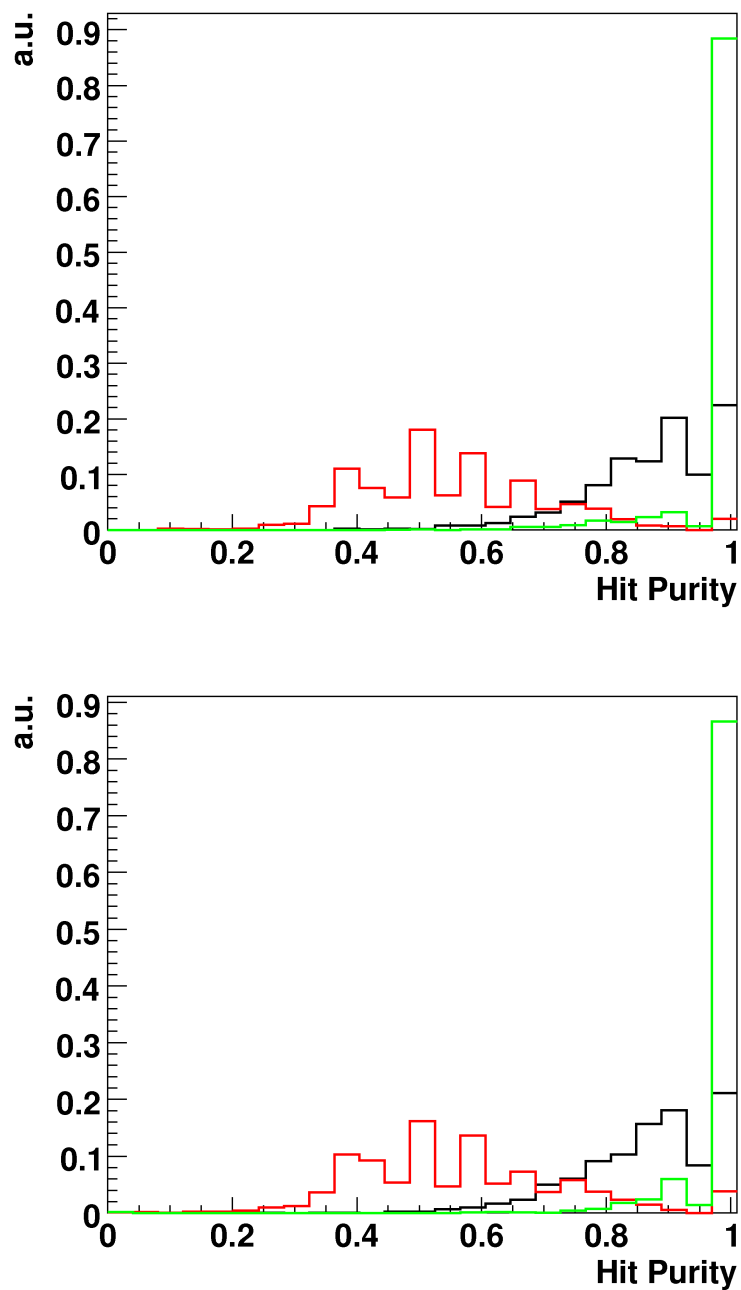


Figure 7.4: Hit selection purity distributions and average selection purities for neutrino events with the atmospheric neutrino flux energy spectrum up to neutrino energies of 6 TeV (top) and 600 GeV (bottom), respectively. Black: Cluster hits, Red: L1 hits, Green: L2 hits. Average purity for top/bottom is for Cluster: 0.87/0.86, for L1: 0.55/0.56, for L2: 0.97/0.97

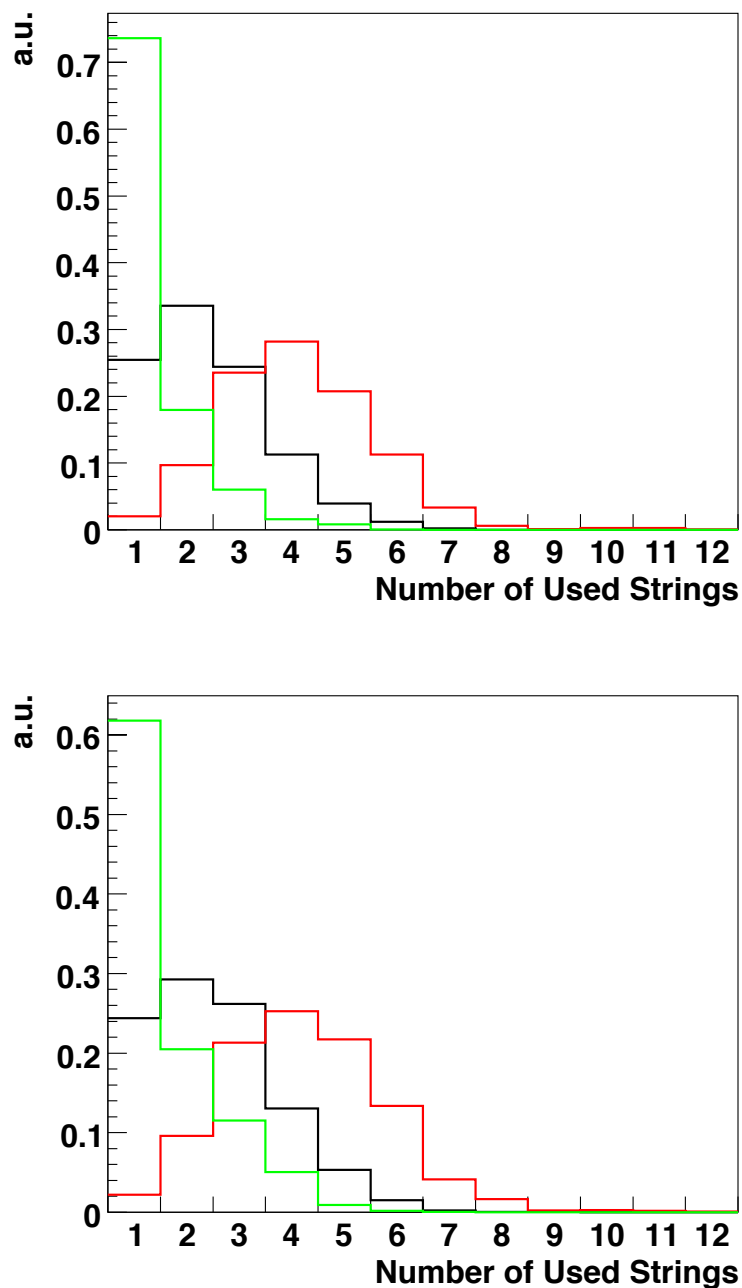


Figure 7.5: Distribution of the number of lines with hits included in the hit selections for neutrino events with the atmospheric neutrino flux energy spectrum up to neutrino energies of 6 TeV (top) and 600 GeV (bottom), respectively. Black: Cluster hits, Red: L1 hits, Green: L2 hits

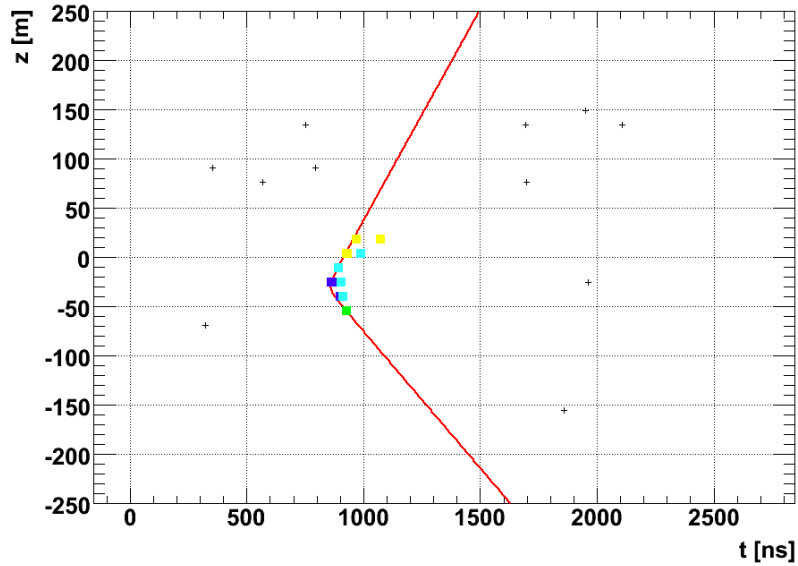


Figure 7.6: Signature of a simulated neutrino event in height z versus time t representation. Red Line: Expected arrival time of Cherenkov light emitted by the track, Green: Direct hits from the muon track, Yellow: Scattered hits from the muon track, Blue: Direct shower hit, Turquoise: Scattered shower hit, Black: Optical background hits

hyperbolic shape of a muon track in this representation is approximated by segments of straight lines with the procedure explained in the following.

For each hit, all other hits within a given time (Δt_{\max}) and distance ($dist_{\max}$) window are selected. If the number of these hits is larger than a chosen size of the cluster to be formed, the directions of the connecting lines in the time versus height plane are calculated for all other hits in the cluster, as well as the root mean square (RMS) of their distribution. If the RMS is larger than a given maximum (RMS_{\max}), the hit with the largest deviation from the mean value is removed. This is iterated until the RMS falls below the prescribed maximum, or the number of hits is lower than the prescribed cluster size ($n_{hit_{\min}}$). In the first case, all hits belonging to the cluster are selected, in the second case, all hits of the cluster are discarded, but may still be included in the selection when they themselves or another hit is examined. A combination of several sub-selections with the parameters chosen to exploit correlations on different scales proved to be efficient. In table 7.1 the parameters for three selections, designated X-, Y-, and Z-Cluster hits are listed. Those sub-selections are created from the

input hits, whereas only the originating hit of the cluster is selected, not those associated with it. The combined hit selection, named Cluster hits, consists of those hits which belong to two of the sub-selections, or which belong to one and surpass a certain minimum hit amplitude (amp_{\min}). The value of amp_{\min} was estimated for each sub-selection to complement its initial selection power. The Cluster Hit Selection has a higher efficiency than both selections from the trigger algorithms, especially at low energies, where it selects 78% of all signal hits on average. It has a high purity of over 85%, and includes multiple lines in about 3/4 of all events.

7.4 BBFit Reconstruction

BBFit is a fast and robust algorithm for track reconstruction [103]. It is based on a hit selection combining the hits on each storey into a single metahit. Coincident hits within 20 ns are merged to the time of the first hit, and the combined hit is assigned an additional virtual charge of 1.5 pe. This sample of metahits is cut at a lower threshold of 2.5 pe, throwing away all other hits. Actually this selection represents two cut criteria: For coincident hits, the sum of both hits has to exceed 1 pe, while large hits have to be above 2.5 pe. Only hits on lines with a T3 cluster (see section 5.4.5) formed by these hits are considered in the fit. Further hits are added recursively to the input hit selection, which occur on adjacent storeys with distance Δz in a time window Δt defined by

$$-10\text{ns} < \Delta t < 10\text{ns} + \Delta z \cdot \frac{n}{c} \quad (7.1)$$

or on next to adjacent storeys with the width of the time window doubled. The original hits with an amplitude above 2.5 pe are assigned an error of 10 ns on the time residuals in the fit, the additional hits 20 ns. In addition to the time residual, a normalised term representing the product of its measured amplitude and the distance to the emission point of the Cherenkov photons is calculated for each hit. The fit consists in the minimisation of the sum over all input hits of the time residuals plus the amplitude terms, using ROOT's MINUIT package [61]. A fit performed on the hits on a single line can not determine the azimuth angle of the track. With four degrees of freedom, hits on five storeys have to pass the above mentioned selection criteria for a single fit to succeed. For a fit on multiple lines six hits are required, as it determines also the azimuth angle. For two lines, there is another ambiguity on the azimuth angle, as the two lines form a plane on which the whole geometric setup can be mirrored. This can be partly overcome by examining the direction of the detected photons, which requires

knowledge on the orientation of the OMs provided by the alignment, a feature implemented in a more recent version of the algorithm [104]. The detector geometry used in the original version of BBFit, which was used for this work, is the trigger geometry, where all OMs are on the centre of the line. The limited angular resolution arising from this is no significant factor in an analysis of low energy events though. BBFit not only tests the muon track hypothesis, but also a possible pointlike emission of light by electromagnetic or hadronic showers. In this case simultaneous emission from a single point in space is assumed, disregarding the direction.

7.4.1 Quality Cuts

The minimal χ^2 from the fit divided by the number of degrees of freedom (which usually and also in this work is called χ^2) is the primary cut parameter for BBFit, together with the number of lines used in the fit. If χ^2 is better for the point emission hypothesis than for the track hypothesis, the event is regarded as a shower event, and not used in the further analysis. Separate cuts were applied for single line events, double line events and events with three or more lines. For the analysis presented in chapter 9, optimized cuts were used, with the optimisation of the cut parameters and their dependence on the number of lines explained later in section 9.2.2. For testing the quality of the different reconstruction elements as well as the comparison between data and simulation, estimated cuts were used, which were chosen as $\chi^2 < 1$ for one line events, $\chi^2 < 1.5$ for two line events, $\chi^2 < 2$ for three or more line events.

7.5 Artificial Neural Networks

7.5.1 Event Classification

In parallel to the reconstruction an Artificial Neural Network (ANN) is used, analysing input parameters like the hit distribution, total hit amplitude and many others to distinguish downgoing muon events from neutrino events. The development of this code and its properties are described in [105]. The ANNs used for this work were trained using MC simulations with real background from minimum bias events added. To account for different background rates, two networks were trained, one for the range from 60 kHz to 80 kHz, and one for the range from 80 kHz to 100 kHz. The applied procedure of adding measured background to simulated events developed within this work is described in section 8.1.5.

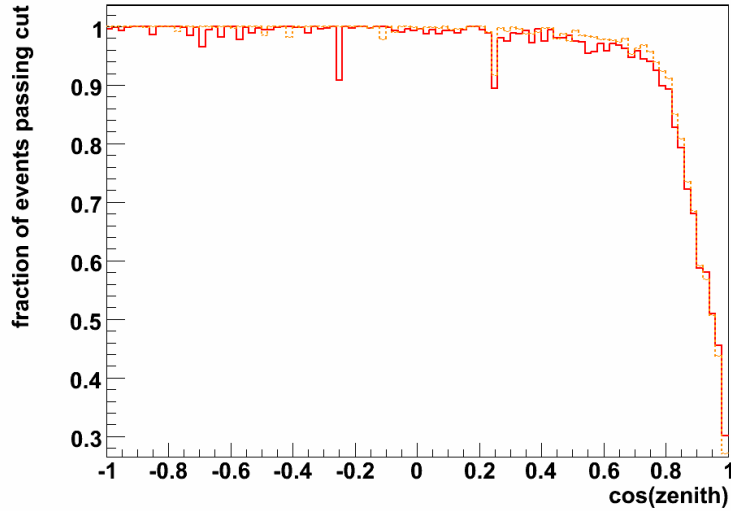


Figure 7.7: Fraction of events passing the neural net for event classification as a function of the cosine of the zenith angle. Red (solid): MC with background and gain distribution from Minimum Bias Events, Orange (dashed): MC with simulated background and gaussian gain distribution (for details see section 8.2).

For the low background optimised network runs 042588 and 042640 were used, and runs 042652 and 042695 for the high background optimised one. The efficiency of the selection was tested with the two different simulations for runs 054171 to 054201 described in section 8.2 (see also Appendix A for details), for which the ANN proved to work equally well. As seen from figure 7.7, the efficiency is strongly dependent on the zenith angle. The ANN is well suited to reject straight downgoing muon events, but loses rejection power for more horizontal directions. Virtually all events with $\cos(\text{zenith}) < 0$ pass the selection, so there is only a negligible loss of upgoing neutrino events.

7.5.2 Energy Reconstruction

An ANN, similar to that for the event classification, is also employed for energy reconstruction. Again, two networks for the different background levels were trained with the same MC samples as the event classification networks. The input of the energy reconstruction are primarily numbers

and amplitudes of all hits and triggered hits, as well as their distribution on lines and OMs. The resolution improves if the direction of a reconstructed track is also evaluated. For this purpose, the result of BBFit was used. More information on this project named ANNergy is available in [106].

The precision of the energy reconstruction was also tested with the simulations for runs 054171 to 054201. The reconstructed energy is compared to the energy of the MC muon track at the point where it enters the sensitive volume around the detector, called 'can' (see section 8.1.1), or at the neutrino interaction point, if it is inside the can. Figure 7.8 shows the distribution of the difference between reconstructed energy and true muon energy. For those events which pass the cuts defined in section 7.4.1, the difference is on average smaller than for all events. Still, virtually all events are correctly reconstructed within a precision of one order of magnitude for both cases, albeit with a small systematic shift towards higher energies from the reconstruction. For the neutrino candidate events however, those which are reconstructed as upgoing by BBFit and pass the cuts, larger differences and a significant shift to higher reconstructed energies are found.

7.6 Simulated Annealing Track Reconstruction

A series of innovations to improve the reconstruction efficiency at very low energies were explored within the scope of this work. One approach was to take advantage of the simulated annealing minimisation method already used in ANTARES for shower reconstruction [107]. It converges on the minimum of a log-likelihood function by successively reducing the scale of a random walk search. Unlike algorithms following the gradient of the log-likelihood function, it is able to find the minimum of functions which are neither smooth nor continuous. Based on and named after this minimiser, the Simulated Annealing Fit is used in addition to the BBFit reconstruction.

In general, an initial hit selection excludes some events a priori by not providing sufficient hits for the fit to succeed. BBFit uses a selection combining all hits on a storey into one, further reducing the number from those selected by coincidence and amplitude. In order to avoid such a strict preselection, the Simulated Annealing Fit is based on the Cluster hit selection, which does not merge hits. Furthermore, the possibility to start the reconstruction from all L0 hits was included as well. Another aspect was to search alternatives for cutting on a parameter representing the reconstruction quality in order to reject wrongly reconstructed muon

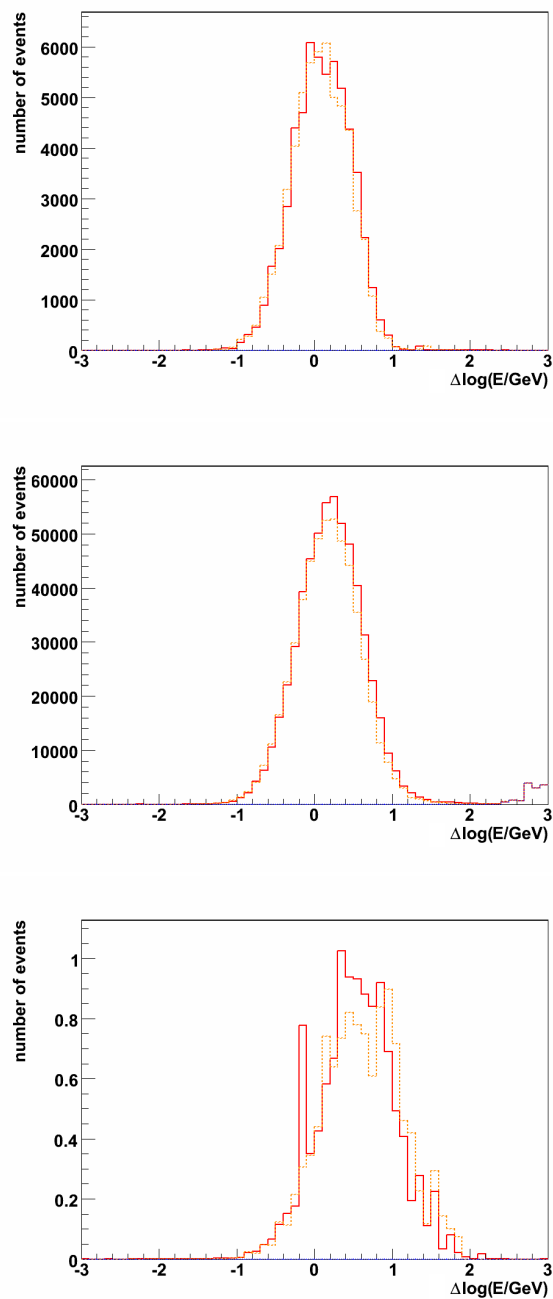


Figure 7.8: Reconstructed energy minus true muon energy of BBFit and ANNergy reconstructed events with cut on BBFit reconstruction quality from section 7.4.1 (top), without cut (middle) and for upgoing reconstructed events after cuts (bottom). Red (solid): MC with background and gain distribution from Minimum Bias Events, Orange (dashed): MC with simulated background and gaussian gain distribution(for details see section 8.2)

events. Such a cut, like on χ^2 in BBFit and Λ in the Aart Reconstruction, has a high probability to remove low energy events in which light from the vertex shower degrades the time residual distribution of the reconstructed track. In the Simulated Annealing Reconstruction three prefits with different probability density functions and initial hit samples are combined to actively identify downgoing events instead.

7.6.1 The Gulliver Reconstruction Framework

Gulliver is a sub-framework within IceTray and SeaTray for easy combination of the elements needed for a reconstruction algorithm. Those elements are a track parametrisation, an initial seed track to start the minimisation, a minimiser and a likelihood function L . The fit consists in a minimisation of $-\log(L)$, which is calculated in each minimisation step from the track hypothesis proposed by the minimiser. The track parametrisation serves as an interface which translates the parameters varied by the minimiser to the I3Particle format, which is passed to the service that calculates L . $-\log(L)$ is usually calculated as the sum over the the probabilities p_{hit} for all n_{hit} hits in the input hit selection to match the track hypothesis:

$$-\log(L) = \sum_{\text{hit}=1}^{n_{\text{hits}}} -\log(p_{\text{hit}} \cdot a) \quad (7.2)$$

For each hit, p is extracted from a Probability Density Function (PDF), which in the simplest case is the expected distribution of the time residuals, but in general can contain additional terms depending on the hit's amplitude. The contribution of each hit is weighted by a factor a , which for the Simulated Annealing Fit is the individual hit amplitude normalised to the sum of amplitudes in the input hit selection. A collection of basic reconstruction elements exists in the Gulliver-Modules and Lilliput projects of IceTray and SeaTray, while the additional code written for the development of this reconstruction method was bundled in the Seagull project.

7.6.2 Track Parallel Parametrisation

The standard track parametrisation in Gulliver has six parameters, three position coordinates, as well as time, zenith and azimuth. An alternative track parametrisation was developed for the Simulated Annealing Fit, which assumes one hit to have a time residual of zero. The hit with the largest amplitude from the input hit selection serves as this reference hit. The emission time t_0 of the Cherenkov light causing the reference hit is

expressed as a function of the distance of closest approach d between track and reference hit by the linear expression

$$t_0 = t_{\text{ref}} - \frac{c \cdot n \cdot d}{\sin(42^\circ)} \quad (7.3)$$

with the speed of light c and the refractive index n of seawater. The track's position is expressed in a coordinate system aligned to the direction of the track hypothesis as the horizontal and vertical orthogonal distance of the track to the reference hit. Along the coordinate z' of the track direction, the light emission point z'_0 corresponding to t_0 is given by

$$z'_0 = z'_{\text{ref}} - \frac{d}{\tan 42^\circ} \quad (7.4)$$

With this coordinate transformation and partial linearisation, the number of parameters to be minimised is reduced to the four degrees of freedom. From the original five degrees of freedom, one is fixed by choosing the time residual of the reference hit as zero. Because the track is passed to the likelihood service in I3Particle format, which stores the position and orientation using the original six parameters, a coordinate transformation is done for each minimisation step.

7.6.3 Probability Density Function

To calculate a realistic global likelihood L for the parameters describing the actual track, a Probability Density Function (PDF) has to provide the precise likelihood p for each hit in the input hit selection. Background hits and hits from scattered light have to be included, if they are not removed by a previously applied hit selection algorithm. For the Simulated Annealing Fit a PDF for the Cluster Hit Selection was created by extracting the time residual distributions from the MC simulation of upgoing neutrinos. The difference Δt between the expected arrival time of the photons if they were emitted by the simulated muon track and the real hit's time was calculated for all hits in the simulated events, which passed the Cluster Hit selection. The hits were categorised by the natural logarithm of their amplitude and the distributions normalised for each amplitude range.

To facilitate the convergence of the minimisation, the PDF is also required to be well defined for time residuals exceeding those covered by the simulation, and to be smooth and continuous. Therefore an analytical expression with this behaviour was fitted to the simulated distribution as shown in figure 7.9. The observed distribution of a symmetric peak

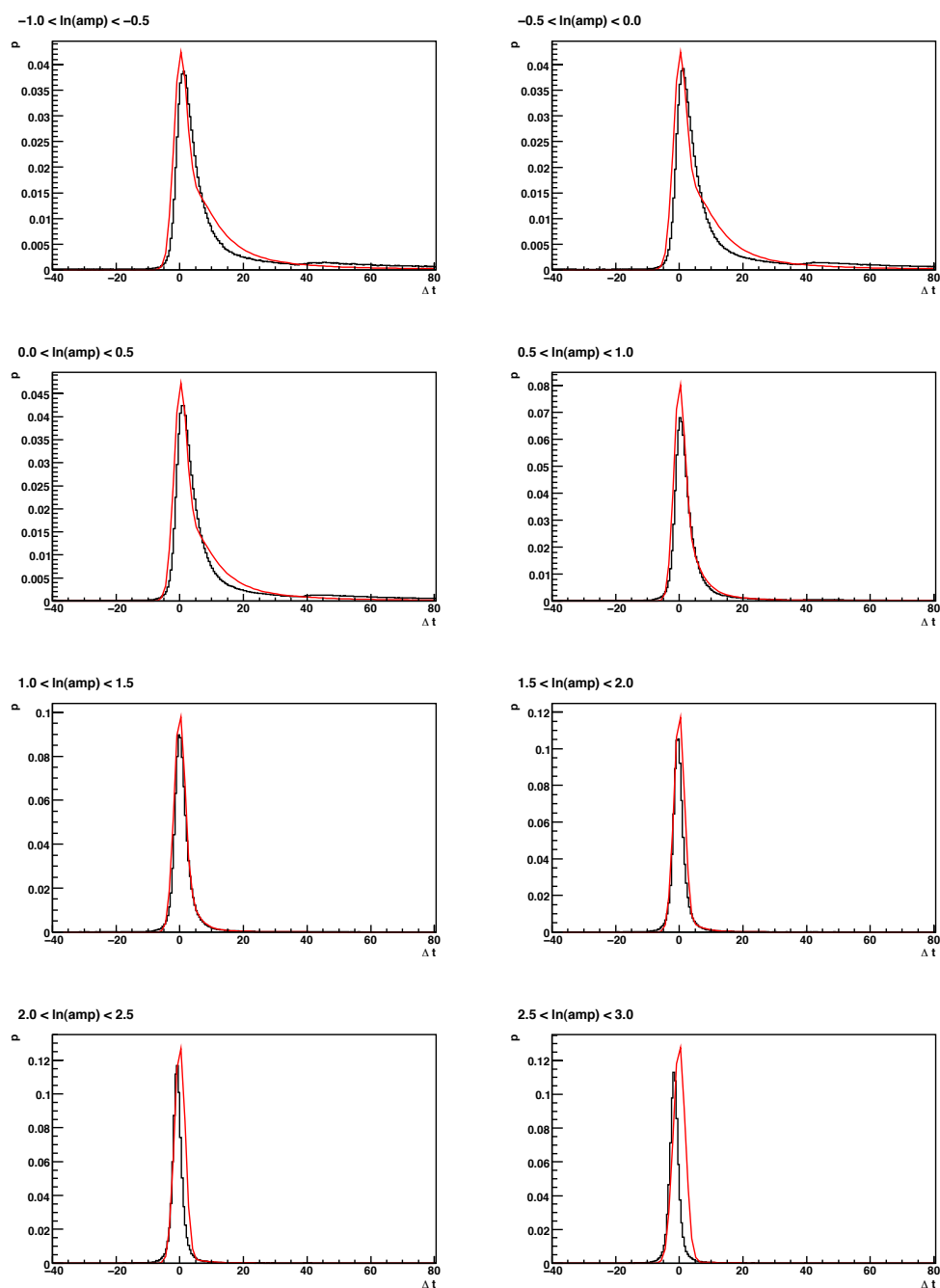


Figure 7.9: Time residual distributions extracted from the MC simulation (black) and the fitted PDF (red) used in the first prefit and final fit of the Simulated Annealing Fit, for different $\ln(\text{amp})$ in bins of 0.5 width, ascending from top left (-1 to -0.5) to bottom right (2.5 to 3).

around zero and a tail of larger Δt representing later arriving photons was parametrised by the sum of the Landau distribution and a gaussian distribution, with four free parameters for each amplitude bin.

$$p(\Delta t, a, b, c, d, e) = a \cdot \Phi(\Delta t, b, c) + d \cdot \exp\left(\frac{-\Delta t^2}{2e}\right) \quad (7.5)$$

where $\Phi(\Delta t, b, c)$ is of the shape

$$\Phi(\Delta t) = \frac{1}{\pi} \int_0^\infty \exp(-s \ln(s) - \Delta t s) \sin(\pi s) ds \quad (7.6)$$

but with the maximum probability of the distribution shifted to b , and a parameter c scaling the width of the distribution. The exact numerical implementation is described in [108], and a list of the values fitted for the parameters is given in Appendix B.

7.6.4 Prefits

To reduce the number of muons misreconstructed as upward going, three prefits are performed in parallel, one optimised to find the best reconstruction solution for an actual upgoing neutrino, and two in addition to identify downgoing muon events. The first prefit, specialised for upgoing neutrinos, uses the Cluster hit selection as input hit selection and the PDF described in section 7.6.3.

The second prefit also uses the Cluster Hit Selection, but all hits on a storey are shifted to the time and position of the first hit. Hits from secondary electromagnetic showers and scattered light, which are especially abundant in downgoing muon events, occur after direct hits from unscattered Cherenkov light emitted by the muon track itself. Large numbers of those late hits can form a pattern wrongly identified as an upgoing event by a fit with a PDF optimised for upgoing events. Only the time of the first, but the amplitude information of all selected hits on a storey enter into the calculation of the likelihood, to further reduce the influence of random optical background. With the tail from later arriving photons removed, a gaussian distribution of 5 ns width serves as the PDF. In summary, the second prefit proves that the direct hits in shower dominated events are also compatible with an upgoing track solution.

The third prefit is performed on the full, unmodified L0 hit sample. The PDF is a 50 ns wide gaussian distribution, suitable to reconstruct high energy muon bundles and shower dominated events, but also retaining a reconstruction possibility for low energy events which contain less than

three hits in the initial hit selection of the other prefits. The primary aim of this coarse fit procedure is to safeguard against cases, in which the Cluster Hit Selection picks out a subset of hits resembling a single muon track, ignoring correlations on a larger scale.

For each prefit, the hits with a time residual of less than 40 ns are selected out of the input hit selection, and the fit is considered as converged if three hits on one line are found. If one of the converged prefits reconstructs the event as downgoing, which is defined as $zenith < 100^\circ$ in order to include muons close to the horizon, it is discarded.

7.6.5 Final Fit

To improve the angular resolution, a Final Simulated Annealing Fit is performed with one of the prefits as the starting point, and its respective hits selected as the input hits. From the converged prefits, the one closest to the weighted average of the zenith angles reconstructed by the prefits is chosen. The first prefit is assigned triple weight, if the number of cluster hits is below 10, the second if it is between 10 and 20 and the third if it is above 20. This ad-hoc selection procedure reflects the assumption that the second and third prefit are better suited to reconstruct events with large numbers of hits caused by secondary showers. If the prefit has converged close to the actual muon track, the influence from shower hits is reduced by the removal of all hits with time residuals larger than 40 ns. Therefore, the PDF described in section 7.6.3 is used for the final fit, which promises the best angular resolution. The minimisation is restricted to a zenith angle band of $\pm 10^\circ$ around the solution of the selected prefit.

7.6.6 Event Preselection

Since the computing time requirements of this reconstruction method are quite high, only events which have not been successfully reconstructed by BBFit, and are not identified as high energy atmospheric muons, are processed. Events, to which one of the following criteria applies, are not passed to the Simulated Annealing algorithm:

- pass the general BBFit quality cuts as defined in section 7.4.1,
- are reconstructed as downgoing by BBFit,
- are reconstructed as a pointlike emission by BBFit,

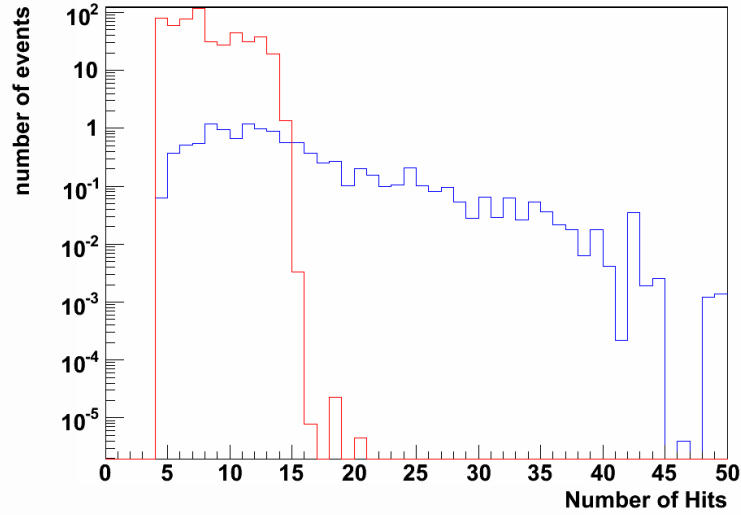


Figure 7.10: The distribution of $n_{\text{directhits}}$ for events passing the 4-hit-cut of the Simulated Annealing Reconstruction. Red: Misreconstructed muons, Blue: Correctly reconstructed neutrinos

- are sorted out by the neural network for event classification as down-going muons,
- are reconstructed with an energy above 600 GeV by the energy reconstruction.

To obtain the reconstruction efficiency on all events (instead of only those not reconstructed by BBFit), a Monte Carlo set with 60 kHz white noise optical background per OM, modelled after the conditions in runs 054171 to 054201 (see 8.2 for more details), was reconstructed. From this test sample only those events were removed which:

- are sorted out by the neural network for event classification as down-going muons,
- are reconstructed with an energy above 600 GeV by the energy reconstruction.

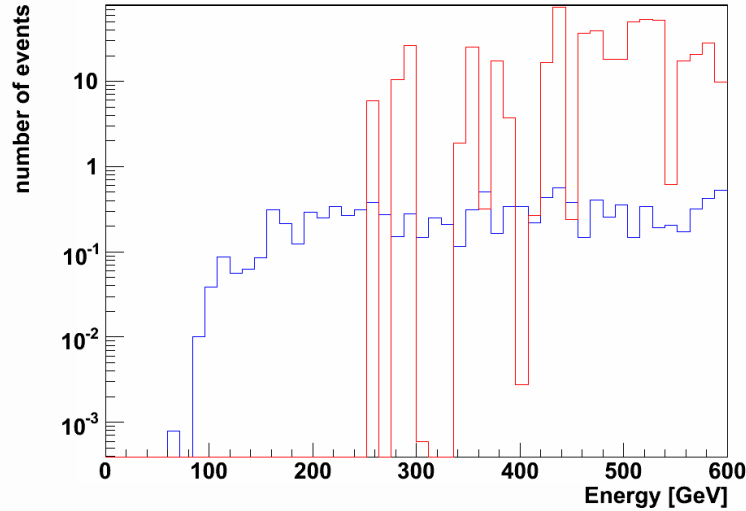


Figure 7.11: The distribution of the reconstructed energy for events passing the 4-hit-cut of the Simulated Annealing Reconstruction. Red: Misreconstructed muons, Blue: Correctly reconstructed neutrinos

7.6.7 Quality Cuts

A first basic quality cut is to check whether four direct hits, defined as having a time residual smaller than 15 ns, exist for the reconstructed track in the L0 hits. This 4-hit-cut is to ensure that the minimisation has converged on all four degrees of freedom. The tracks reconstructed as upgoing by all three prefits already have a high purity against misreconstruction of muons. The number of direct hits, $n_{\text{directhits}}$, is further used as a cut parameter to separate misreconstructed muons from the neutrino events, as a high number of direct hits indicates, that the light was directly emitted from the track. Since the PMTs are oriented downward at an angle of 45° , the light detected from downgoing muon events is mostly scattered light or from electromagnetic subshowers, resulting in larger time residuals than for light emitted directly by an upgoing track. The distribution of the number of direct hits for muon and neutrino events from MC simulation as shown in figure 7.10 supports this conclusion. From the results of the MC simulation it was also perceived that the energy, as reconstructed by the algorithm presented in section 7.5.2, can be used to separate wrongly reconstructed muons from the neutrino events. As demonstrated by the distributions in figure 7.11, the reconstructed energy of neutrino events is

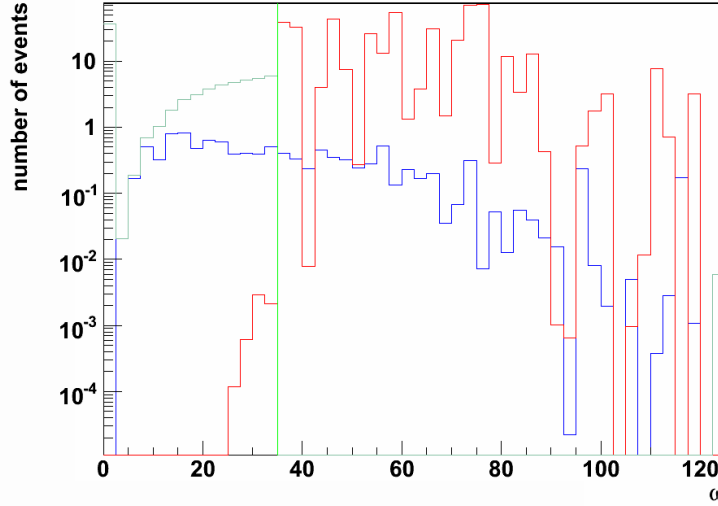


Figure 7.12: The distribution of ω for events passing the 4-hit-cut of the Simulated Annealing Reconstruction with a cut limiting the number of misreconstructed muons to be the same as the number of neutrino events. Red: Misreconstructed muons, Blue: Correctly reconstructed neutrinos. Turquoise: Integrated number of neutrino minus muon events, Green: Position of the cut

lower on average than for muon events. To combine the separation power of both distributions, their ratio

$$\omega = \frac{E[\text{GeV}]}{n_{\text{directhits}}} \quad (7.7)$$

was chosen as a cut parameter. For the test sample, the cut on ω was set at the point where the additional background from misreconstructed atmospheric muons is equal to the number of reconstructed events from atmospheric neutrinos. The distribution and this cut are explained by figure 7.12. Due to the preselection of events reconstructed below an energy of 600 GeV and the 4-hit-cut, ω can take a maximum value of 125.

7.6.8 Reconstruction Performance

The reconstructed events from the test sample after executing the ω cut were used to assess the reconstruction efficiency. Figure 7.13 shows the

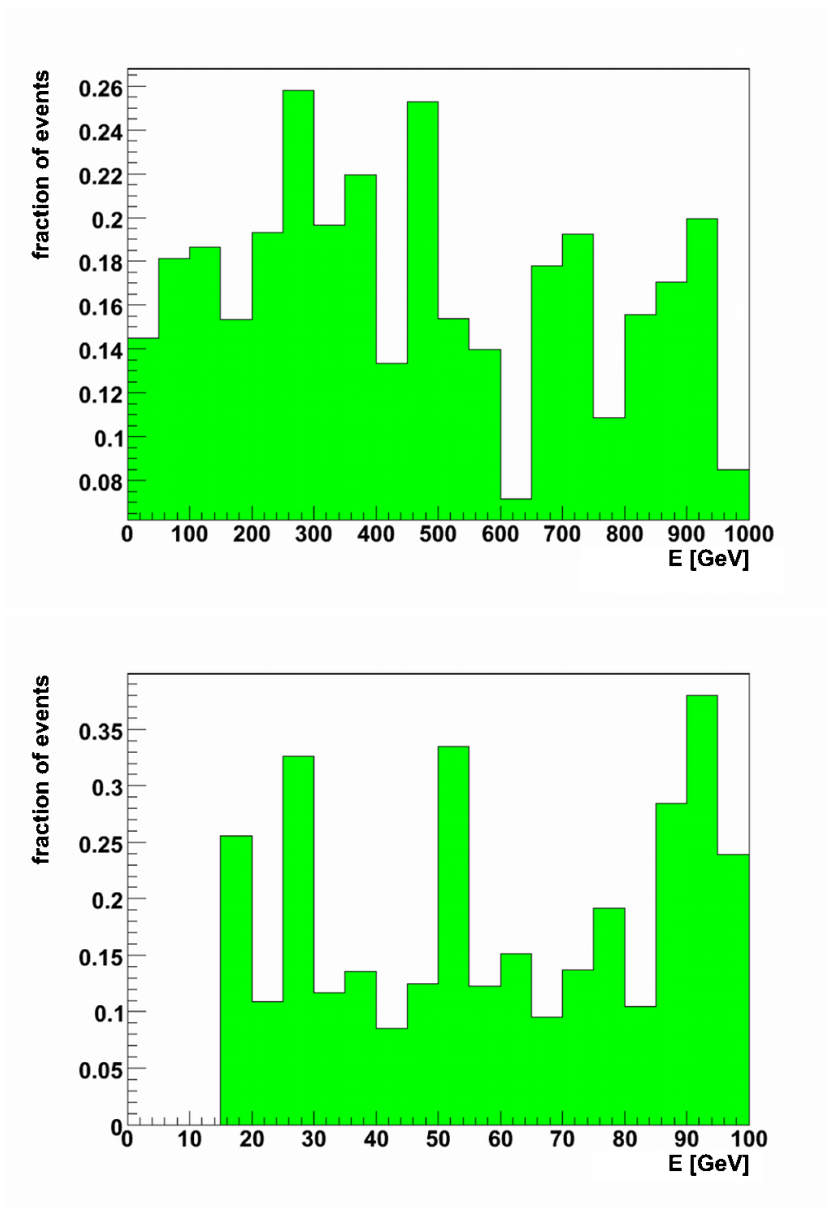


Figure 7.13: Ratio of Simulated Annealing Fit reconstructed events to triggered events as a function of neutrino energy up to 1 TeV (top), and up to 100 GeV (bottom).

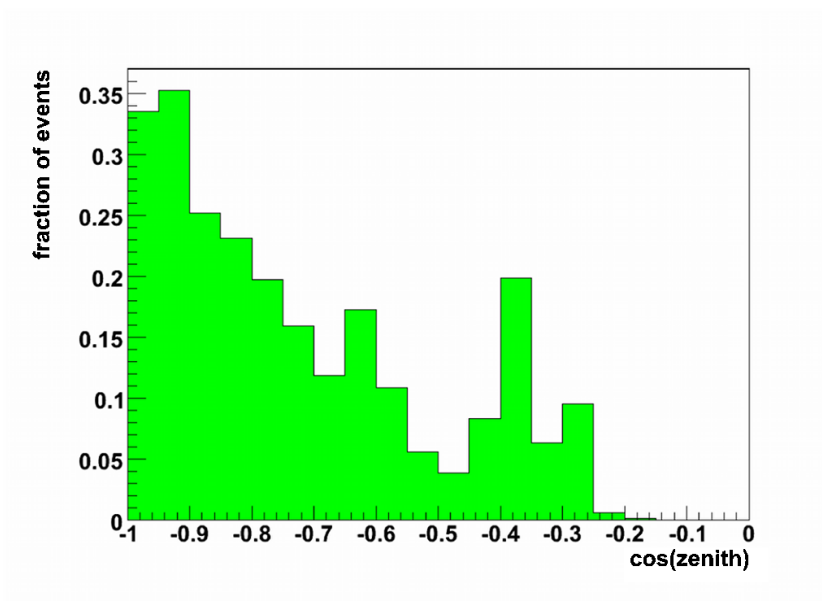


Figure 7.14: Ratio of Simulated Annealing Fit reconstructed events to triggered events as a function of the cosine of the zenith angle.

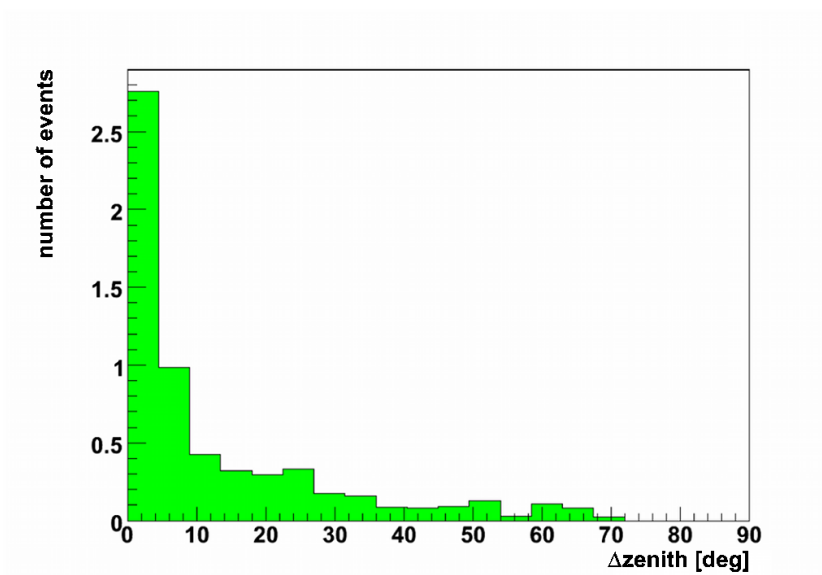


Figure 7.15: Difference in zenith angle between Simulated Annealing Fit reconstructed and true muon track.

efficiency as a function of the true neutrino energy, however with large fluctuations due to the low statistics of the test sample. Notwithstanding an efficiency of about 20% varying by about 10% throughout the whole tested energy range is achieved, even down to 15 GeV neutrino energy as emphasised in the figure's lower panel. The efficiency is highly dependent on the zenith angle, with events going straight upward reaching up to 35% probability to pass reconstruction and cuts, as seen from figure 7.14. The mean zenith difference between the reconstructed and simulated track is 13° with its distribution shown in figure 7.15.

7.7 Aart Reconstruction

The Aart Reconstruction strategy, named after its inventor Aart Heijboer, is a muon track reconstruction algorithm for ANTARES, optimised for good angular resolution at high neutrino energies. It was

7.7.1 Reconstruction Steps

As a starting point for the reconstruction chain serves a linear fit on the positions and times of the L1 hits. To create linear relations, all hits are assumed to be on the muon track, disregarding different light propagation times. The next steps are two more precise consecutive fits. In the first one, a robust M-estimator function based on the sum of the time residuals, weighted by the hit amplitude, is maximised. The function is linear for large time residuals and quadratic for small ones. The second fit uses a log-likelihood minimisation. The Probability Density Function (PDF) for the time residuals is modelled after the hit distributions obtained from simulated tracks without hits from optical background. Both fits also contain an additional term comparing the measured amplitudes with those predicted by simulation. This procedure is performed with nine starting points derived from the linear prefit, the fit result itself, four tracks translated parallel by 30 m and four tracks tilted by 25° each. The final fit uses the prefit with the best likelihood as starting point and all hits with time residuals from -250 ns to 250 ns with respect to it. Its likelihood, which takes the presence of background hits into account, is also based on the time residuals, but depending on the measured amplitudes of the hits.

7.7.2 Cut Parameters $\hat{\alpha}_\mu$ and Λ

Each final fit comes with parameters $\hat{\alpha}_\mu$ and Λ , describing the reconstruction quality. $\hat{\alpha}_\mu$ is the error estimate on the direction extracted from the error matrix of the fit. It is calculated from the fitted zenith $\hat{\Theta}$, the zenith error $\hat{\sigma}_\Theta$ and the azimuth error $\hat{\sigma}_\Phi$ as

$$\hat{\alpha}_\mu = \sqrt{\sin^2(\hat{\Theta})\hat{\sigma}_\Phi^2 + \hat{\sigma}_\Theta^2} \quad (7.8)$$

Λ is the logarithm of the likelihood L from the final fit, divided by its number of degrees of freedom, n_{dof} , minus the number of prefits from the second step with a deviation of less than one degree from the best one, N_{comp} , divided by ten.

$$\Lambda = \frac{\log(L)}{n_{\text{dof}} - 0.1(N_{\text{comp}} - 1)} \quad (7.9)$$

Downgoing atmospheric muons which were falsely reconstructed as upgoing neutrino events have on average a lower Λ than true neutrino events, which is used to separate them. However, the distribution of the muon events falls quite steep with increasing Λ . This makes it necessary to adapt the cut to different detector configurations and background rates, and also makes it most likely sensitive to inaccuracies in the simulation of the detector, like those investigated in 8.2. For the Λ distribution of simulated events with a full twelve line ANTARES detector and a background rate of 60 kHz per OM, see [77]. Assuming these conditions, the events with $\Lambda > -5.3$ contain 10% misreconstructed atmospheric muons in addition to the atmospheric neutrinos.

Chapter 8

Monte Carlo Simulation

8.1 Simulation Chain

Simulating the expectation of detected events from a given neutrino flux takes many steps and is connected to the processing of the measured data in many aspects to account for the varying conditions of the detector. The succession of the simulation elements explained in this chapter as well as their dependencies among each other and from the data processing are outlined in figure 8.1.

8.1.1 Atmospheric Muon Simulation

The ANTARES MC production used for this work, models the background from atmospheric muons on an event by event basis. For the first step, which is the simulation of the interaction of cosmic ray particles with Earth's atmosphere, the CORSIKA (Cosmic Ray Simulations for Cascade) program with the QGSJET hadronic interaction model[109] is used. The propagation of the particles created in the interaction to the sea surface is also included in CORSIKA. To take the composition of the cosmic rays into account, interactions with primary particles p, He, N, Mg and Fe are simulated. At the sea surface level, the muons are selected out of the shower particles, and the effects of their propagation to the detector, especially scattering and energy loss, are simulated with a program based on MUSIC (Muon Simulation Code) [110]. Due to the limited range of light in water, only the part of the muon track intersecting a cylindrical volume around the detector, called 'can', with a radius $R_{\text{can}} = 238.6$ m and height $H_{\text{can}} = 592$ m is considered for the simulation of light production and detector response, for which KM3 [74] is used. Because of the high number

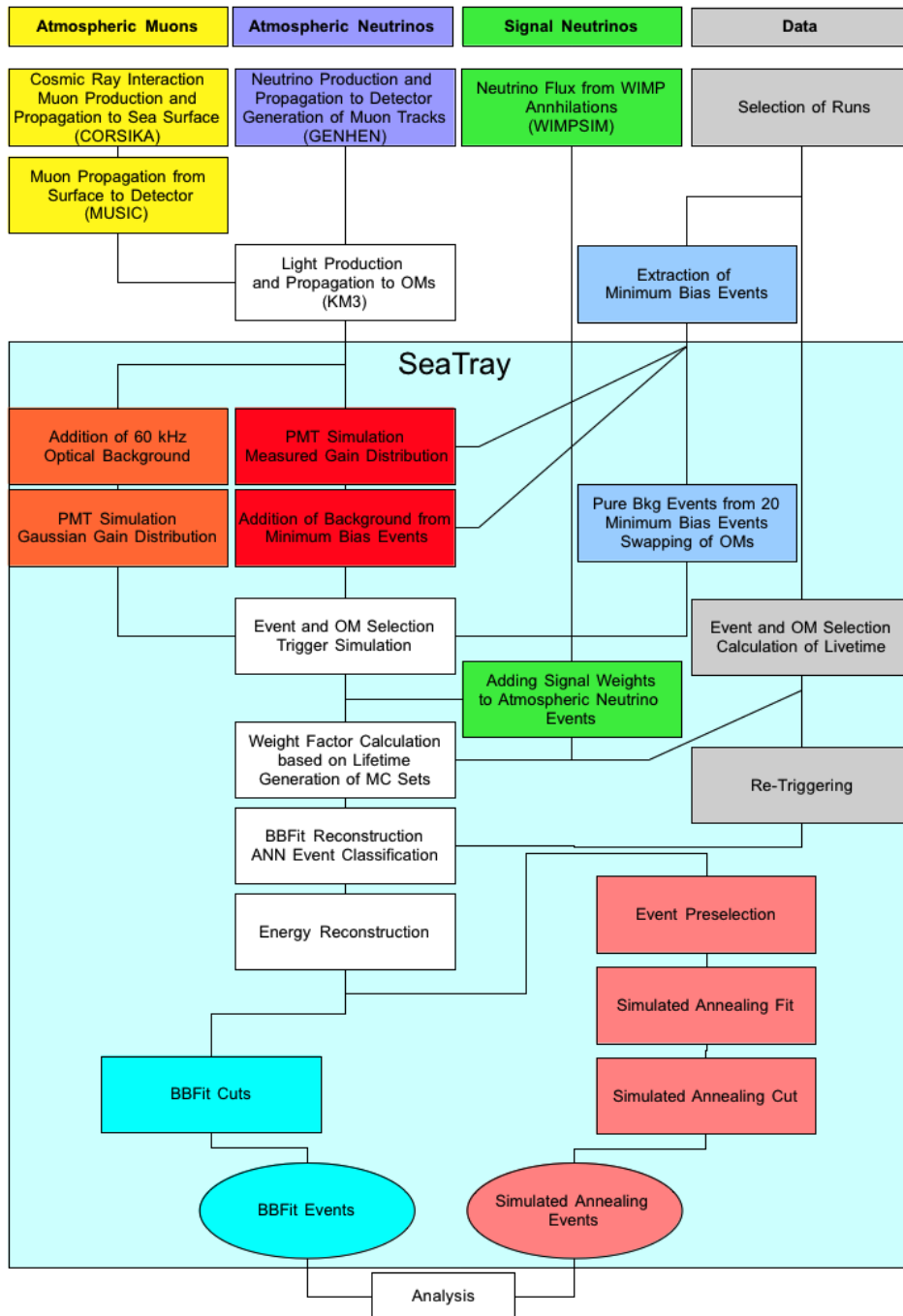


Figure 8.1: Block diagram of the MC simulation chain and data processing, illustrating the dependencies between the elements. White: Common elements, Grey: Data processing, Yellow: Atmospheric muon MC, Purple: Atmospheric neutrino MC, Green: Signal MC, Orange: MC with simulated background and gaussian gain distribution, Red: MC with background and gain distribution from Minimum Bias Events, Light Blue: Pure optical background event MC, Turquoise: BBFit event sample, Salmon: Simulated Annealing event sample.

Energy/Angle Bin Primary	v1	v2	v3	h1	h2	h3
p	200	1000	400	200	1000	400
He	900	100	900	900	100	900
N	200	200	240	200	100	240
Mg	200	335	300	200	200	120
Fe	200	120	200	200	120	200

Table 8.1: Number of atmospheric muon MC files for different primary types, with zenith range h from 0° to 60° , v from 90° to 60° and energy range 1 from 1 TeV to 10 TeV, 2 from 10 TeV to 100 TeV, 3 from 100 TeV to 10^5 TeV

of photons generated, a full simulation of each event is not feasible. Instead the number of photons and their arrival times, dependent on the relative position and orientation of an OM, are taken from precalculated tables. The absorption and scattering length, as well as the total efficiency and angular acceptance of the OM enter into this calculation, with decisive impact on the total number of photons detected by the OMs. The MC production used for this work is based on the angular acceptance from [111], and the water properties, 55 m absorption length and 52.85 m scattering length, from [112]. The simulated events are stored in files divided into two zenith angle ranges, horizontal (h) from 0° to 60° , and vertical (v) from 90° to 60° . Furthermore, they are divided into three energy ranges, 1 from 1 TeV to 10 TeV, 2 from 10 TeV to 100 TeV and 3 from 100 TeV to 10^5 TeV. For each primary type, energy bin and zenith bin, the number of files in table 8.1 is available from the production. For each of these files, the number of events listed in table 8.2 was simulated. The actual number of events in the files is lower, since only events causing at least one hit were stored.

8.1.2 Neutrino Simulation

The used MC simulation of neutrino events was created with the GENHEN software [73]. It calculates possible absorption of the neutrinos on their passage through Earth from different directions and at different energies, as well as the generation of muon tracks by interactions close to the detector, and their propagation to the can. At this point, the simulation chain merges with the one for atmospheric muons, as light production and detector response are done with KM3. The neutrino events are generated with an $E^{-1.4}$ spectrum and stored in low energy files with 10^{10} events from 10 GeV to 10^7 GeV, and high energy files with 10^8 events from 10^6 GeV to 10^8 GeV.

Energy/Angle Bin Primary	v1	v2	v3	h1	h2	h3
p	$5 \cdot 10^6$	$1 \cdot 10^6$	$2.5 \cdot 10^5$	$6 \cdot 10^6$	$1 \cdot 10^6$	$2.5 \cdot 10^5$
He	$1 \cdot 10^6$	$1 \cdot 10^6$	$1 \cdot 10^5$	$1 \cdot 10^6$	$1 \cdot 10^6$	$1 \cdot 10^5$
N	$5 \cdot 10^5$	$5 \cdot 10^5$	$2.5 \cdot 10^4$	$5 \cdot 10^5$	$1 \cdot 10^6$	$2.5 \cdot 10^4$
Mg	$5 \cdot 10^5$	$3 \cdot 10^5$	$1 \cdot 10^4$	$5 \cdot 10^5$	$5 \cdot 10^5$	$2.5 \cdot 10^4$
Fe	$5 \cdot 10^5$	$2.5 \cdot 10^5$	$5 \cdot 10^3$	$5 \cdot 10^5$	$2.5 \cdot 10^5$	$1 \cdot 10^4$

Table 8.2: Number of simulated events per atmospheric muon MC file for different primary types, with zenith range h from 0° to 60° , v from 90° to 60° and energy range 1 from 1 TeV to 10 TeV, 2 from 10 TeV to 100 TeV, 3 from 100 TeV to 10^5 TeV

The number of files for each type is given in table 8.3.

8.1.3 Event Weights

To model the flux of atmospheric muons and neutrinos from theoretical predictions or parametrisations of measurements with the simulated events, each event has to be weighted by the ratio of simulated events to predicted events. This factor, divided by the irradiation time, is referred to as *GlobalWeight*. Each event is assigned the *W3* weight during simulation, which is the *GlobalWeight* divided by the number of simulated events, which is broken down to the number of events per MC file times the number of files used. Its unit is defined to be yr^{-1} . *W3* is still associated with a certain flux prediction, in the case of muon MC the Hörandel model [113] for the atmospheric flux, and in the case of neutrinos the Bartol atmospheric neutrino flux prediction [92] [93]. The sensitivity of the detector, independent of the simulated neutrino flux, is expressed as the weight factor *W2*, from which *W3* is calculated by multiplication with the predicted flux per GeV, m^2 , sr and s. Its unit is $\text{GeV m}^2 \text{sr s yr}^{-1}$.

8.1.4 Simulation of the PMT and DAQ Electronics

The detector model used for this work's MC is a twelve line detector with straight lines, but with the orientation of the storeys taken from measurement at a fixed date. The information on the detector layout is stored in a text file, read in before processing the MC files.

The photons hitting a PMT and producing photoelectrons according to the KM3 simulation are read in from the MC files by the SeaTray frame-

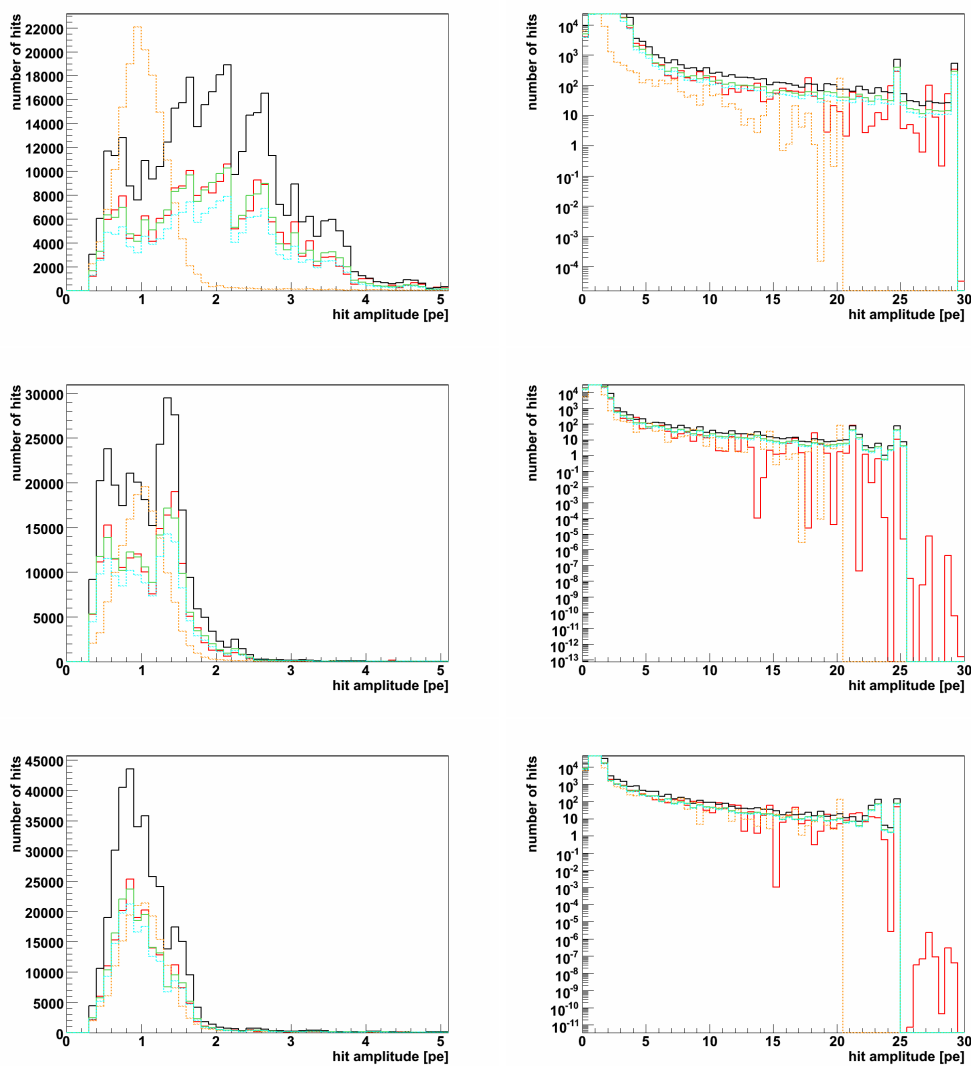


Figure 8.2: Amplitude distribution in linear (left) and logarithmic (right) scale for Line 3 OM 19 (top), Line 6 OM 3 (middle) and Line 6 OM 43 (bottom). Black: Data, Red: MC with background and amplitude distributions from MBEs, Orange: MC with gaussian gain smearing and simulated background, Green: Data normalised to red MC, Turquoise: Data normalised to orange MC.

Energy Type	low energy	high energy
ν upgoing	130	180
$\bar{\nu}$ upgoing	40	90
ν downgoing	120	180
$\bar{\nu}$ downgoing	90	90

Table 8.3: Number of atmospheric neutrino MC files for energy ranges low from 10 GeV to 10^7 GeV and high from 10^6 GeV to 10^8 GeV

work, which stores and processes the information as I3MCHits as mentioned in section 7.2.

The amplification of each photoelectron by the PMT and the response of the readout electronics smear both the hit's time and amplitude, which has to be modelled. For this purpose, the I3MCHits are processed by a PMT simulation code. It randomly determines a new hit time after a 1.5 ns wide gaussian distribution to model the PMT's transit time spread. The charge from each photoelectron is randomized as well, to simulate the PMT gain spread. Finally, the signals from the single photoelectrons are subjected to a simulation of the 25 ns AVC integration window and dead-time cycle of the OM introduced in section 5.4.2. The output is in the form of I3RecoPulses, which are then passed to the reconstruction algorithms, as it is the case for calibrated hits from measured data.

The gain spread of the PMTs is supposed to be gaussian, as also assumed in the charge calibration. However, the single photoelectron data recorded in Minimum Bias events (MBEs) shows a deviation from this assumed behaviour, examples of which are given in figure 8.2. Line 6 OM 43 for instance is an OM at which certain channels are amplified by differential nonlinearities (DNLs) in the AVC [114], leading to a distorted, yet still around 1 pe centered amplitude distribution. Line 3 OM 19 on the other hand suffers from a distribution which is much wider than 1 pe, and will often return large amplitudes in response to a single photon. As an example of an OM with correct tuning and minimal influence from DNLs serves Line 6 OM 43. Since the amplitude distribution of the hits has a large influence on the trigger rate and all hit selection algorithms making use of the hit amplitude, like the BBFit algorithm's initial hit selection, the gain smearing simulation was modified to better reproduce the behaviour of the OMs. The previously used gaussian distribution with a width of 0.3 pe was replaced by the measured distribution for each individual PMT. In order to achieve this, the resulting charge for each photon at the photocathode is randomised after the probability to find it in the MBEs. The

total amplitude is the sum of the charges for the single photons, with a cut-off at the maximum of the AVC's dynamic range. This cutoff $maxamp_{AVC}$, which was previously set to a nominal value of 20 pe, was changed to the following actual maximum value:

$$maxamp_{AVC} = (255 - channel_{pedestal}) \cdot slope_{AVC} \quad (8.1)$$

From the two AVCs associated with an OM, one is chosen randomly for each charge integration window simulated. With those modifications, a better match of the amplitude distribution for the problematic OMs could be achieved, both for the SPE peak as magnified on the left hand side of figure 8.2 as well as the tail towards high amplitudes shown on the right hand side. This is despite the fact that the measured amplitude distribution contains the part of the electronics noise pedestal extending above 0.3 pe, which reduces the average amplitude slightly. On the other hand they lack the part of the SPE peak below that threshold, with the opposite effect. While this is an improvement to correctly simulate the shortcomings of the electronics, it would be better to mitigate their effects. Some OMs are known to have an awkward ADC setting with the pedestal and SPE peak not well separated [115]. Therefore those OMs with less than five channels distance between the pedestal and the SPE peak, where this distance is less than a tenth of the pedestal value, or where the pedestal is at more than 64 channels, were removed in both data and MC simulations.

8.1.5 Addition of Optical Background from Minimum Bias Events

The standard way of simulating the optical background in ANTARES is to add single photon I3MCHits at random times and OMs to those originating from the KM3 particle simulation. To improve the precision from taking a default rate of 60 kHz per OM, as for the study from chapter 6, the average measured rate during the data taking period to be simulated is used. After these white noise background hits are distributed within a time range of ± 2200 ns, equal to the trigger snapshot window, around the hits of the simulated event, the electronics simulation is applied to the union of both hit samples. There are several effects not simulated by this method. With regard to the electronics, these are afterpulses in the PMTs, which are signals caused by delayed emission of electrons from the photocathode or the dynodes, and the irregularities in their amplitude distribution mentioned in section 8.1.4.

The local distribution of the background hits, which often is not uniform throughout the detector but varies with height over ground, is also not

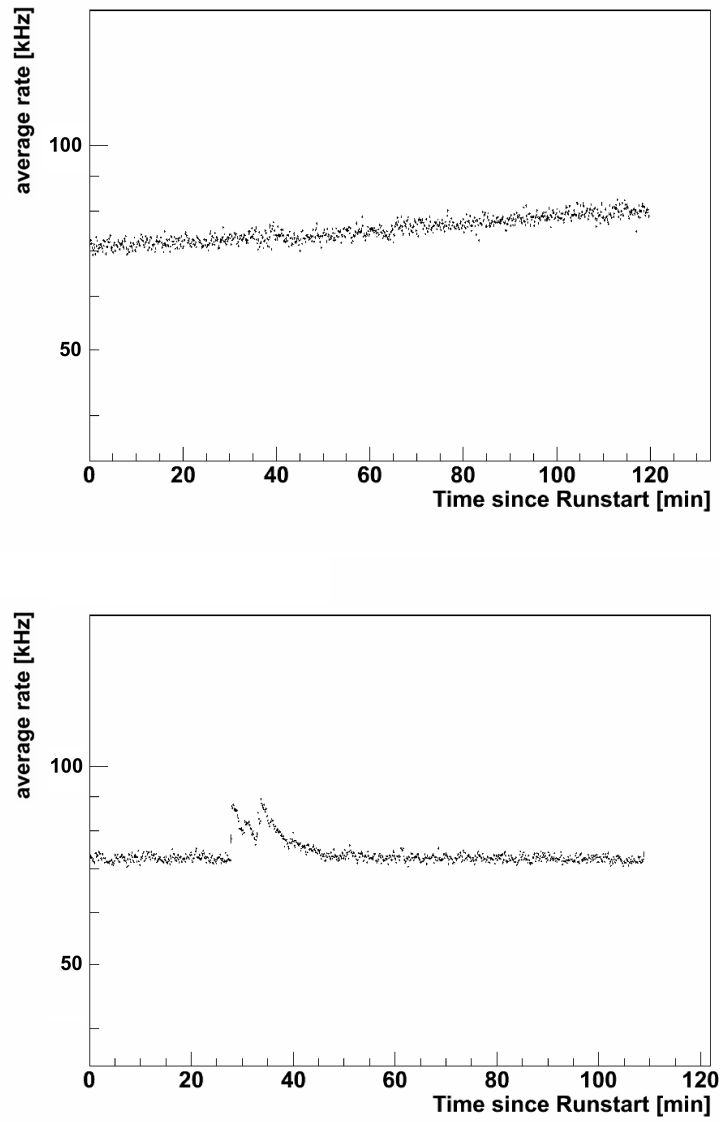


Figure 8.3: Average background rate in kHz per OM for run 053971 (top) and 054043 (bottom) versus time since runstart.

Energy/Angle Bin Primary	v1	v2	v3	h1	h2	h3
p	20	5	1	5	2	1
He	5	1	1	2	1	1
N	5	1	1	5	1	1
Mg	5	1	1	5	1	1
Fe	5	1	1	5	1	1

Table 8.4: Number of atmospheric muon MC files used in each MC set for different primary types, with zenith range h from 0° to 60° , v from 90° to 60° and energy range 1 from 1 TeV to 10 TeV, 2 from 10 TeV to 100 TeV, 3 from 100 TeV to 10^5 TeV

taken into account. In addition, variations of the background rate over the time of a run are possible, either as short bursts or a continuous change, examples of which are given in figure 8.3. Therefore, a method has been developed to directly add the hits from MBEs to the simulated events. The hits in MBEs are to a high degree pure optical background, since the muon rate at 2500 m depth over the whole detector of 10000 m^2 area is in the order of 10 s^{-1} [116] compared to the 4400 ns length of the MBEs taken every 10 s. The probability of a muon present in a MBE is thus about 0.14 percent. A physics trigger event has a length of 4400 ns plus the time between first and last triggered hit, a MBE however covers only exactly 4400 ns. To cover the whole duration of the simulated event, three MBEs are lined up to form an event of 13200 ns length. The time of all background hits is shifted by the difference of their average time to the average time of the hits from the simulated particle. After the electronics simulation for the hits from the particle, the calibrated hits from the MBE are added, and hits closer together than the AVC integration window of 20 ns are merged by transferring their amplitude to the first hit.

8.1.6 Generation of Monte Carlo Sets for Groups of Runs

Towards the aim of analysing data from extended time periods, a timescale had to be chosen from which to sample MBEs for using their background hits and hit amplitude distributions for the generation of a Monte Carlo Set (MC set), which is a collection of files containing correctly weighted events of all types, simulated under the conditions of a certain data taking period. The minimum number of events of a type in each MC set is given by the size of the KM3 output files, of which at least one per type has to be processed to correctly calculate the weights. Each MC set is based on four files with

neutrino events, one each of upgoing neutrinos, upgoing antineutrinos, downgoing neutrinos and downgoing antineutrinos. Because very few events pass the trigger for the low energy and vertical muon files, a larger number of files was used for them. The number of muon MC files per MC set for each type is listed in table 8.4. The files to be used were drawn randomly from the available pool, to avoid any bias in those cases where the number of files in the production is not sufficient to use each file only once over the analysed period. To create a MC set for each run is not feasible due to the computing resources needed. Instead, up to 20 runs with not more than 20 kHz difference in average background rate per OM and a total lifetime not longer than 36 hours were grouped together. For each event from the KM3 files, a random MBE from one of these runs, chosen also randomly weighted by the lifetime of each run, is selected. To add the background as described in 8.1.5, two more MBEs are selected in this way. After adding the background, the OM-condition information from the central one of the three lined up MBEs is used to remove hits on OMs which are not in the 'ok' state (see section 5.4.6). Also hits on the OMs with a bad ADC setting (see section 8.1.4) are discarded. Next, the L0 threshold of 0.3 pe is applied, and the L1 hit selection created, on which the trigger conditions for the 3N and 2T3 Triggers (see section 5.4.5) are applied. The total lifetime of the grouped runs and the total number of events generated for the respective primary type are written into the frame for each event, to enable the calculation of the correct weighting factor from the *W3*.

The resulting MC set contains the full repertoire of atmospheric muons from all simulated primary types and atmospheric neutrinos, correctly weighted for a time equal to the lifetime of the runs for which they were created. The background rates and OM-condition for each OM are transferred to the MC, returning the same distributions as found in data, as shown in figures 8.4 and 8.5, except for a global factor discussed later in 8.2.

8.1.7 Events from Dark Matter Annihilation

A possible signal from Dark Matter annihilations at the Earth's centre would be from a cone straight downward, with a size depending on the WIMP mass as shown in section 4.2.4. A special MC simulation for a 15° cone from 180° to 165° zenith angle was done with an increased statistics of 20 neutrino and antineutrino files per MC set in contrast to one each for the the flux outside the cone. In this simulation, additional *W3* event weights,

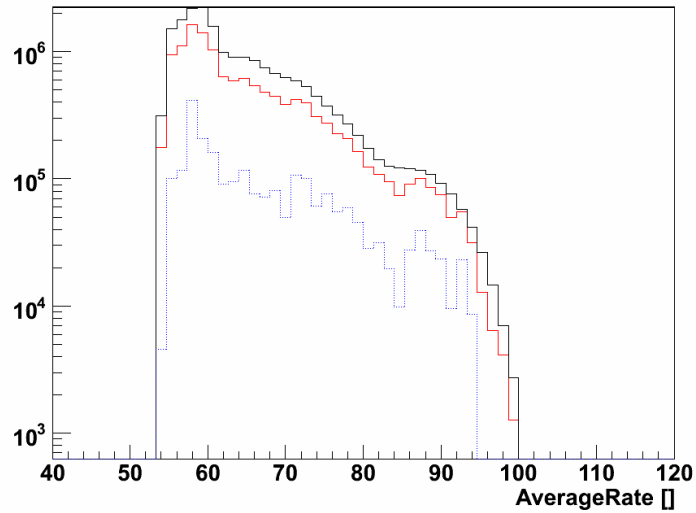


Figure 8.4: Distribution of the average background rate per OM over all analysed/simulated events. Black: Data, Red: MC, Blue: Events from pure optical background

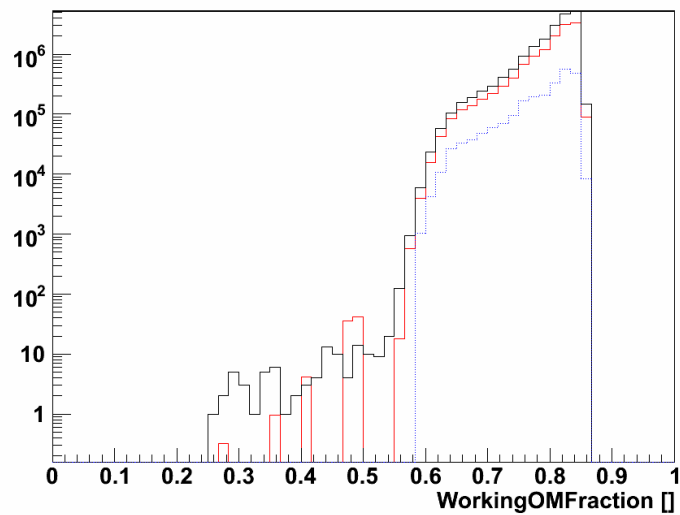


Figure 8.5: Distribution of the fraction of working ('ok' state) OMs over all analysed/simulated events. Black: Data, Red: MC, Blue: Events from pure optical background

normalised to the neutrino emission from 200 annihilations into the $c\bar{c}$, $b\bar{b}$, $t\bar{t}$, gg , $\tau^+\tau^-$, W^+W^- and Z^0Z^0 annihilation channels at several WIMP masses, were calculated and stored in the event's frame. The number of neutrinos for WIMP masses of 25, 50, 80.3, 91.2, 100, 150, 176, 200, 250, 350, 500, 750, 1000, 1500, 3000 and 5000 GeV at a given energy was taken from the annihilation spectra calculated with WimpSim and provided at the project's website [117]. By division through the Earth's surface, the number of neutrinos per area at the detector was calculated. Neutrino absorption during propagation to the surface is in the order of a few percent for energies up to 5000 GeV [77], and was therefore neglected. Modification of the flux due to neutrino oscillation was also ignored, since no MSW effect occurs at the energy range in question and the annihilation neutrino yield features no large differences between the three flavours [118]. To compute the number of neutrinos expected from a certain zenith angle, the formula

$$\frac{d\Phi}{d\Theta} = \Phi_{(\theta=0)} \exp\left(\frac{-(0.56 \cdot R_{\text{Earth}})^2}{m_{\text{WIMP}}} \Theta^2\right) \quad (8.2)$$

from [54] was used, which parametrises the distribution of the flux Φ differential in nadir angle Θ as a function of the WIMP mass, with the Earth's radius $R_{\text{Earth}} = 6400$ km. The $W2$ weight of each event in the KM3 processed files was multiplied with the so estimated number for the respective zenith angle, creating an effective *GlobalWeight* for the flux expected at an annihilation rate of 200 annihilations per nanosecond. Instead of using the intermediate step of an effective area, which is virtually impossible to calculate adapting it to all the different run conditions because of the required computing resources, the expected numbers of background and signal events are calculated directly from the simulated events. To use the very same events with different weights for background and signal estimation can be considered an advantage over separate simulations, since each single event provides the correct signal to background ratio. This is an important feature at low energies, where only samples with quite limited statistics can be simulated because a large fraction of events is lost due to the inefficiency of trigger and reconstruction.

8.1.8 Events from Pure Optical Background

The trigger algorithms used are not perfectly pure, the signature they look for can not only be created by high energy particle tracks, but also accidentally by a combination of background hits, which are assumed to be uncorrelated. This was already studied in [119], but for simulated white

noise and a gaussian gain distribution. Since the condition for L1 hits includes the selection due to a hit amplitude above 3 pe, the fact that some OMs, as shown in figure 8.2, regularly return this amplitude as response to a single photon, significantly reduces trigger purity. To simulate such 'empty events' for each run, a dedicated MC simulation was set up, in which the trigger is run on data from MBEs. Since their duration is only 4400 ns, 25 of them were put together to form an event of 110 μs length. To increase the variability, which is limited to about 1000 MBEs taken during each physics run, the hits were randomly reassigned among the OMs which were hit in the merged events. For each run 250000 events of this type are generated, the *GlobalWeight* of each event is $(length_{\text{event}} \cdot n_{\text{events}})^{-1} = (110\mu\text{s} \cdot 250000)^{-1}$. For the studied runs, this results in weights ranging from about 100 to 500, as indicated by figure 8.6, higher than the weights of the atmospheric muon and neutrino events. While better statistics would be desirable, this method is limited by the variability gained by swapping the OMs. It emerged that the swapping of the OMs and thus positions of the hits also transferred the amplitude distributions of those OMs, regrouping OMs with erratically wide amplitude distributions (see 8.1.4), which often return high amplitudes in response to single photons. Locally clustering the hits on those OMs, which remain separated in the real detector gives an explanation for the excesses in the distributions shown in figures 8.9 and 8.8, where the contribution of pure optical background events to the MC prediction is indicated by a dotted blue line. Despite this overestimation of the number of triggered events, it is shown later in section 8.2.2 and chapter 9 that, though the reconstruction algorithms are prone to find false track signatures in those events, all are removed by the cuts on the reconstruction quality.

8.2 Comparison of Measured Data and Simulation

To test how well the MC simulation matches the real situation, various quantities are compared between the measured data and the expectation from the simulation. Since the atmospheric muon flux at the detector outnumbers the neutrino flux by about six orders of magnitude, and a separation of the events from the latter source in data already requires a working reconstruction or event classification, the comparison done in this chapter is based on those downgoing events. The comparison of the events reconstructed as upgoing neutrino events is part of the analysis presented

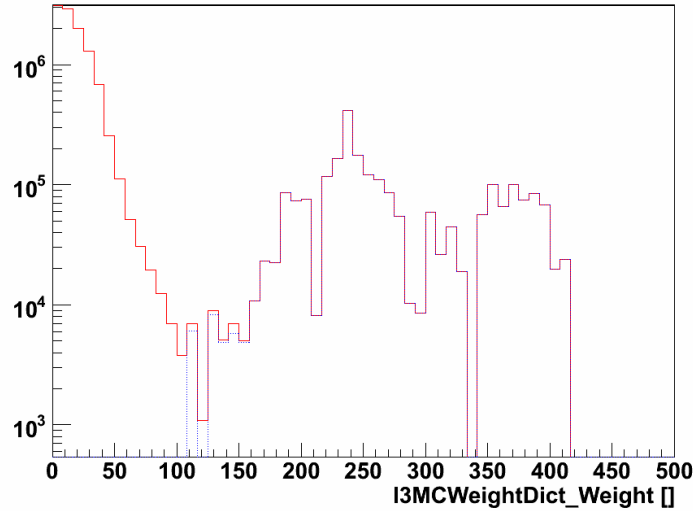


Figure 8.6: Distribution of event weights over all analysed/simulated events. Red: MC, Blue: Events from pure optical background

later in chapter 9. Expecting several thousand atmospheric muon events per day, the MC created for runs 054171 to 054201 (see MC set 19 from the runlist in Appendix A for details) provides sufficient statistics to do a decent comparison. To document the changes from the introduction of the new simulation methods presented in 8.1.4 and 8.1.5, a simulation with the original MC was done in parallel for those runs. This simulation uses simulated white noise background at the average count rate for the OMs in 'ok' state, which is 60.4 kHz, and a gaussian gain distribution of 0.3 pe width. The information on the status of each OM from the OM-condition in the Minimum Bias data was used, so that the sample of simulated OMs matches the one for which the average rate was calculated and in order to apply the same hit selection criteria as for data. Furthermore, the amplitude distribution is cut off at 20 pe instead of the individual upper end of each OM's dynamic range. The events from pure optical background are added to both MC simulations.

8.2.1 Trigger Level Hit Distributions

The comparison in this section is performed after the trigger simulation in the case of MC events, and the application of the same trigger conditions

on data events after they were calibrated with the Offline Calibration sets ('re-triggering', see section 9.1.3). Comparing the sum of events in data and the sum of weights in MC, 1.5 times more triggered events are found in data than predicted by the new MC and 1.6 times more than by the original MC. The ratio varies for the individual MC sets between 1.2 and 1.8 as listed in Appendix A. To investigate the reason for this mismatch and its variation over time, the characteristics of the events are further examined.

The distribution of the measured hit amplitudes summed up over all triggered events is a basic quantity to check, whether the muon flux, the background and the characteristics of the detector, especially the sensitivity of the OMs, is simulated correctly. For all (L0) hits it is found, as displayed in figure 8.7, that the normalised shape of the amplitude distributions for data and the improved MC matches well, requiring a normalisation factor slightly lower than the data/MC event ratio. This indicates a larger total amplitude in each event for MC than for data, which is confirmed by the average hit amplitude distribution in figure 8.8, and can be attributed to the shortcomings of the pure optical background event simulation. Also in figure 8.9, showing the distribution of the total number of hits per event, an excess of events with a high number of hits from this source is found. The shape of the amplitude distribution (see figure 8.7) for the original MC deviates from data even after normalisation, as it predicts a narrower SPE peak. Between 20 pe and 25 pe an equally wide peak is caused in data and improved MC due to the cutoff at the individual maximum ranges for the OMs, while the original MC and the pure optical background events are sharply cut off at 20 pe. The integrated amplitude for the bulk of the events found at 150 pe to 400 pe is after normalisation correctly predicted by the improved MC, while it is shifted to lower values for the original MC. This is due to a lower amplitude per hit as supported by figure 8.10.

Regarding the L1 hits, which are composed of coincident hits and big hits as explained in section 5.4.5 and visible as two distinct peaks in figure 8.11, the normalised distribution for the improved MC also is in better agreement with data than for the original MC. The normalisation factor is at about 1.6 larger than for the L0 Hit distributions and the event numbers, indicating that data events contain more L1 hits than predicted by the MC.

8.2.2 Reconstruction Level Event Distributions

After performing the BBFit reconstruction introduced in section 7.4 on the MC for runs 054171 to 054201 and the corresponding data files, at 1.6 an

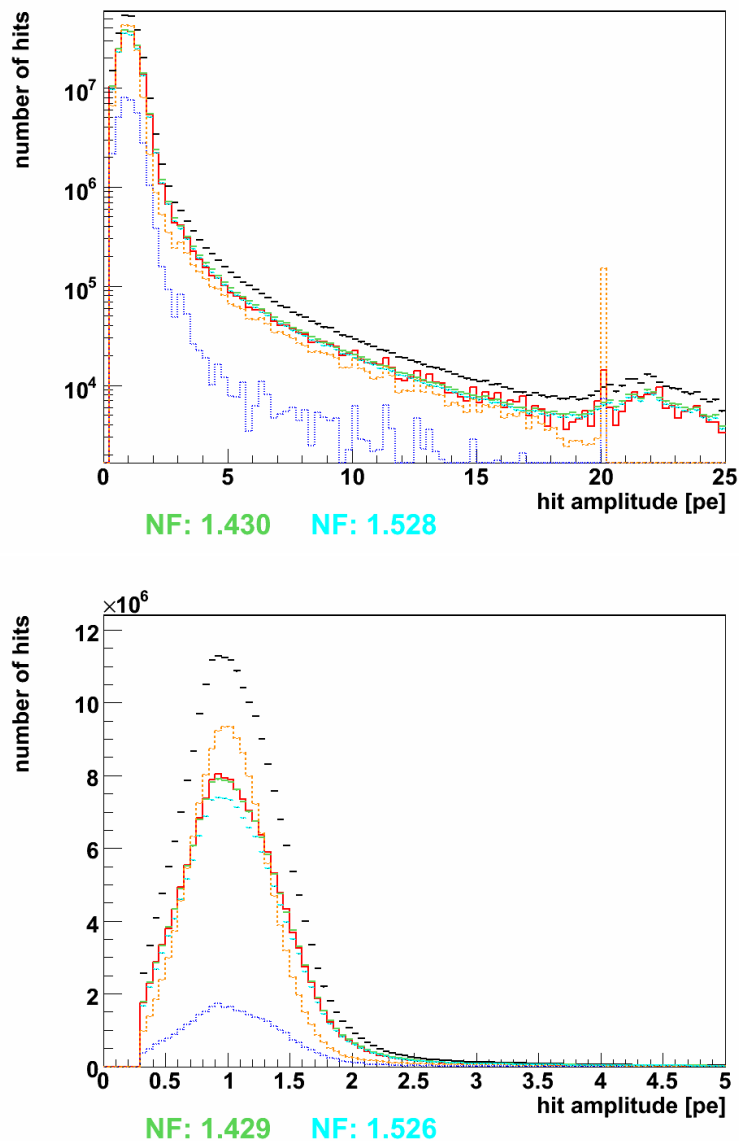


Figure 8.7: Amplitude distribution of L0 hits after trigger, logarithmic scale up to 25 pe (top), linear scale up to 5 pe (bottom), Black: Data, Red: MC with background and gain distribution from Minimum Bias Events, Orange: MC with simulated background and gaussian gain distribution, Green: Data normalised to red MC, Turquoise: Data normalised to orange MC, Blue: Events from pure optical background. The normalisation factors NF are given in matching colour.

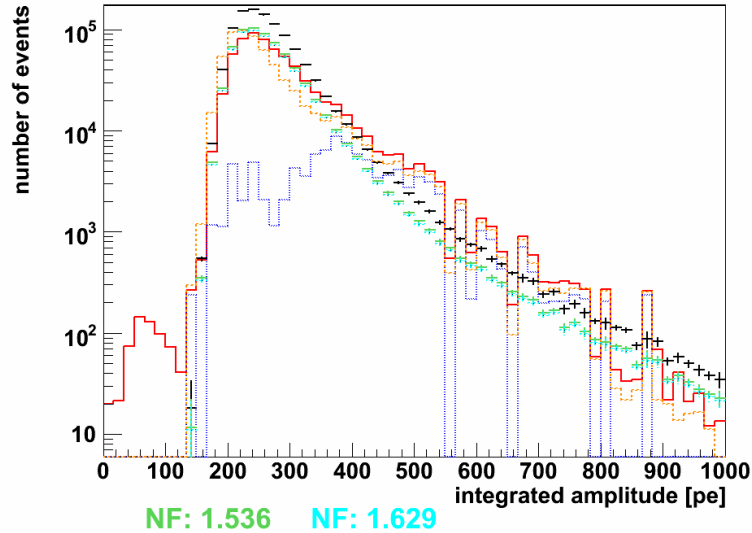


Figure 8.8: Integrated amplitude of L0 hits per event after trigger. Black: Data, Red: MC with background and gain distribution from Minimum Bias Events, Orange: MC with simulated background and gaussian gain distribution, Green: Data normalised to red MC, Turquoise: Data normalised to orange MC, Blue: Events from pure optical background. The normalisation factors NF are given in matching colour.

even slightly larger factor between the numbers of data and MC events than on the trigger level is obtained. The outcome of the BBFit algorithm is encoded as the result type, which is either *none* for an event lacking the minimum number of hits to reconstruct an event or a failed fit, *track* for an event where the χ^2 for the track hypothesis is better than for the point source hypothesis or *shower* if the point source hypothesis fits better. From figure 8.12 it is evident, that actually a larger fraction of triggered events in data is reconstructed than in both versions of the MC. There is not only a significant plus in *track* and *shower* events, but also the number of events with result type *none* is almost equal, despite the larger number of triggered data events. A possible explanation is that for data a higher number of hits passes the initial hit selection of BBFit, which, like the L1 hits, combines coincident and big hits. The number of hits available to the reconstruction algorithm is linked to the number of reconstructed events in a non linear way, since every single hit out of the five respective six needed to reconstruct a single line or multi line event is required. Furthermore

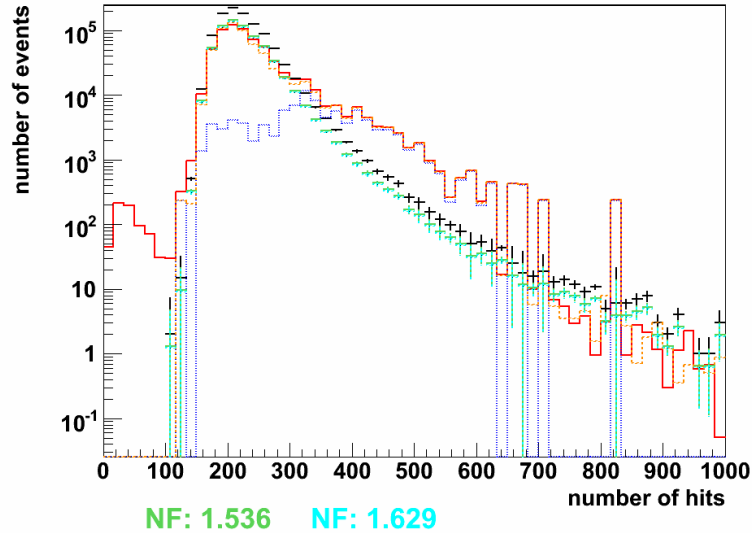


Figure 8.9: Number of L0 hits per event after trigger. Black: Data, Red: MC with simulated background and gaussian gain distribution, Orange: MC with simulated background and gaussian gain distribution, Green: Data normalised to red MC, Turquoise: Data normalised to orange MC, Blue: Events from pure optical background. The normalisation factors NF are given in matching colour.

this graphic shows, that only in a very small fraction of the pure optical background events, a false track or pointlike light source signature is found and reconstructed.

For the primary quality cut parameter χ^2 good agreement between data and MC prediction is essential, as cuts determined from the MC distribution are required to perform in the same way on data. For the events with result type *track* the χ^2 distribution is presented in figure 8.13. The MC prediction fits the data well, especially for low values of χ^2 where the quality cuts are set. The pure optical background events have $\chi^2 > 2$, with the majority far higher. They are therefore all removed by the cuts as defined in section 7.4.1.

Since the BFit events are classified by the number of lines used in the reconstruction, the relation of data and MC regarding this parameter, shown in figure 8.14, is also of importance. Before application of the cuts, the number of events in data and MC declines in equal measure with the number of lines and the excess in data is distributed evenly, except that

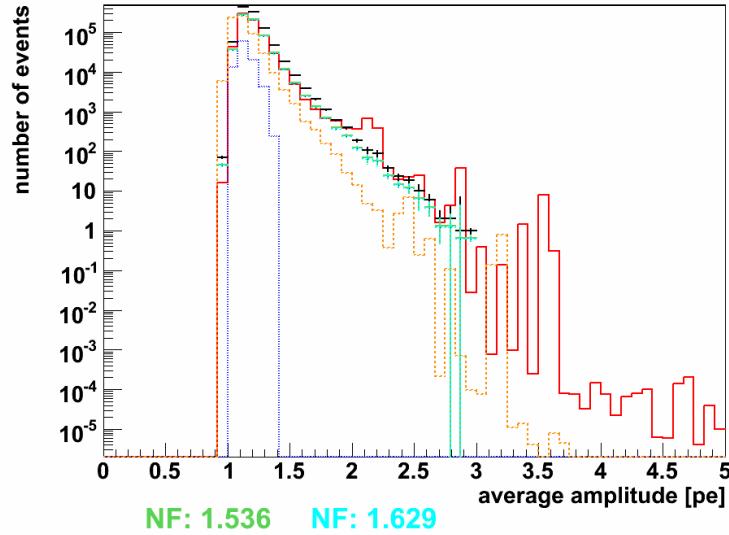


Figure 8.10: Average amplitude of L0 hits per event after trigger. Black: Data Red: MC with background and gain distribution from Minimum Bias Events, Orange: MC with simulated background and gaussian gain distribution, Green: Data normalised to red MC, Turquoise: Data normalised to orange MC, Blue: Events from pure optical background. The normalisation factors NF are given in matching colour.

the number of failed fits, which enter as zero line events, is equal in data and MC, as already noted from figure 8.12. The events from pure optical background which are identified as a track from hits on one or two lines only, with the latter interestingly occurring an order of magnitude more often. Due to the stricter cut on single line events, their number is lower than the number of two line events after cuts, but equally in data and MC.

Together with these χ^2 cuts, the event selection from the neural network described in 7.5.1 was applied to identify downgoing events, which were discarded as they are not relevant for the goal of an analysis on upgoing neutrinos. The hit distributions of L0 hits and the L1 hits after these cuts are identical to the distributions on trigger level, with the exception that the pure optical background events no longer contribute.

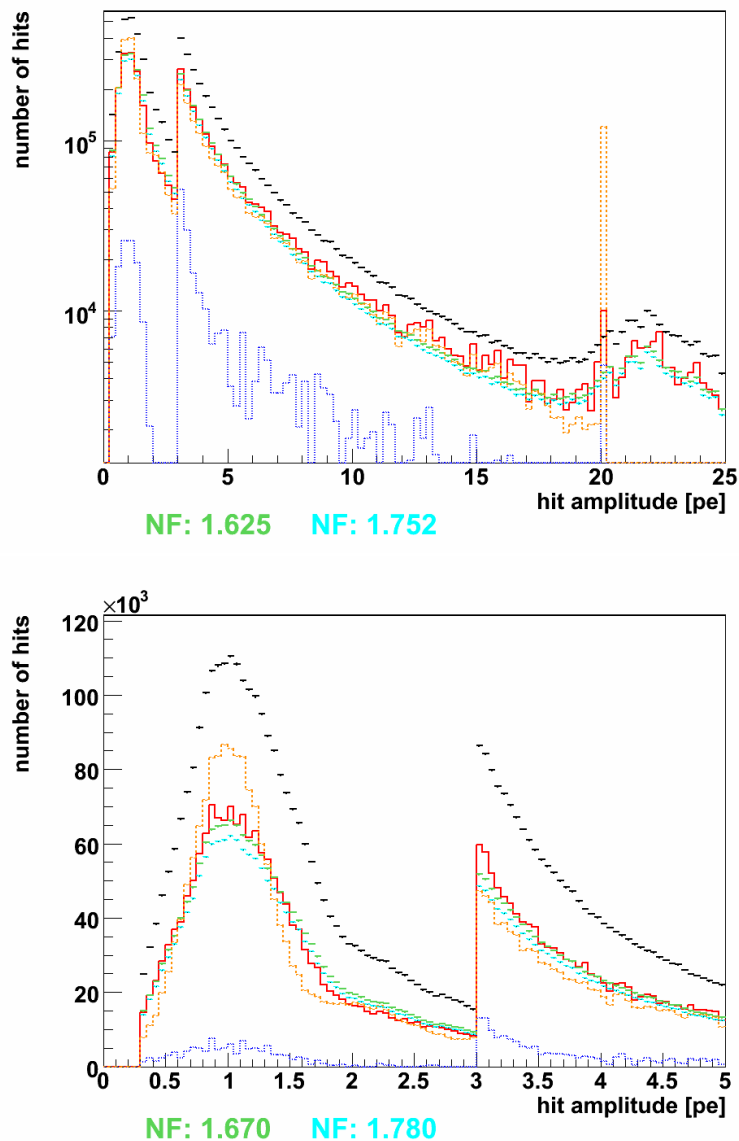


Figure 8.11: Amplitude distribution of L1 hits after trigger. Black: Data Red: MC with background and gain distribution from Minimum Bias Events, Orange: MC with simulated background and gaussian gain distribution, Green: Data normalised to red MC, Turquoise: Data normalised to orange MC, Blue: Events from pure optical background. The normalisation factors NF are given in matching colour.

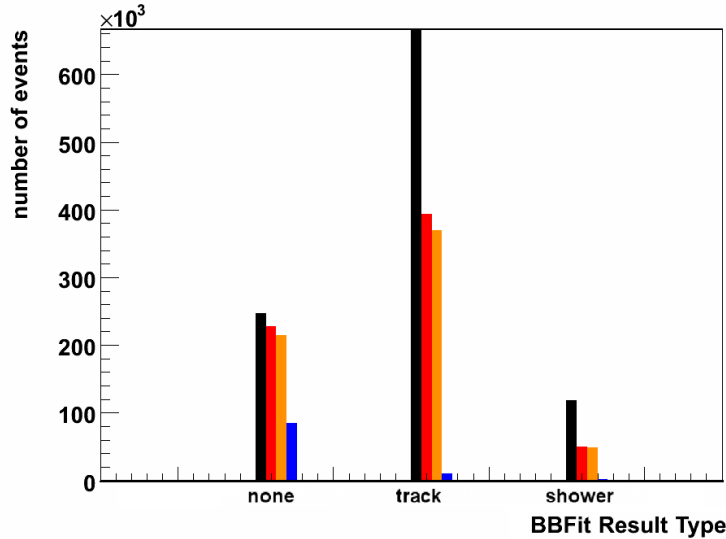


Figure 8.12: The distribution of the Result Type of BBFit reconstructed events before applying quality cuts. Black: Data, Red: MC with background and gain distribution from Minimum Bias Events, Orange: MC with background and gain distribution from Minimum Bias Events, Blue: Events from pure optical background. The normalisation factors NF are given in matching colour.

8.2.3 Angular Distribution of Events

As mentioned before, the general comparison of event numbers and hit distributions is based on downgoing atmospheric muon events. The shape of the measured distribution in zenith angle of these events depends on the initial atmospheric muon flux and the direction dependent response of the detector. Concerning the azimuth angle, there is no variation in the muon flux, but a large one in the the sensitivity of the detector. In directions for which the track passes several lines at close distance the event numbers are up to an order of magnitude higher than in between those axes, both before and after application of the χ^2 cuts, as displayed in figures 8.15 and 8.16. Single line events are arbitrarily assigned a default azimuth of 180° , causing the spike observed in the plot. It should be noted, that the misreconstructed muons, which dominate the upgoing zenith angle distribution before the quality cuts, do not exhibit the same factor between data and MC as the downgoing reconstructed ones. Instead, there is good agreement for zenith angles larger than 130° . Still, the few upgoing events

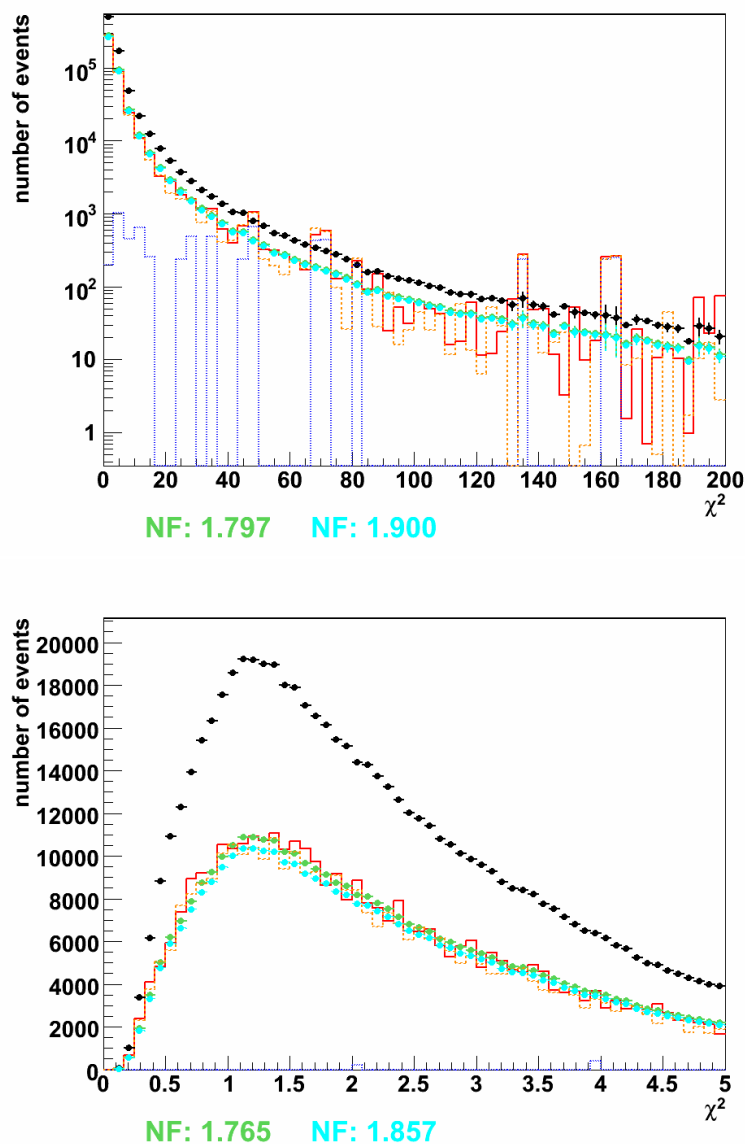


Figure 8.13: The distribution of χ^2 of BFit reconstructed events before applying quality cuts. Black: Data, Red: MC with background and gain distribution from Minimum Bias Events, Orange: MC with background and gain distribution from Minimum Bias Events. Green: Data normalised to red MC, Turquoise: Data normalised to orange MC, Blue: Events from pure optical background. The normalisation factors NF are given in matching colour.

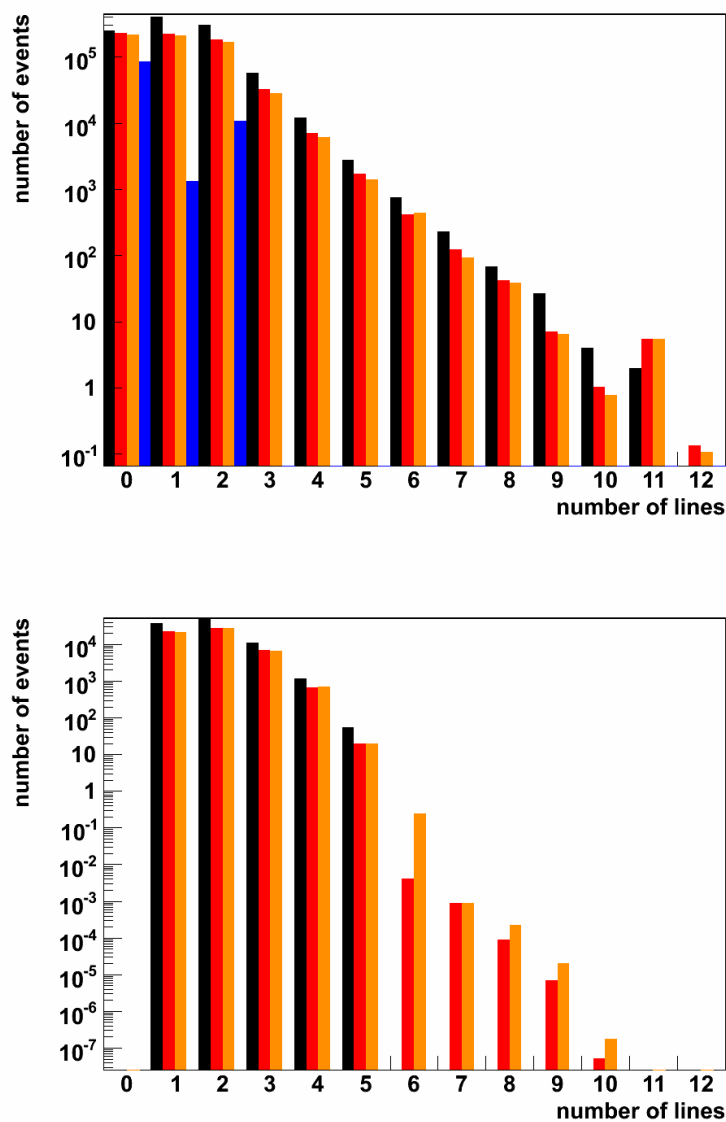


Figure 8.14: The distribution of the number of lines used in the BBFit reconstruction for all triggered events (top), with zero lines for reconstructed events, and after application of the quality cuts from 7.4.1 (bottom). Black: Data, Red: MC with background and gain distribution from Minimum Bias Events, Orange: MC with simulated background and gaussian gain distribution, Blue: Events from pure optical background. The normalisation factors NF are given in matching colour.

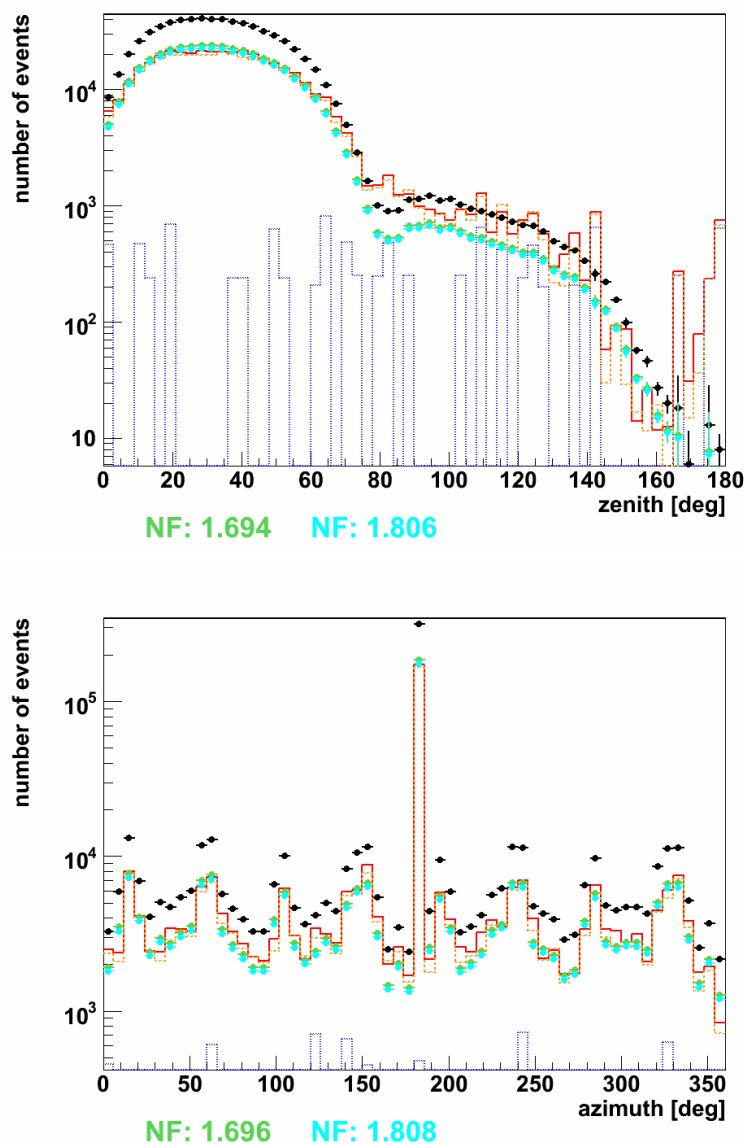


Figure 8.15: Zenith (top) and azimuth (bottom) distribution of BBFit reconstructed events before applying quality cuts. Black: Data Red: MC with background and gain distribution from Minimum Bias Events, Orange: MC with simulated background and gaussian gain distribution, Green: Data normalised to red MC, Turquoise: Data normalised to orange MC, Blue: Events from pure optical background. The normalisation factors NF are given in matching colour.

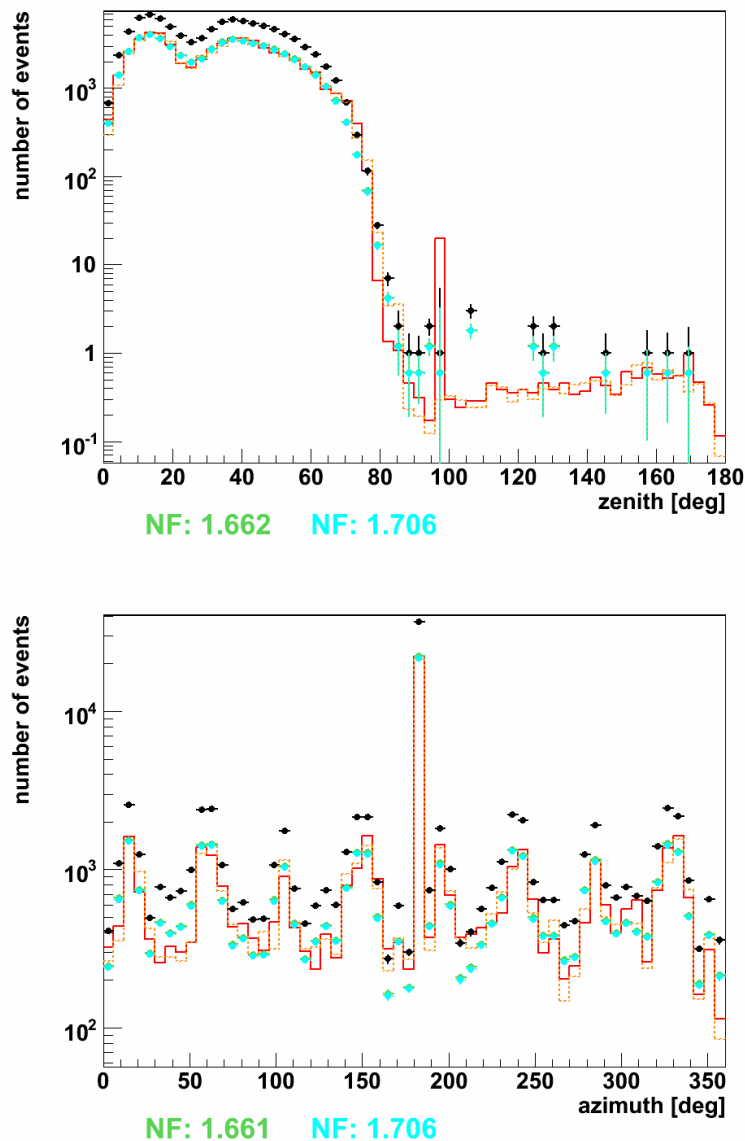


Figure 8.16: Zenith (top) and azimuth (bottom) distribution of BBFit reconstructed events after cuts from 7.4.1. Black: Data Red: MC with background and gain distribution from Minimum Bias Events, Orange: MC with simulated background and gaussian gain distribution, Green: Data normalised to red MC, Turquoise: Data normalised to orange MC. The normalisation factors NF are given in matching colour.

remaining after cuts do not allow for a conclusion. With the statistics of all analysed runs, the comparison for upgoing events is revisited in section 9.2.3. Furthermore, a peak from pure optical background events which are reconstructed with a zenith angle around 180° is present before the cuts, but completely gone after application of the cuts.

8.2.4 Energy Distribution of Events

Together with BBFit, the ANNergy energy reconstruction algorithm (see section 7.5.2) was performed, using the BBFit result as an input parameter, if present. The obtained energy distributions are characterised by distinct differences between data and MC, for all events (see figure 8.17) as well as for the ones passing the cuts (see figure 8.18). A general shift of data events to higher energies is observed, resulting in even fewer events than in MC for the separately displayed energy range up to 600 GeV, despite the overall larger number of data events. In addition, the event numbers for data fall off much slower with energy after the first peak at around 1 TeV or, for the distributions after cuts, even raises again to a second maximum at about 4 TeV. It should be noted, that the original MC exhibits the same differences to data as the one using the measured amplitude distributions. The inclusion of the pedestal in simulating the gain as discussed in section 8.1.4 is thus not the cause for the lower energy in the MC.

8.2.5 Discussion

The observed mismatch in event numbers between data and MC triggered an investigation into its origin, whose findings and results have been described in this section. From the comparison of the hit distributions for data and MC, mainly information on the correct simulation of the PMTs and the characteristics of the DAQ electronics was gained and used to improve it, as described above. While improving the agreement on the hit distributions, the global factor between measured data and MC was not cured by these modifications which cover nearly all known aspects influencing the translation of photons hitting the PMT to the recorded signal. The conclusion is therefore, that the reason for the discrepancy is to be found at an earlier stage of the simulation chain, with the angular acceptance of the OMs and the treatment of light scattering, which are especially important in the case of downgoing muon tracks (see sections 7.1.3 and 8.1.1) as possible sources.

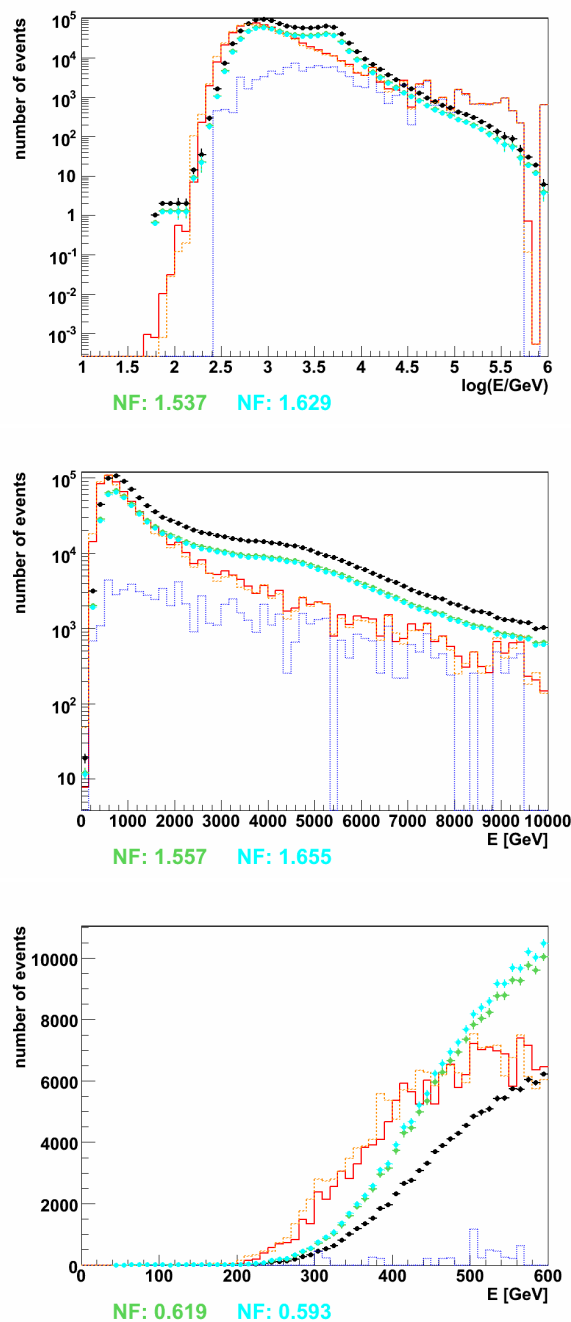


Figure 8.17: Energy distribution of ANNergy reconstructed events with BBfit as input track before applying χ^2 quality cuts, in double logarithmic scale (top), logarithmic scale (middle) and the low energy range in linear scale (bottom). Black: Data, Red: MC with background and gain distribution from Minimum Bias Events, Orange: MC with simulated background and gaussian gain distribution, Green: Data normalised to red MC, Turquoise: Data normalised to orange MC, Blue: MC events from purely optical background. The normalisation factors NF are given in matching colour.

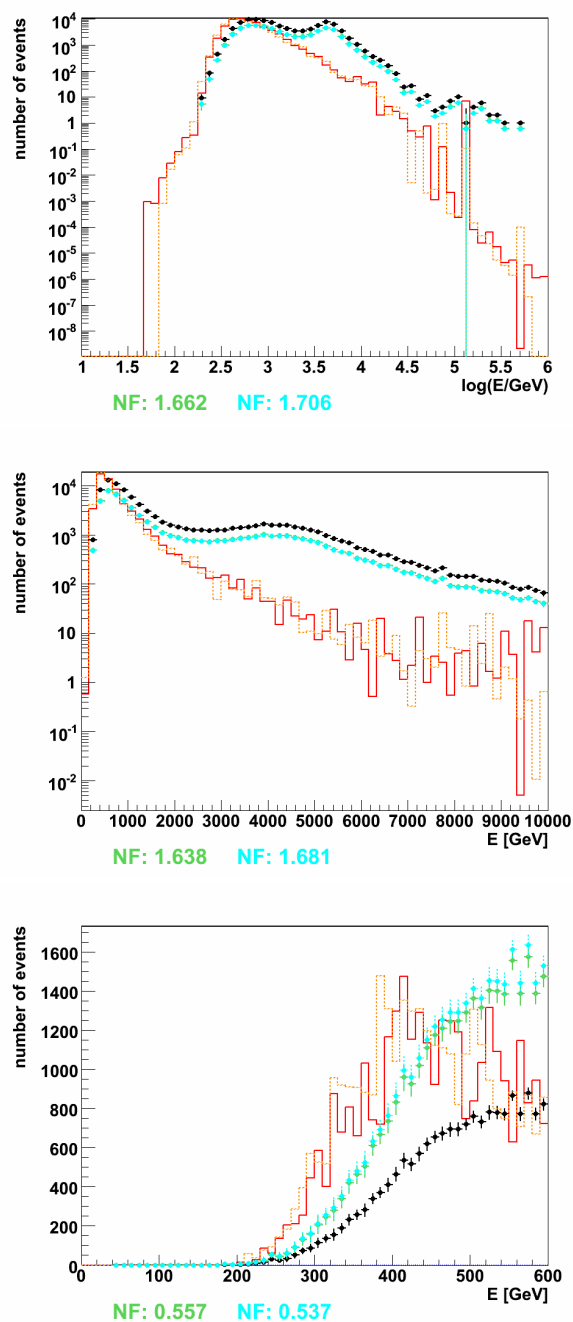


Figure 8.18: Energy distribution of ANNergy reconstructed events with BBfit as input track after the χ^2 cuts described in section 7.4.1, in double logarithmic scale (top), logarithmic scale (middle) and the low energy range in linear scale (bottom). Black: Data, Red: MC with background and gain distribution from Minimum Bias Events, Orange: MC with simulated background and gaussian gain distribution, Green: Data normalised to red MC, Turquoise: Data normalised to orange MC. The normalisation factors NF are given in matching colour.

Chapter 9

Limit on Dark Matter Annihilation in Earth

The reconstruction algorithms described in chapter 7 together with the improvements achieved on the MC simulation discussed in section 8.2 were applied to the data taken by the ANTARES detector in December 2010. The analysis aims at setting upper limits on the Dark Matter Annihilation rate inside Earth in a model independent way, assuming WIMPs of a given mass purely annihilating into a single annihilation channel. Due to the short period analysed, it is to be regarded as a prototype procedure for a later analysis on the full dataset taken by ANTARES. Compared to analysing the neutrino flux coming from the direction of the Sun, the reconstruction of a tracks azimuth angle is not necessary, which allows to use single line events, decreasing the energy threshold, and increasing the reconstruction efficiency significantly. However, the challenging aspect of this analysis is, that no 'off-source' region with equal detector sensitivity exist, as the vertical direction is a unique symmetry axis of the detector. Therefore, the results of the MC simulation are the only basis for estimating the expected background, and special emphasis was put on assuring the reliability and precision of this estimation. A statistical error from the limited number of simulated events is associated with the MC prediction, shown as a red error band in the figures presented in this chapter.

9.1 Data Preparation

The data on which the analysis is based was taken in the form of the runs listed in Appendix A. Those runs were selected from all runs during December 2010 by removing runs not intended to record physics data, e.g.

calibration runs, runs with an average background rate per OM above 500 kHz and runs with less than 30 min duration. Before submitting the data to the reconstruction algorithms, further steps to improve the data quality and agreement with the MC were taken, extracting a 'final sample' of events to be processed and used in the analysis.

9.1.1 Selection on Optical Modules

Using the OM-condition information recorded during data taking, all hits from OMs which are not in the 'ok' state (see section 5.4.6) are removed, as done in the corresponding MC simulation as well. Furthermore, those OMs, which are known to have a awkward ADC setting as explained in section 8.1.4 are also removed.

9.1.2 Timeframe Quality Selection

As for the detector as a whole, a minimum percentage of 25% of the OMs in 'ok' state, and an average single OM background rate below 100 kHz among those OMs were set as a general cut condition, defining whether to keep or remove a certain 104 ms timeframe (see section 5.4) of a run. The lifetime of each run was calculated by summing up the duration of all selected timeframes containing events and the empty time intervals between them, unless no frames were recorded during twice the set interval between taking Minimum Bias events. In the latter case the detector is regarded as temporarily not taking data properly and the respective time interval is not added to the lifetime.

9.1.3 Retriggering of Events

The online triggering during data taking is done based on the Online Calibration (see section 5.4.4) dataset. For the analysis, the Offline Calibration dataset is used, crosstalk and walk effect corrections are applied and the hits on OMs not in the 'ok' state are removed. Hits below the intended L0 threshold of 0.3 pe are removed and a new L1 hit sample with coincident hits and big hits above the original threshold of the run is created. On this hit sample, the 3N Trigger and, if also active during data taking, the 2T3 Trigger (see section 5.4.5) are applied again, in order to remove events which do not pass the trigger conditions with the new calibration and OM selection.

9.2 Event Selection Cuts

Before the data is analysed with statistical methods for a possible signal contribution, quality cuts extracted from the MC simulation are applied to it, in order to include only well reconstructed events in the analysis. The cut parameter distributions in data and MC have to be compared as a verification that the cuts will have the same effect on data as on MC.

9.2.1 Performance of the Event Classification

An initial step to remove background events is the application of the artificial neural network algorithm introduced in section 7.5.1, which was run in parallel to the BBFit reconstruction. It was found that it successfully rejects downgoing reconstructed events, especially those straight downgoing (around $zenith = 0$), as demonstrated from the zenith angle distributions before and after its application in figure 9.1. However, it has little influence on the events reconstructed as upward going, except for those reconstructed close to the horizon ($zenith = 90^\circ$).

9.2.2 Cuts to Reject Atmospheric Muons for BBFit

A crucial step in the event selection are cuts which suppresses the background from misreconstructed atmospheric muons. The events reconstructed as upward going initially contain about two to three orders of magnitude more misreconstructed muons than actual neutrino events. To remove the downgoing muon events, a cut on χ^2 is used for the BBFit reconstructed events. The normalised distribution of χ^2 for data is in excellent agreement with the simulation, especially for the relevant range of $\chi^2 < 5$, as proven by figure 9.2. The events from pure optical background are found mostly at high values of χ^2 . When defining the value for the cut, its efficiency in rejecting misreconstructed muon events has to be balanced out against the loss of correctly reconstructed neutrino events. Another aspect is the predictability of the remaining additional background from a MC simulation with limited statistics. For this reason the cut is set at the point where the misreconstructed muon background is equal to the background from atmospheric neutrinos, leaving some statistics to study the muon events passing the cut. A global cut for the combination of all MC sets was applied in order to base the cut on as many simulated events as possible, though a better performance might have been achieved with separate cuts adapted to the detector conditions of each MC set. While

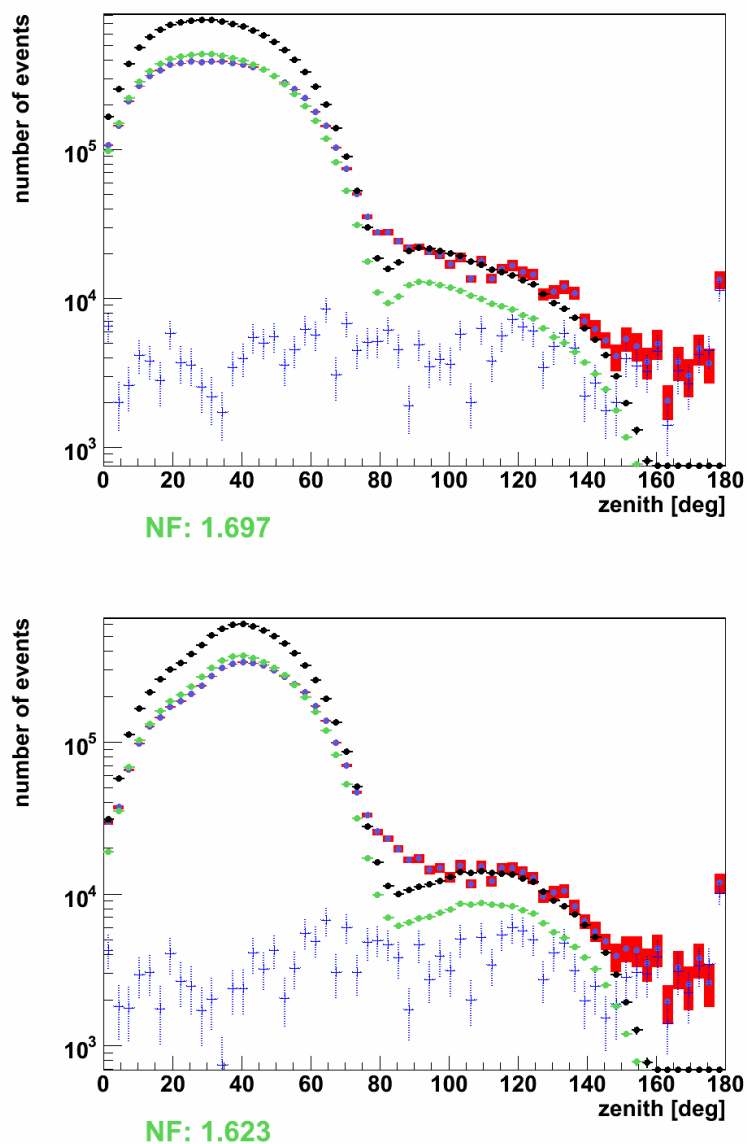


Figure 9.1: Comparison of the zenith distributions of data and MC for the final sample before cuts (top) and after removing events identified as downgoing by the ANN for event classification (bottom). Black: Data, Blue dots with red error bars: MC with background and gain distribution from Minimum Bias Events, Green: Data normalised to blue/red MC, Blue: Events from pure optical background. The normalisation factors NF are given in matching colour.

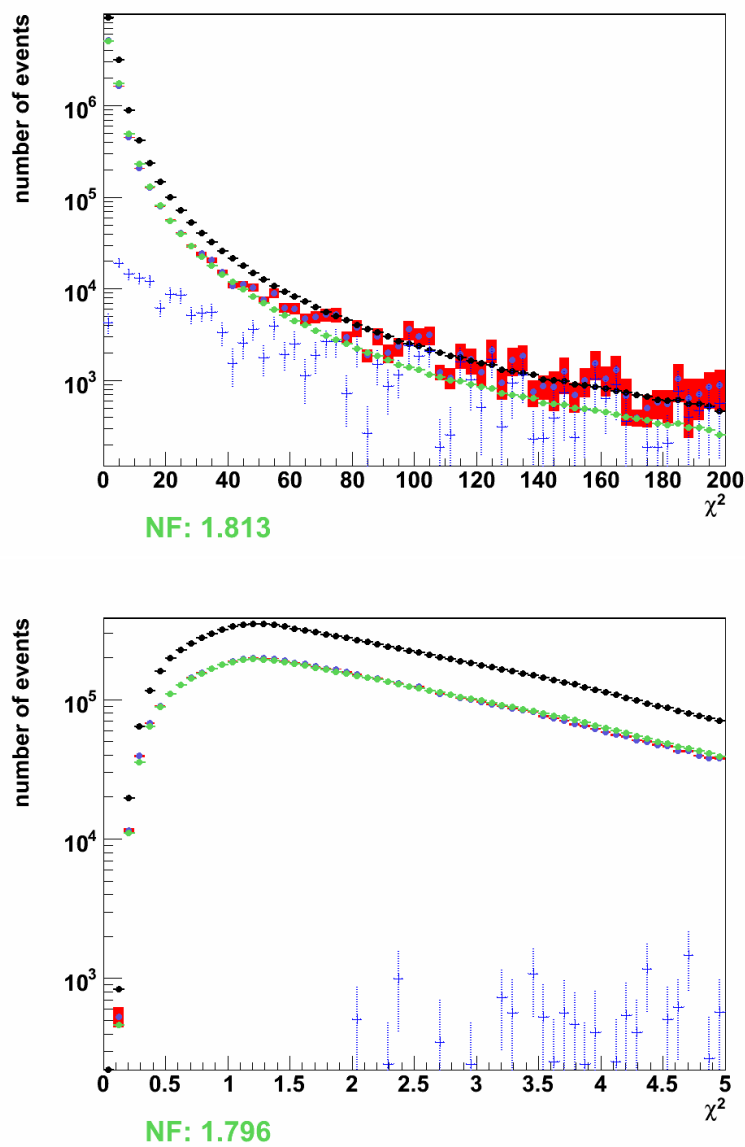


Figure 9.2: Comparison of BBFit χ^2 distributions up to 5 (top), and up to 100 (bottom) of data and MC for the final sample before cuts. Black: Data, Blue dots with red error bars: MC with background and gain distribution from Minimum Bias Events, Green: Data normalised to blue/red MC, Blue: Events from pure optical background. The normalisation factors NF are given in matching colour.

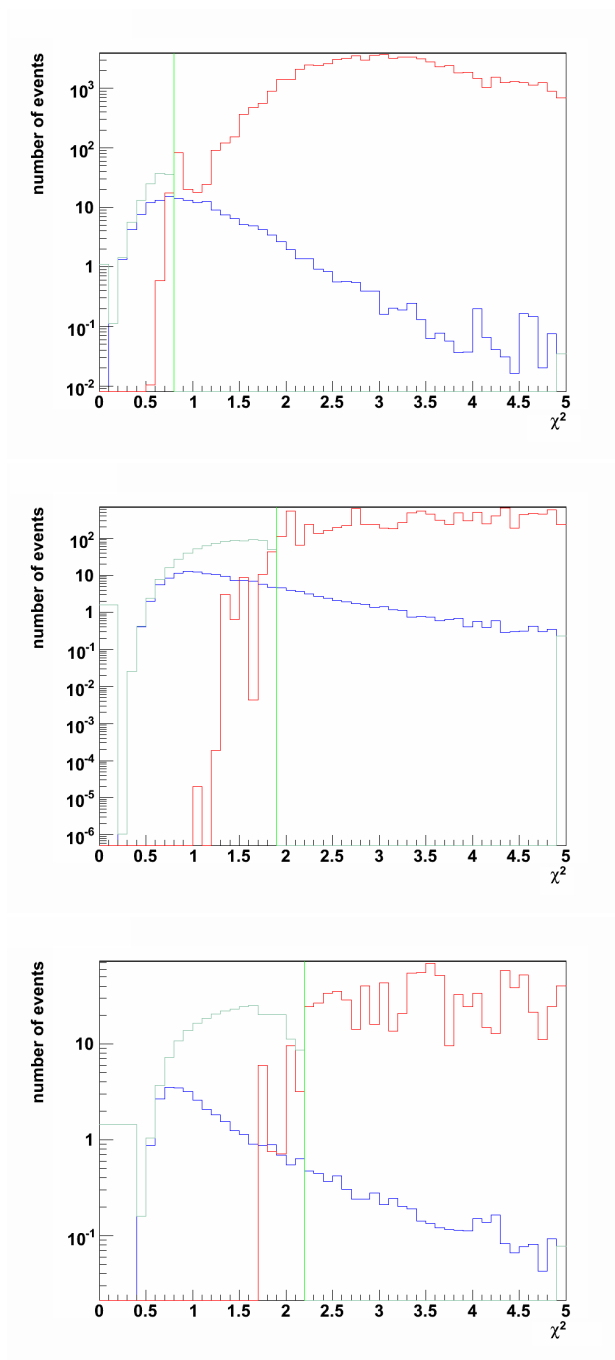


Figure 9.3: BBFit χ^2 distributions of true upgoing neutrino events (blue) and misreconstructed downgoing events (red) for one line events (top), two line events (middle) and three or more line events (bottom). The green lines indicate the cut values where the sum of the true upgoing events minus the sum of the misreconstructed downgoing events (turquoise) becomes negative.

the effect of the global cut might depend on the different detector conditions, they are represented in the simulation as they occurred in data, as explained in section 8.1.6. The cut value was determined separately from the χ^2 distributions for one line events, two line events and three or more line events. For one line events, the ghost solution of a downgoing muon track with a zenith tilted by twice the Cherenkov angle exhibits worse time residuals compared to upward going tracks only due to the larger fraction of scattered light reaching the PMTs and the possible presence of subshowers. Therefore a much stricter χ^2 cut is required than for multiline events, where the hit pattern mistaken for an upgoing track consists of several incidentally matching parts from different particles and optical background. This is reflected by the χ^2 distributions of figure 9.3, in which wrongly reconstructed muon events on a single line reach low χ^2 values not present for multiline events. Since muon events close to the horizon are reconstructed with a certain angular error, the events considered as upgoing were defined by a zenith angle larger than 100° , retaining a 10° safety margin. From the histograms filled with those events, the cut values were extracted as the lower edge of the leftmost bin where the sum of the true neutrino events minus the sum of the misreconstructed muon events, shown as a turquoise curves in figure 9.3 is negative, as indicated by the green lines. They are $\chi^2 < 0.8$ for one line events, $\chi^2 < 1.9$ for two line events and $\chi^2 < 2.2$ for three or more line events. Due to the size of the signal region and the large kinematic angle of the low energy signal events, no quality cuts to improve the angular resolution were added.

9.2.3 Data to Monte Carlo Comparison on Neutrino Events

Prior to specifically examining the source region for a possible signal, it has to be checked if the general angular and energy distributions of the alleged neutrino events in data and MC are in agreement. Whereas the comparison presented in section 8.2 was based on the downgoing muon events, the relevant parameters are investigated in the following for those events, which are reconstructed as upgoing neutrino candidates by BBFit after the cuts defined in section 9.2.2.

The zenith distribution in figure 9.4 indicates that, unlike for the downgoing events, the simulation fits to the data for the upgoing reconstructed events. Indeed, the ratio between measured and simulated events integrated over zenith from 100° to 180° is found to be 1.087 ± 0.148 . Thus the measured number of events, 328 with an statistical error of ± 17.4 , shows no significant systematic shift from the expected, which in total amounts to

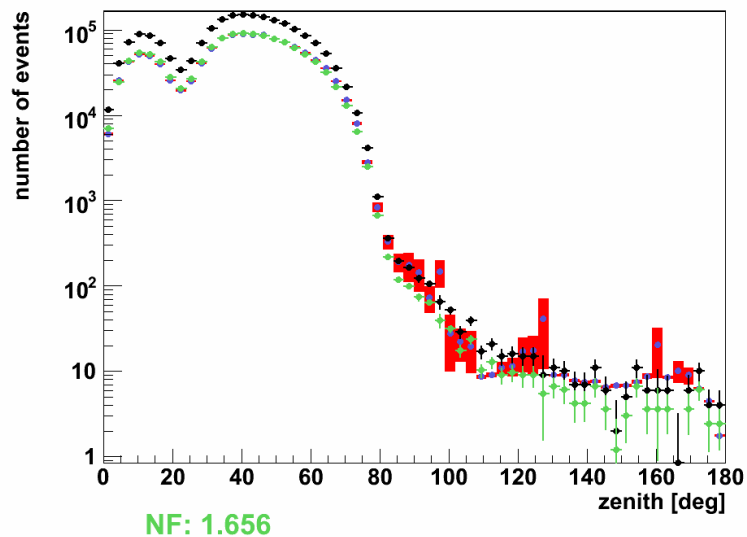


Figure 9.4: Comparison between zenith angle distributions of data and MC for the final sample after cuts. Black: Data, Blue dots with red error bars: MC with background and gain distribution from Minimum Bias Events. The normalisation factors NF are given in matching colour.

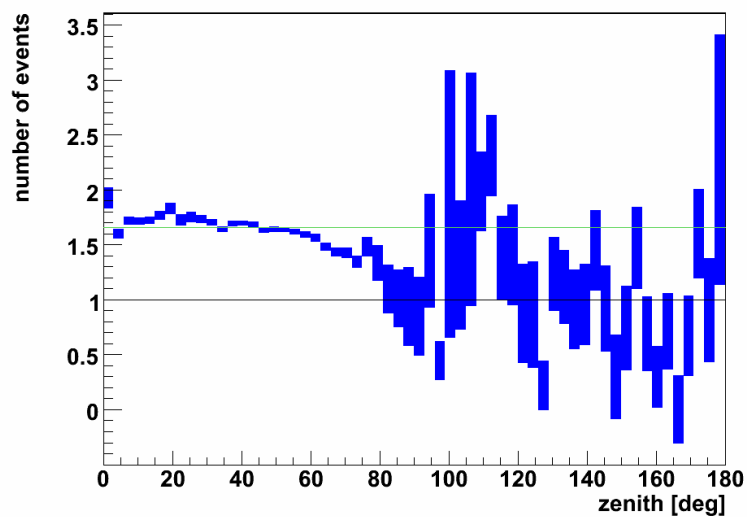


Figure 9.5: Ratio between data and MC as a function of the zenith for the final sample after cuts, with the green line indicating the average ratio

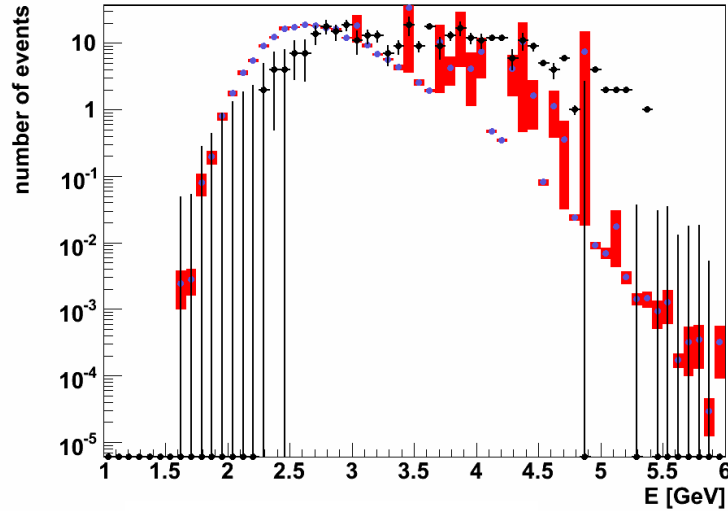


Figure 9.6: Comparison between energy distributions of data and MC for events reconstructed with zenith $> 100^\circ$ from the final sample after cuts. Black: Data, Blue dots with red error bars: MC with background and gain distribution from Minimum Bias Events, Green: Data normalised to blue/red MC

301.6 with a statistical error of ± 37.8 . Mismeasured muon events with their large weights cause large errors for the simulation at some zenith bins, with the uncertainty induced by their uneven spread over zenith not taken into account. The error on data is calculated as the square root of the number of events expected from the simulation at each bin, because of the low, and therefore fluctuating, measured number of events. In figure 9.5 the ratio of measured to simulated number of events as a function of the zenith angle is displayed, along with its statistical errors and lines indicating the hypothesis of no scaling and that of the global factor from all events.

The distribution in energy reconstructed with ANNergy (see section 7.5.2) for the upward going events exhibits a deficit in measured events compared to simulated events up to about 1 TeV, shown in figure 9.6. Below 200 GeV, no events are found in data, which is covered by the statistical uncertainty though. From 200 GeV to 1 TeV, the number of measured events is significantly lower than the predicted. Above 1 TeV, the predicted numbers come with large error bars, since mismeasured

muons are predominantly found there, not allowing to determine exactly if it matches the data. However, from the fact that the total number of events is predicted correctly, it can be deduced that there is a shift in energy between data and MC for neutrino candidate events.

9.2.4 Cut to Reject Atmospheric Muons for the Simulated Annealing Fit

For the events which were not discarded by the event preselection from section 7.6.6, the Simulated Annealing Fit procedure was performed. If an event was also reconstructed by BBFit and accepted by the final cuts presented in section 9.2.2, its BBFit result was used. From all other upgoing reconstructed events, those passing the initial cut asking for at least four direct hits are passed to an upper cut on the parameter ω (see section 7.6.7), set at the point where the atmospheric muon and neutrino background are equal. Since ω is composed of the number of direct hits and the reconstructed energy, the concurrence of data and MC in both parameters for the events in question has to be verified. The comparison is based on limited statistics, but as figure 9.7 indicates, no systematic deviation larger than the estimated errors exists. There is a generally higher number of events in MC compared to data, with the initial zenith distribution shown in the upper part of figure 9.9. They are found again at high energies and low number of direct hits though, hence the cut parameter ω is in agreement at low values, where the cut is expected to be. The actual cut is chosen to be $\omega < 17.5$ from the lower edge of the leftmost bin in figure 9.8, where the sum of the true neutrino events minus the sum of the misreconstructed muon events is negative. The zenith angle distribution of the events selected by this cut is shown in the lower part of figure 9.9. Their total number is 10, with 8.9 ± 1.0 expected from MC.

9.2.5 Search Cone Optimisation

A signal from the annihilation region at the centre of the Earth would be expected as additional events clustered around the vertically upgoing direction. The spread of the simulated signal events encompasses the expanse of the annihilation region (see figure 4.4) and the dilution due to the angular resolution of the fit. For the calculation of the limit, the events from a search cone around $zenith=180^\circ$ are used, with its opening angle defined as the angle from the vertical axis. To find the best cut value on the opening angle (which is equivalent to a cut on the zenith angle) from MC,

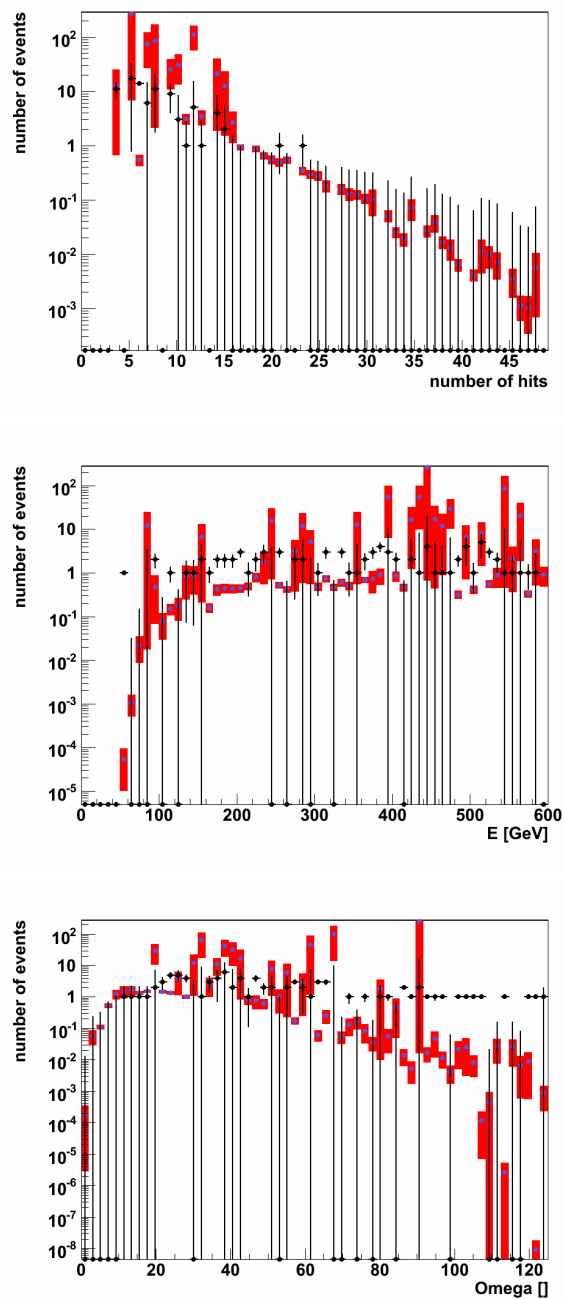


Figure 9.7: Distributions of the number of direct hits (top), the reconstructed energy (middle) and ω (bottom) after the 4-hit-cut for the final sample. Black: Data, Blue dots with red error bars: MC with background and gain distribution from Minimum Bias Events

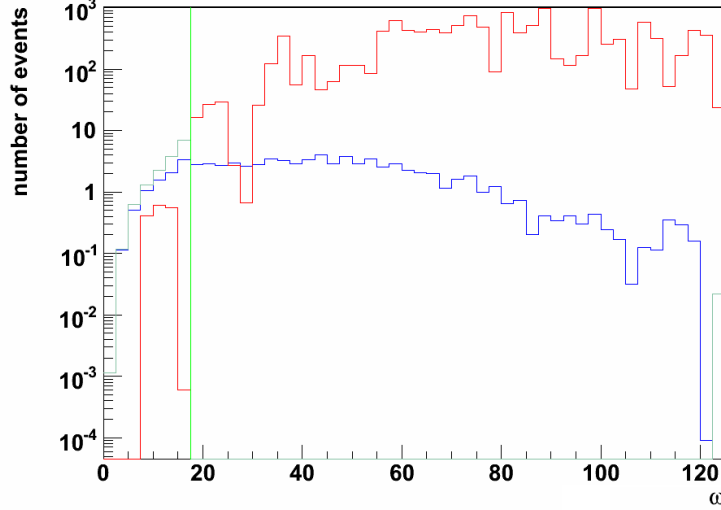


Figure 9.8: ω distribution of true upgoing neutrino events (blue) and misreconstructed downgoing events (red) after the 4-hit-cut for the final sample. The green line indicates the cut value where the sum of the true upgoing events minus the sum of the misreconstructed downgoing events (turquoise) becomes negative.

the Model Rejection Factor (MRF) minimization method [120] was used. For each WIMP mass from the list in section 8.1.7, a separate optimisation was performed, since the direction spread of the signal neutrinos depends on it. The MRF is defined as the average upper limit $\bar{\mu}_{90}$ divided by the expected number of signal events n_s , based on the assumption of a WIMP annihilation rate of 200 ns^{-1} . Using the implementation of the methods by Feldman and Cousins [91] in ROOT [61], the average upper limit was calculated for an expected background of n_{bkg} as

$$\bar{\mu}_{90} = \sum_n p_n(n_{\text{bkg}}) \cdot \mu_{90}(n) \quad (9.1)$$

with the probability $p_n(n_{\text{bkg}})$ to detect n events given by the poissonian distribution with mean n_{bkg} . Due to the discovered differences between data and MC in the energy distributions as discussed in sections 8.2.4 and 9.2.3, an initially foreseen energy cut was omitted and only the search cone cut was applied and optimised by the MRF minimisation for the creation of the upper limit based on the analysed data.

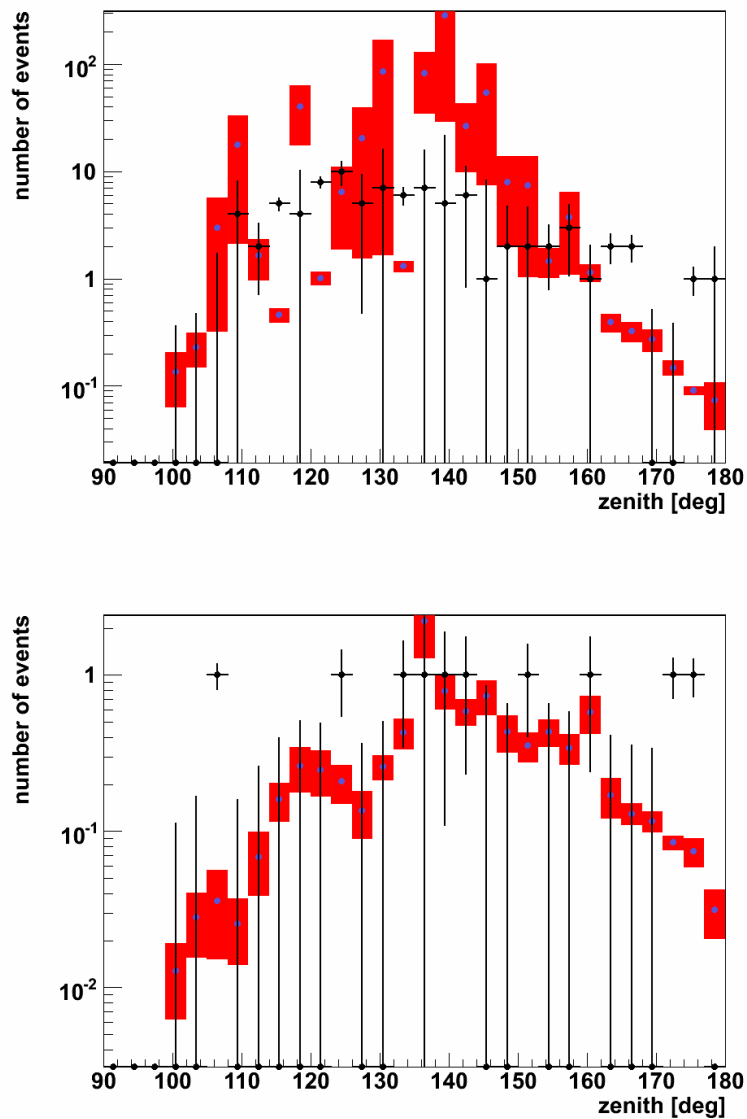


Figure 9.9: Zenith distribution after 4-hit-cut (top) and after ω cut (bottom) for the final sample. Black: Data, Blue dots with red error bars: MC with background and gain distribution from Minimum Bias Events

9.2.6 Systematic Errors

With systematic deviations between data and MC in the total number of events and their energy distribution, it must be discussed how they influence a limit derived from the comparison of expected and measured events in the signal region. The ratio presented in figure 9.5 suggests that no systematically higher number of events in data is observed for upgoing reconstructed events, in contrast to downgoing events. Data and MC agree on the number of upgoing events within the tolerance of the associated statistical errors. Furthermore, the continuous reduction of the scale factor from 60° to 90° zenith corroborates the presumption that the source of the effect is zenith dependent and only affects downgoing events. If there was a systematically higher number of events in data than MC also for upgoing events in general or in the signal region, this underestimation of the background would cause any derived limit to be worse than if the background was estimated correctly. The alleged systematic shift in the reconstructed energy of upgoing events from figure 9.6, assigning higher energies to data than MC, poses the risk of an overestimation of the background events, if an upper energy cut is applied. Therefore this cut was not applied and its use in the MRF minimisation was skipped.

9.3 Results

9.3.1 Limit from December 2010 Data

The best cone was set at the minimum of the MRF as a function of $\cos(\text{zenith})$. The MRF was calculated from $\cos(\text{zenith}) = -0.95$ to $\cos(\text{zenith}) = -1.0$ in 50 bins. The MRF as a function of $\cos(\text{zenith})$ for a 100 GeV WIMP annihilating into W^+W^- is given as an example in figure 9.10. The optimal search cone is a function of the WIMP mass and also different for each annihilation channel, as shown in figure 9.12. The search cone widens for light WIMPs and soft annihilation channels compared to heavy WIMPs and hard annihilation channels, due to the larger annihilation region and the lower average energy of the neutrinos from the former. The minimum considered opening angle is 3.6° ($\cos(\text{zenith}) = -0.998$), though further reducing it might give a better MRF, since the reliability of the event by event background estimation also decreases with the size of the search cone. The actual value of the MRF at its optimum, shown in figure 9.11, is inversely proportional to the expected number of signal events from the search cone, which is given in figure 9.13.

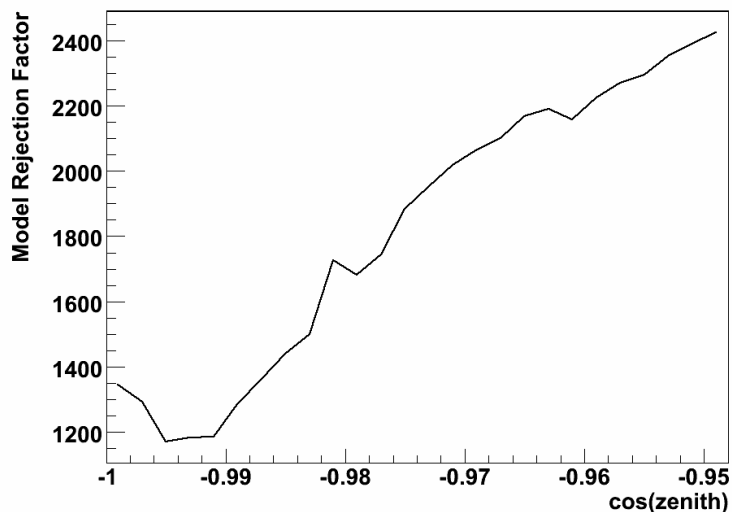


Figure 9.10: The model rejection factor as a function of the cut on $\cos(\text{zenith})$ for the W^+W^- channel at $m_{\text{DM}} = 100$ GeV

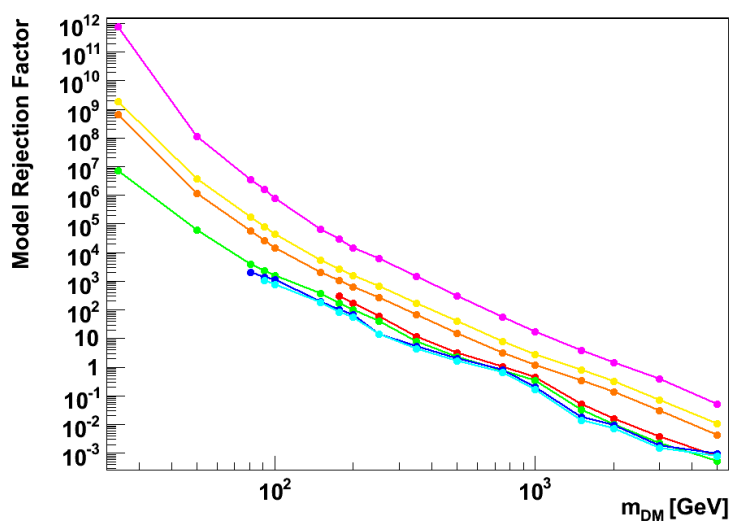


Figure 9.11: Best model rejection factor as a function of m_{DM} for annihilation channels $c\bar{c}$ (yellow), $b\bar{b}$ (orange), $t\bar{t}$ (red), gg (magenta), $\tau^+\tau^-$ (green), W^+W^- (blue) and Z^0Z^0 (turquoise)

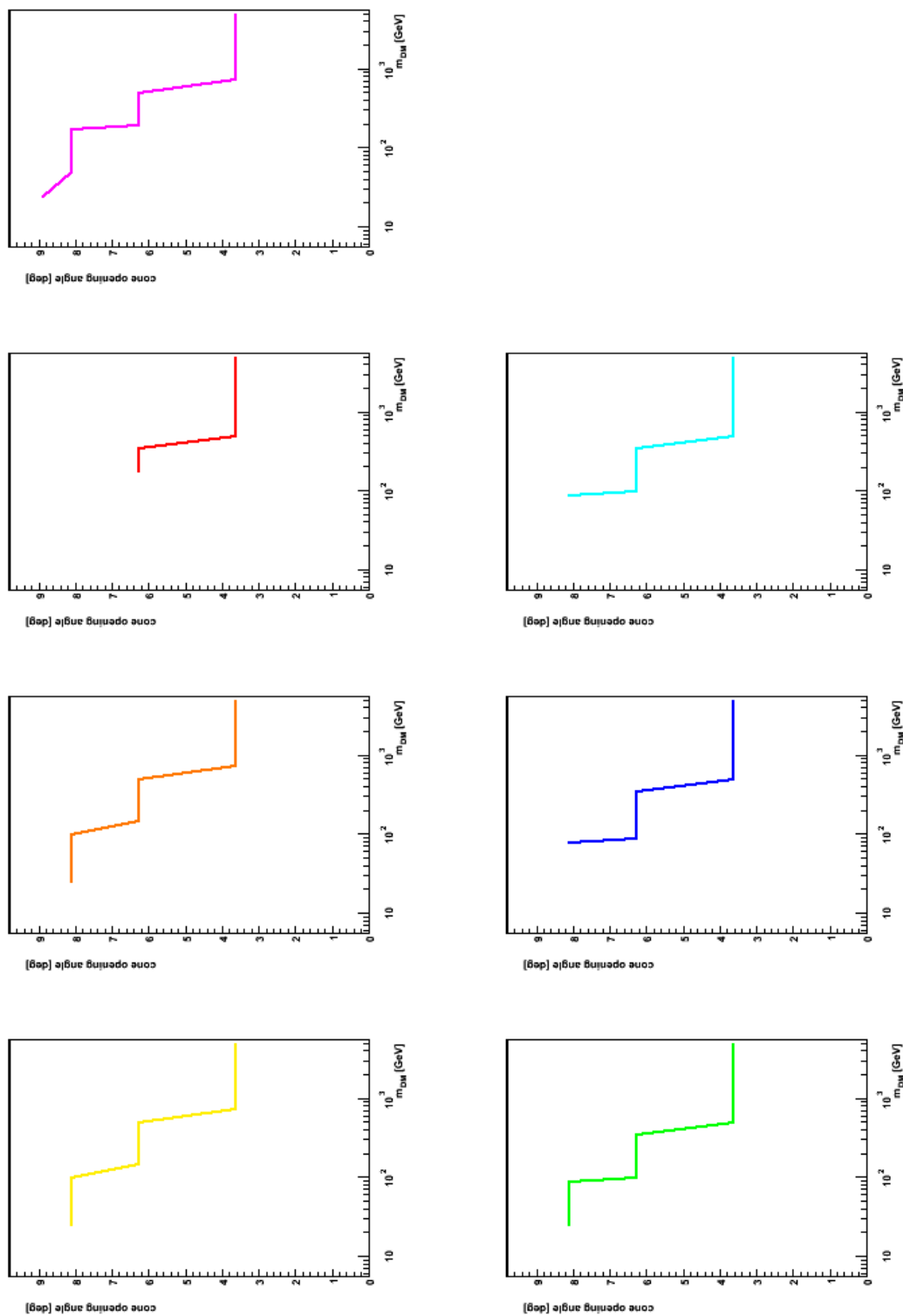


Figure 9.12: The optimum search cone opening angle for the one month limit calculation as a function of m_{DM} for annihilation channels $c\bar{c}$ (yellow), $b\bar{b}$ (orange), $t\bar{t}$ (red), W^+W^- (blue) and Z^0Z^0 (turquoise)

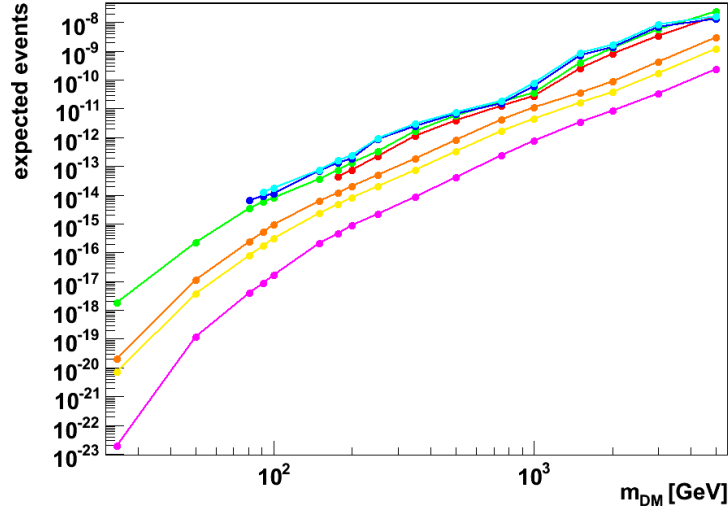


Figure 9.13: Expected number of signal events for an annihilation rate of 200 ns^{-1} from the optimised search cone as a function of m_{DM} for annihilation channels $c\bar{c}$ (yellow), $b\bar{b}$ (orange), $t\bar{t}$ (red), gg (magenta), $\tau^+\tau^-$ (green), W^+W^- (blue) and Z^0Z^0 (turquoise)

The estimated background, the measured number of events and the resulting 90% CL upper limit on a signal in addition to the estimated background events are listed in figure 9.14. While a higher number of events has been measured than expected, the excess is not significant to indicate an increased neutrino flux.

Division by the expected number of events per annihilation for each WIMP mass and channel provides a limit on the total annihilation rate in the Earth, presented in figure 9.15. For comparison with theoretical estimates on this quantity, a prediction for the capture rate of WIMPs from [52] is utilised. If capture and annihilation of WIMPs are in equilibrium, the rate of annihilations is half the capture rate, as two particles are used up in each annihilation. The annihilation rate for WIMPs with a spin independent cross section of 10^{-43} cm^2 and a spin dependent cross section of 10^{-36} cm^2 is included in figure 9.15. The capture rate is dependent on the WIMP mass, with maxima where it is near the mass of elements prevalent in the Earth. Using the WimpSim [117] flux tables, the limit on the annihilation rate was translated into a limit on the neutrino flux at the Earth's surface. This flux limit with a lower threshold neutrino energy of 10 GeV

cone [deg]	n_{expected}	n_{measured}	limit
3.62	2.86	5	7.14
5.13	4.97	8	9.03
6.28	7.05	10	9.45
7.25	9.06	11	8.75
8.11	10.73	16	13.26
8.89	12.48	19	15.03
9.60	14.06	21	15.94

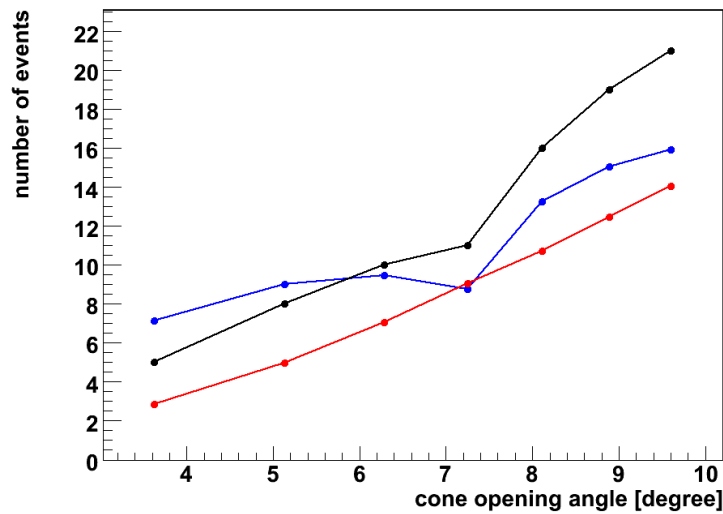


Figure 9.14: Number of expected (red) and measured (black) events and the corresponding limit (blue) on additional events from Dark Matter annihilation for all search cone opening angles used in the analysis

is shown in figure 9.16.

To check the sensibility of the limit to the selection of the search cone cut, the expected signal and the limit on annihilations for the 100 GeV WIMP and W^+W^- channel case were plotted against the search cone opening angle. As figure 9.17 imparts, the opening angle obtained from the MRF minimisation is at a value where no substantial increase in signal events can be gained by widening it. Though after analysing the measured data, the opening angle derived from the MRF is found not to return the best limit, the variation of the limit around the chosen cut is in the order of 10% of the limit's value. This indicates that the precision of the search cone cut is not a determining factor in the achieved limit, which corroborates the

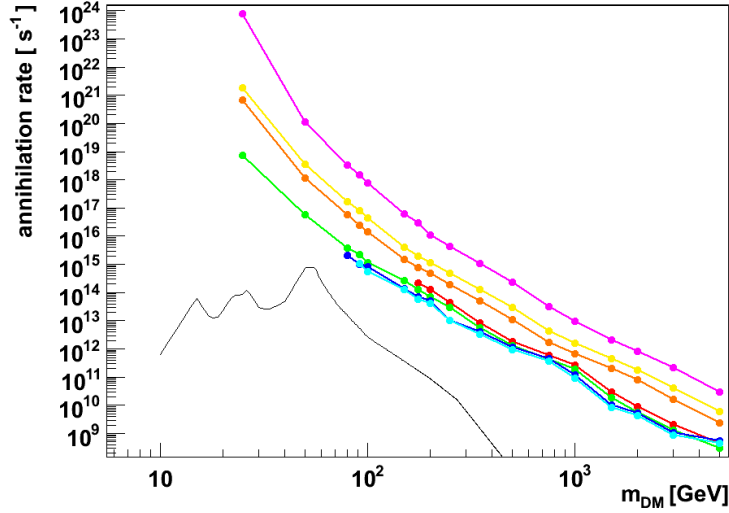


Figure 9.15: Limit on the annihilation rate as a function of m_{DM} for annihilation channels $c\bar{c}$ (yellow), $b\bar{b}$ (orange), $t\bar{t}$ (red), $g g$ (magenta), $\tau^+\tau^-$ (green), W^+W^- (blue) and Z^0Z^0 (turquoise). The black line represents the theoretical prediction for the capture rate from [52]

robustness of the limit and validates the background estimation directly from simulated events and the cone cut selection procedure.

9.3.2 Sensitivity for Five Years

Based on the conditions of the period of one month examined for the analysis, a sensitivity prediction for five years was calculated by multiplication of the background with 60 and assuming the expected background to be measured. The sensitivity is calculated by the interpolation of the Feldman Cousins constructed upper limits for the integer values adjacent to the background estimate. With the 60 times higher expected background, a dedicated optimisation of the search cone was performed, with the sensitivity divided by the expected signal events as MRF. As presented in figure 9.18, by trend smaller optimal cones than for the one month limit were found. For the exclusion of annihilations inside Earth, the results in figure 9.19 indicate that the sensitivity gets close to the theoretical model from [52]. The corresponding neutrino flux exclusion capabilities are shown in figure 9.19 as well.

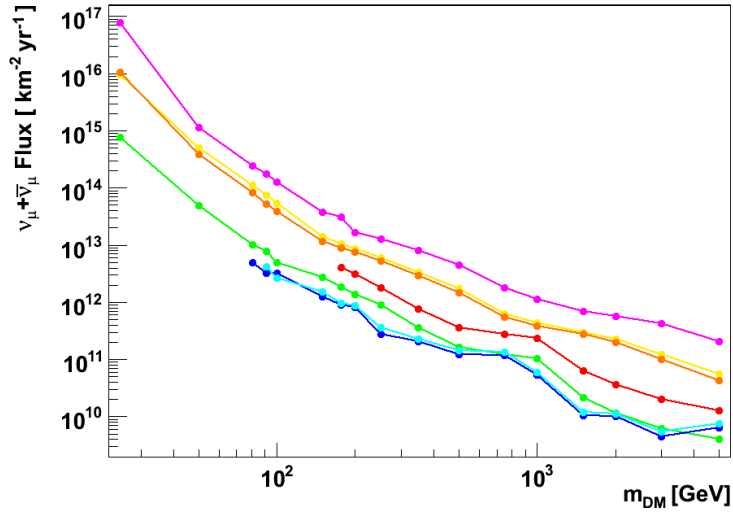


Figure 9.16: Limit on the neutrino flux from Dark Matter annihilation above 10 GeV neutrino energy as a function of m_{DM} for annihilation channels $c\bar{c}$ (yellow), $b\bar{b}$ (orange), $t\bar{t}$ (red), $g g$ (magenta), $\tau^+\tau^-$ (green), W^+W^- (blue) and Z^0Z^0 (turquoise)

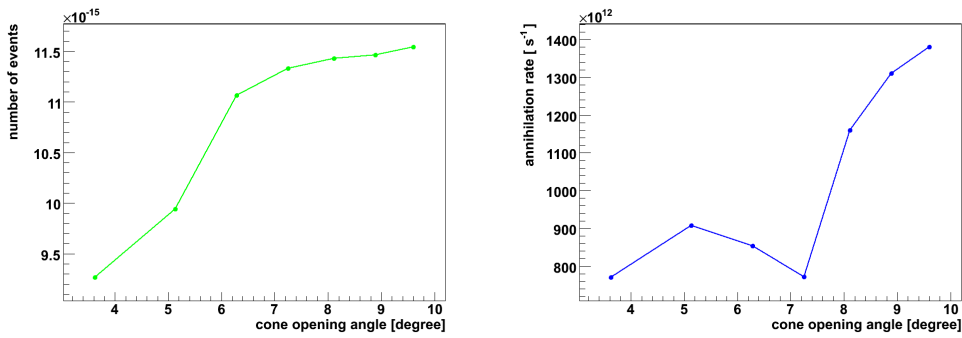


Figure 9.17: Expected number of signal events for an annihilation rate of 200 ns^{-1} as a function of the search cone opening angle (left) and the corresponding limit on the annihilation rate (right) for the W^+W^- channel at $m_{DM} = 100 \text{ GeV}$

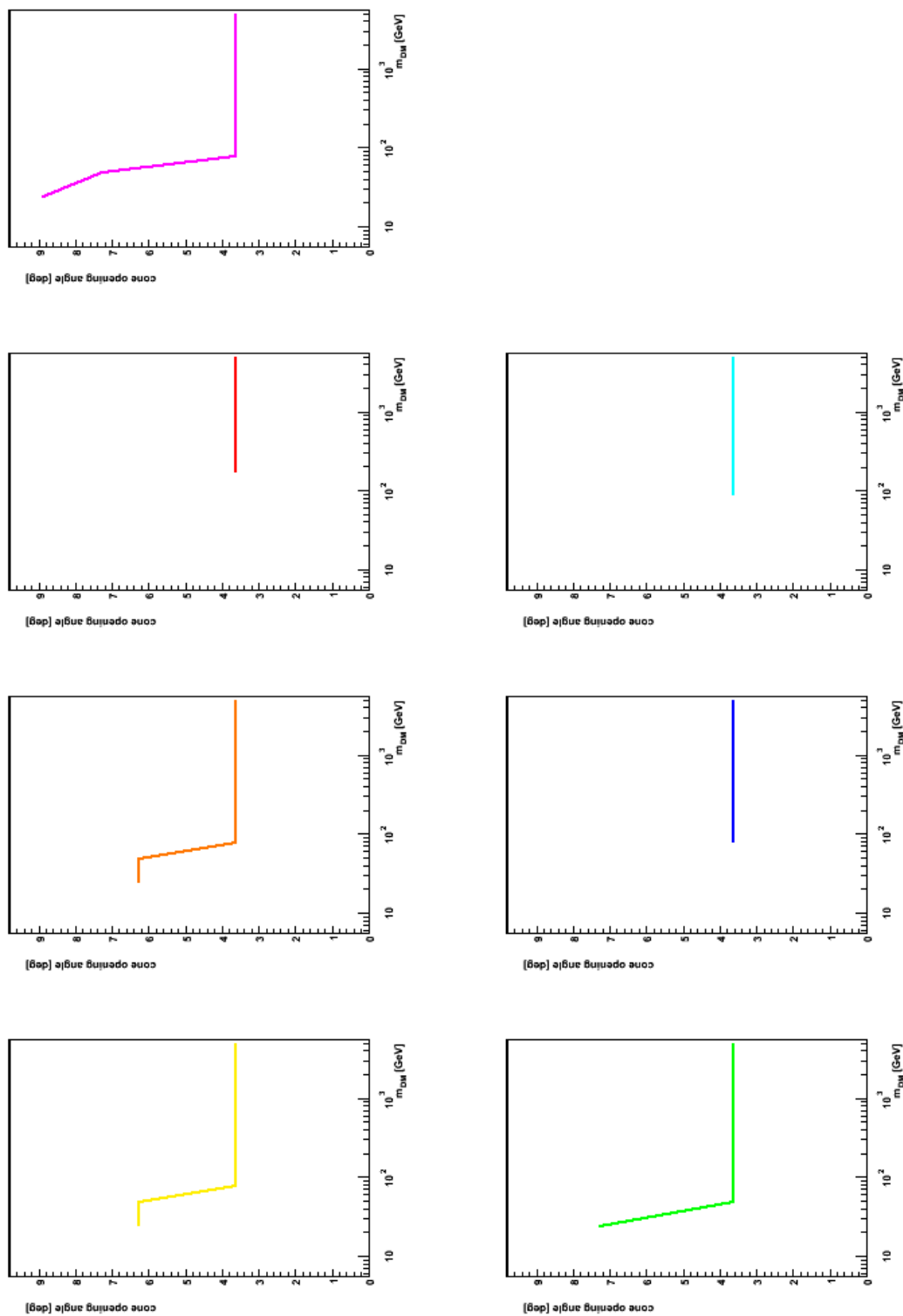


Figure 9.18: The optimum search cone opening angle for the five year sensitivity calculation as a function of m_{DM} for annihilation channels $c\bar{c}$ (yellow), $b\bar{b}$ (orange), $t\bar{t}$ (red), W^+W^- (blue), $g g$ (green), $\tau^+\tau^-$ (cyan), Z^0Z^0 (turquoise) and W^+W^- (magenta)

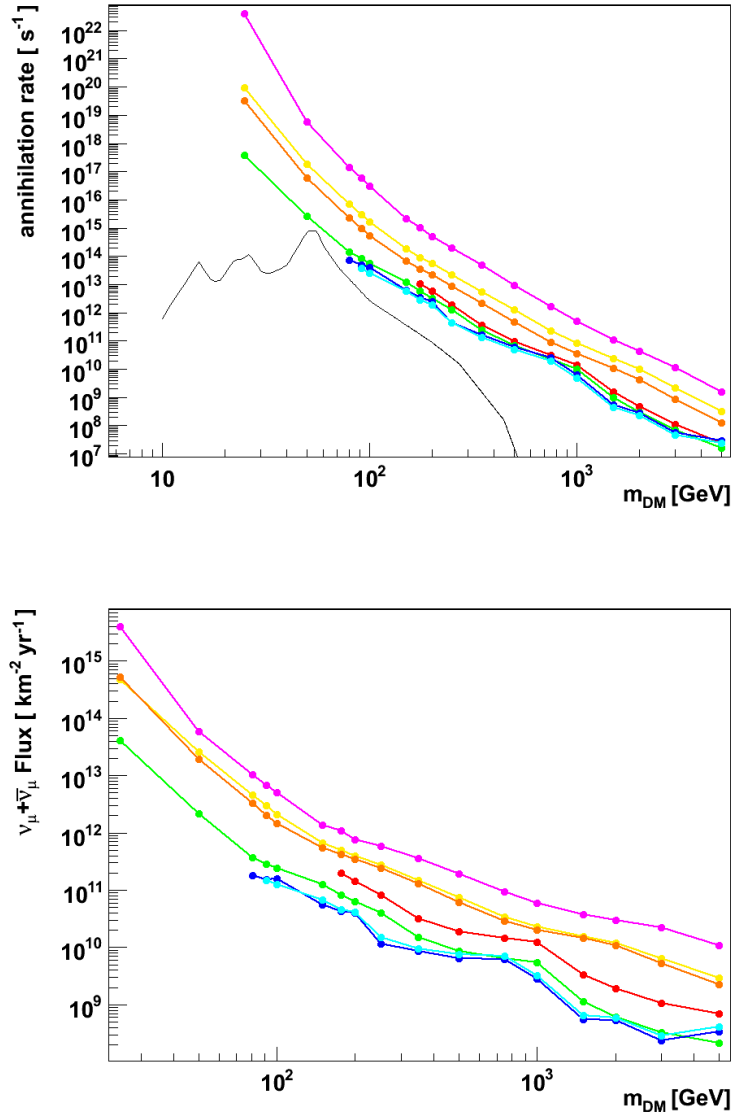


Figure 9.19: Five year sensitivity for the annihilation rate (top) and the neutrino flux from Dark Matter annihilation above 10 GeV neutrino energy (bottom) as a function of m_{DM} for annihilation channels $c\bar{c}$ (yellow), $b\bar{b}$ (orange), $t\bar{t}$ (red), $g g$ (magenta), $\tau^+\tau^-$ (green), W^+W^- (blue) and Z^0Z^0 (turquoise). The black line represents the theoretical prediction for the capture rate from [52]

9.4 Performance of the Reconstruction Algorithms

9.4.1 Atmospheric Neutrino Flux

Four types of reconstructions contribute to the sample for the analysis, BBFit with one, two and three lines, as well as the Simulated Annealing Fit. The composition of the event sample is strongly dependent on the zenith angle. As figure 9.20 points out, is the single line BBFit highly efficient for straight upgoing events, where the muon track emits light next to a large part that line, facilitating the reconstruction. Since a single line fit needs less storeys to be hit, the overall efficiency is larger than for more horizontal directions. For these, multi line BBFit is predominant, since neutrinos entering the detector from the side cause a track that can pass several lines at close distance. The weaker cuts applied to the multi line events does not make up for the requirement of hits on six storeys passing the hit selection. The simulated annealing fit, which does not discern between single and multi line events by its initial hit selections, is shown to be able to reconstruct additional events especially around $\cos(\text{zenith}) = -1$, but also for more horizontal directions.

The deviation of the reconstructed zenith angle from that of the simulated neutrino direction, which is shown in figure 9.21, is on average 5.1° for BBFit 1-Line, 1.3° for BBFit 2-Line, 0.9° for BBFit 3-Line, and 5.6° for the Simulated Annealing Fit.

As a function of the neutrino energy, the reconstruction efficiency of the combined reconstruction displayed in figure 9.22, with the triggered events as basis, reaches a level of about 40% at 200 GeV. Below that energy, the efficiency steadily increases with energy. In absolute event numbers, shown in figure 9.23, the decline of the atmospheric neutrino flux with energy and the increase of the efficiency lead to a maximum around 100 GeV.

9.4.2 Signal Neutrino Flux

The event weights calculated from the neutrino flux as explained in 8.1.7 translate to expected event distributions, distinct in energy and zenith spread for the different annihilation channels and WIMP masses.

The simulated signal from WIMP annihilations is confined to an angular range from 180° to 165° zenith angle, and to neutrino energies below the WIMPs mass. Due to the vertical direction and low energies, the main contributions are from 1-Line BBFit and the Simulated Annealing Fit, with the latter shown to be able to reconstruct events with extremely low energies. Examples of the MC zenith and energy distribution for the $b\bar{b}$ -channel

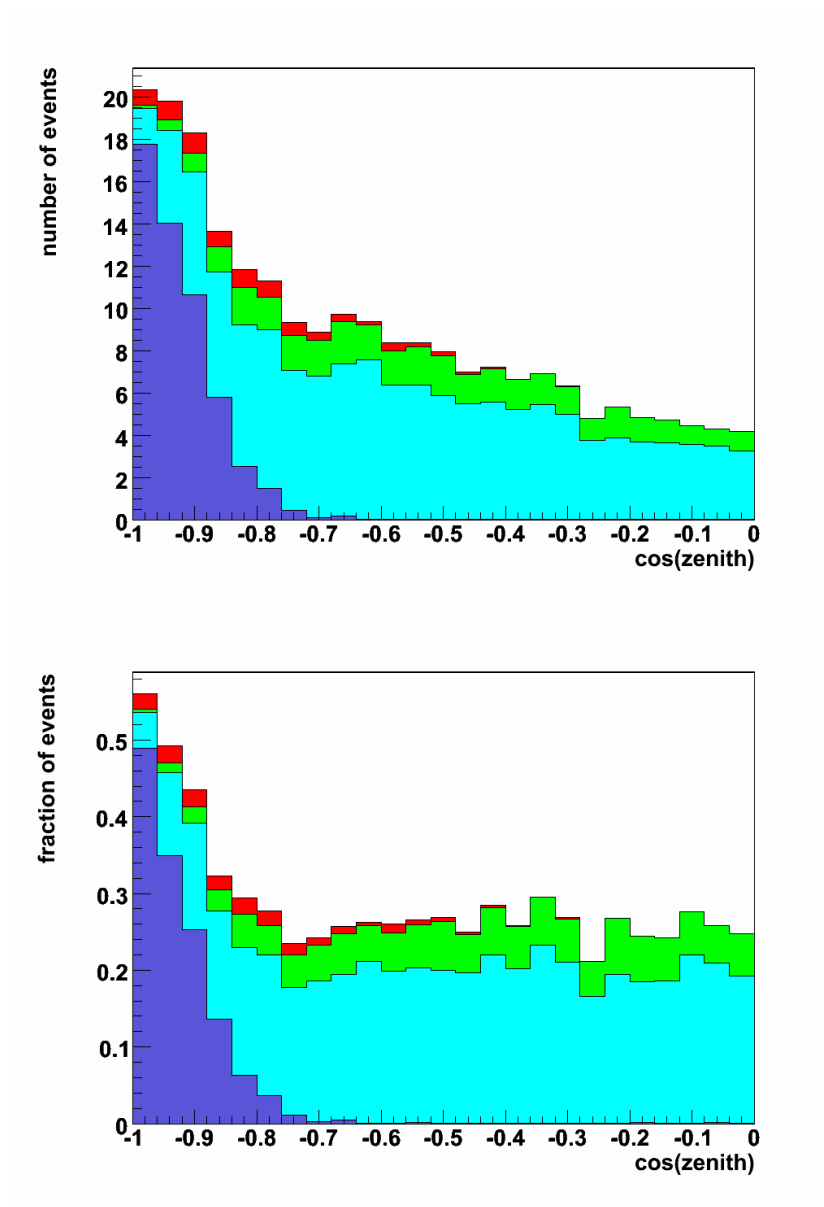


Figure 9.20: Expected zenith distribution of events from atmospheric neutrinos and muons after cuts with the colours showing the contribution of the reconstruction algorithms. Blue: BBFit 1-Line, Turquoise: BBFit 2-Line, Green: BBFit 3-Line, Red: Simulated Annealing Fit

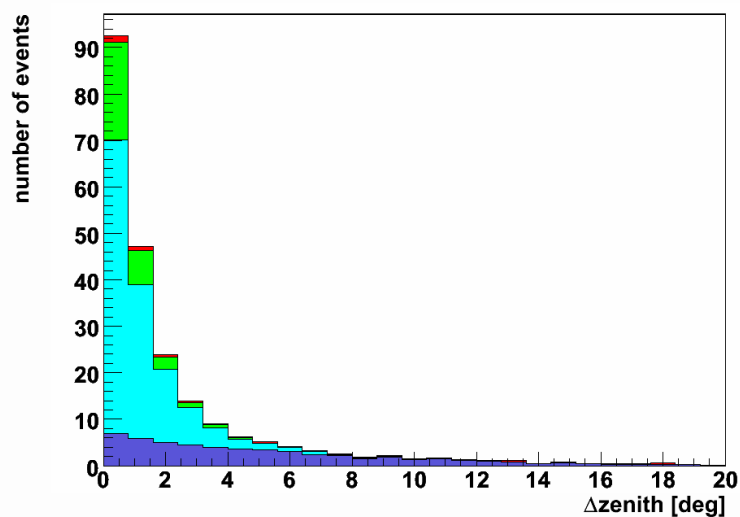


Figure 9.21: Difference in zenith angle between reconstructed and true neutrino direction after cuts with the colours showing the contribution of the reconstruction algorithms. Blue: BBFit 1-Line, Turquoise: BBFit 2-Line, Green: BBFit 3-Line, Red: Simulated Annealing Fit

at 25 GeV and 250 GeV WIMP mass are given in figure 9.24, and for the W^+W^- -channel at 100 GeV and 250 GeV in figure 9.25. The larger annihilation region for lighter WIMPs is found again in these distributions as a larger angular spread of the expected neutrino events.

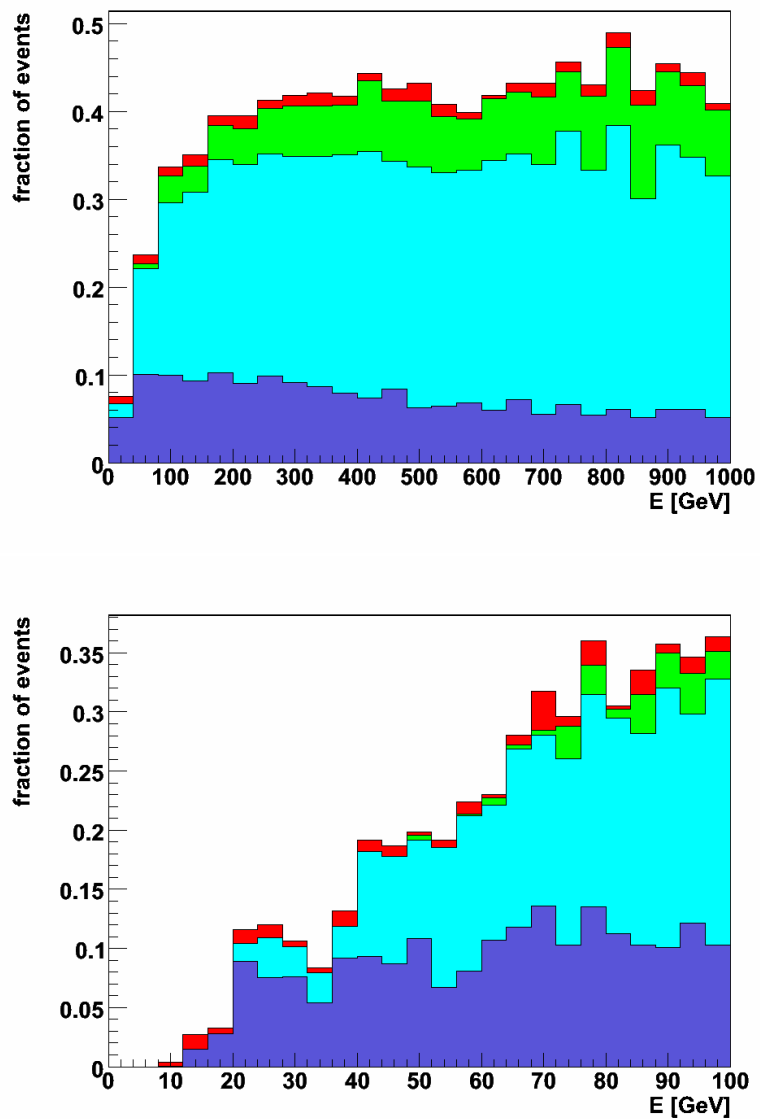


Figure 9.22: Contribution of the reconstruction algorithms to the total efficiency - reconstructed divided by triggered events - as a function of MC neutrino energy of atmospheric neutrinos and muons after cuts. Blue: BBFit 1-Line, Turquoise: BBFit 2-Line, Green: BBFit 3-Line, Red: Simulated Annealing Fit

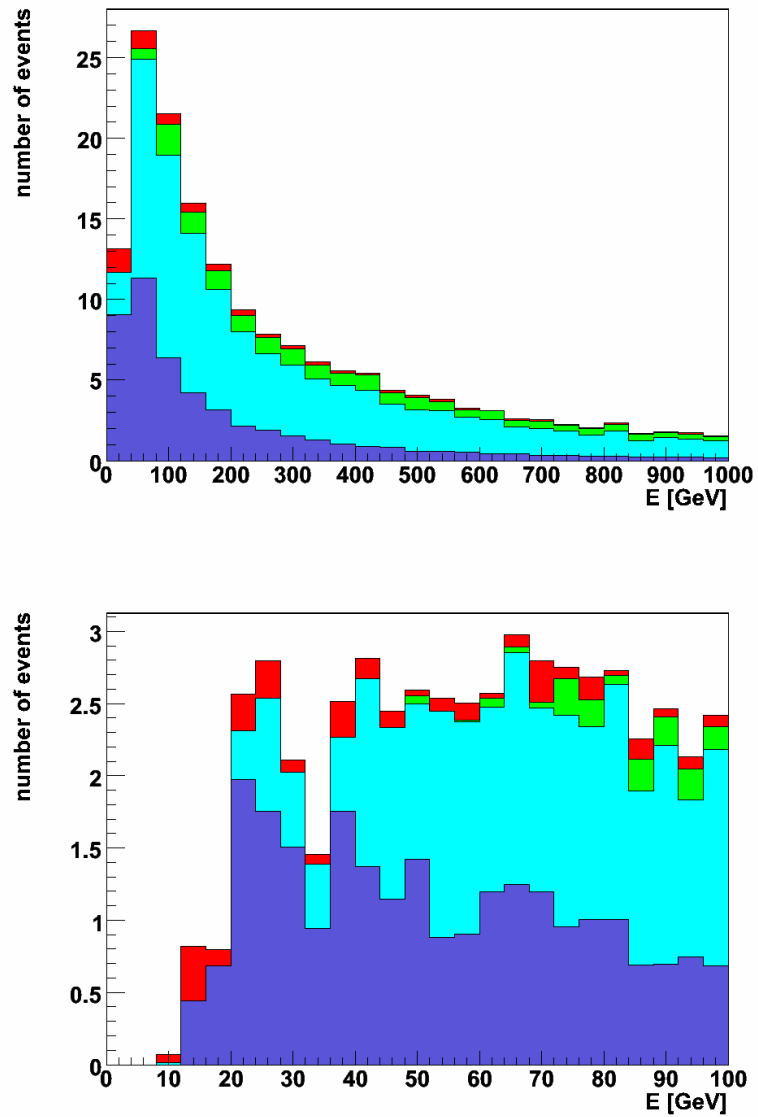


Figure 9.23: Contribution of the reconstruction algorithms as a function of MC neutrino energy of atmospheric neutrinos and muons after cuts. Blue: BBFit 1-Line, Turquoise: BBFit 2-Line, Green: BBFit 3-Line, Red: Simulated Annealing Fit

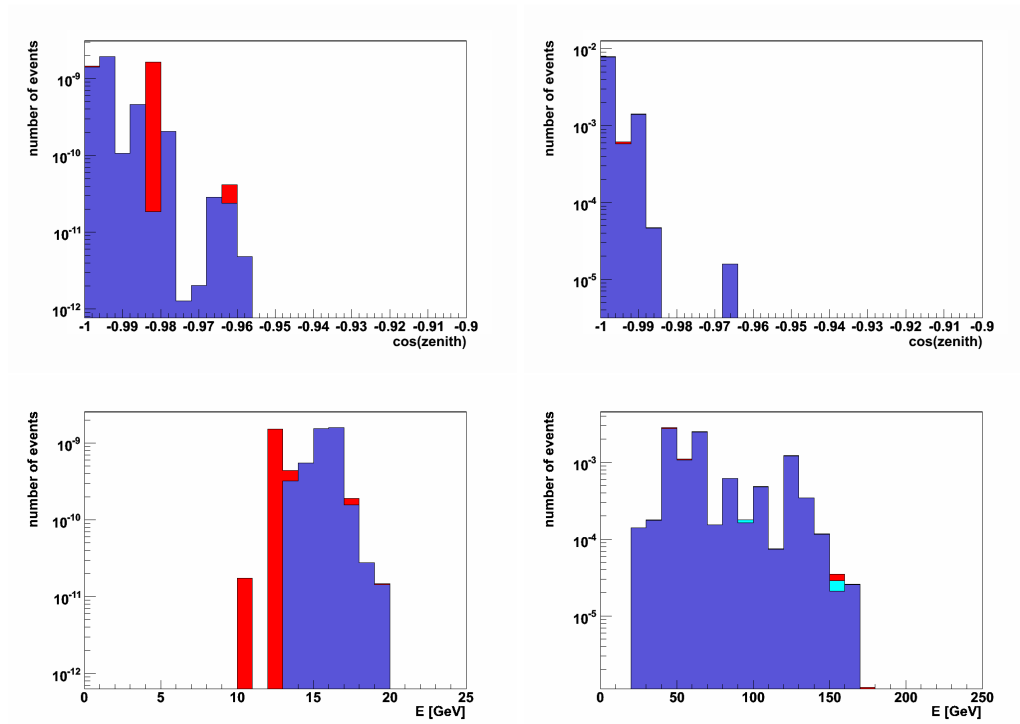


Figure 9.24: Distributions of true MC zenith (top) and energy (bottom) of the simulated signal events for the $b\bar{b}$ channel at $m_{\text{DM}} = 25$ GeV and $m_{\text{DM}} = 250$ GeV. Blue: BBFit 1-Line, Turquoise: BBFit 2-Line, Red: Simulated Annealing Fit

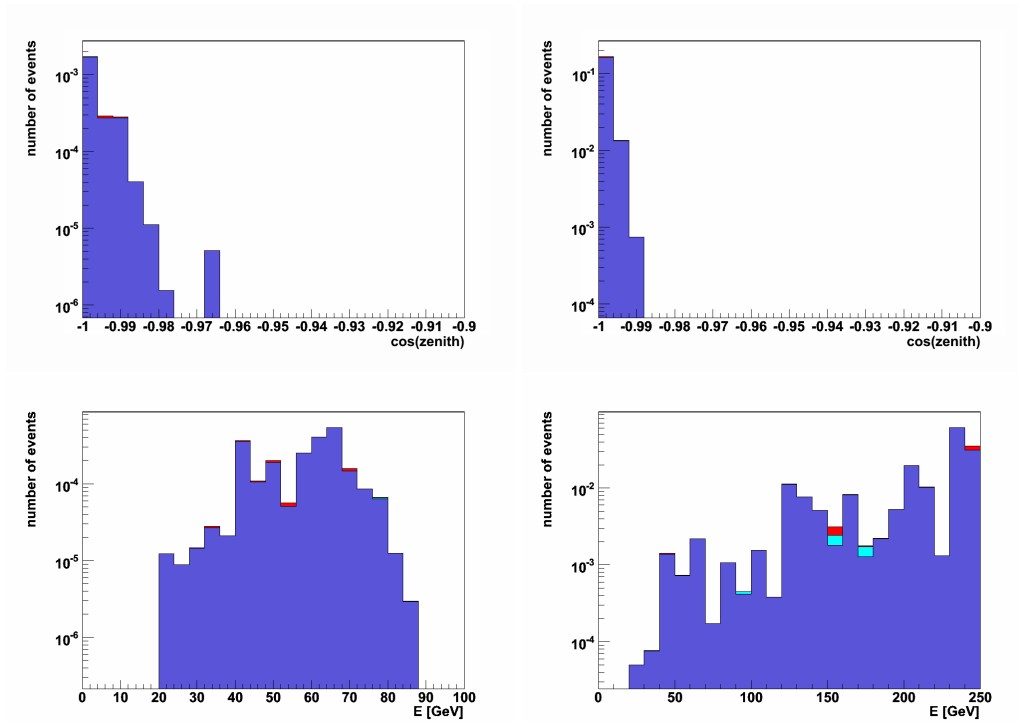


Figure 9.25: Distributions of true MC zenith (top) and energy (bottom) of the simulated signal events for the W^+W^- channel at $m_{\text{DM}} = 100$ GeV and $m_{\text{DM}} = 250$ GeV. Blue: BBFit 1-Line, Turquoise: BBFit 2-Line, Red: Simulated Annealing Fit

Chapter 10

Conclusions and Outlook

While the focus of this work is on setting a limit on the annihilation of Dark Matter in Earth, the achievements in the various subprojects undertaken towards this analysis contribute to the progress of the ANTARES project as a whole. Their status and future prospects are reviewed in the following, before a summary of the physics analysis is given.

10.1 Detector Alignment

Notably, the alignment program (see section 5.5) is an essential prerequisite for the precise reconstruction of neutrino events. A continuous processing of the triangulated hydrophone positions, compass and tiltmeter data is possible, to provide the detector geometry information in the database lookup tables for offline data analysis. The processed time covers a vast majority of the data taking, with gaps only where the input from the position and orientation measurements is not complete or not present at all. To close those gaps, efforts are ongoing to find ways to reconstruct the detector geometry from incomplete data while retaining the required precision. An improvement currently being implemented is a method to compensate for not working compasses by predicting the storey orientation dynamically from the movements of neighbouring storeys [71]. Furthermore, the error estimates for the line fit are being made available to the reconstruction codes via SeaTray [121], to the end of accounting for OM position uncertainty in the track reconstruction fit algorithms. A future development promising an increase in precision and reliability is a global fit over all lines, and the development of a dynamical detector model. This could be facilitated by integrating the code into SeaTray, making use of its stream environment to combine the individual measurements from different points

in time.

10.2 Sensitivity Studies

The sensitivity studies for the mSugra parameter space (see section 6) demonstrate how ANTARES can contribute to pinpoint the parameters of a possible Dark Matter particle from that well studied scenario, supporting indirect search for Dark Matter as a cornerstone of the physics case for neutrino telescopes. In this context, these studies were extended to aid in the planning of the KM3Net detector by judging its capabilities in terms of Dark Matter search [122]. In translating the exclusion or detection of a certain neutrino flux to the corresponding mSugra parameters in a model specific way, indirect detection can contribute to the combined efforts to identify the nature of the Dark Matter together with direct detection and collider experiments. Starting out from the studies presented in this work, an investigation not only into mSugra, but also the AMSB (Anomaly Mediated Supersymmetry Breaking), GMSB (Gauge Mediated Supersymmetry Breaking) and pMSSM scenarios is being undertaken [123], using the SuperBayes package [124] to incorporate a large variety of experimental results and cosmological constraints.

10.3 Event Reconstruction

Not only for indirect Dark Matter search, but also for neutrino oscillation studies, an effective low energy reconstruction algorithm is of great importance. ANTARES aims to detect neutrinos down to a threshold of 10 GeV in neutrino energy. Due to the spacing of the OMs, only very few hits from the emitted Cherenkov light are recorded for events of this energy. With the presence of an optical background rate of at least 60 kHz per OM, the identification of the signal hits before trying a fit of the muon direction is essential. To this end, the Cluster Hit Selection (see section 7.3.2) algorithm efficiently separates the hits caused by the muon track from the optical background, based on a combination of spatial and time correlations of the hits, as well as the hit amplitude. Providing this useful functionality independent of any preceding fit or event selection, it can be easily ported to other event reconstruction and analysis projects, thanks to the modularity of the SeaTray framework. Envisioned improvements to this algorithm are a fine tuning of the so far ad-hoc chosen correlation distances and amplitude thresholds, along with their adaption to the individual average

background rate. With the angular resolution at low energies limited by the kinematic angle between neutrino and muon, different aspects of event reconstruction than for high energy point source searches come to the fore, such as to reliably distinguish genuine neutrino events from misreconstructed atmospheric muons. The Simulated Annealing Fit (see section 7.6) explores the new concept of actively rejecting downgoing events by additional prefits suited for their reconstruction. With many misreconstructed tracks already removed, less stringent cuts on the reconstruction quality are needed after the reconstruction. Showing promising results for neutrinos of very low energy, down to 10 GeV, it was used in the analysis in addition to the BBFit algorithm (see section 7.4), further increasing the already good efficiency to a total of up to 40%, depending on the energy and zenith angle of the events. Starting points for a further sophistication of this strategy exist in the integration of Probability Density Functions truly specialised for different types of events by either gaining them from MC simulation, as done for the neutrino event case (see section 7.6.3), or deriving them from first principles. To reduce the currently unfavorable computing time per event, tuning of the convergence parameters of the simulated annealing minimizer to the properties of the event might prove promising.

10.4 Understanding the Detector Properties

The ANTARES detector is a complex system with the information used in the detection of neutrinos passing many processing steps, all of which have to be performed adequately to reliably reconstruct events. This processing chain is mirrored in a Monte Carlo simulation, providing a reference for comprehending each aspect. While in general there is good agreement between the simulation and the measured data, deviations have been identified in the hit amplitude distributions, the total number of downgoing events and the energy reconstructed by the ANNergy algorithm introduced in section 7.5.2. A detailed comparison of data and MC (see section 8.2) allowed to trace back the deviations in the amplitude distributions to the simulation of the PMT gain, and to bring the distributions into agreement by including measured gain distributions into the simulation (see section 8.1.4). The observed excess of about a factor of 1.6 in the measured number of downgoing events compared to the MC prediction was studied on each stage (see diagram 8.1 for an overview) of data processing and simulation from the PMT simulation onward, with the conclusion that it originates from an earlier stage, e.g. the light or muon propagation sim-

ulation. Accordingly the number of upgoing neutrino candidate events was scrutinised before the analysis as described in section 9.2.3 with good agreement found between data and MC. While originally an upper energy cut based on the ANNergy results was foreseen to improve the signal to background ratio for the analysis, the finding that the reconstructed energy in data is shifted significantly to higher energies compared to MC (see section 8.2.4), for downgoing as well as upgoing reconstructed events, gave reason to omit it. With the amplitude distributions in agreement, a future investigation into the other input parameters of the artificial neural network might give further insight.

To improve the reproduction of the real detector in the simulation, methods to create MC simulated events in parallel to the data processing were developed (see section 8.1.6), improving the reproduction of the real detector situation significantly by combining simulated events with measured background and recorded detector conditions from Minimum Bias Events. Instead of selecting the data to be analysed by the average data quality over a whole run, a preselection and lifetime calculation based on single timeframes was implemented,

Using measured background, the impact of events only triggered by hits from optical background only was simulated (see section 8.1.5), to assure that they play no role in the final event samples for the analysis. Still, it was found that their contribution to the triggered events and reconstructed events before quality cuts is significant.

10.5 Physics Analysis

Using the data taken in December 2010, the neutrino flux around the vertical upward direction was analysed for a possible excess from emission of neutrinos in the annihilation of Dark Matter accumulated at the Earth's core. Based on published flux calculation results with WimpSim [117], the expected neutrino events for a given rate of annihilations were modelled using the atmospheric neutrino MC, by assigning additional event weights corresponding to the expected flux from Dark Matter annihilations. The prediction was simulated for a series of WIMP masses and annihilation channels, assuming the WIMPs to annihilate exclusively into the given channel. With the shape and expected signal depending on the WIMP mass and the annihilation channel, a Model Rejection Factor optimisation was performed to find the best search cone cut for each combination of them. With the number of events matching the expectation from background within the statistical uncertainty for all cases, a limit on

the annihilation rate in Earth for the simulated channels and WIMP masses was derived, and also translated into a limit on an integrated neutrino flux at the Earth's surface. This limit obtained from a single month of data demonstrates the feasibility of the analysis procedure, and an extension to the full repertory of data taken by ANTARES would be possible. To rate the potential of an analysis comprising five years of data, a sensitivity estimation from multiplying the signal and background estimation of the analysed month by 60. This sensitivity is revealed to come close to a representative theoretical prediction of the WIMP capture rate, indicating that the concept of searching for neutrinos from Dark Matter annihilation in Earth can reach the relevant sensitivity range.

Appendix A

Runlist

MC-Set	trig Data	trig MC	ratio	BB data	BB MC	ratio
1	1061266	868305.963	1.222	116508	71006.964	1.641
run	start	stop	duration	lifetime	avg rate	
053543	01 00:44:30	01 02:46:35	7325.0	7235.9084032	56.745	
053545	01 02:48:19	01 04:48:41	7222.0	6903.1952384	57.991	
053547	01 04:50:08	01 06:32:13	6125.0	6031.7237248	61.539	
053548	01 06:33:38	01 08:00:15	5197.0	5121.5597568	64.704	
053550	01 08:19:41	01 10:46:57	8836.0	8745.3335552	63.651	
053552	01 10:50:00	01 13:29:48	9588.0	9465.495552	59.852	
053553	01 13:31:17	01 16:24:10	10373.0	10285.2722688	56.588	
053555	01 16:26:14	01 19:17:32	10278.0	10185.7624064	57.245	
053557	01 19:19:10	01 22:15:51	10601.0	10512.0792576	56.759	
053559	01 22:18:00	02 01:19:46	10906.0	10813.5448576	55.720	
053561	02 01:21:15	02 04:25:54	11079.0	10988.3424768	55.648	
053563	02 04:28:02	02 07:23:12	10510.0	10417.8122752	57.033	
053565	02 07:24:49	02 08:29:37	3888.0	3796.9985536	57.903	
053568	02 09:01:56	02 10:53:59	6723.0	6634.2354944	57.689	
053570	02 10:55:23	02 12:50:11	6888.0	6797.39392	57.134	
053595	03 17:00:05	03 18:31:42	5497.0	5396.1818112	56.643	

MC-Set	trig Data	trig MC	ratio	BB data	BB MC	ratio
2	1054287	638058.027	1.652	119153	69643.813	1.711
run	start	stop	duration	lifetime	avg rate	
053571	02 12:51:39	02 14:52:51	7272.0	7184.318464	55.591	
053573	02 14:57:29	02 16:45:47	6498.0	6409.2110848	55.494	
053575	02 16:59:14	02 19:01:20	7326.0	7142.6899968	55.738	
053576	02 19:02:45	02 21:01:18	7113.0	7025.8786304	56.363	
053578	02 21:02:49	02 22:59:01	6972.0	6662.4421888	57.957	
053580	02 23:03:31	03 00:51:01	6450.0	6358.8794368	59.397	
053581	03 00:53:39	03 02:43:02	6563.0	6471.7062144	59.586	
053583	03 02:45:15	03 04:41:49	6994.0	6804.6290944	57.727	
053584	03 04:43:47	03 06:44:41	7254.0	7166.1780992	55.816	
053586	03 06:46:46	03 08:50:24	7418.0	7325.876224	55.207	
053588	03 08:52:23	03 10:34:22	6119.0	5981.8115072	55.034	
053589	03 10:44:13	03 12:45:51	7298.0	7215.4611712	54.918	
053592	03 12:47:17	03 14:50:30	7393.0	7217.2437504	55.001	
053594	03 14:53:41	03 16:55:30	7309.0	7217.2437504	55.437	
053597	03 18:40:26	03 20:37:27	7021.0	6918.0850176	56.523	
053600	03 21:11:04	03 23:12:16	7272.0	7189.4564864	56.096	
053601	03 23:13:44	04 01:19:08	7524.0	7340.032	55.241	
053603	04 01:20:32	04 03:28:00	7648.0	7466.5951232	54.820	
MC-Set	trig Data	trig MC	ratio	BB data	BB MC	ratio
3	1074496	668828.006	1.607	120541	72308.065	1.667
run	start	stop	duration	lifetime	avg rate	
053605	04 03:31:08	04 05:36:50	7542.0	7416.3683328	54.642	
053607	04 05:38:30	04 07:42:00	7410.0	7322.5207808	54.728	
053608	04 07:43:28	04 09:45:28	7320.0	7192.0779264	55.024	
053610	04 09:47:03	04 11:44:25	7042.0	6953.8414592	55.810	
053612	04 11:45:57	04 13:47:10	7273.0	7071.9111168	55.936	
053613	04 13:48:39	04 15:47:43	7144.0	7055.5533312	55.972	
053615	04 15:49:24	04 17:50:14	7250.0	7162.1935104	55.562	
053617	04 17:52:29	04 19:54:40	7331.0	7239.368704	55.166	
053618	04 19:58:00	04 21:59:36	7296.0	7204.8705536	55.637	
053620	04 22:02:16	05 00:01:15	7139.0	7048.1084416	56.153	
053622	05 00:02:44	05 02:03:50	7266.0	7131.9945216	56.258	
053623	05 02:08:28	05 04:13:06	7478.0	7261.4936576	55.726	
053625	05 04:14:35	05 06:18:09	7414.0	7289.4906368	55.462	
053627	05 06:19:34	05 08:21:47	7333.0	7244.087296	55.907	
053628	05 08:23:54	05 10:26:31	7357.0	7194.0702208	55.587	
053631	05 10:40:13	05 12:40:21	7208.0	7121.6136192	55.448	
053633	05 12:42:03	05 14:42:14	7211.0	7113.9590144	55.697	
053635	05 14:43:46	05 16:43:29	7183.0	7094.0360704	56.084	

MC-Set	trig Data	trig MC	ratio	BB data	BB MC	ratio
4	1020432	655759.626	1.556	111212	70596.513	1.575
run	start	stop	duration	lifetime	avg rate	
053637	05 16:44:52	05 18:41:46	7014.0	6831.7872128	57.077	
053639	05 18:45:00	05 20:39:21	6861.0	6768.2435072	57.788	
053641	05 20:47:39	05 22:42:37	6898.0	6760.9034752	57.880	
053642	05 22:44:42	06 00:42:27	7065.0	6866.3902208	57.335	
053644	06 00:43:59	06 02:45:03	7264.0	7175.929856	56.509	
053646	06 02:46:34	06 04:44:48	7094.0	7005.536256	57.182	
053647	06 04:48:00	06 06:40:09	6729.0	6601.6247808	58.527	
053649	06 06:42:09	06 08:31:20	6551.0	6424.3105792	59.092	
053651	06 08:32:44	06 10:14:14	6090.0	6002.1538816	60.230	
053654	06 10:28:51	06 12:11:02	6131.0	6013.2687872	59.614	
053656	06 12:12:27	06 14:01:54	6567.0	6388.2395648	58.433	
053657	06 14:03:20	06 15:54:24	6664.0	6552.3417088	58.331	
053660	06 15:55:49	06 17:45:05	6556.0	6464.2613248	58.917	
053662	06 17:46:32	06 19:39:17	6765.0	6639.8978048	58.446	
053664	06 19:41:21	06 21:42:34	7273.0	7035.2109568	56.660	
053665	06 21:43:59	06 23:45:44	7305.0	6992.1144832	56.672	
053667	06 23:48:56	07 01:45:22	6986.0	6893.6531968	57.693	
053669	07 01:46:57	07 03:39:55	6778.0	6689.8100224	58.867	
053670	07 03:41:58	07 05:39:38	7060.0	6826.5443328	57.865	
MC-Set	trig Data	trig MC	ratio	BB data	BB MC	ratio
5	556769	355427.744	1.566	60617	38612.722	1.570
run	start	stop	duration	lifetime	avg rate	
053672	07 05:41:14	07 07:40:43	7169.0	7080.6142976	56.382	
053674	07 07:43:57	07 09:43:18	7161.0	7071.596544	56.231	
053675	07 09:44:51	07 11:43:41	7130.0	7035.7352448	55.919	
053677	07 11:45:25	07 13:45:13	7188.0	7064.5710848	55.890	
053679	07 13:46:34	07 15:43:09	6995.0	6904.348672	57.264	
053680	07 15:46:16	07 17:37:52	6696.0	6608.0210944	58.402	
053682	07 17:39:21	07 19:33:36	6855.0	6762.8957696	57.462	
053683	07 19:38:51	07 21:41:43	7372.0	7063.3127936	56.914	
053685	07 21:43:46	07 23:39:13	6927.0	6834.618368	58.052	
053687	07 23:40:45	08 01:26:32	6347.0	6093.6945664	62.297	

MC-Set	trig Data	trig MC	ratio	BB data	BB MC	ratio
6	979891	610263.155	1.606	101434	59295.259	1.711
run	start	stop	duration	lifetime	avg rate	
053688	08 01:28:05	08 03:20:38	6753.0	6675.4445312	59.347	
053690	08 03:25:48	08 05:13:33	6465.0	6388.0298496	60.008	
053692	08 05:14:57	08 06:57:54	6177.0	6094.4285696	60.714	
053693	08 07:02:54	08 08:49:24	6390.0	6292.1900032	59.880	
053695	08 08:50:57	08 10:28:43	5866.0	5681.0799104	60.292	
053696	08 10:37:29	08 12:20:00	6151.0	6071.8841856	60.642	
053698	08 12:22:17	08 13:59:38	5841.0	5708.6574592	62.697	
053700	08 14:01:38	08 15:35:18	5620.0	5498.732544	64.061	
053701	08 15:37:55	08 17:08:58	5463.0	5370.1771264	64.761	
053703	08 17:11:16	08 18:44:26	5590.0	5463.7101056	64.001	
053704	08 18:46:26	08 20:14:11	5265.0	5170.3185408	65.104	
053706	08 20:17:21	08 21:43:29	5168.0	5075.4224128	65.387	
053708	08 22:03:04	09 00:27:10	8646.0	8564.0347648	67.661	
053710	09 00:28:38	09 02:59:39	9061.0	8975.9154176	68.167	
053712	09 03:03:10	09 05:31:50	8920.0	8829.4293504	67.374	
053714	09 05:33:21	09 07:53:30	8409.0	8316.0465408	67.736	
053715	09 07:56:38	09 10:07:35	7857.0	7730.8362752	69.048	
053718	09 10:09:12	09 12:18:29	7757.0	7573.5498752	69.916	
053719	09 12:23:38	09 14:29:46	7568.0	7428.2172416	72.043	
MC-Set	trig Data	trig MC	ratio	BB data	BB MC	ratio
7	948783	565981.928	1.676	93111	51146.818	1.820
run	start	stop	duration	lifetime	avg rate	
053722	09 15:10:24	09 18:05:41	10517.0	10425.991168	75.690	
053724	09 18:07:45	09 21:07:48	10803.0	10647.6601344	71.638	
053726	09 21:12:24	10 00:14:39	10935.0	10848.567296	69.281	
053728	10 00:16:44	10 03:18:15	10891.0	10799.7036544	70.491	
053730	10 03:19:56	10 06:20:08	10812.0	10719.2778752	72.345	
053732	10 06:22:18	10 09:19:07	10609.0	10297.7503232	71.366	
053734	10 09:36:13	10 12:37:58	10905.0	10813.964288	69.124	
053736	10 12:39:23	10 15:41:26	10923.0	10835.984384	68.563	
053739	10 15:43:20	10 18:48:04	11084.0	10901.520384	67.336	
053741	10 18:49:50	10 21:52:40	10970.0	10845.3167104	68.469	
053743	10 21:54:14	11 00:56:36	10942.0	10854.2296064	68.061	
053745	11 00:58:11	11 04:00:41	10950.0	10860.101632	68.234	

MC-Set	trig Data	trig MC	ratio	BB data	BB MC	ratio
8	1004434	629725.207	1.595	106698	65201.252	1.636
run	start	stop	duration	lifetime	avg rate	
053747	11 04:02:59	11 07:08:49	11150.0	11061.2185088	64.916	
053749	11 07:10:18	11 10:15:43	11125.0	10917.6684544	64.092	
053751	11 10:18:59	11 12:44:03	8704.0	8621.4967296	65.272	
053753	11 12:45:30	11 15:11:30	8760.0	8638.2739456	66.525	
053755	11 15:13:03	11 17:39:04	8761.0	8674.1352448	66.294	
053756	11 17:42:20	11 20:07:02	8682.0	8548.7255552	64.991	
053758	11 20:18:47	11 22:51:43	9176.0	9086.435328	65.107	
053760	11 22:53:05	12 01:33:47	9642.0	9555.9876608	64.135	
053762	12 01:35:15	12 04:25:21	10206.0	10118.0243968	61.219	
053764	12 04:27:20	12 07:12:54	9934.0	9841.6197632	60.226	
053766	12 07:14:20	12 09:54:31	9611.0	9409.5015936	60.914	
053768	12 09:56:02	12 12:25:58	8996.0	8903.8782464	63.441	
053770	12 12:29:05	12 15:00:02	9057.0	8967.3170944	64.721	
053775	12 20:33:52	12 22:59:40	8748.0	4360.6081536	58.624	
MC-Set	trig Data	trig MC	ratio	BB data	BB MC	ratio
9	767742	418828.802	1.833	85289	45352.967	1.881
run	start	stop	duration	lifetime	avg rate	
053772	12 15:01:21	12 17:40:20	9539.0	9450.815488	62.194	
053773	12 17:42:13	12 20:32:25	10212.0	10126.2032896	59.297	
053777	12 23:17:35	13 02:14:28	10613.0	10528.3321856	59.921	
053779	13 02:16:23	13 05:08:01	10298.0	10221.3091328	60.581	
053781	13 05:09:56	13 07:56:17	9981.0	9889.7494016	60.293	
053783	13 07:58:05	13 10:42:13	9848.0	9762.6619904	59.189	
053785	13 10:43:37	13 13:30:58	10041.0	9946.267648	58.922	
053787	13 13:32:22	13 15:50:10	8268.0	8084.6258176	59.230	
053804	13 20:06:28	13 22:13:29	7621.0	7528.4611072	59.476	
053806	13 22:20:12	14 00:10:40	6628.0	6547.308544	58.895	

MC-Set	trig Data	trig MC	ratio	BB data	BB MC	ratio
10	1071671	691971.013	1.549	117530	69769.960	1.685
run	start	stop	duration	lifetime	avg rate	
053808	14 00:12:41	14 02:06:10	6809.0	6724.0984576	58.585	
053809	14 02:07:40	14 03:58:31	6651.0	6558.0040192	58.866	
053811	14 04:00:25	14 05:46:15	6350.0	6226.5491456	59.819	
053813	14 05:47:38	14 07:29:47	6129.0	6039.6929024	60.462	
053814	14 07:31:10	14 08:49:06	4676.0	4545.1575296	61.714	
053816	14 08:53:29	14 13:24:09	16240.0	11336.155136	61.794	
053818	14 13:32:20	14 15:18:38	6378.0	6294.1822976	59.834	
053819	14 15:20:43	14 17:08:46	6483.0	6406.1702144	59.136	
053820	14 17:10:08	14 19:01:10	6662.0	6564.1906176	58.454	
053822	14 19:03:15	14 20:53:45	6630.0	6503.8974976	59.121	
053823	14 20:55:41	14 22:34:07	5906.0	5813.5150592	61.929	
053825	14 22:35:31	14 23:30:54	3323.0	3144.2599936	64.420	
053826	14 23:42:34	15 02:22:50	9616.0	9446.2017536	65.825	
053828	15 02:24:12	15 05:08:37	9865.0	9772.6234624	62.950	
053830	15 05:10:18	15 07:56:45	9987.0	9899.9205888	60.123	
053832	15 07:58:09	15 10:43:31	9922.0	9833.8603008	58.965	
053834	15 10:45:30	15 13:25:01	9571.0	9444.2094592	61.612	
053836	15 13:27:15	15 14:50:20	4985.0	4882.9038592	64.158	
MC-Set	trig Data	trig MC	ratio	BB data	BB MC	ratio
11	675838	455828.760	1.483	71138	42826.589	1.661
run	start	stop	duration	lifetime	avg rate	
053856	15 18:38:19	15 20:10:37	5538.0	5464.129536	62.783	
053857	15 20:12:07	15 21:55:55	6228.0	6144.0262144	59.916	
053859	15 21:57:53	15 23:47:22	6569.0	6483.7648384	58.484	
053860	15 23:48:54	16 01:40:01	6667.0	6571.3209344	58.554	
053862	16 01:41:59	16 03:23:57	6118.0	5994.4992768	60.879	
053863	16 03:25:21	16 04:58:33	5592.0	5391.8826496	63.280	
053865	16 05:00:04	16 06:26:24	5180.0	5087.9004672	64.965	
053866	16 06:27:48	16 07:47:41	4793.0	4704.5410816	66.448	
053868	16 07:49:39	16 09:00:39	4260.0	4170.2916096	68.713	
053900	16 15:11:46	16 16:42:17	5431.0	5378.146304	62.689	
053901	16 16:43:42	16 18:12:35	5333.0	5278.007296	63.477	
053903	16 18:13:55	16 19:37:09	4994.0	4940.4706816	65.454	
053905	16 19:52:15	16 21:01:30	4155.0	4098.0447232	68.370	
053907	16 21:06:59	16 23:11:42	7483.0	7421.6112128	71.926	
053909	16 23:13:11	17 01:30:46	8255.0	8199.6546048	71.393	

MC-Set	trig Data	trig MC	ratio	BB data	BB MC	ratio
12	956968	663580.413	1.442	94272	57167.981	1.649
run	start	stop	duration	lifetime	avg rate	
053910	17 01:32:08	17 04:00:56	8928.0	8867.9120896	68.324	
053912	17 04:02:39	17 06:31:41	8942.0	8870.2189568	66.275	
053914	17 06:33:08	17 09:00:35	8847.0	8794.406912	64.534	
053916	17 09:02:11	17 11:12:53	7842.0	7769.3190144	67.676	
053917	17 11:14:14	17 13:25:44	7890.0	7837.581312	69.484	
053919	17 13:27:07	17 15:35:20	7693.0	7638.7713024	71.656	
053927	17 16:58:01	17 18:48:43	6642.0	6560.940032	75.440	
053928	17 18:50:10	17 20:54:22	7452.0	7384.1770496	73.543	
053930	17 20:55:42	17 22:48:52	6790.0	6729.4461952	75.204	
053932	17 22:50:13	18 00:58:49	7716.0	7654.4999424	73.259	
053933	18 01:00:17	18 03:21:16	8459.0	8392.1731584	71.104	
053935	18 03:22:59	18 05:31:40	7721.0	7668.0265728	72.359	
053937	18 05:33:02	18 07:40:44	7662.0	7588.4396544	71.231	
053938	18 07:42:25	18 09:36:19	6834.0	6773.5912448	72.872	
053940	18 09:37:42	18 11:29:29	6707.0	6634.1306368	73.360	
053942	18 11:30:54	18 13:24:12	6798.0	6737.7299456	74.458	
053943	18 13:25:35	18 15:30:08	7473.0	7399.800832	73.151	

MC-Set	trig Data	trig MC	ratio	BB data	BB MC	ratio
13	904157	668614.098	1.352	85796	53620.208	1.600
run	start	stop	duration	lifetime	avg rate	
053945	18 15:31:33	18 17:34:15	7362.0	7301.758976	71.856	
053948	18 18:47:03	18 20:53:04	7561.0	7496.8989696	72.449	
053950	18 20:54:25	18 22:58:41	7456.0	7402.422272	71.968	
053952	18 23:00:02	19 01:21:40	8498.0	8438.3105024	69.091	
053953	19 01:23:11	19 03:42:43	8372.0	8311.6425216	70.607	
053955	19 03:44:12	19 05:48:17	7445.0	7392.2510848	73.921	
053957	19 05:49:37	19 07:37:48	6491.0	6418.333696	76.874	
053958	19 07:39:23	19 09:15:28	5765.0	5691.3559552	78.377	
053960	19 09:19:55	19 12:14:54	10499.0	10427.564032	77.730	
053964	19 13:18:01	19 15:14:40	6999.0	6946.1868544	75.737	
053966	19 15:16:07	19 17:21:46	7539.0	7470.6845696	71.094	
053968	19 17:23:07	19 19:45:07	8520.0	8458.6528768	67.394	
053969	19 19:46:31	19 22:08:22	8511.0	8434.0113408	68.039	
053971	19 22:10:01	20 00:10:48	7247.0	7180.0193024	75.186	
053973	20 00:12:18	20 01:58:34	6376.0	6321.9695616	81.992	
053974	20 01:59:56	20 03:36:22	5786.0	5727.322112	85.034	
053976	20 03:37:44	20 05:04:31	5207.0	5151.7587456	86.139	
053977	20 05:05:58	20 06:26:31	4833.0	4779.933696	87.029	

MC-Set	trig Data	trig MC	ratio	BB data	BB MC	ratio
14	1007374	725480.441	1.389	103322	62244.309	1.660
run	start	stop	duration	lifetime	avg rate	
054031	21 21:26:19	22 00:16:57	10238.0	10156.4022784	75.660	
054033	22 00:21:41	22 02:19:18	7057.0	6995.9942144	77.365	
054034	22 02:20:37	22 04:09:01	6504.0	6443.0800896	79.630	
054036	22 04:13:18	22 06:00:50	6452.0	6381.109248	77.980	
054037	22 06:02:12	22 07:56:07	6835.0	6773.80096	74.754	
054039	22 07:57:28	22 09:49:28	6720.0	6648.7058432	72.611	
054041	22 09:55:47	22 11:52:39	7012.0	6958.5600512	72.379	
054043	22 12:05:37	22 13:55:27	6590.0	6528.2244608	73.909	
054045	22 13:56:46	22 16:03:08	7582.0	7518.1850624	70.989	
054047	22 16:06:17	22 18:20:31	8054.0	7994.0288512	68.164	
054049	22 18:21:52	22 19:41:21	4769.0	4706.7430912	65.915	
054050	22 19:43:53	22 21:12:17	5304.0	5245.8160128	64.808	
054052	22 21:13:39	22 22:40:37	5218.0	5164.8659456	65.245	
054053	22 22:41:59	23 00:09:05	5226.0	5172.8351232	65.999	
054054	23 00:10:27	23 01:36:32	5165.0	5111.5982848	66.452	
054056	23 01:37:54	23 03:02:11	5057.0	4988.076032	66.746	
054057	23 03:03:33	23 04:25:23	4910.0	4842.5336832	66.459	
054059	23 04:26:47	23 05:53:43	5216.0	5146.411008	65.112	
054060	23 05:55:05	23 07:27:31	5546.0	5465.4926848	63.628	
054062	23 07:28:53	23 09:02:36	5623.0	5549.6933376	63.326	
054063	23 09:03:58	23 10:34:29	5431.0	5377.9365888	63.653	

MC-Set	trig Data	trig MC	ratio	BB data	BB MC	ratio
15	996817	656499.120	1.518	105248	62709.416	1.678
run	start	stop	duration	lifetime	avg rate	
054065	23 10:35:52	23 12:04:37	5325.0	5252.0026112	64.265	
054066	23 12:06:00	23 13:32:15	5175.0	5113.380864	65.157	
054088	23 16:32:03	23 18:06:37	5674.0	5612.6078976	62.892	
054089	23 18:07:59	23 19:50:44	6165.0	6104.0754688	61.114	
054091	23 19:52:07	23 21:38:03	6356.0	6294.7065856	60.204	
054093	23 21:39:25	23 23:28:46	6561.0	6500.0177664	59.474	
054094	23 23:30:08	24 01:20:11	6603.0	6548.4619776	60.147	
054096	24 01:21:33	24 03:02:56	6083.0	6010.3327744	62.173	
054097	24 03:04:18	24 04:37:41	5603.0	5541.5144448	63.907	
054099	24 04:39:21	24 06:04:47	5126.0	5051.6197376	65.779	
054100	24 06:06:11	24 07:33:20	5229.0	5168.431104	64.995	
054102	24 07:34:42	24 09:10:33	5751.0	5690.5170944	61.929	
054103	24 09:11:54	24 10:54:20	6146.0	6092.750848	60.401	
054105	24 10:55:39	24 12:41:09	6330.0	6262.4104448	59.988	
054107	24 12:42:31	24 14:29:31	6420.0	6358.7745792	59.584	
054108	24 14:56:35	24 16:42:03	6328.0	6273.8399232	60.100	
054110	24 16:43:11	24 18:25:31	6140.0	6086.8788224	61.097	
054111	24 18:26:41	24 20:06:09	5968.0	5907.4674688	62.444	
054113	24 20:07:18	24 21:49:09	6111.0	6039.0637568	61.928	
054115	24 21:53:27	24 23:28:20	5693.0	5628.0219648	60.606	
054116	24 23:33:38	25 01:21:11	6453.0	6384.5695488	60.232	

MC-Set	trig Data	trig MC	ratio	BB data	BB MC	ratio
16	853194	630828.850	1.352	76704	50139.599	1.530
run	start	stop	duration	lifetime	avg rate	
053980	20 06:54:46	20 09:49:18	10472.0	10412.2548224	77.795	
053983	20 09:50:40	20 12:50:09	10769.0	10701.0326528	69.528	
053986	20 13:03:27	20 15:14:20	7853.0	7781.6922112	71.159	
053988	20 15:15:42	20 17:00:37	6295.0	6242.0680704	76.413	
053997	20 17:49:03	20 20:39:21	10218.0	9911.4549248	87.363	
053999	20 20:40:42	20 23:26:07	9925.0	9863.8495744	88.791	
054001	20 23:27:49	21 02:19:33	10304.0	10234.2066176	81.443	
054003	21 02:20:56	21 05:16:30	10534.0	10473.8062336	76.923	
054005	21 05:17:57	21 08:15:18	10641.0	10568.073216	75.163	
054007	21 08:16:40	21 11:00:02	9802.0	9743.2633344	82.513	
054009	21 11:05:39	21 13:54:44	10145.0	9713.3789184	89.447	
054027	21 15:49:10	21 18:32:42	9812.0	9749.3450752	86.674	
054029	21 18:34:04	21 21:24:57	10253.0	10183.770112	80.080	
054124	25 08:20:47	25 09:20:44	3597.0	3533.8059776	72.680	
MC-Set	trig Data	trig MC	ratio	BB data	BB MC	ratio
17	848947	582808.820	1.457	79207	48199.655	1.643
run	start	stop	duration	lifetime	avg rate	
054118	25 01:22:20	25 03:11:34	6554.0	6493.9360256	59.636	
054119	25 03:12:43	25 05:03:05	6622.0	6553.7048576	59.196	
054121	25 05:04:34	25 06:49:13	6279.0	6226.0248576	60.169	
054123	25 06:50:21	25 08:19:38	5357.0	5303.9071232	63.941	
054125	25 09:23:57	25 10:57:11	5594.0	5523.7935104	78.796	
054127	25 10:59:28	25 13:51:55	10347.0	10277.4079488	79.856	
054129	25 13:53:04	25 16:52:23	10759.0	10686.8768768	71.856	
054131	25 16:54:47	25 19:16:51	8524.0	8455.192576	67.742	
054133	25 19:18:02	25 21:20:04	7322.0	7259.7110784	73.851	
054135	25 21:22:10	26 00:12:56	10246.0	10185.5526912	81.556	
054136	26 00:14:05	26 03:00:38	9993.0	9939.6616192	87.065	
054138	26 03:01:46	26 05:44:34	9768.0	9656.1266688	92.267	
054140	26 05:45:43	26 08:28:04	9741.0	9584.1943552	92.897	
054142	26 08:29:13	26 11:15:11	9958.0	9904.1148928	87.911	
054144	26 11:16:20	26 14:05:08	10128.0	10067.1684608	83.772	

MC-Set	trig Data	trig MC	ratio	BB data	BB MC	ratio
18	836638	595185.869	1.406	77423	47462.283	1.631
run	start	stop	duration	lifetime	avg rate	
054146	26 14:06:19	26 17:00:40	10461.0	10407.8508032	77.205	
054148	26 17:01:48	26 19:52:15	10227.0	10160.4917248	82.962	
054150	26 19:53:24	26 22:37:39	9855.0	9765.5980032	90.543	
054152	26 22:38:47	27 01:20:08	9681.0	9494.7508224	93.423	
054154	27 01:21:17	27 04:06:01	9884.0	9820.1239552	89.156	
054156	27 04:07:11	27 06:58:06	10255.0	10194.4655872	81.699	
054158	27 06:59:23	27 09:58:10	10727.0	10663.8082048	69.762	
054161	27 10:28:01	27 13:33:35	11134.0	11063.9448064	66.011	
054163	27 13:34:44	27 16:33:27	10723.0	10651.959296	73.798	
054165	27 16:34:35	27 19:28:40	10445.0	10383.8384128	78.373	
054167	27 19:29:48	27 22:29:35	10787.0	10709.630976	72.023	
054169	27 22:31:07	28 01:40:30	11363.0	11302.4958464	62.612	
MC-Set	trig Data	trig MC	ratio	BB data	BB MC	ratio
19	1032329	671935.726	1.536	111940	68976.885	1.623
run	start	stop	duration	lifetime	avg rate	
054171	28 01:41:40	28 04:53:11	11491.0	11430.1075456	60.376	
054173	28 04:54:17	28 08:04:38	11421.0	11360.0626688	61.295	
054175	28 08:05:49	28 11:13:18	11249.0	11174.9890048	63.434	
054177	28 11:15:39	28 12:57:06	6087.0	6016.9388032	60.316	
054179	28 12:58:12	28 14:47:40	6568.0	6496.2428928	58.654	
054181	28 14:48:46	28 16:37:48	6542.0	6469.189632	58.505	
054182	28 16:38:56	28 18:28:54	6598.0	6514.1735424	58.424	
054184	28 18:30:05	28 20:21:08	6663.0	6580.338688	58.644	
054186	28 20:22:17	28 22:11:00	6523.0	6462.373888	59.133	
054188	28 22:12:10	29 00:06:25	6855.0	6782.0847104	58.366	
054189	29 00:07:35	29 02:03:51	6976.0	6902.775808	57.837	
054191	29 02:05:00	29 04:02:42	7062.0	6995.050496	57.460	
054193	29 04:03:51	29 05:59:27	6936.0	6862.0910592	57.629	
054194	29 06:00:35	29 07:48:34	6479.0	6412.04224	59.075	
054196	29 07:49:42	29 09:25:05	5723.0	5639.766016	62.162	
054198	29 09:26:13	29 10:58:28	5535.0	5481.43104	63.655	
054199	29 10:59:36	29 12:34:51	5715.0	5654.3412224	62.676	
054201	29 12:36:00	29 14:17:18	6078.0	6023.9642624	61.349	

MC-Set	trig Data	trig MC	ratio	BB data	BB MC	ratio
20	1001013	689501.101	1.452	107643	67466.105	1.596
run	start	stop	duration	lifetime	avg rate	
054202	29 14:21:21	29 16:06:56	6335.0	6273.630208	59.290	
054204	29 16:08:05	29 17:59:05	6660.0	6606.8676608	58.571	
054205	29 18:00:14	29 19:53:10	6776.0	6715.3952768	58.498	
054207	29 19:54:21	29 21:42:16	6475.0	6402.5001984	59.299	
054209	29 21:43:25	29 23:25:00	6095.0	6021.971968	61.233	
054210	29 23:26:09	30 01:10:46	6277.0	6223.822848	60.823	
054212	30 01:11:54	30 02:57:22	6328.0	6254.0218368	60.317	
054213	30 02:58:29	30 04:46:40	6491.0	6429.868032	59.315	
054215	30 04:51:48	30 06:44:41	6773.0	6699.5617792	58.203	
054217	30 06:45:48	30 08:39:01	6793.0	6734.7939328	57.679	
054218	30 08:40:09	30 10:33:19	6790.0	6715.1855616	57.327	
054220	30 10:39:47	30 12:33:29	6822.0	6768.033792	57.469	
054222	30 12:34:37	30 14:26:46	6729.0	6662.651904	58.317	
054224	30 14:39:08	30 16:31:58	6770.0	6708.4746752	57.766	
054226	30 16:33:06	30 18:26:12	6786.0	6725.566464	58.018	
054228	30 18:27:23	30 20:22:40	6917.0	6864.0833536	57.817	
054229	30 20:23:48	30 22:20:20	6992.0	6938.427392	57.043	
054231	30 22:21:31	31 00:21:01	7170.0	7109.2404224	56.974	
054233	31 00:22:07	31 02:18:54	7007.0	6945.9771392	57.726	
MC-Set	trig Data	trig MC	ratio	BB data	BB MC	ratio
21	604753	415270.488	1.456	40987	24594.635	1.667
run	start	stop	duration	lifetime	avg rate	
054234	31 02:20:02	31 04:11:04	6662.0	6602.4636416	58.791	
054236	31 04:12:15	31 05:58:27	6372.0	6311.7983744	59.570	
054237	31 05:59:36	31 07:46:49	6433.0	6360.2425856	59.083	
054239	31 07:47:58	31 09:39:16	6678.0	6624.903168	57.814	
054241	31 09:40:25	31 11:35:02	6877.0	6823.9228928	56.858	
054242	31 11:36:11	31 13:33:17	7026.0	6973.554688	56.567	
054244	31 13:34:26	31 15:28:12	6826.0	6765.7269248	57.926	
054246	31 15:29:20	31 17:17:29	6489.0	6416.1316864	59.281	
054247	31 17:18:38	31 19:00:18	6100.0	6037.700608	61.095	
054249	31 19:01:26	31 20:44:29	6183.0	6110.2620672	60.640	
054250	31 20:45:35	31 22:29:39	6244.0	6185.6546816	60.328	
054252	31 22:30:48	01 00:20:16	6568.0	6508.6160896	59.309	

Appendix B

Simulated Annealing Fit PDF

$$(\Delta t, b, c, d, e) = a \cdot \Phi(\Delta t, b, c) + d \cdot \exp\left(\frac{-\Delta t^2}{2e}\right)$$

	<i>a</i>	<i>b</i>	<i>c</i>	<i>d</i>	<i>e</i>
$-1.0 < \ln(\text{amp}) < -0.5$	$8.259 \cdot 10^{-2}$	$5.512 \cdot 10^0$	$3.366 \cdot 10^0$	$3.500 \cdot 10^{-2}$	$4.116 \cdot 10^0$
$-0.5 < \ln(\text{amp}) < 0.0$	$8.220 \cdot 10^{-2}$	$5.514 \cdot 10^0$	$3.378 \cdot 10^0$	$3.500 \cdot 10^{-2}$	$4.141 \cdot 10^0$
$0.0 < \ln(\text{amp}) < 0.5$	$8.233 \cdot 10^{-2}$	$5.246 \cdot 10^0$	$3.174 \cdot 10^0$	$4.000 \cdot 10^{-2}$	$3.972 \cdot 10^0$
$0.5 < \ln(\text{amp}) < 1.0$	$9.656 \cdot 10^{-2}$	$4.016 \cdot 10^0$	$1.603 \cdot 10^0$	$8.000 \cdot 10^{-2}$	$2.987 \cdot 10^0$
$1.0 < \ln(\text{amp}) < 1.5$	$4.999 \cdot 10^{-2}$	$4.701 \cdot 10^0$	$1.176 \cdot 10^0$	$1.000 \cdot 10^{-1}$	$3.161 \cdot 10^0$
$1.5 < \ln(\text{amp}) < 2.0$	$1.666 \cdot 10^{-2}$	$5.979 \cdot 10^0$	$1.304 \cdot 10^0$	$1.200 \cdot 10^{-1}$	$2.876 \cdot 10^0$
$2.0 < \ln(\text{amp}) < 2.5$	$8.228 \cdot 10^{-3}$	$6.995 \cdot 10^0$	$1.522 \cdot 10^0$	$1.300 \cdot 10^{-1}$	$2.843 \cdot 10^0$
$2.5 < \ln(\text{amp}) < 3.0$	$3.286 \cdot 10^{-3}$	$8.866 \cdot 10^0$	$1.788 \cdot 10^0$	$1.300 \cdot 10^{-1}$	$3.629 \cdot 10^0$

List of Figures

2.1	Parameters of the Concordance Model of Cosmology	11
2.2	Dark Energy measured by SN Ia	13
2.3	CMB skymap	14
2.4	Multipole spectrum of the CMB	14
2.5	Rotation Curves of Spiral Galaxies	18
3.1	Running Coupling in the Standard Model and in the MSSM	24
3.2	Feynman Graph of Proton Decay	25
4.1	Dark Matter Halo Profiles	31
4.2	Indirect Detection Scheme for the Sun	33
4.3	Indirect Detection Scheme for the Earth	34
4.4	Angular Distribution of Neutrinos Emitted by Dark Matter Annihilation in the Earth	35
5.1	Schematic drawing of the ANTARES detector	38
5.2	Computer Generated Image of an ANTARES Storey	40
5.3	Time Calibration Scheme	41
5.4	Charge Calibration AVC Spectrum	42
5.5	Walk Effect Correction Values	44
5.6	In Situ Calibration with ^{40}K	46
5.7	In Situ Calibration of Magnetic Field Measurement	48
5.8	In Situ Calibration of Tilt Measurement	49
5.9	Lineshape Schematic	50
5.10	Lineshape for different sea current velocities	51
5.11	Comparison of the Velocity as a Result from the Fit of Dif- ferent Lines	52
5.12	Deviation of a Single Hydrophone from the Fitted Lineshape	54
5.13	Comparison of sea current velocity from fitted lineshape and ADCP	54
6.1	Aart Reconstruction Effective Area for Low Energies	56

6.2	Neutrino Flux from Regions of mSugra Parameter Space . . .	58
6.3	Neutrino Flux versus m_χ with Relic Density	59
6.4	Sun's Zenith Angle Distribution	60
6.5	Expected Events versus m_χ with Relic Density	61
6.6	Expected Events versus m_χ with ANTARES Sensitivity . . .	62
6.7	Neutrino Flux versus m_χ with ANTARES Sensitivity	63
6.8	Exclusion Capability on mSugra Parameter Space	64
6.9	Comparison of ANTARES Sensitivity on Spin Independent Cross Section with Direct Detection Limits	65
6.10	Comparison of ANTARES Sensitivity on Spin Dependent Cross Section with Direct Detection Limits	66
7.1	Types of Neutrino Interactions	68
7.2	Mirror Solution for Single Line Event	70
7.3	Hit selection Efficiency	73
7.4	Hit Selection Purity	74
7.5	Hit Selection Number of Lines	75
7.6	Time vs. Height Representation of an Event	76
7.7	Efficiency of Event Classification ANN as a Function of the Cosine of the Zenith Angle	79
7.8	Energy Resolution of ANNergy	81
7.9	Simulated Annealing Final Fit PDF	84
7.10	Simulated Annealing $n_{\text{directhits}}$ Cut Parameter Distribution . .	87
7.11	Simulated Annealing Energy Cut Parameter Distribution . .	88
7.12	Simulated Annealing ω Cut Parameter Distribution	89
7.13	Simulated Annealing Fit Efficiency as a Function of Neutrino Energy	90
7.14	Simulated Annealing Fit Efficiency as a Function of Zenith Angle	91
7.15	Simulated Annealing Angular Resolution	91
8.1	Block Diagram of MC Simulation Chain and Data Processing	95
8.2	Amplitude Distribution for Selected OMs	98
8.3	Time Dependence of the Average Background Rate per OM	101
8.4	Distribution of Average Background Rate per OM	104
8.5	Distribution of Working OM Fraction	104
8.6	Distribution of Event Weights	107
8.7	Amplitude Distribution of L0 Hits after Trigger	109
8.8	Integrated Amplitude of L0 Hits after Trigger	110
8.9	Number of L0 Hits after Trigger	111
8.10	Average Amplitude of L0 Hits after Trigger	112

8.11	Amplitude Distribution of L1 hits after trigger	113
8.12	Result Type Distribution for BBFit Reconstructed Events . .	114
8.13	χ^2 Distribution for BBFit Reconstructed Events	115
8.14	Distribution of the Number of Lines Used in BBFit Recon- struction	116
8.15	Angular Distribution of BBFit Reconstructed Events before Cuts	117
8.16	Angular Distribution of BBFit Reconstructed Events after Cuts from 7.4.1	118
8.17	Energy Distribution of ANNergy Reconstructed Events with- out Cut	120
8.18	Energy Distribution of BBFit and ANNergy Reconstructed Events with Cut	121
9.1	Data-MC Comparison of Zenith Distributions for the Final Sample Before and After Neural Net Cut	125
9.2	Data-MC Comparison of the χ^2 Distribution for the Final Sample	126
9.3	χ^2 Distributions and Cuts for the Final Sample	127
9.4	Data-MC Comparison for Zenith Distribution of the Final Sample after Cuts	129
9.5	Ratio of Data to MC as a Function of the Zenith for the Final Sample after Cuts	129
9.6	Data-MC Comparison for Energy Distribution of Neutrino Events from the Final Sample after Cuts	130
9.7	Cut Parameter Distributions of the Simulated Annealing Fit for the Final Sample	132
9.8	ω Distribution and Cut for the Final Sample	133
9.9	Zenith Distribution of the Simulated Annealing Fit for the Final Sample	134
9.10	Model Rejection Factor as a Function of the Search Cone for $m_{\text{DM}} = 100$ GeV, W^+W^- Channel	136
9.11	Best Model Rejection Factor for Ann. Channels and WIMP Mass	136
9.12	Optimised Search Cone (Limit) for Different Ann. Channels and WIMP Masses	137
9.13	Expected Signal for for Different Ann. Channels and WIMP Masses	138
9.14	Number of Expected and Measured Events as a Function of the Search Cone	139

9.15	Limit on Ann. Rate for Different Ann. Channels and WIMP Masses	140
9.16	Limit on Neutrino Flux for Different Ann. Channels and WIMP Masses	141
9.17	Expected Signal and the Annihilation Rate Limit as a Function of the Search Cone for $m_{\text{DM}} = 100$ GeV, W^+W^- Channel .	141
9.18	Optimised Search Cone (Sensitivity) for Different Ann. Channels and WIMP Masses	142
9.19	Sensitivity for Neutrino Flux for Different Annihilation Channels and WIMP Masses	143
9.20	Contribution of Reconstruction Algorithms to Zenith Distribution of Atmospheric Neutrinos and Muons	145
9.21	Angular Resolution for Neutrino Events	146
9.22	Efficiency of Reconstruction Algorithms as a Function of MC Neutrino Energy	147
9.23	Contribution of Reconstruction Algorithms to the Final Sample as a Function of the MC Energy	148
9.24	Zenith and Energy Distributions of the Simulated Signal Events for the $b\bar{b}$ Channel at $m_{\text{DM}} = 25$ GeV and $m_{\text{DM}} = 250$ GeV	149
9.25	Zenith and Energy Distributions of the Simulated Signal Events for the W^+W^- Channel at $m_{\text{DM}} = 100$ GeV and $m_{\text{DM}} = 250$ GeV	150

List of Tables

3.1	List of Higgs Bosons in the MSSM	21
3.2	List of Standard Model Particles and Superpartners	22
7.1	Cluster Hit Sub-Selection Parameters	72
8.1	Number of Atmospheric Muon MC Files	96
8.2	Number of Simulated Events per Muon MC File	97
8.3	Number of Atmospheric Neutrino MC Files	99
8.4	Number of Muon MC Files per MC Set	102
9.1	Number of Expected and Measured Events as a Function of the Search Cone	139

Bibliography

- [1] <http://www-sk.icrr.u-tokyo.ac.jp/sk/index-e.html>.
- [2] <http://baikalweb.jinr.ru/>.
- [3] <http://icecube.wisc.edu/>.
- [4] <http://antares.in2p3.fr/>.
- [5] R. Amanullah *et al.*, "Spectra and Light Curves of Six Type Ia Supernovae at $0.511 < z < 1.12$ and the Union2 Compilation," *Astrophys. J.*, vol. 716, pp. 712–738, 2010.
- [6] E. Komatsu *et al.*, "Seven-Year Wilkinson Microwave Anisotropy Probe (WMAP) Observations: Cosmological Interpretation," *Astrophys. J. Suppl.*, vol. 192, p. 18, 2011.
- [7] M. Hicken *et al.*, "Improved Dark Energy Constraints from 100 New CfA Supernova Type Ia Light Curves," *Astrophys. J.*, vol. 700, pp. 1097–1140, 2009.
- [8] J. Guy *et al.*, "SALT2: using distant supernovae to improve the use of Type Ia supernovae as distance indicators," *Astron. Astrophys.*, vol. 466, pp. 11–21, 2007.
- [9] M. Hamuy *et al.*, "The Absolute Luminosities of the Calan/Tololo Type Ia Supernovae," *Astron. J.*, vol. 112, p. 2391, 1996.
- [10] A. A. Penzias and R. W. Wilson, "A Measurement of Excess Antenna Temperature at 4080 Mc/s.," *ApJ*, vol. 142, pp. 419–421, July 1965.
- [11] The Planck Collaboration, "The Scientific Programme of Planck," *ArXiv Astrophysics e-prints*, Apr. 2006.
- [12] A. Challinor, "The cosmic microwave background: a theorists perspective," *Cosmology, Galaxy Formation and Astroparticle Physics on the pathway to the SKA*, 2006.

- [13] L. Verde *et al.*, "The 2dF Galaxy Redshift Survey: The bias of galaxies and the density of the Universe," *Mon. Not. Roy. Astron. Soc.*, vol. 335, p. 432, 2002.
- [14] J. R. I. Gott *et al.*, "Topology of structure in the Sloan Digital Sky Survey: model testing," *Astrophys. J.*, vol. 675, pp. 16–28, 2008.
- [15] J. R. Primack, "Dark matter and structure formation," 1997.
- [16] J. E. Kim, "Light pseudoscalars, particle physics and cosmology.," *Phys. Rep.*, vol. 150, pp. 1–177, 1987.
- [17] F. Zwicky, "On the Masses of Nebulae and of Clusters of Nebulae," *ApJ*, vol. 86, pp. 217–+, Oct. 1937.
- [18] P. Natarajan, A. Loeb, J.-P. Kneib, and I. Smail, "Constraints on the Collisional Nature of the Dark Matter from Gravitational Lensing in the Cluster A2218," *ApJ*, vol. 580, pp. L17–L20, Nov. 2002.
- [19] G. S. Shostak, "Aperture Synthesis Study of Neutral Hydrogen in NGC 2403 and NGC 4236. II. Discussion," *A&A*, vol. 24, pp. 411–+, May 1973.
- [20] M. Persic, P. Salucci, and F. Stel, "The Universal rotation curve of spiral galaxies: 1. The Dark matter connection," *Mon. Not. Roy. Astron. Soc.*, vol. 281, p. 27, 1996.
- [21] V. C. Rubin, N. Thonnard, and W. K. Ford, Jr., "Extended rotation curves of high-luminosity spiral galaxies. IV - Systematic dynamical properties, SA through SC," *ApJ*, vol. 225, pp. L107–L111, Nov. 1978.
- [22] H. Balasin and D. Grumiller, "Significant reduction of galactic dark matter by general relativity," *Int. J. Mod. Phys.*, vol. D17, pp. 475–488, 2008.
- [23] M. Milgrom, "MD or DM? Modified dynamics at low accelerations vs dark matter," 2011.
- [24] M. Milgrom, "MOND — a Pedagogical Review," *Acta Physica Polonica B*, vol. 32, pp. 3613–+, Nov. 2001.
- [25] R. H. Sanders and S. S. McGaugh, "Modified Newtonian Dynamics as an Alternative to Dark Matter," *ARA&A*, vol. 40, pp. 263–317, 2002.

- [26] D. Clowe, M. Bradač, A. H. Gonzalez, M. Markevitch, S. W. Randall, C. Jones, and D. Zaritsky, "A Direct Empirical Proof of the Existence of Dark Matter," *ApJ*, vol. 648, pp. L109–L113, Sept. 2006.
- [27] A. Signer, "Abc of SUSY," *J. Phys.*, vol. G36, p. 073002, 2009.
- [28] S. P. Martin, "A Supersymmetry Primer," 1997.
- [29] P. Gondolo *et al.*, "Darksusy: Computing supersymmetric dark matter properties numerically," *JCAP*, vol. 0407, p. 008, 2004.
- [30] A. Djouadi *et al.*, "The Minimal supersymmetric standard model: Group summary report," 1998.
- [31] J. Edsjö, E. Lundström, S. Rydbeck, and J. Sjölin, "Early search for supersymmetric dark matter models at the LHC without missing energy," *Journal of High Energy Physics*, vol. 3, pp. 54–+, Mar. 2010.
- [32] P. Langacker and M.-x. Luo, "Implications of precision electroweak experiments for $M(t)$, $\rho(0)$, $\sin^2\theta(W)$ and grand unification," *Phys. Rev.*, vol. D44, pp. 817–822, 1991.
- [33] S. Raby, "Grand Unified Theories," 2006.
- [34] K. Inoue, A. Kakuto, H. Komatsu, and S. Takeshita, "Aspects of Grand Unified Models with Softly Broken Supersymmetry," *Progress of Theoretical Physics*, vol. 68, pp. 927–946, Sept. 1982.
- [35] H. Nishino *et al.*, "Search for Proton Decay via $p \rightarrow e^+ \pi^0$ and $p \rightarrow \mu^+ \pi^0$ in a Large Water Cherenkov Detector," *Phys. Rev. Lett.*, vol. 102, p. 141801, 2009.
- [36] J. L. Feng, "Supersymmetry and cosmology," *Annals Phys.*, vol. 315, pp. 2–51, 2005.
- [37] G. Servant and T. M. P. Tait, "Is the lightest Kaluza-Klein particle a viable dark matter candidate?," *Nucl. Phys.*, vol. B650, pp. 391–419, 2003.
- [38] L. Randall and R. Sundrum, "Large Mass Hierarchy from a Small Extra Dimension," *Physical Review Letters*, vol. 83, pp. 3370–3373, Oct. 1999.
- [39] L. Randall and R. Sundrum, "An Alternative to Compactification," *Physical Review Letters*, vol. 83, pp. 4690–4693, Dec. 1999.

- [40] K. Agashe, A. Delgado, and R. Sundrum, "Grand unification in RS1," *Annals of Physics*, vol. 304, pp. 145–164, Apr. 2003.
- [41] K. Agashe and G. Servant, "Warped Unification, Proton Stability, and Dark Matter," *Physical Review Letters*, vol. 93, pp. 231805–+, Dec. 2004.
- [42] J. Engel, S. Pittel, and P. Vogel, "Nuclear physics of dark matter detection," *Int. J. Mod. Phys.*, vol. E1, pp. 1–37, 1992.
- [43] J. Engel and P. Vogel, "Spin dependent cross-sections of weakly interacting massive particles on nuclei," *Phys. Rev.*, vol. D40, pp. 3132–3135, 1989.
- [44] P. B. Cushman, "Dark matter searches: Technology and backgrounds," *Nuclear Instruments and Methods in Physics Research A*, vol. 579, pp. 437–442, Aug. 2007.
- [45] L. Baudis, "Direct Detection of Cold Dark Matter," *ArXiv e-prints*, Nov. 2007.
- [46] M. Blennow, H. Melbus, and T. Ohlsson, "Neutrinos from kaluza-klein dark matter in the sun," *Journal of Cosmology and Astroparticle Physics*, vol. 2010, no. 01, p. 018, 2010.
- [47] M. Weber and W. de Boer, "Determination of the local dark matter density in our Galaxy," *A&A*, vol. 509, pp. A25+, Jan. 2010.
- [48] W. de Boer, M. Herold, C. Sander, V. Zhukov, A. V. Gladyshev, and D. I. Kazakov, "Excess of EGRET Galactic Gamma Ray Data interpreted as Dark Matter Annihilation," *ArXiv Astrophysics e-prints*, Aug. 2004.
- [49] M. Kuhlen and D. Malyshev, "ATIC, PAMELA, HESS, and Fermi data and nearby dark matter subhalos," *Phys. Rev.*, vol. D79, p. 123517, 2009.
- [50] J. Lavalle, Q. Yuan, D. Maurin, and X. J. Bi, "Full Calculation of Clumpiness Boost factors for Antimatter Cosmic Rays in the light of Λ CDM N-body simulation results," *Astron. Astrophys.*, vol. 479, pp. 427–452, 2008.
- [51] J. Zavala, V. Springel, and M. Boylan-Kolchin, "Extragalactic gamma-ray background radiation from dark matter annihilation," *Mon. Not. Roy. Astron. Soc.*, vol. 405, p. 593, 2010.

- [52] A. H. G. Peter, "Dark matter in the solar system I: The distribution function of WIMPs at the Earth from solar capture," *Phys. Rev.*, vol. D79, p. 103531, 2009.
- [53] R. Catena and P. Ullio, "A novel determination of the local dark matter density," *J. Cosmology Astropart. Phys.*, vol. 8, pp. 4–+, Aug. 2010.
- [54] J. Edsjo and P. Gondolo, "WIMP mass determination with neutrino telescopes," *Phys. Lett.*, vol. B357, pp. 595–601, 1995.
- [55] A. Gould, "Resonant enhancements in weakly interacting massive particle capture by the earth," *ApJ*, vol. 321, pp. 571–585, Oct. 1987.
- [56] A. M. Dziewonski and D. L. Anderson, "Preliminary reference Earth model," *Physics of the Earth and Planetary Interiors*, vol. 25, pp. 297–356, June 1981.
- [57] A. H. G. Peter, "Dark matter in the solar system III: The distribution function of WIMPs at the Earth from gravitational capture," *Phys. Rev.*, vol. D79, p. 103533, 2009.
- [58] A. Gould and S. M. K. Alam, "Can Heavy WIMPS Be Captured by the Earth?," *ApJ*, vol. 549, pp. 72–75, Mar. 2001.
- [59] E. Aslanides *et al.*, "A deep sea telescope for high energy neutrinos," 1999.
- [60] J. A. Aguilar *et al.*, "ANTARES: the first undersea neutrino telescope," 2011.
- [61] <http://root.cern.ch/>.
- [62] S. Escoffier and G. Lambard, "Comparison of Dark Room and on-line computation of the hit time," 2008.
- [63] J. D. D. Zornoza, "Characterization of two photomultiplier models and study by Monte Carlo simulation of several calibration systems based on optical beacons for the ANTARES detector," 2001.
- [64] A. Kouchner, J. Aublin, E. Delanges, F. Druillolle, S. Loucatos, T. Pradier, and B. Vallage, "On the linearity response of the ARS charge channels," 2007.

- [65] G. Guillard, "Étude de la sensibilité du télescope à neutrinos ANTARES aux photons de très haute énergie - Contribution à l'étalonnage en temps du détecteur," 2010. PhD thesis at CPPM.
- [66] F. Fehr, "Systematic studies, calibration, and software development for event reconstruction and data analysis using the ANTARES deep-sea neutrino telescope," 2010. PhD thesis at ECAP.
- [67] M. Bouwhuis, "Search for gamma-ray bursts with the Antares neutrino telescope," 2009.
- [68] D. Zaborov, "Coincidence analysis in ANTARES: Potassium-40 and muons," *Phys. Atom. Nucl.*, vol. 72, pp. 1537–1542, 2009.
- [69] P. Corporation, "TCM2 Electronic Compass Module User's Manual Revision 1.09," 2002. <http://www.pnicorp.com>.
- [70] P. Vernin, "The UTM grid," 2008. internal note ANTARES-SOFT-2008-002.
- [71] A. Gleixner. private communication.
- [72] J. A. Aguilar *et al.*, "The positioning system of the antares neutrino telescope," in preparation.
- [73] D. J. L. Bailey, "Genhenv5r1: Software Documentation," 2002.
- [74] D. J. L. Bailey, "KM3 v2r1: UserGuide," 2002.
- [75] M. de Jong, "The ANTARES trigger software," 2005.
- [76] Y. Becherini, N. Cottini, and T. Stolarczyk, "Offline reconstruction and analysis software," 2006.
- [77] A. J. Heijboer, "Track Reconstruction and Point Source Searches with ANTARES," 2004. PhD thesis at NIKHEF.
- [78] G. Lim and H. Motz, "The ANTARES Neutrino Effective Area in the Low-Energy Regime and Sensitivity of ANTARES to mSugra Dark Matter," 2008. internal note ANTARES-PHYS-2008-007.
- [79] G. Lim, "Indirect search for Dark Matter with the ANTARES neutrino telescope," 2007.

- [80] A. B. Lahanas and V. C. Spanos, "Implications of the pseudo-scalar higgs boson in determining the neutralino dark matter," *Eur. Phys. J.*, vol. C23, pp. 185–190, 2002.
- [81] J. R. Ellis, T. Falk, K. A. Olive, and M. Srednicki, "Calculations of neutralino stau coannihilation channels and the cosmologically relevant region of mssm parameter space," *Astropart. Phys.*, vol. 13, pp. 181–213, 2000.
- [82] J. L. Feng, K. T. Matchev, and T. Moroi, "Focus points and naturalness in supersymmetry," *Phys. Rev.*, vol. D61, p. 075005, 2000.
- [83] E. A. Baltz and P. Gondolo, "Markov chain monte carlo exploration of minimal supergravity with implications for dark matter," *JHEP*, vol. 10, p. 052, 2004.
- [84] F. E. Paige, S. D. Protopescu, H. Baer, and X. Tata, "Isajet 7.69: A monte carlo event generator for p p, anti-p p, and e+ e- reactions," 2003.
- [85] D. N. Spergel *et al.*, "First year wilkinson microwave anisotropy probe (wmap) observations: Determination of cosmological parameters," *Astrophys. J. Suppl.*, vol. 148, p. 175, 2003.
- [86] J. F. Navarro, C. S. Frenk, and S. D. M. White, "A universal density profile from hierarchical clustering," *Astrophys. J.*, vol. 490, pp. 493–508, 1997.
- [87] T. Sjostrand *et al.*, "High-energy-physics event generation with pythia 6.1," *Comput. Phys. Commun.*, vol. 135, pp. 238–259, 2001.
- [88] L. Wolfenstein, "Neutrino oscillations in matter," *Phys. Rev.*, vol. D17, p. 2369, 1978.
- [89] T. Ohlsson and H. Snellman, "Three flavor neutrino oscillations in matter," *J. Math. Phys.*, vol. 41, pp. 2768–2788, 2000.
- [90] M. Maltoni, T. Schwetz, M. A. Tortola, and J. W. F. Valle, "Status of global fits to neutrino oscillations," *New J. Phys.*, vol. 6, p. 122, 2004.
- [91] G. J. Feldman and R. D. Cousins, "Unified approach to the classical statistical analysis of small signals," *Phys. Rev. D*, vol. 57, pp. 3873–3889, Apr. 1998.

- [92] W. Frati, T. K. Gaisser, A. K. Mann, and T. Stanev, "Atmospheric neutrino data and neutrino oscillations," *Phys. Rev. D*, vol. 48, pp. 1140–1149, Aug 1993.
- [93] M. Honda, T. Kajita, K. Kasahara, and S. Midorikawa, "Calculation of the flux of atmospheric neutrinos," *Phys. Rev. D*, vol. 52, pp. 4985–5005, Nov 1995.
- [94] J. Filipini, R. Gaitskel, V. Mandic, and D. Speller, "Dark matter limit plot generator," <http://cedar.berkeley.edu/plotter/>.
- [95] S. Desai *et al.*, "Search for dark matter WIMPs using upward through-going muons in Super-Kamiokande," *Phys. Rev.*, vol. D70, p. 083523, 2004.
- [96] R. Abbasi *et al.*, "Limits on a muon flux from neutralino annihilations in the Sun with the IceCube 22-string detector," *Phys. Rev. Lett.*, vol. 102, p. 201302, 2009.
- [97] G. Wikstrom, "A Search for solar dark matter with the IceCube neutrino telescope," PhD thesis at the University of Stockholm.
- [98] B. Hartmann, "Reconstruction of neutrino induced hadronic and electromagnetic showers with the ANTARES experiment," 2006. PhD thesis.
- [99] Y. Becherini, A. Margiotta, M. Sioli, and M. Spurio, "A parameterisation of single and multiple muons in the deep water or ice," *Astropart. Phys.*, vol. 25, pp. 1–13, 2006.
- [100] T. Eberl and C. Kopper, "The SeaTray software framework," 2009. internal note ANTARES-SOFT-2009-013.
- [101] T. DeYoung, "IceTray: A software framework for IceCube," Prepared for Computing in High-Energy Physics (CHEP'04), Interlaken, Switzerland, 27 Sep - 1 Oct 2004.
- [102] D. Abrahams, "Boost.Python." <http://www.boost.org>.
- [103] J. A. Aguilar *et al.*, "A Fast Algorithm for Muon Track Reconstruction and its Application to the ANTARES Neutrino Telescope," *Astropart. Phys.*, vol. 34, pp. 652–662, 2011.
- [104] S. Galata, "The BBfit reconstruction with full detector geometry in Seatray," 2010. internal note ANTARES-SOFT-2010-005.

- [105] K. Geyer, "Ereignisklassifikation mit Hilfe von Neuronalen Netzen für das ANTARES Neutrino-Teleskop," 2010. diploma thesis at ECAP.
- [106] J. Schnabel, "Muon Energy Reconstruction for the Neutrino Telescope ANTARES using Neural Networks," 2010. diploma thesis at ECAP.
- [107] R. Auer, "Reconstruction Strategy for Hadronic Shower Detection with the ANTARES Detector," 2005. diploma thesis.
- [108] K. S. Kolbig and B. Schorr, "A PROGRAM PACKAGE FOR THE LANDAU DISTRIBUTION," *Comput. Phys. Commun.*, vol. 31, pp. 97–111, 1984.
- [109] J. Wentz *et al.*, "Simulation of atmospheric muon and neutrino fluxes with CORSIKA," *Phys. Rev.*, vol. D67, p. 073020, 2003.
- [110] P. Antonioli, C. Ghetti, E. V. Korolkova, V. A. Kudryavtsev, and G. Sartorelli, "A three-dimensional code for muon propagation through the rock: MUSIC," *Astropart. Phys.*, vol. 7, pp. 357–368, 1997.
- [111] M. Anghinolfi, H. Costantini, V. Kulikovski, and M. Taiuti, "GEANT4 simulation of the ANTARES Optical Module," 2009. ANTARES-OPMO-2009-003.
- [112] A. Margiotta, "Study of the effects of water properties on Monte Carlosimulation of the atmospheric muon flux," 2007. internal note ANTARES-SOFT-2007-006.
- [113] J. R. Hörandel, "On the knee in the energy spectrum of cosmic rays," *Astroparticle Physics*, vol. 19, pp. 193–220, May 2003.
- [114] E. Delagnes, F. Druillolle, A. Kouchner, H. Lafoux, H. Le Provost, L. S., and B. Vallage, "ARS: tests, settings and performance for physics, version 4.8," 2006.
- [115] F. Fehr. private communication.
- [116] J. A. Aguilar *et al.*, "Measurement of the atmospheric muon flux with a 4 GeV threshold in the ANTARES neutrino telescope," *Astropart. Phys.*, vol. 33, pp. 86–90, 2010.
- [117] <http://copsosx03.physto.se/wimpsim/>.

- [118] M. Cirelli *et al.*, "Spectra of neutrinos from dark matter annihilations," *Nucl. Phys.*, vol. B727, pp. 99–138, 2005.
- [119] S. Mangano, "Calculation of the trigger rates due to accidental background," 2006. internal note ANTARES-PHYS-2006-008.
- [120] G. C. Hill and K. Rawlins, "Unbiased cut selection for optimal upper limits in neutrino detectors: The model rejection potential technique," *Astropart. Phys.*, vol. 19, pp. 393–402, 2003.
- [121] A. Spies. private communication.
- [122] <http://www.km3net.org/KM3NeT-TDR.pdf>.
- [123] A. Spies, "Neutrinoraten aus Neutralinoannihilationen in der Sonne in verschiedenen Modellen," 2008. diploma thesis at ECAP.
- [124] <http://www.ft.uam.es/personal/rruiz/superbayes/index.php>.

Acknowledgements

The research and writing of this thesis would not have been possible without the support of many people, of which I can only mention few here. I want to acknowledge the continued encouragement and support from my supervisor Professor Dr. Gisela Anton and thank Professor Dr. Uli Katz for providing the second report. Special gratitude I owe to Julia Schmid, Dr. Jürgen Hößl and Ulf Fritsch for proofreading the thesis draft. Furthermore, I thank Professor Dr. Wolfgang Kretschmer and Dr. Jürgen Hößl for daily discussions and guidance, as well as pretzels and coffee. I enjoyed working with Professor Dr. Gerard van der Steenhoven, Dr. Vincent Bertin and Dr. Gordon Lim in the Neutralino Working Group. I am also grateful towards Jutta Schnabel and Klaus Geyer for providing me their ANN codes and Ulf Fritsch, Andi Spies and Andi Gleixner for taking over and continuing the alignment project. Finally I want express my appreciation for the work of the administrators of the ECAP computing cluster, especially Ralf Auer and Dr. Claudio Kopper who put it together in the first place.